Phenomenological applications of η and η' mesons

Sergi Gonzàlez-Solís

Institut de Física d'Altes Energies

Universitat Autònoma de Barcelona

Thesis advisor: Dr. Rafel Escribano

A thesis submitted for the degree of

Doctor of Philosophy

Bellaterra, Juliol 2016

A la Montserrat i en Rafael,
us en devia una.

El més bonic del mar
és allò que no hem navegat

(Nâzim Hikmet Ran)

Nota d'agraïments

L'escrit que el lector té entre les mans és el fruit del meu pas per l'Institut de Física d'Altes Energies. Han estat quatre anys d'aquells que passen d'allò més ràpid però també d'aquells que deixen empremta de per vida. Passat aquest temps puc constatar, si més no, que m'he forjat una opinió més crítica i subjectiva del món que ens envolta. Això que m'enduc, i que no és precissament poc, li vull agrair a en Rafel Escribano i Carrascosa per haver confiat en mi i haver-me donat l'oportunitat de saber-ne una mica més de tot plegat. Gràcies per la teva tutela, un plaer.

Al meu parer el que queda del nostre pas pels llocs en són principalment les amistats i els records, més que no pas les nostres obres o èxits. En aquest sentit, ha estat un altre plaer compartir l'espai-temps d'aquesta tesi amb: Bernat, Clara, Dani, Dirk, Joan, Ke-Yang, Mateo, Matteo, Marc M., Marc R., Sebastian, Thibaud, Xabier, Yuan, amb els diferents postdocs, amb menció especial per a en Pablo, i amb tot el grup de sèniors. Nogensmenys, també voldria agrair l'Institut für Kernphysik–Johannes Gutenberg Universität per acollir-me durant quatre mesos, en especial a en Pere i en Pablo per fer de la meva estada a Mainz d'allò més enriquidora. Mikhail, això també va per tu.

Diuen els lingüistes que les paraules i frases que existeixen en uns idiomes i no en d'altres són material interessant sobre les resistències i les singularitats culturals. Vet aquí la riquesa de la llengua d'aquestes paraules. *Pochemuchka* en rus significa una persona, normalment un nen(a), que fa moltes preguntes. Aquesta va pel pare, per respondre-les totes. En grec, *meraki* significa fer algo amb l'ànima, creativitat i amor. I aquesta en majúscules per la mare. En català, *els arbres no et deixen veure el bosc* és una de les meves predilectes. Només he trobat correspondència amb *nie żałuj róż gdy płonie las* (No ploris per les teves roses quan els boscos cremen) del polonès. Per l'Anna. *Last but not least*, al meu germà i a tota la meva família.

List of acronyms

BR: Branching Ratio

BW: Breit-Wigner

CL: Canterbury or Chisholm Approximants

CL: Confidence Level

ChPT or χ**PT**: Chiral Perturbation Theory

EW: ElectroWeak

LO: Leading Order

NLO: Next-to-Leading Order

OPE: Operator Product Expansion

PA: Padé Approximants

PDG: Particle Data Group

QA: Quadratic Approximants

QCD: Quantum Chromodynamics

QED: Quantum Electrodynamics

RChT or **R**χ**T**: Resonance Chiral Theory

SCC: Second-Class Currents

SFF: Scalar Form Factor

SL: Space-Like

SM: Standard Model

TFF: Transition Form Factor

TL: Time-Like

VMD: Vector Meson Dominance

VFF: Vector Form Factor

Contents

Contents

Introduction

The Standard Model (SM) of particle physics is the best theory for describing all known particles and their interactions we have in Nature so far. It is a renormalizable quantum field theory, based on the gauge symmetry group $SU(3)_C \otimes SU(2)_L \otimes U(1)_Y$, which describes strong, weak and electromagnetic interactions[1], through the exchange of gluons, $W^{\pm}$ and Z bosons and photons, respectively. Despite the SM does leave unexplained phenomena[2], it has successfully described a huge amount of experimental results and predicted a large variety of phenomena. In the framework of the SM, predictions for physical quantities arise from using perturbation theory expanding in terms of the coupling constant of the considered interaction. As a matter a example, in quantum electrodynamics (QED) the expansion is performed in terms of α_{QED} and perturbation theory has led to predictions with astonishing precision. For instance, the QED prediction of the anomalous magnetic moment of the electron is the most precisely verified prediction in the human history, it is know to an accuracy of around one part in one billion. The reason of the success of perturbative tools applied to QED lies on the magnitude of the coupling strength α_{QED} which, as it is rather small, the higher the order of a term the lesser their contribution it will be and, as a consequence, infinite series can be approximated quite well by a finite sum. However, this method is no longer valid to describe strong interactions in its full glory. In quantum chromodynamics (QCD), the theory of strong interactions in the SM, the coupling strength α_s depends very much on the energy regime we want to explore. At high-energies (or equivalently, at very short distances), the strong coupling α_s is small and, consequently, the quarks and gluons interact weakly behaving like free particles. This outcome is known as *asymptotic freedom* [1, 2, 3]. Thus, physical observables in this energy regime can be suitably described by means of a perturbative expansion in

---

[1]The SM describe strong and electroweak interactions i.e. three of the four fundamental forces of Nature. The remaining force, the gravity, is completely separate from the SM, but instead described by Einstein's general relativity. This is one incentive to look for physics beyond the SM.

[2]The standard model does not accommodate phenomena such dark matter, dark energy, neutrino masses or the matter-antimatter asymmetry of the universe.

powers of α_s, the so-called perturbative QCD (pQCD) approach. On the contrary, α_s at low-energies (or equivalently, at large distances) becomes larger, thus invalidating the use of perturbative techniques and making impossible to find isolated quarks and gluons in Nature so far. Instead, one observes hadrons (baryons and mesons), which can be considered as bound states made of quarks and gluons. This is the peculiarity of the strong force that does not decrease but grow with distance which, based on our experience with the electromagnetic or gravitational forces, causes a counterintuitive scenario. This is a consequence of the so-called *confinement* mechanism, which has not been mathematically proven yet[3]. Therefore, the low-energy region requires another approach to be described. Numerical QCD simulations on the lattice or the S-matrix theory method are two examples that have provided interesting and useful results to deal this regime. On the lattice QCD side, it has been possible to determine from first principles some of the QCD input parameters such quark masses or the strong coupling constant among other things while the S-matrix theory, based on mathematical guidelines such as analyticity, unitarity and symmetry arguments, has given rise to the dispersion relation techniques we will widely employ in this thesis. Another possibility is an effective field theory where the hadrons become the relevant degrees of freedom. Chiral Perturbation Theory (ChPT) [5, 6, 7] is such effective theory for mesons which, based on the chiral symmetry, encodes the relevant dynamics occurring in the low-energy domain of QCD. It is described in terms of eight pseudo-Goldstone bosons, three π, two K and the η, as the relevant degrees of freedom and organized through a double perturbative expansion in momenta and quark masses. ChPT is predictive when the energy (or momenta) and masses of the mesons is small compared to the chiral symmetry breaking scale, in this case of the order of one GeV. From a phenomenological point of view, it has successfully been applied for describing lots of processes involving π and K but much less for the η. Actually, the η entering in ChPT is not the physical ones but rather a part of it corresponding to the octet. In reality, the η meson has a second component, coming from the pseudoscalar singlet, which is not systematically included in ChPT. A plausible framework to describe the dynamics of the physical η and η' mesons is the extended large-N_c limit of ChPT [8] which includes the pseudoscalar singlet η_1 and considers also the number of colors in the expansion. From the experimental point of view, there is a series of ongoing experiments e.g. BELLE-II, BESIII [9], CrystalBall@MAMI [10], KLOE@DAPHNE and WASA@COSY [11], with the study of the phenomenology associated to the η

---

[3]In fact, under the name of "Yang-Mills existence and mass gap", its proof belongs to one of the so-called seven Millennium Problems [4].

and η' among their main objectives. Fruit of this experimental activity in the field, we are entering into a precision era on the η and η' system which makes the physics of both mesons a question of great theoretical interest which should result in having a better and more complete knowledge of strong interactions at low-energies. The main goal of this thesis has been devoted to deal with some phenomenological applications involving the η and η' mesons.

This thesis is structured as follows. The first two chapters are dedicated to discuss the theoretical basics relevant for presenting the processes investigated in the rest of the work. Chapter 1 is devoted to provide a brief overview of the theory of strong interactions with particular attention on the description of the low-energy realm, while chapter 2 is reserved to present the concept of dispersion relations where we derive the Omnès equation in good detail. Then, we will go on to discuss the topics studied in this thesis which is divided into two main parts as summarized below. Finally, we collect and discuss the most important results obtained in the dissertation in chapter 9.

Hadronic tau decays

In part I of this work, we will analyze different semileptonic decays of the tau lepton. Such processes provide a clean and advantageous framework for investigating QCD in the non-perturbative regime since half of the process is purely electroweak and, therefore, free of uncertainties at the required precision. Tau decays constitute an ideal scenario for understanding the hadronization of QCD currents as well as for determining the physical parameters, mass and width, of the intermediate resonances that drive the processes. The strong dynamics is codified in the hadronic matrix element which in turn is represented in terms of form factors whose parameterization is of utmost importance for having a good understanding of the decays.

First, in section 3 we will analyze the experimental measurement of the invariant mass distribution released by the Belle Collaboration on the exclusive decay $\tau^- \to K^- \eta \nu_\tau$ [12] and predict the decay $\tau^- \to K^- \eta' \nu_\tau$ for which only an upper bound for the branching ratio exists. The analysis have been performed by means of dispersion relations after a proper description of the participant form factors based on ChPT including resonances as explicit degrees of freedom. The results for the mass and the width of the $K^*(1410)$ we have obtained in our study [13] appeared to be in accordance with those from the $K^*(892)$ dominating mode $\tau^- \to K_S \pi^- \nu_\tau$ obtained in previous works [14, 15]. This fact motivated us to perform a combined analysis of

both decays channels afterwards [16] with the main goal of improving our knowledge on the $K^*(1410)$ resonance parameters.

The combined analysis of the experimental decay spectra of $\tau^- \to K_S \pi^- \nu_\tau$ and $\tau^- \to K^- \eta \nu_\tau$ is done in section 4. We have obtained the physical $K^*(892)$ and $K^*(1410)$ resonance parameters defined by the pole position in the complex plane. The mass and the width of the $K^*(1410)$ have been determined with a substantial improvement as a main result and discussed prospects of improvement for Belle-II. We have also investigated possible isospin violations in the low-energy form factor parameters as the $K^- \pi^0$ vector form factor enters the description of the $K^- \eta$ decay mode. In this respect, we emphasize the necessity of making available the acceptance corrected spectrum of the transition $\tau^- \to K^- \pi^0 \nu_\tau$ [17], as it would allow to further investigate the source of those isospin violations.

We close the first part of the thesis with the study of the decays $\tau^- \to \pi^- \eta^{(\prime)} \nu_\tau$ in section 5. These processes occur via isospin violation and belong to the so-called second class currents unseen in Nature so far. Our study [18] is focused in the representation of the required vector and scalar form factors which is based in ChPT including resonances. Following the analytical properties of a form factor, we have discussed elastic and inelastic unitarity corrections in the parameterization of the required scalar form factor while the vector form factor has been extracted in a model-independent way benefited from existing data on the well-known $\pi^- \pi^0$ one [19]. According to our results, their discovery may be possible at forthcoming hadron facilities Belle-II and BESIII thanks to the increased luminosity respect to predecessor laboratories. In this section, the form factors entering the description of $\tau^- \to \pi^- \eta^{(\prime)} \nu_\tau$ decays have been also applied to describe the semileptonic $\eta^{(\prime)} \to \pi^- \ell^+ \nu_\ell$ $(\ell = e, \mu)$ decays since they are related by crossing symmetry.

Phenomenological applications of Padé approximants

Regarding part II of the thesis, we will begin with a brief introduction to the mathematical method of Padé approximants (PA) in chapter 6, where we sketch their most important features and provide some pedagogical examples.

The usefulness of PA as fitting functions have been extensively illustrated in literature, see e.g Ref. [20] aimed at describing the pion vector form factor. In Refs. [21, 22, 23], PA have also shown a remarkable ability in describing the existing experimental data [24] on the single virtual pseudoscalar transition form factor (TFF) $\gamma^* \gamma \to \mathcal{P}$ $(\mathcal{P} = \pi^0, \eta$ and $\eta')$, extracted from the reaction $e^+ e^- \to e^+ e^- \mathcal{P}$ in the space-like region. Regarding the experimental measurement of the transition form

factor of double virtuality, $\gamma^*\gamma^* \to \mathcal{P}$, it is still an experimental challenge which may be unveiled in the near future. These TFF have recently attracted a lot of attention, both from the experimental and theoretical sides, since enter the determination of the pseudoscalar-exchange contribution to the hadronic light-by-light scattering part of the anomalous magnetic moment of the muon, a_μ, whose SM prediction results in $(3-4)$ standard deviation difference with the current experimental value. It is then clear that a good description of these TFF is indispensable in the SM precision physics era.

The time-like region of these TFF can be accessed at present meson facilities either through the single and double Dalitz decays $\mathcal{P} \to \ell^+\ell^-\gamma$ and $\mathcal{P} \to \ell^+\ell^-\ell^+\ell^-$ ($\ell = e$ or μ). Here it lies our interest in these decays which we will examine in section 7 by means of a data-driven approach based on the use of Padé approximants applied to π^0, η and η' TFF experimental data in the space-like region. We anticipate the remarkable ability of the PA as obtained from fits to the space-like region in describing the time-like regime. Our predictions are in accordance with those decays measured at present time. We hope our work also to serve as a motivation for the experimental groups to pursue the unmeasured one.

Finally, in section 8 we will perform a combined a analysis of both space-and time-like experimental data on the η' transition form factor benefited by the recent measurement on $\eta' \to e^+e^-\gamma$ released by the BESIII Collaboration [25]. The reason why PA applied to the time-like region work so well will be discussed. Our combined study allows for the extraction of the low-energy parameters of the TFF as well as their values at zero and infinity momentum transfer with substantial improved precision. The impact on the mixing parameters of the $\eta - \eta'$ system will be also addressed.

Chapter 1

Theoretical framework

The intent of this chapter is not to discuss QCD in its totality but rather to provide the sufficient theoretical background relevant for presenting the topics investigated in this thesis. We have tried hence to highlight the most important aspects regarding the theory of strong interactions providing details where they are needed for later use. Nonetheless, the interested reader is referred to Refs. [26, 27, 28, 29, 30] to deepen on the subject.

1.1 Quantum Chromodynamics

Quantum Chromodynamics is the theory aimed at describing the strong interactions among quarks and gluons. The most general QCD Lagrangian reads

$$\mathcal{L}_{QCD} = \sum_f \bar{q}_f \left(i\slashed{D} - \mathcal{M} \right) q_f - \frac{1}{4} G^a_{\mu\nu} G^{\mu\nu}_a \,, \tag{1.1}$$

where the sum runs over the six quark flavours, $f = u, d, s, c, b, t$, for the up, down, strange, charm, bottom and top, respectively. $\mathcal{M}$ represents the quark mass matrix and it is given by $\mathcal{M} = \mathrm{diag}(m_u, m_d, m_c, m_s, m_t, m_b)$, where m stands for the mass of the specific quark flavour.

The covariant derivative keeps the kinetic term in Eq. (1.1) invariant under local $SU(3)_C$ gauge transformations and is given by

$$D_\mu = \partial_\mu - ig_s \sum_{a=1}^{8} \frac{\lambda_a}{2} \mathcal{A}^a_\mu \,. \tag{1.2}$$

The interactions among quarks and gluons emerge due to the gluon field $\mathcal{A}^a_\mu$ entering the covariant derivate while the strength of the interaction is dictated by the strong coupling constant g_s (commonly referred as $\alpha_s \equiv g_s^2/4\pi$). The color index a runs

Quark flavour	Mass
u	$2.3^{+0.7}_{-0.5}$ MeV
d	$4.8^{+0.7}_{-0.3}$ MeV
s	95 ± 5 MeV
c	1.275 ± 0.025 GeV
d	4.66 ± 0.03 GeV
d	$173.21 \pm 0.51 \pm 0.71$ GeV

Table 1.1: Quark masses as given by the pdg [37].

from 1 to 8 due to the $SU(3)$ group has eight generators, λ_a, known as Gell-Mann matrices [31] satisfying

$$[\lambda_a, \lambda_b] = 2i f_{abc} \lambda^c \,, \tag{1.3}$$

where f^{abc} are the structure constants of the group, which are real and antisymmetric. Finally, the non-abelian field strength tensor containing the gauge gluons fields $\mathcal{A}^a_\mu$ is defined by

$$G^a_{\mu\nu} = \partial_\mu \mathcal{A}^a_\nu - \partial_\nu \mathcal{A}^a_\mu + g_s f^{abc} \mathcal{A}^b_\mu \mathcal{A}^c_\nu \,, \tag{1.4}$$

which enters Eq. (1.1) squared, thus leading a kinetic term for the gluon field as well as self-interaction terms among three and four gluon fields proportionals to g_s and g_s^2, respectively. The responsible for the appearance of self-interactions among gauge fields is the last term of Eq. (1.4) as consequence of the non-Abelian nature of QCD. This feature becomes a change of paradigm respect QED, since this property is not present there. It is then reasonable to think that the existence of self-gluon interactions may be the responsible of two capital features of QCD that are not present in QED either: *asymptotic freedom* and *confinement*. These two effects can be better understood if we take a look at Figure 1.1 where we provide a graphical account of the behaviour of the strength of the strong coupling α_s as a function of the energy scale of the interaction. From the figure we can clearly differentiate two regions. On one side, asymptotic freedom occurs in the high-energy region where the coupling strength α_s is weak and quarks and gluons behave, inside the hadrons, almost as free particles. In this regime, perturbation theory techniques are allowed to make predictions on measurable quantities such cross sections or decays widths. In other words, interactions can be accounted for through a perturbative series expansion around the free theory in terms of the coupling constant. As in this domain the strength of the coupling is small, the importance of the contributions decreases quickly with increasing the order, thus giving a fast convergence of the series. This leads to the so-called perturbative approach to QCD (pQCD). On the other side, the coupling
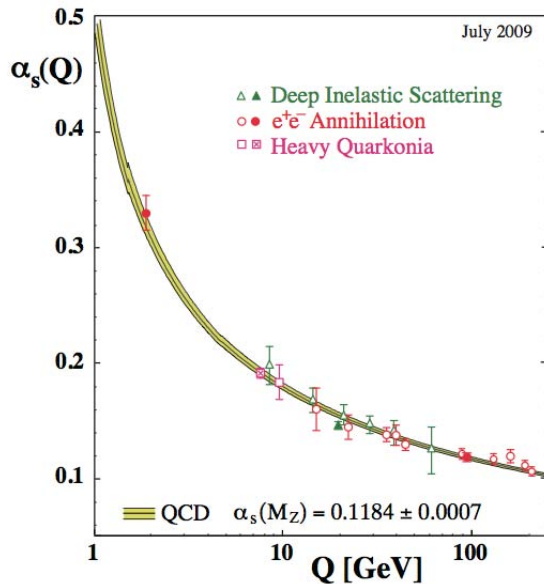
Figure 1.1: Behaviour of the strong coupling α_s as a function of the energy scale Q [GeV] (the image has been borrowed from Ref. [32]).

constant asymptotically grows at low-energies which leads the quarks become more and more tightly bounded. In fact, if one try to separate a quark-antiquark pair the force joining them increases. At some moment, it is energetically favorable to create a new quark-antiquark pair that recombine into two mesons and so one and so forth. This is known as confinement and explains why it is not possible to find isolated quarks and gluons in Nature but hadrons instead. The size of the QCD coupling at a typical hadronic scale $\approx 1\,\text{GeV}$, $\alpha_s(1\,\text{GeV}) \approx 0.5$, indicates that the low-energy realm of QCD can not be adequately described my means of a perturbative expansion in terms of α_s since it becomes larger. At first sight the situation may seem worrisome: we have written down the QCD Lagrangian Eq. (1.1) for describing the interactions among quarks and gluons which can not account for what we really see in Nature so far, the hadrons. This fact gave birth to Chiral Perturbation Theory, the effective field theory aimed at describing the low-energy region of QCD for mesons. We devote section 1.2 to introduce the most important aspects and equations of ChPT useful for the development of the thesis.

1.1.1 Symmetries in the QCD Lagrangian

In the SM, fermions and gauge bosons acquire mass via the Brout-Englert-Higgs-Guralnik-Hagen-Kibble mechanism [33, 34, 35, 36], usually also known in short as

the Higgs mechanism. However, the Higgs field is certainly not the responsible for most of the visible mass in the universe, made essentially of protons and neutrons, but rather QCD. In other words, the contribution of the quark masses to the mass of proton is negligible and almost the entire proton mass arise from the energy binding the quarks together, the so-called binding energy. Actually, this phenomenon also occurs in the hydrogen atom for example, where the isolated mass of the proton plus the isolated mass of the electron is slightly different than the mass of the two entities combined, because the energy due to the interaction among them influences the mass of the entire system. In the hydrogen atom this effect is tiny but inside a nucleus the interaction energy is large and can not be neglected. This is a consequence of what the famous Einstein's equation $E = mc^2$ is telling us. It is then reasonable to associated the mass of the proton $m_p \approx 1$ GeV as Λ_{QCD}, the scale that determines the strength of strong interactions. Λ_{QCD} splits up the six quarks given in table 1.1 in two groups. One formed by the u, d and s quarks whose masses lie below Λ_{QCD} and another composed of the c, b and t quarks with masses above Λ_{QCD}. These two sets are called accordingly light and heavy quarks. As low-energy QCD deal with the physics occurring below Λ_{QCD}, we will only consider the light quarks as the explicit degrees of freedom entering the QCD Lagrangian in the following and ignore the heavy quarks henceforth.

The QCD Lagrangian Eq. (1.1) can be re-expressed in terms of the left-and right-handed components of the quark field, $q_L = P_L q$ and $q_R = P_R q$, by means of the helicity projection operators

$$P_R = \frac{1}{2}(1 + \gamma_5) = P_R^\dagger, \quad P_L = \frac{1}{2}(1 - \gamma_5) = P_L^\dagger, \tag{1.5}$$

which fullfil

$$P_R + P_L = 1, \quad P_{R,L}^2 = P_{R,L}, \quad P_R P_L = P_L P_R = 0, \tag{1.6}$$

yielding

$$\mathcal{L}_{QCD} = \mathcal{L}_{QCD}^0 + \mathcal{L}_{QCD}^m, \tag{1.7}$$

with

$$\mathcal{L}_{QCD}^0 = \bar{q}_R i \slashed{D} q_R + \bar{q}_L i \slashed{D} q_L - \frac{1}{4} G_{\mu\nu}^a G_a^{\mu\nu} \tag{1.8}$$

$$\mathcal{L}_{QCD}^m = -\bar{q}_L \mathcal{M} q_R - \bar{q}_R \mathcal{M} q_L. \tag{1.9}$$

The reason to split Eq. (1.7) into two pieces is that while the first term, $\mathcal{L}_{QCD}^0$, do not mix left-and right-handed quark fields, the second $\mathcal{L}_{QCD}^m$, which involve the quark mass matrix $\mathcal{M}$, do mix. In the so-called chiral limit, where the quarks masses

are neglected, only the $\mathcal{L}^0_{QCD}$ term in Eq. (1.7) is allowed and the QCD Lagrangian remains invariant under the transformations

$$q_L \to U_L q_L, \quad q_R \to U_R q_R, \tag{1.10}$$

where

$$U_L = \exp\left(-i\sum_{a=1}^{8}\theta_a^L \frac{\lambda_a}{2}\right)\exp^{-i\theta^L}, \quad U_R = \exp\left(-i\sum_{a=1}^{8}\theta_a^R \frac{\lambda_a}{2}\right)\exp^{-i\theta^R}. \tag{1.11}$$

Therefore, in the chiral limit Eq. (1.7) exhibits a global $U(3)_L \otimes U(3)_R$ symmetry, the so-called chiral symmetry since the transformations act on the left-and right-handed components independently. The symmetry group $U(3)_L \otimes U(3)_R$ can be rewritten as

$$U(3)_L \otimes U(3)_R = SU(3)_L \otimes SU(3)_R \otimes U(1)_L \otimes U(1)_R, \tag{1.12}$$

to study the conserved currents corresponding to each of the sub-groups. There are 9 left-and 9 right-handed currents that led the $\mathcal{L}^0_{QCD}$ Lagrangian invariant

$$L^{\mu,a} = \bar{q}_L \gamma^\mu \frac{\lambda_a}{2} q_L, \quad L^\mu = \bar{q}_L \gamma^\mu q_L, \quad R^{\mu,a} = \bar{q}_R \gamma^\mu \frac{\lambda_a}{2} q_R, \quad R^\mu = \bar{q}_R \gamma^\mu q_R, \tag{1.13}$$

which according to Noether's theorem are conserved

$$\partial_\mu L^{\mu,a} = \partial_\mu L^\mu = \partial_\mu R^{\mu,a} = \partial_\mu R^\mu = 0. \tag{1.14}$$

These currents are however usually given in terms of vector and axial-vector currents via the linear combinations

$$V^{\mu,a} = R^{\mu,a} + L^{\mu,a} = \bar{q}\gamma^\mu \frac{\lambda_a}{2} q, \quad V^\mu = R^\mu + L^\mu = \bar{q}\gamma^\mu q, \tag{1.15}$$

$$A^{\mu,a} = R^{\mu,a} - L^{\mu,a} = \bar{q}\gamma^\mu \gamma_5 \frac{\lambda_a}{2} q, \quad A^\mu = R^\mu - L^\mu = \bar{q}\gamma^\mu \gamma_5 q, \tag{1.16}$$

which lead the corresponding conserved charges

$$Q_V^a = \int d^3 x V^{0,a}(t,x), \quad Q_V = \int d^3 x V^0(t,x), \tag{1.17}$$

$$Q_A^a = \int d^3 x A^{0,a}(t,x), \quad Q_A = \int d^3 x A^0(t,x). \tag{1.18}$$

The global phase transformations with $\theta^L = \theta^R$ belong to $U(1)_V \equiv U(1)_{L+R}$ while the ones with $\theta^L = -\theta^R$ to $U(1)_A \equiv U(1)_{R-L}$. Then, the singlet vector charge Q_V can be interpreted as the conservation of the baryon number arising from the invariance of the QCD Lagrangian under $U(1)_V$ symmetry transformations yielding

$$B = \frac{1}{3}\int d^3 x \bar{q}\gamma^0 q = \frac{1}{3}\int d^3 x q^\dagger q, \tag{1.19}$$

which assigns 1/3 for quarks and -1/3 for antiquarks leading $B = 0$ for mesons and $B = 1$ for baryons. On the contrary, the singlet axial vector current A^μ obeying $U(1)_A$ symmetry transformations remains conserved at the classical level but brakes down upon quantization leading

$$\partial_\mu A^\mu = \frac{3g^2}{32\pi^2} \varepsilon_{\mu\nu\rho\sigma} \mathcal{G}_a^{\mu\nu} \mathcal{G}_a^{\rho\sigma} \,. \tag{1.20}$$

This phenomenon is known as the axial anomaly of QCD and will be further discussed in section 1.5. Regarding the octets, the vector-and axial vector-currents $V^{\mu,a}$ and $A^{\mu,a}$, associated to $SU(3)_L \otimes SU(3)_R$ symmetry are conserved both at the classical and quantum level. In all, the QCD Lagrangian in the chiral limit, $\mathcal{L}_{QCD}^0$, is therefore invariant under transformations of the symmetry group

$$SU(3)_L \otimes SU(3)_R \otimes U(1)_V \,. \tag{1.21}$$

However, if the quark mass matrix term $\mathcal{L}_{QCD}^m$ in Eq. (1.7) is also allowed, the QCD Lagrangian is not invariant under $SU(3)_L \otimes SU(3)_R$ symmetry transformations anymore leading to the chiral symmetry breaking phenomenon. Consequently, the vector and axial vector currents are not conserved

$$\partial_\mu V^{\mu,a} = i\bar{q} \left[\mathcal{M}, \frac{\lambda_a}{2} \right] q \,, \quad \partial_\mu V^\mu = 0 \,,$$
$$\partial_\mu A^{\mu,a} = i\bar{q} \left[\mathcal{M}, \frac{\lambda_a}{2} \right] \gamma_5 q \,, \quad \partial_\mu A^\mu = 2i\bar{q}\mathcal{M}\gamma_5 q + \frac{3g^2}{32\pi^2} \varepsilon_{\mu\nu\rho\sigma} \mathcal{G}_a^{\mu\nu} \mathcal{G}_a^{\rho\sigma} \,. \tag{1.22}$$

So far, we have seen that the explicit source of the chiral $SU(3)_L \otimes SU(3)_R$ symmetry breaking arise from the quark masses and since these are small the chiral symmetry of QCD is usually referred as an approximate symmetry. Actually, the QCD dynamics at low energies can be described by means of a perturbative expansion in terms of the small quark masses. Notice that for equal quark masses, $m_u = m_d = m_s$, the eight vector currents $V^{\mu,a}$ are conserved since $[\lambda_a, 1] = 0$. We would also like notice that the quark masses induces a new source of $U(1)_A$ symmetry breaking on the singlet axial vector current A^μ apart from the anomaly and that the QCD Lagrangian remains invariant under $U(1)_V$ symmetry group in any case.

1.1.2 Spontaneous chiral symmetry breaking

Regarding the meson spectrum, in an exact $SU(3)_L \otimes SU(3)_R$ flavour symmetric world one may expect the particles collected in the same multiplet to have the same spin and masses. In the real world, the flavor symmetry is basically broken due to

the large mass of the strange quark compared to the up and down quark masses. Because of that we do not expect the particles in the same multiplet to have exactly the same mass. Moreover, the associated charges Q_V^a and Q_A^a as obtained in Eq. (1.18) transform under parity, respectively, as a vector and axial vector operators

$$Q_V^a \to Q_V^a \,, \quad Q_A^a \to -Q_A^a \,, \tag{1.23}$$

and are time independent i.e. they commute with the massless QCD Hamiltonian

$$[Q_V^a, H_{QCD}^0] = [Q_A^a, H_{QCD}^0] = 0 \,. \tag{1.24}$$

Consider the eigenstates $|\phi\rangle$ of H_{QCD}^0 with eigenvalues E

$$H_{QCD}^0|\phi\rangle = E|\phi\rangle \,. \tag{1.25}$$

Then, since Q_V^a and Q_A^a commute with the H_{QCD}^0 (cf. Eq. (1.24)) one would expect the states $Q_V^a|\phi\rangle$ and $Q_A^a|\phi\rangle$ to have the same energy E carrying opposite parity (cf. Eq. (1.23)). This means that for each particle with specific spin (J) and parity (P) quantum numbers, there should exist another one with the same spin but opposite parity both of them with the same mass. However, by looking at the meson spectrum in table 1.2, we see that there is no trace of such a symmetry in nature so far since the masses of the pseudoscalar particles ($J^P = 0^-$) are drastically different than the scalar ($J^P = 0^+$) one. The solution to this puzzle was provided by Vafa and Witten

J^P	Particle	Mass (MeV)	Quark content
0^-	π^0	134.9766	$(u\bar{u} - d\bar{d})/\sqrt{2}$
	π^+, π^-	139.57018	$u\bar{d}, \bar{u}d$
	K^+, K^-	493.677	$u\bar{s}, \bar{u}s$
	$K^0, \bar{K}^0$	497.614	$d\bar{s}, \bar{d}, s$
	η	547.853	$(u\bar{u} + d\bar{d} - 2s\bar{s})/\sqrt{6}$
	η'	957.78	$(u\bar{u} + d\bar{d} + s\bar{s})/\sqrt{3}$
0^+	a_0^0	~ 980	$(u\bar{u} - d\bar{d})/\sqrt{2}$
	a_0^+, a_0^-	~ 980	$u\bar{d}, \bar{u}d$
	K^{*+}, K^{*-}	~ 892	$u\bar{s}, \bar{u}s$
	$K^{*0}, \bar{K}^{*0}$	~ 800	$d\bar{s}, \bar{d}, s$
	f_0	~ 980	$(u\bar{u} + d\bar{d} - 2s\bar{s})/\sqrt{6}$

Table 1.2: Mass spectrum of the lightest mesons according to pdg [37].

[38], who proved that the vector charges Q_V^a annihilates the vacuum, and by Nambu

and Lasinio [39, 40], who proved that the vacuum is not invariant under the action of axial charges Q_A^a,

$$Q_V^a|0\rangle = 0, \quad Q_A^a|0\rangle \neq 0.$$ (1.26)

Consequently, as the full symmetry of the (massless) hamiltonian is not shared by the ground state (vacuum), the chiral $SU(3)_L \otimes SU(3)_R$ symmetry is said to be spontaneously broken down to the subgroup $SU(3)_V$,

$$SU(3)_L \otimes SU(3)_R \xrightarrow{\text{SCSB}} SU(3)_V.$$ (1.27)

In that case, there is no need for the masses of the pseudoscalar and scalar particles to be equal. According to Goldstone's theorem [41, 42], for a global continuous symmetry of the Lagrangian, the theory must contain a massless and spinless particle for every spontaneously broken generator, the so-called *Goldstone Bosons*. In our particular case, as we have eight axial charges that do not annihilate the vacuum one expect eight pseudoscalar Goldstone bosons to appear. Actually, since $SU(3)_V$ is an approximate symmetry which is broken by the presence of the quark masses, in the real world one would expect the Goldstone bosons to acquire small masses via the symmetry breaking parameter. Thus, they are usually called pseudo-Goldstone bosons. Therefore, from the above discussions, the pseudo-Goldstone bosons must be light pseudoscalars transforming as an octet under $SU(3)_V$. This is actually what is inferred by looking at the particle spectrum in table 1.2, the eight lightest mesons (three pions $\pi^\pm$ and π^0, four kaons $K^\pm$, K^0 and $\bar{K}^0$, and the η) become the best candidates for being the pseudo-Goldstone bosons associated to the spontaneous chiral symmetry breaking (SCSB) $SU(3)_L \otimes SU(3)_R \xrightarrow{\text{SCSB}} SU(3)_V$. The next task is then to build a low-energy theory involving these pseudo-Goldstone bosons as dynamical degrees of freedom.

1.2 Chiral Perturbation Theory

Effective Field Theories (EFT) are the appropriate theoretical tool to describe physics below some energy scale Λ. The idea of EFT is to take into account the relevant degrees of freedom for the problem at hand i.e. those states with $m \ll \Lambda$, and integrate out the heavier one $M \gg \Lambda$ from the action. An interesting fact is that we do not lose track from that heavier states at all since the information is contained within the couplings of the resulting effective Lagrangian. The classical example of an EFT is the Fermi theory of weak interactions as the low-energy realization of the

$SU(2) \otimes U(1)$ electroweak SM where the information of the high-energy dynamics, carried by the W boson, is encoded within the Fermi coupling constant.

The general method to construct effective Lagrangians with spontaneous symmetry breaking was proposed by Callan, Coleman, Wess and Zumino [43, 44] who provided a suitable manner to parametrize Goldstone bosons. For the case that concern us, we would like to write down an effective theory for describing low-energy QCD. Of course, it must contain the same symmetries as QCD i.e. Lorentz invariance, parity and charge conjugation, but with mesons as explicit degrees of freedom rather than the quarks. The standard choice to collect the pseudo-Goldstone fields is through (see e.g. Ref. [45] for a detailed derivation)

$$U(\Phi) = \exp\left(i\sqrt{2}\Phi/f\right), \tag{1.28}$$

where

$$\Phi = \sum_a \frac{\lambda_a}{\sqrt{2}}\phi_a = \begin{pmatrix} \frac{1}{\sqrt{2}}\pi_3 + \frac{1}{\sqrt{6}}\eta_8 & \pi^+ & K^+ \\ \pi^- & -\frac{1}{\sqrt{2}}\pi_3 + \frac{1}{\sqrt{6}}\eta_8 & K^0 \\ K^- & \bar{K}^0 & -\frac{2}{\sqrt{6}}\eta_8 \end{pmatrix}, \tag{1.29}$$

is a 3×3 $SU(3)$ traceless matrix and f a constant which we will discuss later. The matrix $U(\Phi)$ under $SU(3)_L \otimes SU(3)_R$ transforms as

$$U(\Phi) \to g_R U(\Phi) g_L^\dagger, \tag{1.30}$$

with $g_{L,R} \in SU(3)_{L,R}$. Once $U(\Phi)$ is defined, the low-energy effective Lagrangian realization of QCD can be obtained. Chiral Perturbation Theory (ChPT) is such effective theory for QCD [6, 7] and it is formulated in terms of the matrix field U, its derivatives $\partial_\mu U$ and the quark mass matrix $\mathcal{M}$. These building blocks of the ChPT Lagrangian count as

$$U = \mathcal{O}(p^0), \quad \partial_\mu U = \mathcal{O}(p), \quad \mathcal{M} = \mathcal{O}(p^2), \tag{1.31}$$

which determines the order of any term built from the meson fields and the quark masses. Thus, the ChPT Lagrangian can be organized in terms of increasing powers of momentum (or equivalently in powers of derivatives) and quark masses

$$\mathcal{L}_{\chi PT} = \sum_{n=1}^{\infty} \mathcal{L}_{2n} = \mathcal{L}_2 + \mathcal{L}_4 + \mathcal{L}_6 \dots, \tag{1.32}$$

where the subindices accounts for the expansion order. As soon as the momentum of the mesons become comparable to Λ, the predictiveness of the χPT Lagrangian

is questioned. The scale Λ is usually settled to the energy region where resonances arise as new degrees of freedom since resonance poles cannot be reproduced by a polynomial expansion series. As the ρ is the lightest resonance, it is reasonable to consider its mass as an estimate of the CHPT range of validity $\Lambda_{\chi PT} \sim M_\rho$.

Because of Lorentz invariance, only even chiral orders are possible. The lowest-order Lagrangian $\mathcal{O}(p^2)$ contains the minimum number of derivatives and in the chiral limit i.e. neglecting the mass term, reads

$$\mathcal{L}_2 = \frac{f^2}{4}\langle \partial_\mu U^\dagger \partial^\mu U \rangle\,, \tag{1.33}$$

which by taking the expansion of Eq. (1.28) in powers of Φ

$$U = \exp\frac{i\sqrt{2}\Phi}{f} = 1 + \frac{i\sqrt{2}\Phi}{f} + \frac{1}{2!}\left(\frac{i\sqrt{2}}{f}\right)^2 \Phi^2 + \frac{1}{3!}\left(\frac{i\sqrt{2}}{f}\right)^3 \Phi^3 \dots\,, \tag{1.34}$$

$$\partial_\mu U = \frac{i\sqrt{2}}{f}\partial_\mu\Phi - \frac{1}{f^2}\partial_\mu\Phi^2 - \frac{i\sqrt{2}}{3f^3}\partial_\mu\Phi^3 \dots\,, \tag{1.35}$$

we get

$$\mathcal{L}_2 = \frac{1}{2}\langle \partial_\mu\Phi\partial^\mu\Phi \rangle + \frac{1}{12f^2}\langle (\Phi(\partial_\mu\Phi) - (\partial_\mu\Phi)\Phi)(\Phi(\partial^\mu\Phi) - (\partial^\mu\Phi)\Phi) \rangle + \mathcal{O}(\Phi^6/f^4)\,, \tag{1.36}$$

where the first and second terms stand, respectively, for the Goldstone kinetic terms and a tower of interactions increasing in the (even) number of pseudoscalars.

However, the lightest mesons do not experience only interactions among themselves but electroweak one as well. Moreover, one should also incorporate the explicit breaking of the chiral symmetry through the quark masses. All this can be achieved by adding to the massless QCD Lagrangian, $\mathcal{L}_{QCD}^0$, quark couplings to external classical fields v^μ (vector), a^μ (axial-vector), s (scalar) and p (pseudoscalar), such that the Lagrangian reads

$$\mathcal{L}_{QCD} = \mathcal{L}_{QCD}^0 + \bar{q}\gamma^\mu(v_\mu + \gamma_5 a_\mu)q - \bar{q}(s - i\gamma_5 p)q\,. \tag{1.37}$$

By separating the quark fields into its left-and right-hand parts, q_L and q_R, and defining the corresponding left-and right-handed external fields as

$$r_\mu = v_\mu + a_\mu\,, \quad l_\mu = v_\mu - a_\mu\,, \tag{1.38}$$

the Lagrangian in Eq. (1.37) can be rewritten as

$$\mathcal{L}_{QCD} = \mathcal{L}_{QCD}^0 + \bar{q}_L\gamma^\mu l_\mu q_L + \bar{q}_R\gamma^\mu r_\mu q_R - \bar{q}_R(s + ip)q_L - \bar{q}_L(s - ip)q_R\,. \tag{1.39}$$

15

Notice, that by comparing Eq. (1.39) with the Lagrangian of the electroweak Standard Model, one can deduce the couplings of the quarks to the external fields r_μ and l_μ to be

$$
\begin{aligned}
r_\mu &= eQA_\mu\,,\\
l_\mu &= eQA_\mu + \frac{2}{\sqrt{2}\sin\theta_W}(W_\mu^\dagger T_+ + h.c.)\,,\\
s &= \mathcal{M}\,,\\
p &= 0\,,
\end{aligned}
\tag{1.40}
$$

where the quark-charge (Q) and the quark-mass matrix $(\mathcal{M})$ are defined by

$$
Q = \frac{1}{3}\mathrm{diag}(2,-1,-2)\,, \quad \mathcal{M} = \mathrm{diag}(m_u, m_d, m_s)\,,
\tag{1.41}
$$

while T_+ is a 3×3 matrix containing the relevant Cabibbo-Kobayashi-Maskawa elements

$$
T_+ = \begin{pmatrix} 0 & V_{ud} & V_{us} \\ 0 & 0 & 0 \\ 0 & 0 & 0 \end{pmatrix}.
\tag{1.42}
$$

The Lagrangian as given in Eq. (1.39) is invariant under $SU(3)_L \otimes SU(3)_R \otimes U(1)_V$ symmetry transformations provided that the externals fields transform as

$$
\begin{aligned}
q_L &\rightarrow g_L q_L\,,\\
q_R &\rightarrow g_R q_R\,,\\
l_\mu &\rightarrow g_L l_\mu g_L^\dagger + i g_L \partial_\mu g_L^\dagger\,,\\
r_\mu &\rightarrow g_R r_\mu g_R^\dagger + i g_R \partial_\mu g_R^\dagger\,,\\
s + ip &\rightarrow g_R(s+ip)g_L^\dagger\,,\\
s - ip &\rightarrow g_L(s-ip)g_R^\dagger\,,
\end{aligned}
\tag{1.43}
$$

with $g_{L,R} \in SU(3)_{L,R}$. In order to preserve local invariance the gauge fields v_μ and a_μ may only appear either through the covariant derivative

$$
D_\mu U = \partial_\mu U - i r_\mu U + i U l_\mu\,, \quad D_\mu U^\dagger = \partial_\mu U^\dagger + i U^\dagger r_\mu - i l_\mu U^\dagger\,,
\tag{1.44}
$$

and through the field strength

$$
F_L^{\mu\nu} = \partial^\mu l^\nu - \partial^\nu l^\mu - i[l^\mu, l^\nu]\,, \quad F_R^{\mu\nu} = \partial^\mu r^\nu - \partial^\nu r^\mu - i[r^\mu, r^\nu]\,.
\tag{1.45}
$$

Finally, the most general locally chiral invariant Lagrangian at lowest order describing the strong, electromagnetic and semileptonic weak interactions of mesons reads [6, 7]

$$
\mathcal{L}_2 = \frac{f^2}{4}\langle D_\mu U D^\mu U^\dagger \rangle + \frac{f^2}{4}\langle U^\dagger \chi + \chi^\dagger U \rangle,
\tag{1.46}
$$

16

where $\chi = 2B_0(s+ip)$ parameterizes the explicit chiral symmetry breaking. Therefore, at leading order in the chiral expansion the theory is fully determined by Eq. (1.46) but for two low-energy constants: the couplings B_0 and f which require to be constrained from experimental data or extracted by direct computation on the lattice. The latter is related to the pion decay constant in the chiral limit f_π, while the former accounts for the strength of the quark condensate in the chiral limit.

By taking one derivative of the classical action, $S_2 = \int d^4x \mathcal{L}_2$, with respect to l_μ or r_μ we find the conserved left-and right-handed currents defined by

$$J_L^\mu = \frac{\delta S_2}{\delta l_\mu} = \frac{i}{2}f^2 D_\mu U^\dagger U = \frac{f}{\sqrt{2}}D_\mu\Phi - \frac{i}{2}\left(\Phi\overset{\leftrightarrow}{D^\mu}\Phi\right) + \mathcal{O}(\Phi^3/f)\,, \quad (1.47)$$

$$J_R^\mu = \frac{\delta S_2}{\delta r_\mu} = \frac{i}{2}f^2 D_\mu U U^\dagger = -\frac{f}{\sqrt{2}}D_\mu\Phi - \frac{i}{2}\left(\Phi\overset{\leftrightarrow}{D^\mu}\Phi\right) + \mathcal{O}(\Phi^3/f)\,, \quad (1.48)$$

or similarly the vector-and axial vector-one

$$J_{V,A}^\mu = J_R^\mu \pm J_L^\mu = \begin{cases} J_V^\mu = -i(\Phi\overset{\leftrightarrow}{D^\mu}_\mu\Phi) & \text{parity invariant (even \# of } \Phi); \\ J_A^\mu = -\sqrt{2}f D_\mu\Phi & \text{parity violating (odd \# of } \Phi)\,. \end{cases} \quad (1.49)$$

Indeed, for the pion to vacuum matrix element of the axial current we have

$$\langle 0|(J_A^\mu)^{12}|\pi^+\rangle = \langle 0| - \sqrt{2}f\partial_\mu\pi^+|\pi^+\rangle = i\sqrt{2}f_\pi p^\mu\,, \quad (1.50)$$

which fixes the coupling f to the pion decay constant, $f = f_\pi = 92.21$ MeV, whose experimental value is usually extracted from the well-known pion decay $\pi^+ \to \mu^+\nu_\mu$. Regarding to the constant B_0, it is related to the quark condensate by taking the derivative with respect the external scalar source s

$$\bar{q}_L^j q_R^i = -\frac{\delta S_2}{\delta(s-ip)^{ji}} = -\frac{f^2}{2}B_0 U^{ij}\,, \quad (1.51)$$

$$\bar{q}_R^j q_L^i = -\frac{\delta S_2}{\delta(s+ip)^{ji}} = -\frac{f^2}{2}B_0 (U^\dagger)^{ij}\,, \quad (1.52)$$

which leads

$$\langle 0|\bar{q}^j q^i|0\rangle = \langle 0|\bar{q}_L^j q_R^i|0\rangle + \langle 0|\bar{q}_R^j q_L^i|0\rangle = -f^2 B_0 \delta^{ij}\,. \quad (1.53)$$

Taking $s = \mathcal{M} = \text{diag}(m_u, m_d, m_s)$ and expanding in powers of Φ in the absence of external fields ($v^\mu = a^\mu = p = 0$), the second term in Eq. (1.46) is quadratic in the fields and thus contains the mass term for the mesons plus additional interaction proportional to the quark masses. For computational purposes, it is useful to provide the Lagrangian in terms of Φ

$$\mathcal{L}_2 = \frac{1}{2}\langle\partial_\mu\Phi\partial^\mu\Phi\rangle + \frac{1}{12f^2}\langle(\Phi(\partial_\mu\Phi) - (\partial_\mu\Phi)\Phi)(\Phi(\partial^\mu\Phi) - (\partial^\mu\Phi)\Phi)\rangle$$

$$+B_0\left\{-\langle\mathcal{M}\Phi^2\rangle + (1/6f^2)\langle\mathcal{M}\Phi^4\rangle\right\} + \mathcal{O}\left(\frac{\Phi^6}{f^4}\right)\,, \quad (1.54)$$

where the third term reads

$$
\begin{aligned}
-B_0 \langle \mathcal{M} \Phi^2 \rangle \;=\; & -B_0(m_u + m_d)\pi^+ \pi^- - B_0(m_u + m_s)K^+ K^- \\
& -B_0(m_d + m_s)K^0 \bar{K}^0 - \frac{B_0}{2}(m_u + m_d)\pi_3^2 \\
& -\frac{B_0}{6}(m_u + m_d + 4m_s)\eta_8^2 - \frac{B_0}{\sqrt{3}}(m_u - m_d)\pi_3 \eta_8 \,.
\end{aligned}
\tag{1.55}
$$

Notice that the π_3 and η_8 states are mixed via an isospin violating term proportional to $\pi_3 \eta_8$. Consequently, in the isospin limit $m_u = m_d$ this term vanishes. The diagonalization of the π_3, η_8 mass matrix is given by the rotation

$$
\begin{pmatrix} \pi^0 \\ \eta \end{pmatrix} = \begin{pmatrix} \cos \varepsilon & \sin \varepsilon \\ -\sin \varepsilon & \cos \varepsilon \end{pmatrix} \begin{pmatrix} \pi_3 \\ \eta_8 \end{pmatrix} = \begin{pmatrix} \pi_3 + \varepsilon \eta_8 \\ -\varepsilon \pi_3 + \eta_8 \end{pmatrix} + \mathcal{O}(\varepsilon^2) \,.
\tag{1.56}
$$

Setting

$$
\varepsilon = \frac{\sqrt{3}}{4} \frac{m_d - m_u}{m_s - \hat{m}} \,, \qquad \hat{m} = \frac{m_u + m_d}{2} \,,
\tag{1.57}
$$

the mixing term in Eq. (1.55) vanishes and the π_3 and the η_8 states become

$$
\frac{B_0}{2} \left\{ (m_u + m_d) + 2\varepsilon \frac{m_u - m_d}{\sqrt{3}} \right\} (\pi^0)^2
$$
$$
-\frac{B_0}{2} \left\{ \frac{m_u + m_d + 4m_s}{3} - 2\varepsilon \frac{m_u - m_d}{\sqrt{3}} \right\} \eta^2 + \mathcal{O}(\varepsilon^2) \,.
\tag{1.58}
$$

Therefore, the quadratic mass terms in Eqs. (1.55) and (1.58) provide the meson masses in terms of the quark one [46]

$$
M_{\pi^\pm}^2 = B_0(m_u + m_d) \,, \quad M_{\pi^0}^2 = B_0(m_u + m_d) + \frac{2\varepsilon}{\sqrt{3}} B_0(m_u - m_d) + \mathcal{O}(\varepsilon^2) \,,
$$
$$
M_{K^\pm}^2 = B_0(m_u + m_s) \,, \quad M_{K^0, \bar{K}^0}^2 = B_0(m_d + m_s) \,,
$$
$$
M_{\eta_8}^2 = B_0 \frac{m_u + m_d + 4m_s}{3} - \frac{2\varepsilon}{\sqrt{3}} B_0(m_u - m_d) + \mathcal{O}(\varepsilon^2) \,.
\tag{1.59}
$$

At this order, the responsible for the small mass difference between neutral pion, π^0, and the charged ones, $\pi^\pm$, is the $\pi^0 \eta_8$ mixing accounting for $SU(2)$ flavor symmetry breaking effects. Therefore, in the isospin limit, where $m_u = m_d = \hat{m}$, the pions and kaons are degenerated in mass leading

$$
M_\pi^2 = 2B_0 \hat{m} + \mathcal{O}(m_u - m_d)^2 \,, \quad M_K^2 = B_0(\hat{m} + m_s) + \mathcal{O}(m_u - m_d) \,,
$$
$$
M_{\eta_8}^2 = 2B_0 \frac{1}{3}(\hat{m} + 2m_s) + \mathcal{O}(m_u - m_d)^2 \,,
\tag{1.60}
$$

which satisfy the well-known Gell-Mann-Okubo relation [31, 47]

$$
4M_K^2 = 3M_{\eta_8}^2 + M_\pi^2 \,.
\tag{1.61}
$$

Finally, from the relation of the quark condensate in Eq. (1.53) and the pion mass in Eq. (1.59) one gets the Gell-Mann-Oakes-Renner relation [46]

$$f_\pi^2 M_\pi^2 = -\frac{1}{2}(m_u + m_d)\langle 0|\bar{u}u + \bar{d}d|0\rangle\,. \tag{1.62}$$

1.2.1 Next-to-leading order Lagrangian

The construction of the next-to-leading order Lagrangian in the chiral expansion, $\mathcal{L}_4$, proceeds with the same building blocks and preserving the same symmetries than the lowest order one $\mathcal{L}_2$. It is given by [6, 7]

$$
\begin{aligned}
\mathcal{L}_4 = \quad & L_1\langle D_\mu U^\dagger D^\mu\rangle^2 + L_2\langle D_\mu U^\dagger D_\nu U\rangle\langle D^\mu U^\dagger D^\nu U\rangle \\
& + L_3\langle D_\mu U^\dagger D^\mu U D_\nu U^\dagger D^\nu U\rangle + L_4\langle D_\mu U^\dagger D^\mu U\rangle\langle U^\dagger\chi + \chi^\dagger U\rangle \\
& L_5\langle D_\mu U^\dagger D^\mu U\left(U^\dagger\chi + \chi^\dagger U\right)\rangle + L_6\langle U^\dagger\chi + \chi^\dagger U\rangle^2 \\
& L_7\langle U^\dagger\chi - \chi^\dagger U\rangle^2 + L_8\langle\chi^\dagger U\chi^\dagger U + U^\dagger\chi U^\dagger\chi\rangle \\
& - iL_9\langle F_R^{\mu\nu}D_\mu U D_\nu U^\dagger + F_L^{\mu\nu}D_\mu U^\dagger D_\nu U\rangle + L_{10}\langle U^\dagger F_R^{\mu\nu}U F_{L,\mu\nu}\rangle \\
& H_1\langle F_{R,\mu\nu}F_R^{\mu\nu} + F_{L,\mu\nu}F_L^{\mu\nu}\rangle + H_2\langle\chi^\dagger\chi\rangle\,,
\end{aligned}
\tag{1.63}
$$

where

$$F_{R,L}^{\mu\nu} = \partial(v^\nu \pm a^\nu) - \partial(v^\mu \pm a^\mu) - i[v^\mu \pm a^\mu, v^\nu \pm a^\nu]\,. \tag{1.64}$$

Notice that the number of low-energy constants (LEC's) has increased considerably respect $\mathcal{L}_2$. Concretely, at order $\mathcal{O}(p^4)$ we have 12 LEC's $(L_1, \ldots, L_{10}, H_{1,2})$ to be determined though the terms proportional to H_1 and H_2 do not involve pseudoscalar fields and are therefore not directly measurable. The rest, parameterize our lack of knowledge about low-energy QCD in analogy to f and B_0 of $\mathcal{L}_2$. *A priori*, they should be calculable in terms of QCD parameters such heavy quark masses or the QCD scale Λ_{QCD}. However, in practice one should resort to phenomenology to infer them. In general, the number of free parameter increases drastically with the order of the chiral expansion so that for $\mathcal{L}_6$ there are 143 free couplings implying that the predictive power of the theory is rapidly lost with higher orders.

As in any quantum field theory, quantum loops must be taken into account. For ChPT, loops with Goldstone boson propagators in the internal lines generating non-polynomial contributions with logarithms and threshold factors arise. Considering the Lagrangian expansion of Eq. (1.32), the diagrams that contribute at order $\mathcal{O}(p^d)$ are dictated by the chiral dimension counting relation [5]

$$D = 2 + 2L + \sum_d N_d(d - 2)\,, \tag{1.65}$$

where L is the number of loops and N_d the number of vertices coming from $\mathcal{O}(p^n)$ operators. With the previous receipt at hand we have that the leading $D = 2$ contributions are obtained with $L = 0$ and $d = 2$ i.e. only tree-level graphs with $\mathcal{L}_2$ contribute. At order $\mathcal{O}(p^4)$, one has two different possibilities: tree-level contributions from $\mathcal{L}_4$ with $L = 0$, $d = 4$ and $N_4 = 1$ and one-loop graphs coming from the $\mathcal{L}_2$ Lagrangian with $L = 1$ and $d = 2$. Regarding these loops, they are divergent and need to be renormalized. These divergences are absorbed in a renormalization of the coupling constants of the Lagrangian $\mathcal{L}_4$ as (in $D = 4 + 2\epsilon$ dimensions)

$$L_i = L_i^r(\mu) + \frac{\Gamma_i}{32\pi^2}\left(\frac{1}{\epsilon} - \ln(4\pi) + \gamma - 1 + \ln\mu^2\right), \qquad (1.66)$$

$$H_i = H_i^r(\mu) + \frac{\tilde{\Gamma}}{32\pi^2}\left(\frac{1}{\epsilon} - \ln(4\pi) + \gamma - 1 + \ln\mu^2\right), \qquad (1.67)$$

where [6, 7]

$$\Gamma_1 = \frac{3}{32}, \quad \Gamma_2 = \frac{3}{16}, \quad \Gamma_3 = 0, \quad \Gamma_4 = \frac{1}{8}, \quad \Gamma_5 = \frac{3}{8}, \quad \Gamma_6 = \frac{11}{144}, \quad \Gamma_7 = 0,$$
$$\Gamma_8 = \frac{5}{48}, \quad \Gamma_9 = \frac{1}{4}, \quad \Gamma_{10} = -\frac{1}{4}, \quad \Gamma_5 = \frac{3}{8}, \quad \Gamma_6 = \frac{11}{144},$$
$$\tilde{\Gamma}_1 = -\frac{1}{8}, \tilde{\Gamma}_2 = \frac{5}{24}. \qquad (1.68)$$

Once renormalized, the constants $L_i^r(\mu)$ depend on the scale μ whose running is given by

$$L_i^r(\mu_2) = L_i^r(\mu_2) + \frac{\Gamma_i}{16\pi^2}\log\left(\frac{\mu_1}{\mu_2}\right). \qquad (1.69)$$

Of course, the physical observables can not depend on μ. That is, the μ dependence in the renormalized couplings $L_i^r(\mu)$ is canceled by that of the one-loop amplitude in any observable.

The convergence of the ChPT series expansion as in Eq. (1.32) is restricted to low-energies, typically for $\sqrt{s} \sim 500$ MeV, although this energy depends very much on the process under evaluation. Note that at higher energies the lightest well-established resonance, the ρ with mass $M_\rho \simeq 770$ MeV, induces a pole in the $T-$matrix which cannot be reproduced by a power expansion. In this sense, the masses of the resonance states put an upper limit to the ChPT series and also give us an idea of the scale $\Lambda_{\chi PT}$ over which the ChPT power series is constructed

$$\frac{\mathcal{O}(p^4)}{\mathcal{O}(p^2)} \sim \frac{p^2}{\Lambda_{\chi PT}^2}, \qquad (1.70)$$

with $\Lambda_{\chi PT} \sim M_\rho$. Hence, in order to explain physics from $\Lambda_{\chi PT}$ on, one may explicitly incorporates resonances as active degrees of freedom into the description respecting, of course, chiral symmetry and its breaking as Resonance Chiral Theory does [48]. This theory will be discussed in section 1.4.

1.3 The $1/N_C$ expansion in Chiral Perturbation Theory

As we have seen in the previous sections, in ChPT the expansion involves the momenta and masses of the pseudo-Goldstone bosons. We finished the last section by showing up the limitation of χPT for describing physics beyond $\Lambda_{\chi PT}$ which occurs as soon as the momentum of the pseudo-Goldstone become comparable to $\Lambda_{\chi PT}$ and, unfortunately, there is no other parameter within ChPT to build the expansion upon for extending it to higher energies. However, 't Hooft suggested to generalize QCD from three to N_C colours, to employ and $SU(N_C)$ gauge group accordingly and proposed to expand QCD in terms of the $1/N_C$ parameter [49]. The idea is to study QCD in the limit of large number of colours $N_C \gg 1$ by keeping the product $\alpha_s N_C$ as a $\mathcal{O}(1)$ constant. This imposes α_s to scale as $1/N_C$ (or equivalently g_s as $1/\sqrt{N_C}$) as we will see in the following by inspecting the gluon self-energy as given in Fig. 1.2. Let us recall first the QCD Lagrangian Eq. (1.1) from which one can read off the QCD vertices and see that both the quark-quark-gluon coupling and the three-gluon vertex are $\mathcal{O}(g_s)$ while the four-gluon interaction is $\mathcal{O}(g_s^2)$. The gluons are $N_C \times N_C$ matrices in colour space and, hence, they have $N_C^2 - 1 \simeq N_C^2$ components. On the other hand, the quarks have N_C components. Consequently, for large-N_C there are more gluon than quark states which translates in a bigger importance of gluon contributions respect to the quarks one. By means of the the Feynman rules we then see that the second diagram in Fig. 1.2 behaves like g_s^2 while the first one diverges going as $g_s^2 N_C$. As we want the gluon self-energy, entering the β-function, to be finite in the $N_C \to \infty$ limit the following redefinition is in order: $g_s \to \frac{g_s}{\sqrt{N_c}}$. With this redefinition at hand, now the quark-quark-gluon coupling and the three-gluon vertex are $\mathcal{O}(1/\sqrt{N_C})$ while the four-gluon interaction is $\mathcal{O}(1/N_C)$ implying the first and second diagrams in Fig. 1.2 to be $\mathcal{O}(1)$ and $\mathcal{O}(1/N_C)$ in the $1/N_C$ counting, respectively. One can construct diagrams with a larger number of loops and prove that, quark-loops are suppressed by $1/N_C$ and that non-planar gluon topologies i.e. they cannot be painted on a plane without cutting or jumping over a propagator, are even more suppressed $\mathcal{O}(1/N_C^2)$. A further indication of gluon dominance in QCD is that
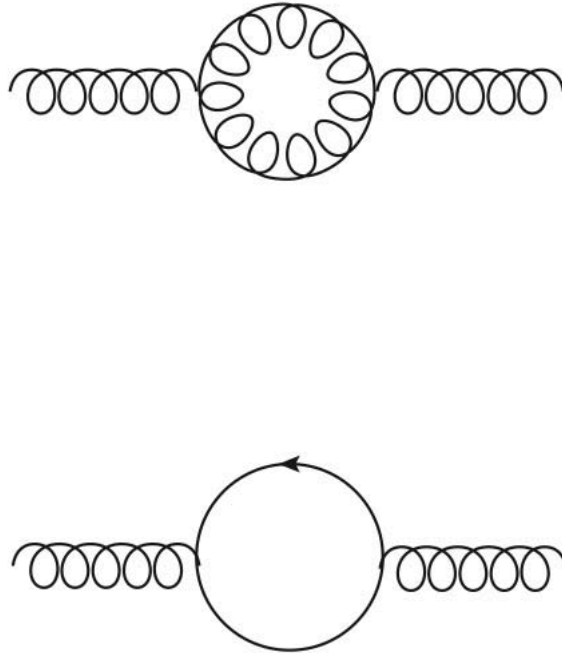
Figure 1.2: Gluon (up diagram) and quark (down diagram) one-loop contributions to the gluon self-energy.

the contribution of the gluon-loops to the low-energy behaviour of the strong coupling constant is larger than the quark-loops. Actually as N_C increases the QCD theory becomes more confining since this feature is mainly due to gluon interactions.

However, the idea of using $1/N_C$ as expansion parameter is sometimes questioned in the sense that for $N_C = 3$ is not very small. One cannot exactly know how large N_C should be for the expansion to be a good approximation but one can always appeal to phenomenology to see what happens. In this respect, there are many phenomenological facts that find their only explanation on large-N_C arguments supporting the $1/N_C$ expansion for QCD. The main results are:

- Suppression of the $\bar{q}q$ sea and exotic $\bar{q}q\bar{q}q$ states: This is due to the fact that there are more gluon states (N_C^2) than quarks states (N_C) as discussed before. Therefore, in the $N_C \to \infty$ limit the $\bar{q}q$ sea disappears. Regarding the $\bar{q}q\bar{q}q$ exotic states, in the $N_C \to \infty$ limit $\bar{q}q$ mesons do no interact and, hence, they can not join to form a exotic states.

- Zweig's rule is exact in the large-N_C limit classifying mesons in nonets. The axial anomaly disappears and flavour $U(n_f)_L \otimes U(n_f)_R$ is restored [50].

- Two body meson decay dominance: Meson decay are of $\mathcal{O}(1/\sqrt{N_C})$ while meson-meson scattering amplitudes are of $\mathcal{O}(1/N_C)$.

- In the large number of colours limit, under some assumptions, $U(n_f)_R \otimes U(n_f)_L$ symmetry breaks spontaneously down to $U(n_f)_V$ leading an spectrum of n_f^2 pseudo-Goldstone bosons [50].

Next, we would like to reassess ChPT by means of the new tool, the $1/N_C$ expansion, we have introduced in this section. The global dependence of the $\mathcal{O}(p^2)$ Lagrangian is $\mathcal{O}(N_C)$: the fields, the masses and momenta are all of them $\mathcal{O}(1)$ while f is $\mathcal{O}(\sqrt{N_C})$. The $U(\Phi)$ as given in Eq. (1.34), generates a power expansion in terms of Φ/f giving the required $1/\sqrt{N_C}$ suppression for each additional meson field. Interaction vertices with n mesons scale as $\sim f^{2-n} \sim \mathcal{O}(N_C^{1-n/2})$. Then, since $\mathcal{L}_2$ has an overall factor of N_C and $U(\Phi)$ is N_C-independent, each loop computed with the chiral Lagrangian will have a $1/N_C$ suppression. At order $\mathcal{O}(p^4)$, the chiral Lagrangian presented in Eq. (1.63) contain ten couplings to determine the low-energy dynamics of the pseudo-Goldstone bosons. Large-N_C QCD claims that terms with single trace are of $\mathcal{O}(N_C)$, while those with two traces of $\mathcal{O}(1)$. Therefore, one would say that L_3, L_5, L_8, L_9 and L_{10} are $\mathcal{O}(N_C)$, while L_4, L_6 and L_7 are $\mathcal{O}(1)$. Regarding L_1 and L_2 it can be demonstrated that, after a bit of algebra, are also $\mathcal{O}(N_C)$. Although it is not possible to compute the values of L_i from QCD, the $1/N_C$ expansion tell us which are the dominants fully characterizing hence the ChPT coefficients up to order $\mathcal{O}(p^4)$. This is further corroborated by looking at table 1.3, where we provide the phenomenological values for the L_i's in the Large-N_C limit from where we see they follow the pattern suggested by the $1/N_C$ counting rules.

1.4 Resonance Chiral Theory

As we have seen in section 1.2, ChPT is the effective field theory of QCD valid below some energy scale $\Lambda_{\chi PT}$, close to the masses of the resonances. By construction, in effective theories the information on the heavier degrees of freedom, $M > \Lambda_{\chi PT}$, is encoded within the coupling constants which in turn determine the interactions among the lighter degrees of freedom. In particular, this means that the constants L_i of the $\mathcal{L}_4$ Lagrangian will receive contributions from the interactions with resonances. Our next goal is then to build an effective Lagrangian including resonances as degrees of freedom respecting the QCD symmetries as well as the $SU(3)_L \otimes SU(3)_R$ chiral symmetry. This is the avenue followed by Resonance Chiral Theory (RχT) which

$L_i(M_\rho)$	Value ($\times 10^3$)	$\mathcal{O}(N_C)$
L_1	0.4 ± 0.6	$\mathcal{O}(1)$
L_2	1.4 ± 0.3	$\mathcal{O}(N_C)$
L_3	-3.5 ± 1.1	$\mathcal{O}(N_C)$
L_4	-0.3 ± 0.5	$\mathcal{O}(1)$
L_5	1.4 ± 0.5	$\mathcal{O}(N_C)$
L_6	-0.2 ± 0.3	$\mathcal{O}(1)$
L_7	-0.4 ± 0.2	$\mathcal{O}(1)$
L_8	0.9 ± 0.3	$\mathcal{O}(N_C)$
L_9	6.9 ± 0.7	$\mathcal{O}(N_C)$
L_{10}	-5.5 ± 0.7	$\mathcal{O}(N_C)$

Table 1.3: Phenomenological values of the $L_i(M_\rho)$ [51] couplings as compared to its order in the $1/N_C$ counting.

can be understood as a link between the chiral and asymptotic QCD regimes which has been proven to be a very useful tool to describe QCD dynamics at intermediate energies $\sim (1-2)$ GeV. RχT uses the $1/N_C$ expansion of QCD in the large number of colors as a guideline to organize the expansion. Therefore, at leading order just tree-level diagrams contribute while loops yield higher order effects and hence they are suppressed. The Lagrangian can be organized according to the number of resonance fields in the interaction terms

$$\mathcal{L}_{R\chi T} = \mathcal{L}_2 + \sum_{R_1} \mathcal{L}_{R_1} + \sum_{R_1,R_2} \mathcal{L}_{R_1 R_2} + \cdots , \tag{1.71}$$

where R_i stands for the resonance multiplets of the type $V(1^{--})$, $A(1^{++})$, $S(0^{++})$ and $P(0^{++})$, and where the dots denote operators with three or more resonance fields which we neglect for the purpose of this work. The first term in the right-hand side of Eq. (1.71) contains the operators without resonance fields (cf. Eq. (1.33)). The second term corresponds to the interaction terms with one resonance given by

$$\mathcal{L}_{R_1} = \mathcal{L}_V + \mathcal{L}_A + \mathcal{L}_S + \mathcal{L}_P , \tag{1.72}$$

where

$$\mathcal{L}_V = \frac{F_V}{2\sqrt{2}} \langle V_{\mu\nu} f_+^{\mu\nu} \rangle + \frac{iG_V}{2\sqrt{2}} \langle V_{\mu\nu} [u^\mu, u^\nu] \rangle , \tag{1.73}$$

$$\mathcal{L}_A = \frac{F_A}{2\sqrt{2}} \langle A_{\mu\nu} f_-^{\mu\nu} \rangle , \tag{1.74}$$

$$\mathcal{L}_S = c_d \langle S_8 u_\mu u^\mu \rangle + c_m \langle S_8 \chi_+ \rangle + \tilde{c}_d S_1 \langle u_\mu u^\mu \rangle + \tilde{c}_d S_1 \langle \chi_+ \rangle , \tag{1.75}$$

$$\mathcal{L}_P = id_m \langle P_8 \chi_- \rangle + i\tilde{d}_m P_1 \langle \chi_- \rangle , \tag{1.76}$$

24

and where

$$u_\mu = iu^\dagger D_\mu U u^\dagger, \quad f_\pm = uF_L^{\mu\nu}u^\dagger \pm u^\dagger F_R^{\mu\nu}u, \quad \chi_\pm = u^\dagger\chi u^\dagger \pm u\chi^\dagger u, \quad (1.77)$$

with $F_{L,R}^{\mu\nu}$ defined in Eq. (1.64) and $u(\Phi)^2 = U(\Phi)$ ($U(\Phi)$ has been defined in Eq. (1.28)).

We write down the first vector and scalar nonets since they are important for the processes considered later on in this thesis. In matrix notation they are written as

$$V_{\mu\nu} = \begin{pmatrix} \frac{1}{\sqrt{2}}\rho^0 + \frac{1}{\sqrt{6}}\omega_8 + \frac{1}{\sqrt{3}}\omega_1 & \rho^+ & K^{*+} \\ \rho^- & -\frac{1}{\sqrt{2}}\rho_0 + \frac{1}{\sqrt{6}}\omega_8 + \frac{1}{\sqrt{3}}\omega_1 & K^{*0} \\ K^{*-} & \bar{K}^{*0} & -\frac{2}{\sqrt{6}}\omega_8 + \frac{1}{\sqrt{3}}\omega_1 \end{pmatrix}_{\mu\nu}, (1.78)$$

for the vector fields, and

$$S_8 = \begin{pmatrix} \frac{1}{\sqrt{2}}a_0^0 + \frac{1}{\sqrt{6}}\sigma_8 & a_0^+ & \kappa^+ \\ a_0^- & -\frac{1}{\sqrt{2}}a_0^0 + \frac{1}{\sqrt{6}}\sigma_8 & \kappa^0 \\ \kappa^- & \bar{\kappa}^0 & -\frac{2}{\sqrt{6}}\sigma_8 \end{pmatrix}, \quad (1.79)$$

$$S_1 = \sigma_1, \quad (1.80)$$

for the scalar one.

For the sake of clarity, expanding the Lagrangian involving vector and scalar resonances in Eq. (1.76) in terms of Φ we get

$$\begin{aligned}
\mathcal{L}_S &= \frac{2c_d}{f^2}\langle S_8(\partial_\mu\Phi)(\partial^\mu\Phi)\rangle + 4B_0c_m[\langle S_8\mathcal{M}\rangle - \frac{1}{4f^2}\langle S_8(\Phi^2\mathcal{M} + \mathcal{M}\Phi^2 + 2\Phi\mathcal{M}\Phi)\rangle] \\
&+ \frac{2\tilde{c}_d}{f^2}S_1\langle(\partial_\mu\Phi)(\partial^\mu\Phi)\rangle + 4B_0\tilde{c}_m S_1[\langle\mathcal{M}\rangle - \frac{1}{4f^2}\langle(\phi^2\mathcal{M} + \mathcal{M}\Phi^2 + 2\Phi\mathcal{M}\Phi)\rangle],
\end{aligned}$$
$$(1.81)$$

and

$$\mathcal{L}_V = \frac{iG_V}{\sqrt{2}f^2}\langle V_{\mu\nu}[(\partial^\mu\Phi)(\partial^\nu\Phi) - (\partial^\nu\Phi)(\partial^\mu\Phi)]\rangle, \quad (1.82)$$

where we have used $\chi = 2B_0\mathcal{M}$ and neglected other external fields $(v^\mu = a^\mu = p = 0)$

The third term in Eq. (1.71) contains the kinetic terms,

$$\mathcal{L}_{kin}^{R=S,P} = \frac{1}{2}\langle\nabla^\mu R_8 \nabla_\mu R_8 - M_{R_8}^2 R_8^2\rangle + \frac{1}{2}\langle\partial^\mu R_1\partial_\mu R_1 - M_{R_1}^2 R_1^2\rangle, \quad (1.83)$$

$$\mathcal{L}_{kin}^{R=V,A} = -\frac{1}{2}\langle\nabla^\lambda R_{\lambda\mu} \nabla_\nu R^{\nu\mu} - \frac{1}{2}M_R^2 R_{\mu\nu}R^{\mu\nu}\rangle, \quad (1.84)$$

where

$$\nabla_\mu R = \partial_\mu R + [\Gamma_\mu, R], \quad (1.85)$$

with

$$\Gamma_\mu = \frac{1}{2}\{u^+[\partial_\mu - ir_\mu]u + u[\partial_\mu - i\ell_\mu]u^\dagger\}. \tag{1.86}$$

The exchange of these resonances have an important impact on the low-energy dynamics of the pseudo-Goldstone bosons. Below the resonance mass scale, $p^2 \ll M_R^2$, the singularity associated with the pole of the resonance propagator can be replaced by the corresponding momentum expansion as of

$$\frac{1}{p^2 - M_R^2} = -\frac{1}{M_R^2}\left(1 + \frac{p^2}{M_R^2} + \left(\frac{p^2}{M_R^2}\right)^2 + \cdots\right). \tag{1.87}$$

Hence, the exchange of virtual resonances generates pseudo-Goldstone bosons couplings proportionals to powers of $1/M_R^2$ which should be embodied in ChPT. In other words, at lowest order in derivatives, this gives predictions for the $\mathcal{O}(p^4)$ couplings of χPT. By integrating out the resonances i.e. going from RχT to χPT, at $\mathcal{O}(p^4)$ the χPT couplings in Eq. (1.63), L_i, are saturated by the resonance exchange parameters (masses and couplings). After a matching procedure one finds [48]

$$L_1 = \frac{G_V^2}{8M_V^2} - \frac{c_d^2}{6M_S^2} + \frac{\tilde{c}_d^2}{2M_{S_1}^2}, \quad L_2 = \frac{G_V^2}{4M_V^2}, \quad L_3 = -\frac{3G_V^2}{4M_V^2},$$

$$L_4 = -\frac{c_d c_m}{3M_S^2} + \frac{\tilde{c}_d \tilde{c}_m}{M_{S_1}^2}, \quad L_5 = \frac{c_d c_m}{M_S^2}, \quad L_6 = -\frac{c_m^2}{6M_S^2} + \frac{\tilde{c}_m^2}{2M_{S_1}^2},$$

$$L_7 = \frac{d_m^2}{6M_P^2} - \frac{\tilde{d}_m^2}{2M_{P_1}^2}, \quad L_8 = \frac{c_m^2}{2M_S^2} - \frac{d_m^2}{2M_P^2} \quad L_9 = \frac{F_V G_V}{2M_V^2},$$

$$L_{10} = -\frac{F_V^2}{4M_V^2} + \frac{F_A^2}{4M_A^2}, \quad H_1 = -\frac{F_V^2}{8M_V^2} - \frac{F_A^2}{8M_A^2}, \quad H_2 = \frac{c_m^2}{M_S^2} + \frac{d_m^2}{M_P^2}. \tag{1.88}$$

As we can see from the above relations, we are left with too many unknown parameters to predict all the chiral couplings L_i. Consequently, the predictive power of this theory may be questionable. In principle, these parameters should be inferred from fits to experimental data. However, by invoking some short-distance constraints from QCD i.e. RχT must match the OPE at high-energies, together with demanding two-body form factors of hadronic currents vanish at large momentum transfer, one can find some useful relations among the couplings which considerably diminish the number of free parameters as we will see in the following.

On one hand, the V octet mass M_V, can be suitably approximated by the ρ mass while the vector couplings F_V and G_V can be obtained, respectively, from the decays $\rho \to e^+e^-$ and $\rho \to \pi\pi$. The values are $F_V = 154$ MeV, $G_V = 53$ MeV

and $M_V = M_\rho = 770$ MeV [48][1]. On the other hand, at leading order in $1/N_C$, the calculation of the two-pion vector form factor within RχT leads [52]

$$F_V^{\pi\pi}(q^2) = 1 + \frac{F_V G_V}{f_\pi^2} \frac{q^2}{M_V^2 - q^2} \,, \tag{1.89}$$

which by imposing that it should vanish at $q^2 \to \infty$, the resonance couplings satisfies

$$F_V G_V = f_\pi^2 \,. \tag{1.90}$$

Similarly, the axial current between one pion and one photon is characterized by the axial-vector form factor [53, 54]

$$F_A^{\pi\gamma}(q^2) = \frac{F_A^2}{M_A^2 - q^2} + \frac{2F_V G_V - F_V^2}{M_V^2} \,, \tag{1.91}$$

which requiring also to vanish at $q^2 \to \infty$ implies the relation

$$F_V = 2G_V \,. \tag{1.92}$$

Then, inserting the previous equation into Eq. (1.90) leads

$$F_V = 2G_V = \sqrt{2} f_\pi \,, \tag{1.93}$$

that is, we get the F_V and G_V in terms of the pion decay constant.

Once the vector parameters F_V, f_π and M_V are known, the axial one F_A and M_A can be subsequently deduced from the Weinberg's sum rules [55]

$$F_V^2 - F_A^2 = f_\pi^2 \,, \quad M_V^2 F_V^2 - M_A^2 F_A^2 = 0 \,, \tag{1.94}$$

obtained after the requirement that the two-point function of a vector correlator between left-and right-handed quarks in the chiral limit vanishes faster than $1/q^4$ at high-energies. The values are $F_A = 123$ MeV and $M_A = 968$ MeV [48], respectively, but also can be derived by introducing Eq. (1.93) into Eq. (1.94) leading

$$F_A = f_\pi \,, \quad M_A = \sqrt{2} M_V \,, \tag{1.95}$$

that is, we get F_A and M_A in terms of the pion decay constant and the mass of the vector multiplet M_V.

Regarding the scalar sector, we consider the $K\pi$ scalar form factor [56]

$$F_S^{K\pi}(q^2) = 1 + \frac{4c_m}{f_\pi^2} \left(c_d + (c_m - c_d) \frac{M_K^2 - M_\pi^2}{M_S^2} \right) \frac{q^2}{M_S^2 - q^2} \,, \tag{1.96}$$

---

[1]For a recent determination of G_V and M_ρ see, for example, the global $U(3) \otimes U(3)$ meson-meson scattering at one-loop analysis of Refs. [57, 58] and also Ref. [59].

which upon the demand to vanish at $q^2 \to \infty$ one obtains the restrictions

$$c_m - c_d = 0\,, \quad 4c_d c_m = f_\pi^2\,. \tag{1.97}$$

This gives a prediction for the scalar couplings in terms of the pion decay constant

$$c_d = c_m = \frac{f_\pi}{2}\,. \tag{1.98}$$

For the pseudoscalar parameters, we invoke the difference of two-point correlation functions of two scalar and two pseudoscalar current. The resulting $\Pi_{SS-PP}(q^2)$ correlator vanishes as $1/q^4$ at large energies with a small coefficient. Demanding this behaviour one gets [60]

$$8(c_m^2 - d_m^2) = f_\pi^2\,, \quad c_m^2 M_S^2 - d_m^2 M_P^2 \simeq 0\,, \tag{1.99}$$

allowing to express the pseudoscalar coupling and mass in terms of pion decay constant and the mass of the scalar multiplet M_S as

$$d_m = \frac{f_\pi}{2\sqrt{2}}\,, \quad M_P \simeq \sqrt{2} M_S\,. \tag{1.100}$$

Regarding the singlet exchange contributions, they can be expressed in terms of the octet parameters using large-N_C arguments leading [48]

$$M_{S_1} = M_S\,, \quad |\tilde{c}_d| = \frac{|c_d|}{\sqrt{3}}\,, \quad |\tilde{c}_m| = \frac{|c_m|}{\sqrt{3}}\,, \quad M_{P_1} = M_P\,, \quad |\tilde{d}_m| = \frac{|d_m|}{\sqrt{3}}\,. \tag{1.101}$$

Therefore, turning to examine the low-energy χPT couplings at lowest-order in $1/N_C$, Eq. (1.88), one observes that they can be expressed in terms of just three parameters f_π, M_V and M_S by means of the use of Eqs. (1.93), (1.95), (1.98) and (1.100) as of

$$
\begin{aligned}
2L_1 = L_2 = \frac{1}{4}L_9 = -\frac{1}{3}L_{10} = \frac{f_\pi^2}{8M_V^2}\,, \\
L_3 = -\frac{3f_\pi^2}{8M_V^2} + \frac{f_\pi^2}{8M_S^2}\,, \quad L_5 = \frac{8}{3}L_8 = \frac{f_\pi^2}{4M_S^2}\,, \\
L_4 = L_6 = L_7 = 0\,, \\
H_1 = -\frac{5}{16}\frac{f_\pi^2}{M_V^2}\,, \quad H_2 = \frac{5f_\pi^2}{16M_S^2}\,,
\end{aligned}
\tag{1.102}
$$

with all non-zero L_i being of $\mathcal{O}(N_C)$ while L_4, L_6 and L_7 vanish since they are subleading constants in the $1/N_C$ expansion.

In table 1.4 we compare the phenomenological values of these couplings given in the second column together with the ones predicted by the resonance exchanges

shown in the last two columns depending whether inputs values (penultimate column) or short-distance QCD constraints Eq. (1.102) (last column) are considered. We can see that the assumption of resonance saturation has given a remarkable prediction for L_i such that there is no reason to include additional resonance multiplets looking at χPT at $\mathcal{O}(p^4)$. We would like to notice that the η_1 is usually integrated out from the χPT Lagrangian. In that case, the coupling L_7 gets a contribution from η_1 exchange

$$L_7^{\eta_1} = -\frac{\tilde{d}_m^2}{2M_{\eta_1}^2} \,. \tag{1.103}$$

i	$L_i(M_\rho)$	$\mathcal{O}(N_C)$	V	A	S	S_1	η_1	Total	Total*
1	0.4 ± 0.6	$\mathcal{O}(1)$	0.6	0.0	-0.2	0.2	0.0	0.6	0.9
2	1.4 ± 0.3	$\mathcal{O}(N_C)$	1.2	0.0	0.0	0.0	0.0	1.2	1.8
3	-3.5 ± 1.1	$\mathcal{O}(N_C)$	-3.6	0.0	0.6	0.0	0.0	-3.0	-4.9
4	-0.3 ± 0.5	$\mathcal{O}(1)$	0.0	0.0	-0.5	0.5	0.0	0.0	0.0
5	1.4 ± 0.5	$\mathcal{O}(N_C)$	0.0	0.0	1.4	0.0	0.0	1.4	1.4
6	-0.2 ± 0.3	$\mathcal{O}(1)$	0.0	0.0	-0.3	0.3	0.0	0.0	0.0
7	-0.4 ± 0.2	$\mathcal{O}(1)$	0.0	0.0	0.0	0.0	-0.3	-0.3	-0.3
8	0.9 ± 0.3	$\mathcal{O}(N_C)$	0.0	0.0	0.9	0.0	0.0	0.9	0.9
9	6.9 ± 0.7	$\mathcal{O}(N_C)$	6.9	0.0	0.0	0.0	0.0	6.9	7.3
10	-5.5 ± 0.7	$\mathcal{O}(N_C)$	-10.0	4.0	0.0	0.0	0.0	-6.0	-5.5

Table 1.4: V, A, S, S_1 and η_1 contributions to the L_i^r coupling constants in units of 10^{-3}. Last column shows the result as obtained by employing the relations of Eq. (1.102).

1.5 Inclusion of the η'

The standard QCD Lagrangian as written in Eq. (1.1) has actually an extra term which is connected with the $U(1)_A$ anomaly. Including this term, the most general QCD Lagrangian becomes

$$\mathcal{L}_{QCD} = \sum_f \bar{q}_f \left(i\slashed{D} - \mathcal{M}_f \right) q_f - \frac{1}{4} G_{\mu\nu}^a G_a^{\mu\nu} - \theta\omega \,, \tag{1.104}$$

where ω is referred the topological charge density which can be written as

$$\omega = \frac{\alpha_s}{8\pi} G\widetilde{G} \,, \tag{1.105}$$

with $G\widetilde{G} = \epsilon^{\mu\nu\alpha\beta}\mathcal{G}_{\mu\nu}\mathcal{G}_{\alpha\beta}$ the product of the gluon field strength tensor and its dual. Similar to the $SU(3)$ flavor symmetry breaking we have discussed in section 1.1.2,

if the QCD Lagrangian in the chiral limit ($\mathcal{M} \to 0$) was invariant under $U(1)_A$ symmetry transformations, $q \to \exp[i\epsilon_A\gamma_5]q$, this would tell us the existence of a ninth Goldstone boson. However, the presence of a quark-mass term breaks down again the $U(1)_A$ symmetry promoting the ninth Goldstone boson to become a pseudo-Goldstone boson with a small mass. Looking at table (1.2), the best candidate for this would be the η' at first sight. However, the η' mass, $m_{\eta'} \sim 958$ MeV, is too large for a pseudo-Goldstone boson. The resolution of this paradox is related with the emergence of an anomaly, the $U(1)_A$ symmetry is broken, even in the massless case, by the dynamics of QCD itself i.e. due to the presence of the third term in Eq. (1.104) which leads to a non-conservation of the singlet axial-vector current as we showed in Eq. (1.22) (see Ref. [61] for a detailed derivation). This makes the η' too heavy and difficult to be accepted as the ninth Goldstone boson associated with the spontaneously broken $U(1)_A$ symmetry. Nonetheless, there exist some approaches that include the η' within ChPT as the ninth Goldstone boson. An example is the large-N_C limit [62] we have discussed so far. In this framework, the third term in Eq. (1.104) is expanded in powers of $\frac{1}{N_C}$ whose contribution will vanish for $N_C \to \infty$. In this limit, the contribution of the axial anomaly to the η' mass disappears letting the η' mass to be comparable with the other pseudo-Golsdstone boson masses. In the large-N_C limit within ChPT, this breaking is introduced through [63]

$$\mathcal{L}^{(1/N_C, p^0)} = -\frac{f^2}{4}\frac{a}{N_C}\left(\frac{i}{2}\left[\log(\det U) - \log(\det U^\dagger)\right]\right)^2 = -\frac{1}{2}m_0^2\eta_1^2, \qquad (1.106)$$

which is $1/N_C$-suppressed with $m_{\eta_0}^2 = 3a/N_C$, where a is a parameter to be fixed from the experiment.

The standard power counting employed in $SU(3)$ ChPT we have discussed in section 1.2 and summarized in Eq. (1.31) is no longer valid in $U(3)$ ChPT due to the large mass of the singlet η_1. Nevertheless, one can still accommodate the singlet η_1 into the description by assigning the same counting to $1/N_C$, the squared momenta p^2 and the light quark masses m_q in order to have a systematic combined power counting. This combined expansion in terms of three variables can be counted by δ scaling as [8, 64]

$$p = \mathcal{O}(\sqrt{\delta})\,, \quad m_q = \mathcal{O}(\delta)\,, \quad 1/N_C = \mathcal{O}(\delta). \qquad (1.107)$$

In the large-N_C framework, the effective $U(3)$ ChPT Lagrangian which simultaneously includes the pseudo-Goldstone bosons octet π, K, η_8 and the singlet η_1 as dynamical fields was introduced in Refs. [8, 63, 64, 65].

Leading order

At lowest order in the δ expansion i.e. $\mathcal{O}(\delta^0)$, the $U(3)$ ChPT Lagrangian has the form

$$\mathcal{L}^{\delta^0} = \frac{f^2}{4} \langle D_\mu U D^\mu U^\dagger \rangle + \frac{f^2}{4} \langle U^\dagger \chi + \chi^\dagger U \rangle - \frac{1}{2} m_0^2 \eta_1^2 \,, \tag{1.108}$$

where m_0^2 is the $U(1)_A$ anomaly contribution to the η_1 mass, and now

$$U = \exp\left(\frac{i\sqrt{2}\widetilde{\Phi}}{f} \right), \tag{1.109}$$

with

$$\widetilde{\Phi} = \begin{pmatrix} \frac{1}{\sqrt{2}}\pi_3 + \frac{1}{\sqrt{6}}\eta_8 + \frac{1}{\sqrt{3}}\eta_1 & \pi^+ & K^+ \\ \pi^- & -\frac{1}{\sqrt{2}}\pi_3 + \frac{1}{\sqrt{6}}\eta_8 + \frac{1}{\sqrt{3}}\eta_1 & K^0 \\ K^- & \bar{K}^0 & -\frac{2}{\sqrt{6}}\eta_8 + \frac{1}{\sqrt{3}}\eta_1 \end{pmatrix}. \tag{1.110}$$

Notice the counting of Eq. (1.108) [66]: the first operator is $\mathcal{O}(N_C, p^2)$, the second $\mathcal{O}(N_C, m_q)$ and the latest, accounting for the anomaly, is $\mathcal{O}(N_C^0, p^0)$, where U is counted as $\mathcal{O}(1)$, $f^2 \sim \mathcal{O}(N_C)$ and $m_0^2 \sim \mathcal{O}(1/N_C)$. The effective Lagrangian has then an overall factor of N_C.

With the inclusion of the singlet state η_1 into the description and assuming $SU(2)$ symmetry i.e. $m_u = m_d = \hat{m}$ implying no mixing between the neutral pion state π_3 and η_8, $\chi = 2B_0\mathcal{M}$ reads

$$\chi = \begin{pmatrix} \overset{\circ}{M}{}_\pi^2 & 0 & 0 \\ 0 & \overset{\circ}{M}{}_\pi^2 & 0 \\ 0 & 0 & \overset{\circ}{M}{}_K^2 - \overset{\circ}{M}{}_\pi^2 \end{pmatrix}, \tag{1.111}$$

where $\overset{\circ}{M}{}_\phi^2$ $(\phi = \pi, K)$ denotes the bare mass at $\mathcal{O}(p^2)$. Therefore, the bilinear terms coming from the lowest-order ChPT Lagragian in Eq. (1.108) becomes

$$\begin{aligned}
\mathcal{L}^{\delta^0} &= \frac{1}{2}\partial_\mu\pi^0\partial^\mu\pi^0 + \partial_\mu\pi^+\partial^\mu\pi^- + \partial_\mu K^+\partial^\mu K^- \\
&\quad + \partial_\mu K^0 \partial^\mu \bar{K}^0 + \frac{1}{2}\partial_\mu\eta_8\partial^\mu\eta_8 + \frac{1}{2}\partial_\mu\eta_1\partial^\mu\eta_1 \\
&\quad - \frac{1}{2}\overset{\circ}{M}{}_\pi^2 (\pi^0)^2 - \overset{\circ}{M}{}_\pi^2\pi^+\pi^- - \overset{\circ}{M}{}_K^2 K^0\bar{K}^0 - \overset{\circ}{M}{}_K^2 K^+K^- \\
&\quad - \frac{1}{2}\left(\frac{4}{3}\overset{\circ}{M}{}_K^2 - \frac{1}{3}\overset{\circ}{M}{}_\pi^2 \right)\eta_8^2 - \frac{1}{2}\left(m_0^2 + \frac{2}{3}\overset{\circ}{M}{}_K^2 + \frac{1}{3}\overset{\circ}{M}{}_\pi^2 \right)\eta_1^2 \\
&\quad + \frac{8}{\sqrt{18}}\left(\overset{\circ}{M}{}_K^2 - \overset{\circ}{M}{}_\pi^2 \right)\eta_1\eta_8 + \mathcal{O}(\Phi^4)\,.
\end{aligned} \tag{1.112}$$

Similar to $\pi^0 - \eta$ mixing in Eq. (1.55), the mass term proportional to $\eta_1\eta_8$ in the previous expression, which accounts for $SU(3)$ flavor symmetry breaking effects, induces a $\eta_8 - \eta_1$ mixing. Therefore, the masses of the two physical η and η' states are obtained as follows. We collect the octet and singlet fields in the doublet $\eta_B^T \equiv (\eta_8, \eta_1)$ and express the quadratic mass term making use of a matrix notation as

$$-\frac{1}{2}\eta_B^T \mathcal{M}\eta_B\,, \tag{1.113}$$

where

$$\mathcal{M} = \begin{pmatrix} M_8^2 & M_{81}^2 \\ M_{81}^2 & M_1^2 \end{pmatrix}\,, \tag{1.114}$$

with

$$\overset{\circ}{M}_8^2 = \frac{1}{3}(4\,\overset{\circ}{M}_K^2 - \overset{\circ}{M}_\pi^2)\,, \quad \overset{\circ}{M}_1^2 = m_0^2 + \frac{1}{3}(2\,\overset{\circ}{M}_K^2 + \overset{\circ}{M}_\pi^2)\,,$$

$$\overset{\circ}{M}_{81}^2 = -\frac{2\sqrt{2}}{3}(\overset{\circ}{M}_K^2 - \overset{\circ}{M}_\pi^2)\,. \tag{1.115}$$

The physical η and η' mass eigenstates are obtained after diagonalising the mass matrix $\mathcal{M}$ with and orthogonal transformation

$$\eta_B = R^T \cdot \eta_P \equiv R^T \cdot \begin{pmatrix} \eta \\ \eta' \end{pmatrix}\,, \quad \mathcal{M} = R^T \cdot \mathcal{M}_{\text{diag}} \cdot R\,, \tag{1.116}$$

where

$$R \equiv \begin{pmatrix} \cos\theta_P & -\sin\theta_P \\ \sin\theta_P & \cos\theta_P \end{pmatrix}\,. \tag{1.117}$$

The resulting η and η' masses and the angle θ_P at lowest order are [57, 66]

$$\overset{\circ}{M}_\eta^2 = \frac{m_0^2}{2} + \overset{\circ}{M}_K^2 - \frac{1}{2}\sqrt{m_0^4 - \frac{1}{3}4m_0^2\Delta + 4\Delta^2}\,, \tag{1.118}$$

$$\overset{\circ}{M}_{\eta'}^2 = \frac{m_0^2}{2} + \overset{\circ}{M}_K^2 + \frac{1}{2}\sqrt{m_0^4 - \frac{1}{3}4m_0^2\Delta + 4\Delta^2}\,, \tag{1.119}$$

$$\sin\theta_P = -\left(\sqrt{1 + \frac{(3m_0^2 - 2\Delta + \sqrt{9m_0^4 - 12m_0^2\Delta + 36\Delta^2})^2}{32\Delta^2}}\right)^{-1}\,, \tag{1.120}$$

with $\Delta^2 = \overset{\circ}{M}_K^2 - \overset{\circ}{M}_\pi^2$.

The parameterization of the mixing phenomenon among the physical η and η' mesons is not unique. It can be also described by means of the quark-flavor basis rather than by the octet-singlet ones we have shown here. Appendix A is devoted to discuss the relation between the octet-singlet and quark-flavor bases.

Next-to-leading order

Calculations at next-to-leading order in ChPT require to consider the tree level diagrams of order $\mathcal{O}(p^2)$ and $\mathcal{O}(p^4)$, together with contributions coming from the mass and wave function renormalizations which should be accounted for to the same order. In fact, the mass renormalization affects only the mass terms coming from the leading order Lagrangian Eq. (1.46) and not the masses coming from the kinematics of the corresponding process i.e. from derivative terms. In addition, one-loop graphs containing the imaginary parts required by unitarity should be also taken into account. At one-loop, the expressions of such renormalizations can be found, for example, in the global meson-meson scattering analysis of Refs. [57, 67] for $SU(3) \otimes SU(3)$ in ChPT and $U(3) \otimes U(3)$ in ChPT with resonances, respectively. For consistency of the present work, we report here the mass and wave function renormalization for pions and kaons leading in large-N_C, which enter the processes we will analyse in sections 3,4, and 5, and discuss the case of the η_8 and η_1 in more detail afterwards. That is, in the ChPT language of counterterms, the contributions coming from L_4 and L_6 vanish since these couplings are subleading in large-N_C as shown in table 1.3. The same applies for loop contributions, since graphs computed from the chiral Lagrangian have a $1/N_C$ suppression for each loop as we have discussed in section 1.3. Therefore, the bare pion and kaon fields entering the Lagrangian are connected with the renormalized ones as

$$\phi = \mathcal{Z}_\phi^{1/2} \phi^{ren},\qquad(1.121)$$

where $\phi = \pi, K$ and the wave function renormalization given by

$$\mathcal{Z}_\pi^{1/2} = 1 - \frac{4\overset{\circ}{M}_\pi^2}{f^2}\frac{c_d c_m}{M_S^2},\quad \mathcal{Z}_K^{1/2} = 1 - \frac{4\overset{\circ}{M}_K^2}{f^2}\frac{c_d c_m}{M_S^2}.\qquad(1.122)$$

In $\mathcal{L}_2$, the masses from the mass matrix $\mathcal{M}$ correspond to the bare $\mathcal{O}(p^2)$ masses (cf. Eq. (1.111)). At order $\mathcal{O}(p^4)$ in large-N_C, these masses are shifted by linear terms in L_5 and L_8 couplings whose connection with the resonance parameters was given in Eq. (1.88). We re-express the bare masses of the pions and kaons $\overset{\circ}{M}_\pi$ and $\overset{\circ}{M}_K$, respectively, by the physical ones at order $\mathcal{O}(p^4)$ through the relations

$$M_\pi^2 = \overset{\circ}{M}_\pi^2\left[1+\frac{8\overset{\circ}{M}_\pi^2}{f^2}\frac{c_m}{M_S^2}(c_m - c_d)\right],\quad M_K^2 = \overset{\circ}{M}_K^2\left[1+\frac{8\overset{\circ}{M}_K^2}{f^2}\frac{c_m}{M_S^2}(c_m - c_d)\right],\quad(1.123)$$

or, what is the same, for computations at $\mathcal{O}(p^4)$ we shall perform the replacements

$$\overset{\circ}{M}_\pi^2 \to \overset{\circ}{M}_\pi^2\left[1 - \frac{8\overset{\circ}{M}_\pi^2}{f^2}\frac{c_m}{M_S^2}(c_m - c_d)\right],\qquad(1.124)$$

$$\overset{\circ}{M}{}^2_K \to \overset{\circ}{M}{}^2_K \left[1 - \frac{8\overset{\circ}{M}{}^2_K}{f^2} \frac{c_m}{M_S^2} (c_m - c_d) \right], \tag{1.125}$$

in the mass matrix $\mathcal{M}$ Eq. (1.111). For illustrative purposes we also provide the correction of the physical decay constants at $\mathcal{O}(p^4)$

$$f_\pi = \mathcal{Z}_\pi^{-1/2} f, \quad f_K = \mathcal{Z}_K^{-1/2} f. \tag{1.126}$$

In this manner, in the amplitudes with terms of order p^4 (and higher), we transform the f constants appearing in the denominator of the amplitudes through

$$\frac{1}{f^2} \to \frac{1}{f_\pi^2} \left(1 + \frac{8\overset{\circ}{M}{}^2_\pi}{f_\pi^2} \frac{c_d c_m}{M_S^2} \right), \quad \frac{1}{f^2} \to \frac{1}{f_K^2} \left(1 + \frac{8\overset{\circ}{M}{}^2_\pi}{f_K^2} \frac{c_d c_m}{M_S^2} \right), \tag{1.127}$$

and hence we will write $f_{\pi,K}$ instead of f.

For the case of the η_8 and η_1 the situation is more involved since not only the mass term mix at $\mathcal{O}(p^4)$ but also the kinetic ones. Working along the same line as for the $\mathcal{O}(p^2)$ we make use again of a matrix notation and parameterize the mixing following the description as given in Refs. [68, 69]. The quadratic term in the Lagrangian reads

$$\mathcal{L} = \frac{1}{2} \partial_\mu \eta_B^T \mathcal{K} \partial^\mu - \frac{1}{2} \eta_B^T \mathcal{M}^2 \eta_B, \tag{1.128}$$

with

$$\mathcal{K} = \begin{pmatrix} 1 + \delta_8 & \delta_{81} \\ \delta_{81} & 1 + \delta_1 \end{pmatrix}, \quad \mathcal{M}^2 = \begin{pmatrix} M_8^2 & M_{81}^2 \\ M_{81}^2 & M_1^2 \end{pmatrix}. \tag{1.129}$$

The elements of the mass matrix are now

$$M_8^2 = \overset{\circ}{M}{}^2_8 + \Delta M_8^2, \quad M_1^2 = m_0^2 + \overset{\circ}{M}{}^2_1 + \Delta M_1^2, \quad M_{81}^2 = \overset{\circ}{M}{}^2_{81} + \Delta M_{81}^2, \tag{1.130}$$

where $\overset{\circ}{M}{}^2_i (i = 8, 1)$ is the $\mathcal{O}(\delta^0)$ quark-mass contributions to the octet and singlet masses we have already obtained in Eq. (1.115), while ΔM_8^2, ΔM_1^2 and ΔM_{81}^2 modify the lowest order values of the mass-matrix elements.

To first order in δ_8, δ_1 and δ_{81}, the kinetic matrix $\mathcal{K}$ can be diagonalised through the redefinition

$$\eta_B = Z^{1/2^T} \cdot \hat\eta \equiv Z^{1/2^T} \cdot \begin{pmatrix} \hat\eta_8 \\ \hat\eta_1 \end{pmatrix}, \quad Z^{1/2} \cdot \mathcal{K} \cdot Z^{1/2^T} = I_2 \tag{1.131}$$

$$Z^{1/2} = \begin{pmatrix} 1 - \delta_8/2 & -\delta_{81}/2 \\ -\delta_{81}/2 & 1 - \delta_1/2 \end{pmatrix}. \tag{1.132}$$

In the $\hat\eta$ basis the mass matrix takes the form

$$\widehat{\mathcal{M}}^2 = Z^{1/2} \cdot \mathcal{M}^2 Z^{1/2^T}, \tag{1.133}$$

where

$$\widehat{\mathcal{M}}_8^2 = \overset{\circ}{M}_8^2(1-\delta_8) - \overset{\circ}{M}_{81}^2\delta_{81} + \Delta M_8^2\,, \tag{1.134}$$

$$\widehat{\mathcal{M}}_1^2 = (m_0^2 + \overset{\circ}{M}_1^2)(1-\delta_8) - \overset{\circ}{M}_{81}^2\delta_{81} + \Delta M_1^2\,, \tag{1.135}$$

$$\widehat{\mathcal{M}}_{81}^2 = \overset{\circ}{M}_{81}^2(1-(\delta_8+\delta_1)/2) - (m_0^2 + \overset{\circ}{M}_8^2 + \overset{\circ}{M}_1^2)\delta_{81}/2 + \Delta M_{81}^2\,, \tag{1.136}$$

to first order in ΔM^2. Similar to Eq. (1.116), the physical mass eigenstates at NLO are obtained after diagonzalising the mass matrix $\widehat{\mathcal{M}}^2$

$$\eta_B = R^T \cdot \eta_P \equiv R^T \cdot \begin{pmatrix} \eta \\ \eta' \end{pmatrix}\,, \quad \widehat{\mathcal{M}}^2 = R^T \cdot \mathcal{M}_{\text{diag}} \cdot R\,, \tag{1.137}$$

with the rotation matrix R defined in Eq. (1.117). Therefore, the matrix from the bare to the physical basis is given by $\eta_B = (R \cdot Z^{1/2})^T \cdot \eta_P$ with

$$R \cdot Z^{1/2} = \begin{pmatrix} \cos\theta_P(1-\delta_8/2) + \sin\theta_P\delta_{81}/2 & -\sin\theta_P(1-\delta_1/2) - \cos\theta_P\delta_{81}/2 \\ \sin\theta_P(1-\delta_8/2) - \cos\theta_P\delta_{81}/2 & \cos\theta_P(1-\delta_1/2) - \sin\theta_P\delta_{81}/2 \end{pmatrix}\,. \tag{1.138}$$

In large-N_C ChPT,

$$\delta_8 = \frac{8L_5}{f^2}\overset{\circ}{M}_8^2\,, \quad \delta_1 = \frac{8L_5}{f^2}\overset{\circ}{M}_1^2 + \Lambda_1\,, \quad \delta_{81} = \frac{8L_5}{f^2}\overset{\circ}{M}_{81}^2\,, \tag{1.139}$$

and

$$\Delta M_8^2 = \frac{16L_8}{f^2}\left(\overset{\circ}{M}_8^4 + \overset{\circ}{M}_{81}^4\right)\,, \tag{1.140}$$

$$\Delta M_1^2 = \frac{16L_8}{f^2}\left(\overset{\circ}{M}_1^4 + \overset{\circ}{M}_{81}^4\right)\,, \tag{1.141}$$

$$\Delta M_{81}^2 = 2\overset{\circ}{M}_{81}^2\left(\frac{16L_8}{f^2}\overset{\circ}{M}_K^2 + \Lambda_2\right)\,, \tag{1.142}$$

while in RChT,

$$\delta_8 = \frac{8c_dc_m}{M_S^2}\frac{\overset{\circ}{M}_8^2}{f^2}\,, \quad \delta_1 = \frac{8c_dc_m}{M_S^2}\frac{\overset{\circ}{M}_1^2}{f^2}\,, \quad \delta_8 = \frac{8c_dc_m}{M_S^2}\frac{\overset{\circ}{M}_{81}^2}{f^2}\,, \tag{1.143}$$

and

$$\Delta M_8^2 = \frac{8c_m^2}{M_S^2 f^2}\left(\overset{\circ}{M}_8^4 + \overset{\circ}{M}_{81}^4\right)\,, \tag{1.144}$$

$$\Delta M_1^2 = \frac{8c_m^2}{M_S^2 f^2}\left(\overset{\circ}{M}_1^4 + \overset{\circ}{M}_{81}^4\right)\,, \tag{1.145}$$

$$\Delta M_{81}^2 = \frac{16c_m^2}{M_S^2 f^2}\overset{\circ}{M}_{81}^2\overset{\circ}{M}_K^2\,. \tag{1.146}$$

For a study of the $\eta-\eta'$ mixing up to next-to-next-to-leading-order in $U(3)$ ChPT we refer the reader to Ref. [66].

1.6 Anomalous sector

We would like to notice that both the leading-and next-to-leading-Lagrangians, $\mathcal{L}_2$ and $\mathcal{L}_4$, always involve an even number of pseudo-Goldstone bosons. This would mean that allowed QCD processes such as $\pi^0, \eta \to \gamma\gamma$, $\eta \to \pi^+\pi^-\gamma$ or $K\bar{K} \to 3\pi$, which are odd in the number of mesons, cannot be described by χPT. Moreover, $\mathcal{L}_2$ and $\mathcal{L}_4$ are invariant under chiral transformations which is in contradiction to the quantized theory of QCD which is not $U(1)_A$ invariant. Therefore, we need some additional term to account for this explicit $U(1)_A$ symmetry breaking including an odd number of pseudo-Goldstone boson fields. The solution was obtained by Wess, Zumino and Witten [70, 71] through the term $\mathcal{L}_{WZW}$ of the order $\mathcal{O}(p^4)$. For a formal derivation of this Lagrangian and wider discussions on this topic, the interested reader is referred to Ref. [28, 29, 72, 73]. For future practical purposes, we only quote here the interaction Lagrangian relevant for describing $\mathcal{P} \to \gamma\gamma$ with $\mathcal{P} = \pi^0, \eta, \eta'$

$$\mathcal{L}_{\mathcal{P}\gamma\gamma} = -\frac{\alpha N_C}{24\pi f_\pi}\epsilon^{\mu\nu\alpha\beta}F_{\mu\nu}F_{\alpha\beta}\mathcal{P}\,, \tag{1.147}$$

since enters the description of the single and double Dalitz decays, $\mathcal{P} \to \ell^+\ell^-\gamma$ and $\mathcal{P} \to \ell^+\ell^-\ell^+\ell^-$ ($\ell = e, \mu$), we will study in section 7. In the previous equation N_C is the number of colors, $\epsilon^{\mu\nu\alpha\beta}$ the Levi-Civita tensor and $F_{\rho\sigma}$ the electromagnetic field strength tensor, and the corresponding invariant amplitude reads

$$\mathcal{M}(\mathcal{P} \to \gamma\gamma) = i\frac{\alpha N_C}{3\pi f_\pi}\mathcal{C}_\mathcal{P}\epsilon^{\mu\nu\alpha\beta}\epsilon_\mu^*(\mathbf{q_1})\epsilon_\nu^*(\mathbf{q_1})q_{1,\alpha}q_{2,\beta}\,, \tag{1.148}$$

where $C_{\pi^0} = 1$, $C_{\eta_8} = 1/\sqrt{3}$ and $C_{\eta_1} = 2\sqrt{2/3}$. Calculating the partial decay width for the neutral pion $\pi^0 \to \gamma\gamma$

$$\Gamma(\pi^0 \to \gamma\gamma) = \frac{N_C^2\alpha^2 M_{\pi^0}^3}{576\pi^3 f_\pi^2} = 7.6 \cdot \left(\frac{N_C}{3}\right)^2 \text{eV}\,, \tag{1.149}$$

and comparing with the measured experimental value (7.7 ± 0.6) eV yields $N_C = 3$, a remarkable QCD measurement of the number of colors .

Chapter 2

Form Factors from dispersion relations

In this chapter we give an introduction to the mathematical aspects of the technique of dispersion relations applied, in particular, to two-meson form factors. The method is based on two powerful theoretical arguments such the use of the analytical properties of the form factor and the unitarity of the $S-$matrix. We will derive in detail the well-known Omnès equation, which will play a central role in the analysis of $\tau^- \to K^-\eta\nu_\tau$ and $\tau^- \to K^-\eta'\nu_\tau$ decays of section 3, in the combined analysis of the decays $\tau^- \to K_S\pi^-\nu_\tau$ and $\tau^- \to K^-\eta\nu_\tau$ of section 4 and in the study of $\tau^- \to \pi^-\eta\nu_\tau$ and $\tau^- \to \pi^-\eta'\nu_\tau$ decays of section 5.

2.1 Analyticity and implications of unitarity

A two-meson form factor is an analytic function $f(s)$ in the whole complex plane except for a branch cut along the real axis originated at the threshold, s_{th}, for producing the first two-particle intermediate state. The case in which the intermediate states are the same as the final one is known as elastic and the corresponding branch cut is called unitary or elastic cut. We will mainly concentrate to the elastic approximation though in section 2.3 we will also illustrate a method to implement inelastic cuts into the description. We have then that for $s > s_{th}$ the form factor develops an imaginary part while for $s < s_{th}$ is real. This implies the Schwartz reflection principle

$$f(s^*) = f^*(s) \,, \tag{2.1}$$

which allows to apply the Cauchy integral formula

$$f(s) = \frac{1}{2\pi i} \oint_\gamma \frac{f(s')}{s' - s} ds' \,, \tag{2.2}$$

where the integration path of the closed contour γ shown in Fig. (2.1) is chosen as an anti-clockwise circle of infinite radius Λ^2 but circumventing the branch cut $[s_{th}, \infty)$.
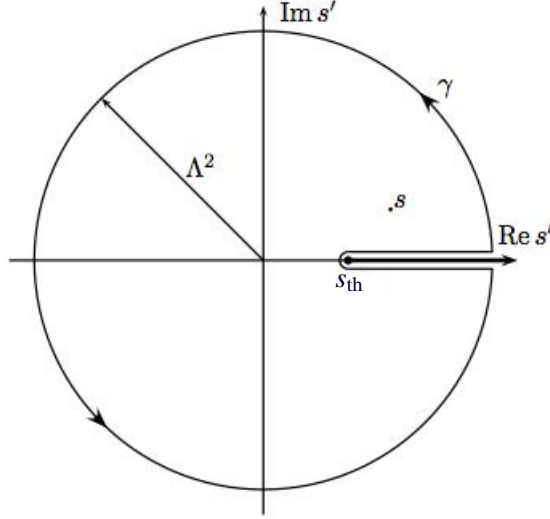
Figure 2.1: The integration contour γ used in Eq. (2.2) for the representation of $f(s)$.

By the use of the definition of the discontinuity across the cut

$$\text{disc } f(s) \equiv \frac{f(s + i\varepsilon) - f(s - i\varepsilon)}{2i} \, , \tag{2.3}$$

we may re-express Eq. (2.2) as

$$f(s \pm i\varepsilon) = \lim_{\varepsilon \to 0^{\pm}} \frac{1}{\pi} \int_{s_{th}}^{r} \frac{\text{disc } f(s')}{s' - s \mp i\varepsilon} ds' + \frac{1}{2\pi i} \oint_{|s'|=\Lambda^2} \frac{f(s')}{s' - s} ds' \, , \tag{2.4}$$

where the $\mp$ prescription in the denominator corresponds, respectively, to evaluate f on the upper (negative sign) or on the lower (positive sign) rim of the cut. From hereafter we will consider the function to be evaluated on the real axis from above the cut with $f(s) \equiv \lim_{\varepsilon \to 0^+} f(s + i\varepsilon)$ and we will omit the symbol $\lim_{\varepsilon \to 0^+}$ to shorten the notation. For the contribution of the infinite circle, second term of Eq. (2.4), we have

$$\left| \oint_{|s'|=\Lambda^2} \frac{f(s')}{s' - s} ds' \right| \leq \max_{|s'|=\Lambda^2} |f(s')| \oint \frac{1}{||s'| - |s||} |ds'| = \tag{2.5}$$

$$= \max_{|s'|=\Lambda^2} |f(s')| \frac{2\pi \Lambda^2}{\Lambda^2 - |s|} \xrightarrow{r \to \infty} \lim_{r \to \infty} 2\pi \max_{|s'|=\Lambda^2} |f(s')| \, , \tag{2.6}$$

where we have made use of the estimation lemma. Eq. (2.6) vanishes if $f(s)$ falls off fast enough when $|s| \to \infty$ and, as a consequence, the first term in Eq. (2.4), the integral along the branch cut, converges since the integrand vanishes asymptotically faster

than $1/s'$. Invoking the Schwartz reflection principle, Eq. (2.1), the discontinuity on the upper rim of the cut can written as

$$\text{disc} f(s) = \frac{f(s + i\varepsilon) - f^*(s + i\varepsilon)}{2i} = \text{Im} f(s + i\varepsilon) = \text{Im} f(s)\,, \tag{2.7}$$

which allow us to write the dispersion relation in the $r \to \infty$ limit as

$$f(s) = \frac{1}{\pi} \int_{s_{th}}^{\infty} \frac{\text{Im} f(s')}{s' - s - i\varepsilon} ds'\,, \tag{2.8}$$

like commonly appears in the literature.

However, if the function $f(s)$ does not vanish quickly enough for $|s| \to \infty$ we can still write dispersion relations by means of subtractions. Let us consider, for instance, that the form factor tends to a constant and s_0 is the subtraction point chosen to be a real number such that $s_0 < s_{th}$. By means of the use of the identity

$$\frac{1}{s' - s} = \frac{1}{s' - s_0} + \frac{s - s_0}{(s' - s_0)(s' - s)} \tag{2.9}$$

in Eq. (2.2), we arrive at

$$f(s) = \frac{1}{2\pi i} \oint_{\gamma} \frac{f(s')}{s' - s_0} ds' + \frac{s - s_0}{2\pi i} \oint_{\gamma} \frac{f(s')ds'}{(s' - s_0)(s' - s)} ds'\,, \tag{2.10}$$

where the first term is nothing but $f(s_0)$ and named a subtraction constant. Following the same reasoning as for the unsubtracted case we get the once subtracted dispersion relation

$$f(s) = f(s_0) + \frac{s - s_0}{\pi} \int_{s_{th}}^{\infty} \frac{\text{Im} f(s')}{(s' - s_0)(s' - s - i\varepsilon)} ds'\,, \tag{2.11}$$

where now the integrand in the second term has one more power of s in the denominator, hence reducing the dependence on $\text{Im} f(s')$ at large s' and improving its convergence. The generalization to an n-times subtracted dispersion relation at s_0 reads [52, 74]

$$f(s) = \sum_{k=0}^{n-1} \frac{(s - s_0)^k}{k!} \frac{d^k f(s)}{ds^k}\bigg|_{s=s_0} + \frac{(s - s_0)^n}{\pi} \int_{s_{th}}^{\infty} \frac{\text{Im} f(s')}{(s' - s_0)^n (s' - s - i\varepsilon)} ds'\,. \tag{2.12}$$

So far, we have seen from the analytical properties of the form factor $f(s)$ that if the discontinuity of the function is known up to infinity we can completely determine $f(s)$. We have also shown that subtractions may be required if $f(s)$ does not fulfill the desired asymptotic behavior, that is $f(s) \neq 0$ as $|s| \to \infty$. However, even in the case that subtractions are not strictly necessary, it may be recommended to perform them since in real physical situations the discontinuity is usually not known up

to arbitrarily large energies as demanded by the dispersive integral. By performing subtractions, we hence diminish the importance of the contribution from the high energy region in the integral. The introduced subtraction constants compensate our lack of knowledge on the discontinuity at high energies by absorbing the information anteriorly encoded in this region. In some sense, they resemble low-energy constants appearing in effective field theories [75, 76]. In all, subtracted dispersion relations as given in Eq. (2.12) show a nice synergy between high-and low-energy regimes.

Implications of unitarity

In quantum field theory, the probability transition amplitude for an initial state $|p_1 p_2 \ldots\rangle_{\text{in}}$, where p_i denotes the momentum of the incoming i particle, evolving into a final state $_{\text{out}}\langle k_1 k_2 \ldots|$, with k_j denoting the momentum of the outgoing j particle, is given by [77]

$$_{\text{out}}\langle k_1 k_2 \ldots | p_1 p_2 \ldots \rangle_{\text{in}} \equiv {}_{\text{in}}\langle k_1 k_2 \ldots | S | p_1 p_2 \ldots \rangle_{\text{in}}, \tag{2.13}$$

with the definition of the operator S

$$_{\text{out}}\langle k_1 k_2 \ldots | = {}_{\text{in}}\langle k_1 k_2 \ldots | S, \tag{2.14}$$

that evolves the initial state asymptotically in time. The $S-$matrix is commonly arranged as

$$S = 1 + iT, \tag{2.15}$$

where the first term accounts for the case in which the particles in the initial state do not interact while the second stands for the interactions. We know that in physical decay or scattering processes the four-momentum is a conserved quantity and so the invariant matrix element $\mathcal{M}$ is usually defined by

$$_{\text{in}}\langle k_1 k_2 \ldots | iT | p_1 p_2 \ldots \rangle_{\text{in}} = i(2\pi)^4 \delta^4 \Big(\sum_j k_j - \sum_i p_i \Big) \mathcal{M}(p_i \to k_j). \tag{2.16}$$

Let us define $P_{i \to f}$ as the probability to encounter a final state $\langle f|$ starting out from an initial definite state $|i\rangle$. Then, probability conservation means $\sum_f P_{i \to f} = 1$, which implies

$$S^\dagger S = S S^\dagger = 1, \tag{2.17}$$

that is, the $S-$matrix is unitary. In other words, probability conservation is generally named unitarity. This fact has interesting and profound consequences on the two-particle form factor's analytical properties as we will show in the following. By inserting Eq. (2.15) into Eq. (2.17) we get

$$T - T^\dagger = iTT^\dagger\,, \tag{2.18}$$

which plugged into Eq. (2.16) for the transition of the vacuum state, $|0\rangle$, to the states $\langle PQ|$ (where P and Q stand for particles), we obtain for the left hand side of Eq. (2.18)

$$\langle PQ|T|0\rangle - \langle PQ|T^\dagger|0\rangle = (2\pi)^4\delta^4(p_P + p_Q - s)\left(f_{PQ}(s) - f_{PQ}^*(s)\right)\,, \tag{2.19}$$

while the right hand side can be rewritten as

$$\langle PQ|iTT^\dagger|0\rangle = i\frac{1}{2}\sum_n \int \prod_n \frac{dp_n^3}{(2\pi)^3 E_n}\langle PQ|T|n\rangle\langle n|T^\dagger|0\rangle =$$

$$\frac{i(2\pi)^8}{2}\sum_n \int \prod_n \frac{dp_n^3}{(2\pi)^3 E_n}\delta^4(p_P + p_Q - p_n)\delta^4(p_n - s)\mathcal{T}_{n\to PQ}(s,\cos\theta)f_n^*(s)\,, \tag{2.20}$$

where we have inserted a complete set of intermediate states. Combining Eqs. (2.19) and (2.20) together we arrive at the unitarity condition

$$f_{PQ}(s) - f_{PQ}^*(s) = \frac{i(2\pi)^4}{2}\sum_n \int \prod_n \frac{dp_n^3}{(2\pi)^3 E_n}\delta^4(p_n - s)\mathcal{T}_{n\to PQ}(s,\cos\theta)f_n^*(s)\,, \tag{2.21}$$

where $f_{PQ}(s) \equiv \langle PQ|T|0\rangle$ and $\mathcal{T}_{n\to PQ}(s,\cos\theta) \equiv \langle PQ|T|n\rangle$. For the sake of simplicity, we restrict the set of intermediate states to two-particle states[1] $n = P'Q'$ which by using $d^3p_n = d\Omega dE_n E_n p_n$ we obtain

$$f_{PQ}(s) - f_{PQ}^*(s) = i\sum_n \frac{\theta(s - s_{th})q_{P'Q'}(s)}{8\pi\sqrt{s}}f_{P'Q'}^*(s)\int \mathcal{T}_{P'Q'\to PQ}(s,\cos\theta)d\cos\theta\,, \tag{2.22}$$

where s_{th} is the $P'Q'$-state production threshold, $q_{P'Q'}(s) \equiv \lambda_{P'Q'}/(2\sqrt{s})$ with

$$\lambda_{P'Q'} = \sqrt{[s - (m_{P'} + m_{Q'})^2][s - (m_{P'} - m_{Q'})^2]}\,, \tag{2.23}$$

is a kinematical factor accounting for the three-momentum of the $P'Q'$ state and θ is the scattering angle. The partial wave projection of the integrand is carried out through

$$\mathcal{T}(s,z) = 16\pi\sum_{l=0}^{\infty}(2l + 1)t_l(s)\mathcal{P}_l(z)\,, \tag{2.24}$$

---

[1]In principle, one should also take into account intermediate multiparticle states though the difficulty of the problem is such that it becomes almost unsolvable.

where $\mathcal{P}_l(z)$ are the Legendre polynomials of degree l with l being the orbital angular momentum and $t_l(s)$ are the partial wave amplitudes.

The left hand part of Eq. (2.22) is nothing else than the imaginary part of the form factor. Finally, the most general unitarity relation for form factors reads

$$\text{Im} f_{PQ}(s) = \sum_n \sigma_{P'Q'}(s) f_{P'Q'}(s) t^*_{P'Q' \to PQ}(s) \,, \tag{2.25}$$

where we have defined

$$\sigma_{P'Q'}(s) \equiv \frac{2q_{P'Q'}(s)}{\sqrt{s}} \theta(s - s_{th}) \,. \tag{2.26}$$

2.2 The Omnès equation

The case in which the intermediate states are the same as the final one is known as elastic and the corresponding branch cut is called unitary or elastic cut accordingly. This implies $P'Q' = PQ$ in Eq. (2.25) which in turn reduces to

$$\text{Im} f(s) = \sigma(s) f(s) t^*(s) \,, \tag{2.27}$$

where we have suppressed the two-particle states PQ subscript here and hereafter. On one hand, the elastic partial wave amplitude can be written in terms of the elastic scattering phase shift $\delta(s)$ as

$$t(s) = \frac{1}{\sigma(s)} \sin \delta(s) e^{i\delta(s)} \,, \tag{2.28}$$

which inserted into Eq. (2.27) leads

$$\text{Im} f(s) = f(s) \sin \delta(s) e^{-i\delta(s)} \,. \tag{2.29}$$

On the other hand, as for any complex function, the form factor $f(s)$ can be expressed as

$$f(s) = |f(s)| e^{i\phi(s)} \,, \tag{2.30}$$

that introduced into Eq. (2.29) gives

$$\text{Im} f(s) = |f(s)| \sin \delta(s) e^{i\phi(s)} e^{-i\delta(s)} \,, \tag{2.31}$$

which fixes the phase $\phi(s) = \delta(s)$ since the left hand side is real. This result is the well-known Watson's final sate theorem [78] which states that, within the elastic approximation, the phase of the elastic scattering amplitude equals that of the corresponding form factor.

By means of the use of the Schwartz reflection principle one has

$$f(s + i\varepsilon) = e^{2i\delta(s)}f(s - i\varepsilon), \tag{2.32}$$

which by taking the logarithm we obtain

$$\text{Im}\log f(s) = \frac{\log f(s + i\varepsilon) - \log f(s - i\varepsilon)}{2i} = \delta(s). \tag{2.33}$$

Using the once subtracted dispersion relation as given in Eq. (2.11) for Eq. (2.33) we have

$$\log f(s) = \log f(s_0) + \frac{s - s_0}{\pi}\int_{s_{th}}^{\infty}\frac{\text{Im}\log f(s')}{(s' - s_0)(s' - s - i\varepsilon)}ds' \tag{2.34}$$

$$= \log f(s_0) + \frac{s - s_0}{\pi}\int_{s_{th}}^{\infty}\frac{\delta(s')}{(s' - s_0)(s' - s - i\varepsilon)}ds'. \tag{2.35}$$

In this case, one subtraction is suitable since $\delta(s)$ tends to a constant at large s. The solution of Eq. (2.35) for $f(s)$ reads

$$f(s) = f(s_0)\exp\left[\frac{s - s_0}{\pi}\int_{s_{th}}^{\infty}\frac{\delta(s')}{(s' - s_0)(s' - s - i\varepsilon)}ds'\right] = f(s_0)\Omega(s), \tag{2.36}$$

where $\Omega(s)$ is the well-known Omnès function [79]

$$\Omega(s) = \exp\left[\frac{s - s_0}{\pi}\int_{s_{th}}^{\infty}\frac{\delta(s')}{(s' - s_0)(s' - s - i\varepsilon)}ds'\right]. \tag{2.37}$$

It is also interesting to provide both the real and imaginary parts of $f(s)$ which can be obtained after using the Skhotski-Plemelj theorem

$$\lim_{\varepsilon \to 0^+}\frac{1}{x' - x - i\varepsilon} = \mathcal{P}\frac{1}{x' - x} + i\pi\delta(x' - x) \tag{2.38}$$

where $\mathcal{P}$ represents the principal value. Inserting the previous equation in Eq. (2.36) we get

$$\text{Re}f(s) = f(s_0)\exp\left[\mathcal{P}\frac{s - s_0}{\pi}\int_{s_{th}}^{\infty}\frac{\delta(s')}{(s' - s_0)(s' - s)}ds'\right]\cos\delta(s), \tag{2.39}$$

and

$$\text{Im}f(s) = f(s_0)\exp\left[\mathcal{P}\frac{s - s_0}{\pi}\int_{s_{th}}^{\infty}\frac{\delta(s')}{(s' - s_0)(s' - s)}ds'\right]\sin\delta(s) = \tan\delta(s)\text{Re}f(s), \tag{2.40}$$

for the real and imaginary parts, respectively. These results are useful to determine the absolute value of the form factor that enters Eq. (2.30) as of

$$|f(s)| = f(s_0)\exp\left[\mathcal{P}\frac{s - s_0}{\pi}\int_{s_{th}}^{\infty}\frac{\delta(s')}{(s' - s_0)(s' - s)}ds'\right]. \tag{2.41}$$

We would like to notice that multiplying Eq. (2.36) by an arbitrary polynomial $P(s)$ it is also a solution since all the requisites demanded for $f(s)$ still hold. Thus, the most general solution becomes

$$f(s) = P(s)\Omega(s) \,. \tag{2.42}$$

In order to fix the polynomial ambiguity one should analyze the asymptotic behavior of the form factor. Studying $f(s)$ in this limit, where usually the phase shift tends to a constant $\delta_\infty \equiv \lim_{s\to\infty} \delta(s)$, from Eq. (2.30) one has [56]

$$\begin{aligned}
\lim_{s\to\infty} f(s) &= \lim_{s\to\infty} P(s) \exp\left[\frac{s-s_0}{\pi} \frac{\delta_\infty(s)}{s-s_0} \log\left(\frac{s_{th}-s}{s_{th}-s_0}\right)\right] e^{i\delta_\infty} \\
&= \lim_{s\to\infty} P(s) \left(\frac{s_{th}-s_0}{s}\right)^{\delta_\infty/\pi} e^{i\delta_\infty} \,.
\end{aligned} \tag{2.43}$$

Assuming $f(s)$ to vanish for $s \to \infty$ implies $P(s)$ to be a constant. This constant can be set to $f(s)$ evaluated at $s = 0$ whose numerical value should be inferred by invoking external information with the help of theoretical arguments.

The solution for n subtractions (cf. Eq. (2.12)) can be cast as [52, 74]

$$f(s) = Q_n(s) \exp\left[\frac{(s-s_0)^n}{\pi} \int_{s_{th}}^\infty \frac{\delta(s')}{(s'-s_0)^n(s'-s-i\varepsilon)} ds'\right] \,, \tag{2.44}$$

where

$$Q_n(s) = \exp\left[\sum_{k=0}^{n-1} \alpha_k (s-s_0)^k\right] \,, \tag{2.45}$$

with the $n-1$ subtraction constants being

$$\alpha_k = \frac{1}{k!} \frac{d^k}{ds^k} \log f(s)\Big|_{s=s_0} \,. \tag{2.46}$$

2.3 Form factors in coupled-channels

In the preceding section we have studied in detail the elastic approximation, by setting $P'Q' = PQ$ in Eq. (2.25), that has led the famous Omnès solution as outcome. This equation has success and extensively been employed in phenomenology for describing unitarity corrections due to elastic final state interactions. However, it does not account for the effect of inelastic intermediate states which, in principle, should also be considered. This can be achieved by inserting the central unitarity relation for form factors, Eq. (2.25), into a dispersion relation as of

$$f^i(s) = \frac{1}{\pi} \sum_{j=1}^{3} \int_{s_i}^\infty ds' \frac{\sigma_j(s') f^j(s') t^{i\to j}(s')^*}{(s'-s-i\varepsilon)} \,, \tag{2.47}$$

where s_i is the threshold for channel i and $t^{i \to j}$ are partial wave T-matrix elements for the $i \to j$ scattering. The unitarized form factors are then obtained by solving the coupled dispersion relations arising from the previous expression fulfilling the analytical requirements and incorporating the information contained in the scattering T-matrix. To solve the coupled channels problem, one typically rely on numerical iterative methods though algebraic closed expressions have also been illustrated as we discuss in appendix D for the later use in section 5. Of course, in the elastic approximation, eq. (2.47) reduces to the usual single-channel Omnès equation.

Part I

Hadronic tau decays

The tau lepton is the only lepton heavy enough ($m_\tau \sim 1.8$ GeV) to decay into hadrons. Actually the 65% of the branching ratio contains hadrons in the final state. Such decays proceed through the exchange of $W^\pm$ gauge bosons which couple the leptonic particles i.e. the tau and the generated neutrino, together with a quark-antiquark pair that subsequently hadronizes. For the sake of clarity, in Fig. (2.2) we provide a graphical account of a tau lepton decaying into a pair hadrons, $P^- P'^0$,
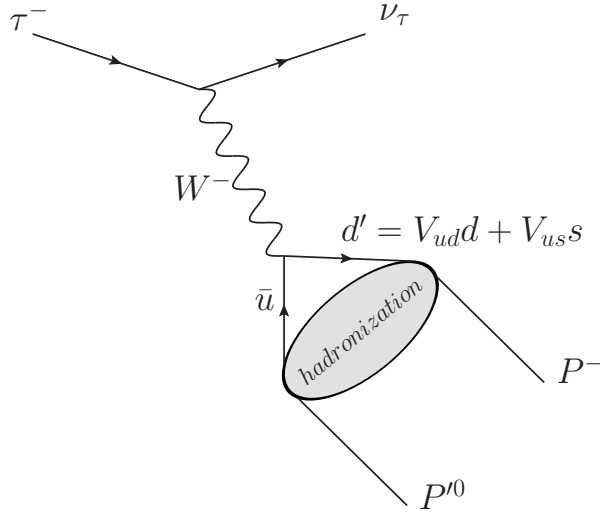
Figure 2.2: Schematic picture of a two mesons decay of the τ.

whose amplitude can be expressed as an electroweak part times an hadronic matrix element as

$$\mathcal{M}\left(\tau^- \to P^- P'^0 \nu_\tau\right) = \frac{G_F}{\sqrt{2}} V_{\text{CKM}} \bar{u}(p_{\nu_\tau}) \gamma^\mu (1 - \gamma^5) u(p_\tau) \langle P^- P'^0 | d' \gamma^\mu u | 0 \rangle, \qquad (2.48)$$

where $d' = V_{ud}^* \bar{d} + V_{us}^* \bar{s}$. Since the energy we are exploring ($\sqrt{s} < m_\tau$) is much lighter than the $W^\pm$ boson mass ($m_\tau \sim 80$ GeV), in the previous equation we have not considered the gauge boson propagator but rather its expansion.

That explains why semileptonic tau decays represent a clean laboratory to study the hadronization properties of QCD since half of the process is purely electroweak and can be computed straightforwardly. Therefore, the unknown QCD dynamics is encoded within the hadronic matrix element whose general parameterization in terms of form factors read [80]

$$\langle P^- P'^0 | d' \gamma^\mu u | 0 \rangle = \mathcal{C}_{P^- P'^0} \left\{ \left(p_- - p_0 - \frac{\Delta_{P^- P'^0}}{s} q \right)^\mu F_+^{P^- P'^0}(s) + \frac{\Delta_{P^- P'^0}}{s} q^\mu F_0^{P^- P'^0}(s) \right\},$$
$$(2.49)$$

where $\mathcal{C}_{P^-P'^0}$ is a Clebsch-Gordon coefficient, p_-^μ and p_0^μ are the momenta of the charged and neutral pseudoscalars, respectively, $q^\mu = (p_- + p_0)^\mu$ is the momentum transfer and $s = q^2$. In Eq. (2.49), the vector and scalar form factors functions, $F_+^{P^-P'^0}(s)$ and $F_0^{P^-P'^0}(s)$, respectively, carry all the information. Notice that the scalar contribution is suppressed by the mass-squared difference $\Delta_{P^-P'^0} = m_{P^-}^2 - m_{P'^0}^2$ since the vector current is conserved in the limit of equal quark masses (cf. Eq. (1.22)). In all, to have a proper parameterization of the form factors is of capital importance for the understanding two meson hadronic tau decays.

At the inclusive level, hadronic tau decays allows to extract fundamental parameters of the SM, most importantly the strong coupling α_S [81, 82, 83, 84], but also the matrix element $|V_{us}|$ [85, 86] and the mass of the strange quark at high precision [87, 88, 89, 90, 91, 92, 93, 94, 95].

At exclusive level, the tau hadronic partial width ($\sim 65\%$) is the sum of the tau partial width to strange ($\sim 3\%$) and to non-strange ($\sim 62\%$) hadronic final states. On one hand, the non-strange decays are vastly dominated by the $\pi^-\pi^0$ mode which, actually, is the main decay channel of the τ with an absolute branching ratio of $\sim 25\%$. This channel has been extensively studied in literature [52, 96, 97] since it becomes a privileged laboratory to prove the vector form factor because the scalar ones is weighted by the $SU(2)$ breaking term, $\Delta_{\pi^-\pi^0}$, and hence negligible. On the other hand, the strange hadronic final states are suppressed respect to the non-strange ones mainly because of the following two reasons: i) the mass of the strange quark is much larger than the mass of the up and down quarks leading a phase-space suppression; ii) strange decays are Cabibbo suppressed since the $|V_{us}|$ element of the CKM matrix enters the description rather than $|V_{ud}|$ as occurs in the non-strange one.

The dominant strangeness-changing τ decays are into $K\pi$ meson systems which adds up to $\sim 42\%$ of the strange spectral function. The corresponding differential decay width was measured at LEP by the ALEPH [98] and OPAL [99] collaborations, and recently the B-factories BaBar [17] and Belle [100] have published increased accuracy measurements. We would like to note that the BaBar collaboration published their analysis for the $K^-\pi^0$ mode, while Belle studied the $K_S\pi^-$ decay mode. Belle's spectrum became publicly available but the published BaBar analysis only concerned the branching ratio while the corresponding spectrum has not been released yet[2]. As a result, all dedicated studies of the $\tau^- \to (K\pi)^-\nu_\tau$ decays focused on the $K_S\pi^-$

---

[2]BaBar reported preliminary results for the $\bar{K}^0\pi^-$ mode at the TAU'08 Conference [101], whereas Belle also plans to study the $K^-\pi^0$ mode and has just published updated values of the branching fractions of decay modes including K_S mesons analysing a larger data sample [102]. We thank Swagato Banerjee, Simon Eidelman, Denis Epifanov and Ian Nugent for conversations on this point.

system [14, 15, 103, 104, 105, 106]. Consequently, even using data from semileptonic Kaon decays ($K \to \pi \ell \nu$, so called $K_{\ell 3}$ decays) [15, 106], important information on isospin breaking effects in the low-energy expansion of the hadronic form factors could no be extracted. The quoted references succeeded in improving the determination of the $K^\star(892)$ and $K^\star(1410)$ resonance properties: their pole positions and relative weight, although the errors on the radial excitation were noticeably larger than in the $K^\star(892)$ case.

In order to increase the knowledge of the strange spectral function, the $\tau^- \to (K\pi\pi(\pi))^- \nu_\tau$ decays have to be better understood (they add up to one third of the strange decay width), the $\tau^- \to K^- \eta \nu_\tau$ and $\tau^- \to (K\pi)^- \eta \nu_\tau$ decays being also important for that purpose. Actually, the threshold for the $K^- \eta$ mode is above the region of $K^\star(892)$-dominance which enhances its sensitivity to the properties of the heavier copy $K^\star(1410)$. This observation leads the $\tau^- \to K^- \eta \nu_\tau$ decay to be competitive with the $\tau^- \to (K\pi)^- \nu_\tau$ decays in the extraction of the $K^\star(1410)$ meson parameters. This is one of the motivations for the study of the $\tau^- \to K^- \eta \nu_\tau$ decay in chapter 3 of this thesis. This has been possible thanks to BaBar [107] and Belle [12] data of the $K^- \eta$ spectrum. In this chapter we will also predict $\tau^- \to K^- \eta' \nu_\tau$ decay channel for which we advocate its measurement in future B-factories.

Then, in chapter 4 we will illustrate the potential of a combined analysis of both $\tau^- \to K_S \pi^- \nu_\tau$ and $\tau^- \to K^- \eta \nu_\tau$ decays in the determination of the $K^\star(1410)$ resonance properties.

Finally, in chapter 5 we will analyze the rare decays $\tau^- \to \pi^- \eta^{(\prime)} \nu_\tau$ which belong to the so-called second-class current processes i.e. parity conservation implies that these transitions must proceed through the vector currents, which has opposed G-parity to the $\pi^- \eta^{(\prime)}$ system (see appendix B for a detailed explanation). In the limit of exact isospin symmetry, these processes are forbidden in the SM. However, isospin is an $SU(2)$ approximate symmetry, slightly broken both by $m_u \neq m_d$ (in QCD) and $q_u \neq q_d$ (in QED) leading a sizable suppression of the considered decays which have not been measured so far.

Chapter 3

$\tau^- \to K^- \eta^{(\prime)} \nu_\tau$ decays

The $\tau^- \to K^- \eta \nu_\tau$ decays were first measured by CLEO [108] and ALEPH [109] in the '90s. Only very recently Belle [12] and BaBar [107] managed to improve these measurements reducing the branching fraction to essentially half of the CLEO and ALEPH results and achieving a decrease of the error at the level of one order of magnitude. Belle [12] measured a branching ratio of $(1.58 \pm 0.05 \pm 0.09) \cdot 10^{-4}$ and BaBar [107] $(1.42 \pm 0.11 \pm 0.07) \cdot 10^{-4}$, which combined to give the PDG average $(1.52 \pm 0.08) \cdot 10^{-4}$ [37]. The related decay $\tau^- \to K^- \eta' \nu_\tau$ has not been detected yet, although an upper limit at the 90% confidence level was placed by BaBar [110] but has not been incorporated to the PDG [37].

Belle's paper [12] cites the few existing calculations of the $\tau^- \to K^- \eta \nu_\tau$ decays based on Chiral Lagrangians [111, 112, 113, 114] and concludes that 'further detailed studies of the physical dynamics in τ decays with η mesons are required' (see also, e.g. Ref. [115])[1]. Our aim is to provide a more elaborated analysis which takes into account the advances in this field since the publication of the quoted references more than fifteen years ago. The considered $\tau^- \to K^- \eta^{(\prime)} \nu_\tau$ decays are currently modeled in TAUOLA [117, 118], the standard Monte Carlo generator for tau lepton decays, relying on phase space. We would like to provide the library with Resonance Chiral Lagrangian-based currents [119, 120] that can describe well these decays for their analyses and for the characterization of the backgrounds they constitute to searches of rarer tau decays and new physics processes.

This chapter is organized as follows: the hadronic matrix element and the participating vector and scalar form factors are defined in section 3.1, where the differential decay distribution in terms of the latter is also given. These form factors are derived within Chiral Perturbation Theory (χPT) [5, 6, 7] including resonances ($R\chi T$)

---

[1]Very recently, the $\tau^- \to K\pi/\eta\nu_\tau$ decays have been studied [116]. However, no satisfactory description of the data can be achieved in both decay channels simultaneously.

[48, 53] in section 3.2. Three different options according to treatment of final-state interactions in these form factors are discussed in section 3.3 and will be used in the remainder of the paper. In section 3.4, the $\tau^- \to K^- \eta \nu_\tau$ decay observables are predicted based on the knowledge of the $\tau^- \to (K\pi)^- \nu_\tau$ decays. These results are then improved in section 3.5 by fitting the BaBar and Belle $\tau^- \to K^- \eta \nu_\tau$ data. We provide our predictions on the $\tau^- \to K^- \eta' \nu_\tau$ decays in section 3.6 and present our conclusions in section 4.3.

3.1 Matrix elements and decay width

We fix our conventions from the general parametrization of the scalar and vector $K^+ \eta^{(\prime)}$ matrix elements [121]:

$$\left\langle \eta^{(\prime)} \middle| \bar{s}\gamma^\mu u \middle| K^+ \right\rangle = c^V_{K\eta^{(\prime)}} \left[(p_{\eta^{(\prime)}} + p_K)^\mu f_+^{K^+\eta^{(\prime)}}(t) + (p_K - p_{\eta^{(\prime)}})^\mu f_-^{K^+\eta^{(\prime)}}(t) \right], \quad (3.1)$$

where $t = (p_K - p_{\eta^{(\prime)}})^2$. From Eq. (3.1) one has

$$\left\langle K^- \eta^{(\prime)} \middle| \bar{s}\gamma^\mu u \middle| 0 \right\rangle = c^V_{K\eta^{(\prime)}} \left[(p_{\eta^{(\prime)}} - p_K)^\mu f_+^{K^-\eta^{(\prime)}}(s) - q^\mu f_-^{K^-\eta^{(\prime)}}(s) \right], \quad (3.2)$$

with $q^\mu = \left(p_{\eta^{(\prime)}} + p_K \right)^\mu$, $s = q^2$ and $c^V_{K\eta^{(\prime)}} = -\sqrt{\frac{3}{2}}$. Instead of $f_-^{K^-\eta^{(\prime)}}(s)$ one can use $f_0^{K^-\eta^{(\prime)}}(s)$ defined through

$$\left\langle 0 \middle| \partial_\mu(\bar{s}\gamma^\mu u) \middle| K^- \eta^{(\prime)} \right\rangle = i(m_s - m_u) \left\langle 0 \middle| \bar{s}u \middle| K^- \eta^{(\prime)} \right\rangle \equiv i\Delta_{K\pi} c^S_{K^-\eta^{(\prime)}} f_0^{K^-\eta^{(\prime)}}(s), \quad (3.3)$$

with

$$c^S_{K^-\eta} = -\frac{1}{\sqrt{6}}, \quad c^S_{K^-\eta'} = \frac{2}{\sqrt{3}}, \quad \Delta_{PQ} = m_P^2 - m_Q^2. \quad (3.4)$$

The mass renormalization $m_s - \bar{m}$ in χPT (or $R\chi T$) needs to be taken into account to define $f_0^{K^-\eta^{(\prime)}}(s)$ and $\bar{m} = (m_d + m_u)/2$ has been introduced. We will take $\Delta_{K\pi}\Big|^{QCD} = \Delta_{K\pi}$, which is an excellent approximation. From eqs. (3.2) and (3.3) one gets

$$\left\langle K^- \eta^{(\prime)} \middle| \bar{s}\gamma^\mu u \middle| 0 \right\rangle = \left[(p_{\eta^{(\prime)}} - p_K)^\mu + \frac{\Delta_{K\eta^{(\prime)}}}{s} q^\mu \right] c^V_{K^-\eta^{(\prime)}} f_+^{K^-\eta^{(\prime)}}(s) + \frac{\Delta_{K\pi}}{s} q^\mu c^S_{K^-\eta^{(\prime)}} f_0^{K^-\eta^{(\prime)}}(s), \quad (3.5)$$

and the normalization condition

$$f_+^{K^-\eta^{(\prime)}}(0) = -\frac{c^S_{K^-\eta^{(\prime)}}}{c^V_{K^-\eta^{(\prime)}}} \frac{\Delta_{K\pi}}{\Delta_{K\eta^{(\prime)}}} f_0^{K^-\eta^{(\prime)}}(0), \quad (3.6)$$

which is obtained from

$$f_-^{K^-\eta^{(\prime)}}(s) = -\frac{\Delta_{K\eta^{(\prime)}}}{s} \left[\frac{c^S_{K^-\eta^{(\prime)}}}{c^V_{K^-\eta^{(\prime)}}} \frac{\Delta_{K\pi}}{\Delta_{K\eta^{(\prime)}}} f_0^{K^-\eta^{(\prime)}}(s) + f_+^{K^-\eta^{(\prime)}}(s) \right]. \quad (3.7)$$

In terms of these form factors, the differential decay width reads

$$\frac{d\Gamma\left(\tau^- \to K^- \eta^{(\prime)} \nu_\tau\right)}{d\sqrt{s}} = \frac{G_F^2 M_\tau^3}{32\pi^3 s} S_{EW} \left|V_{us} f_+^{K^- \eta^{(\prime)}}(0)\right|^2 \left(1 - \frac{s}{M_\tau^2}\right)^2 \quad (3.8)$$

$$\left\{ \left(1 + \frac{2s}{M_\tau^2}\right) q_{K\eta^{(\prime)}}^3(s) \left|\widetilde{f}_+^{K^- \eta^{(\prime)}}(s)\right|^2 + \frac{3\Delta_{K\eta^{(\prime)}}^2}{4s} q_{K\eta^{(\prime)}}(s) \left|\widetilde{f}_0^{K^- \eta^{(\prime)}}(s)\right|^2 \right\},$$

where

$$q_{PQ}(s) = \frac{\sqrt{s^2 - 2s\Sigma_{PQ} + \Delta_{PQ}^2}}{2\sqrt{s}}, \quad \sigma_{PQ}(s) = \frac{2q_{PQ}(s)}{\sqrt{s}} \theta\left(s - (m_P + m_Q)^2\right),$$

$$\Sigma_{PQ} = m_P^2 + m_Q^2, \quad \widetilde{f}_{+,0}^{K^- \eta^{(\prime)}}(s) = \frac{f_{+,0}^{K^- \eta^{(\prime)}}(s)}{f_{+,0}^{K^- \eta^{(\prime)}}(0)}, \quad (3.9)$$

and $S_{EW} = 1.0201$ [122] represents an electro-weak correction factor.

We have considered the $\eta - \eta'$ mixing up to next-to-leading order in the combined expansion in p^2, m_q and $1/N_C$ [8] (see the next section for the introduction of the large-N_C limit of QCD [62] applied to the light-flavoured mesons). In this way it is found that $\left|V_{us} f_+^{K^- \eta}(0)\right| = \left|V_{us} f_+^{K^- \pi^0}(0)\cos\theta_P\right|$, $\left|V_{us} f_+^{K^- \eta'}(0)\right| = \left|V_{us} f_+^{K^- \pi^0}(0)\sin\theta_P\right|$, where $\theta_P = (-13.3 \pm 1.0)^\circ$ [123].

The best access to $\left|V_{us} f_+^{K^- \pi^0}(0)\right|$ is through semi-leptonic Kaon decay data. We will use the value 0.21664 ± 0.00048 [124, 125]. Equation (3.8) makes manifest that the unknown strong-interaction dynamics is encoded in the tilded form factors, $\widetilde{f}_{+,0}^{K^- \eta^{(\prime)}}(s)$ which will be subject of our analysis in the following section. We will see in particular that the use of $\widetilde{f}_{+,0}^{K^- \eta^{(\prime)}}(s)$ instead of the untilded form factors yields more compact expressions that are symmetric under the exchange $\eta \leftrightarrow \eta'$, see eqs. (3.19) and (3.24).

3.2 Scalar and vector form factors in RχT

Although there is no analytic method to derive the $\widetilde{f}_{+,0}^{K^- \eta^{(\prime)}}(s)$ form factors directly from the QCD Lagrangian, its symmetries are nevertheless useful to reduce the model dependence to a minimum and keep as many properties of the fundamental theory as possible.

χPT [5, 6, 7], the effective field theory of QCD at low energies, is built as an expansion in even powers of the ratio between the momenta or masses of the lightest pseudoscalar mesons over the chiral symmetry breaking scale, which is of the order of one GeV. As one approaches the energy region where new degrees of freedom -the lightest meson resonances- become active, χPT ceases to provide a good description

of the Physics (even including higher-order corrections [126, 127, 128]) and these resonances must be incorporated to the action of the theory. This is done without any ad-hoc dynamical assumption by $R\chi T$ in the convenient antisymmetric tensor formalism that avoids the introduction of local χPT terms at next-to-leading order in the chiral expansion since their contribution is recovered upon integrating the resonances out [48, 53]. The building of the Resonance Chiral Lagrangians is driven by the spontaneous symmetry breakdown of QCD realized in the meson sector, the discrete symmetries of the strong interaction and unitary symmetry for the resonance multiplets. The expansion parameter of the theory is the inverse of the number of colours of the gauge group, $1/N_C$. Despite N_C not being small in the real world, the fact that phenomenology supports this approach to QCD [51, 129] hints that the associated coefficients of the expansion are small enough to warrant a meaningful perturbative approach based on it. At leading order in this expansion there is an infinite number of radial excitations for each resonance with otherwise the same quantum numbers that are strictly stable and interact through local effective vertices only at tree level. We have provided the relevant effective Lagrangian for the lightest resonance nonets in Eq. (1.76).
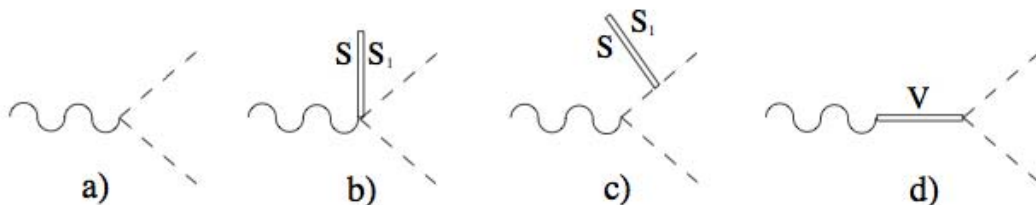
Figure 3.1: Diagrams contributing for calculating the $K^-\eta^{(\prime)}$ vector form factors. From left to right we have: a) χPT at lowest order, $\mathcal{O}(p^2)$; b) Octet, S, and singlet, S_1, scalar resonance exchange coupled to the vacuum; c) $\mathcal{O}(p^4)$ contributions from the $\mathcal{O}(p^2)$ Lagrangian due to wave function and mass renormalizations; d) Explicit exchange of vector resonances, K^* and excitations. The image has been borrowed from Ref. [130].

For the computation of the vector form factors we have to evaluate the diagrams depicted in Fig. 3.1 [130]. Diagram a) results from calculating the vector current in ChPT at $\mathcal{O}(p^2)$ by means of Eq. (1.49)

$$\langle K^-\eta|(J_V^\mu)_{31}|0\rangle \;=\; i\sqrt{\frac{3}{2}}\cos\theta_P\Big[K^+\left(\partial^\mu\eta\right)-\left(\partial^\mu K^+\right)\eta\Big]$$

$$= -\sqrt{\frac{3}{2}} \cos \theta_P (p_\eta - p_K)^\mu \, , \tag{3.10}$$

and

$$\langle K^- \eta' | (J_V^\mu)_{31} | 0 \rangle = i\sqrt{\frac{3}{2}} \sin \theta_P \left[K^+ (\partial^\mu \eta') - (\partial^\mu K^+) \eta' \right] \tag{3.11}$$

$$= -\sqrt{\frac{3}{2}} \sin \theta_P (p_{\eta'} - p_K)^\mu \, , \tag{3.12}$$

which lead

$$f_+^{K^-\eta}(s) = -\sqrt{\frac{3}{2}} \cos \theta_P (1 + \dots) \, ,$$

$$f_+^{K^-\eta'}(s) = -\sqrt{\frac{3}{2}} \sin \theta_P (1 + \dots) \, , \tag{3.13}$$

for the η and η' respectively. The contributions from the vacuum insertion, diagram b), and the ones from the wave function renormalization, diagram c), cancel each other due to charge conservation. For the calculation of the contribution of diagram d) we need the following pieces

$$\curvearrowleft\!\!\sim\!\!\sim\!\!\sim\!= \langle K^{*-} | - \frac{F_V}{\sqrt{2}} \partial_\nu \left(u^\dagger V^{\nu\mu} u + u V^{\nu\mu} u^\dagger \right) | 0 \rangle$$

$$= \langle K^{*-} | - \sqrt{2} F_V \partial_\nu V^{\nu\mu} | 0 \rangle = -i\sqrt{2} F_V (p_K + p_\eta)_\mu \, , \tag{3.14}$$

for the boson-vector interaction,

$$\underline{\mathbf{V}} \quad = \frac{i}{M_{K^*}^2 - s} \left(g_{\mu\rho} g_{\nu\sigma} - g_{\mu\sigma} g_{\nu\rho} \right) \, , \tag{3.15}$$

for the vector resonance propagator in the antisymmetric tensor formalism [48] and

$$\prec \quad = \langle K^- \eta | \frac{iG_V}{\sqrt{2}} \langle V_{\mu\nu} u^\mu u^\nu \rangle | 0 \rangle$$

$$= \frac{iG_V}{\sqrt{3} f^2} \cos \theta_P K_{\mu\nu}^{*-} \left[2 \partial^\mu K^+ \partial^\nu \eta - \partial^\mu \eta \partial^\nu K^+ \right]$$

$$= \frac{iG_V}{\sqrt{3} f^2} i^2 \left(2 p_K^\rho p_\eta^\sigma - p_\eta^\rho p_K^\sigma \right) \, , \tag{3.16}$$

for the interaction between the vector resonance and the $K^- \eta$ system.
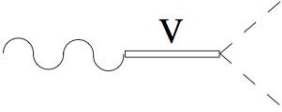
 $= \; i(-i)\sqrt{2}F_V \, (p_K + p_\eta)^\mu \cos\theta_P \frac{i}{M_{K^*}^2 - s} \left(g_{\mu\rho}g_{\nu\sigma} - g_{\mu\sigma}g_{\nu\rho} \right)$

$$\times \frac{iG_V}{\sqrt{3}f^2} i^2 \left(2p_K^\rho p_\eta^\sigma - p_\eta^\rho p_K^\sigma \right) , \tag{3.17}$$

Finally, the explicit expression for the diagram d) arise by multiplying Eqs. (3.14), (3.15) and (3.16) altogether as

which leads

$$-\sqrt{\frac{3}{2}} \cos\theta_P \frac{F_V G_V}{f^2} \frac{1}{M_{K^*}^2 - s} \{ (p_\eta + p_K)_\nu \left(m_K^2 - m_\eta^2 \right) + (p_\eta - p_K)_\nu \, s \} \tag{3.18}$$

after contracting indices. For the η' we just need to replace $\cos\theta_P \to \sin\theta_P$ in the previous equations.

The resulting $K^-\eta^{(\prime)}$ vector form factors emerge by summing up together Eqs. (3.13) and (3.18) as of

$$\tilde{f}_+^{K^-\eta^{(\prime)}}(s) = \frac{f_+^{K^-\eta^{(\prime)}}(s)}{f_+^{K^-\eta^{(\prime)}}(0)} = 1 + \frac{F_V G_V}{F^2} \frac{s}{M_{K^\star}^2 - s} , \tag{3.19}$$

where $f_+^{K^-\eta}(0) = \cos\theta_P$ and $f_+^{K^-\eta'}(0) = \sin\theta_P$. We recall that the normalization of the $K\pi$ vector form factor, $f_+^{K^-\pi}(0)$, was pre-factored in Eq. (3.8) together with $|V_{us}|$.

The strangeness changing scalar form factors and associated S-wave scattering within $R\chi T$ have been investigated in a series of papers by Jamin, Oller and Pich [56, 68, 103, 131] (see also Ref. [132]). For the scalar form factors we also have to evaluate the diagrams in Fig. 3.1, of course with an scalar current in this case, and replacing the exchange of vector resonances in diagram d) by scalar one. The calculation gives:

$$\tilde{f}_0^{K^-\eta}(s) = \frac{f_0^{K^-\eta}(s)}{f_0^{K^-\eta}(0)} = \frac{1}{f_0^{K^-\eta}(0)} \left[\cos\theta_P f_0^{K^-\eta_8}(s) \Big|_{\eta_8 \to \eta} + 2\sqrt{2}\sin\theta_P f_0^{K^-\eta_1}(s) \Big|_{\eta_1 \to \eta} \right] , \tag{3.20}$$

$$\tilde{f}_0^{K^-\eta'}(s) = \frac{f_0^{K^-\eta'}(s)}{f_0^{K^-\eta'}(0)} = \frac{1}{f_0^{K^-\eta'}(0)} \left[\cos\theta_P f_0^{K^-\eta_1}(s) \Big|_{\eta_1 \to \eta'} - \frac{1}{2\sqrt{2}}\sin\theta_P f_0^{K^-\eta_8}(s) \Big|_{\eta_8 \to \eta'} \right] ,$$

and can be written in terms of the $f_0^{K^-\eta_8}(s)$, $f_0^{K^-\eta_1}(s)$ form factors computed in Ref. [56]:

$$f_0^{K^-\eta_8}(s) = 1 + \frac{4c_m}{F^2(M_S^2 - s)} \left[c_d(s - m_K^2 - p_{\eta_8}^2) + c_m(5m_K^2 - 3m_\pi^2) \right]$$

$$+ \frac{4c_m(c_m - c_d)}{F^2 M_S^2}(3m_K^2 - 5m_\pi^2) , \tag{3.21}$$

$$f_0^{K^-\eta_1}(s) = 1 + \frac{4c_m}{F^2(M_S^2 - s)} \left[c_d(s - m_K^2 - p_{\eta_1}^2) + c_m 2m_K^2 \right]$$
$$- \frac{4c_m(c_m - c_d)}{F^2 M_S^2} 2m_\pi^2 \,, \tag{3.22}$$

where, for the considered flavour indices, S should correspond to the $K_0^\star(1430)$ resonance. Besides $f_0^{K^-\pi}(0) = f_+^{K^-\pi}(0)$ (see the comment below equation (3.19)) it has also been used that

$$f_0^{K^-\eta}(0) = \cos\theta_P \left(1 + \frac{\Delta_{K\eta} + 3\Delta_{K\pi}}{M_S^2} \right) + 2\sqrt{2}\sin\theta_P \left(1 + \frac{\Delta_{K\eta}}{M_S^2} \right) \,,$$
$$f_0^{K^-\eta'}(0) = \cos\theta_P \left(1 + \frac{\Delta_{K\eta}}{M_S^2} \right) + \sin\theta_P \left(1 + \frac{\Delta_{K\eta} + 3\Delta_{K\pi}}{M_S^2} \right) \,. \tag{3.23}$$

Indeed, using our conventions, the tilded scalar form factors become simply

$$\tilde{f}_0^{K^-\eta^{(\prime)}}(s) = \frac{f_0^{K^-\eta^{(\prime)}}(s)}{f_0^{K^-\eta^{(\prime)}}(0)} = 1 + \frac{c_d c_m}{4F^2} \frac{s}{M_S^2 - s} \,, \tag{3.24}$$

that is more compact than eqs. (3.20), (3.21) and displays the same symmetry $\eta \leftrightarrow \eta'$ than the vector form factors in Eq. (3.19).

The computation of the leading order amplitudes in the large-N_C limit within $R\chi T$ demands, however, the inclusion of an infinite tower of resonances per set of quantum numbers [2]. Although the masses of the large-N_C states depart slightly from the actually measured particles [133] only the second vector state, i.e. the $K^\star(1410)$ resonance, will have some impact on the considered decays. Accordingly, we will replace the vector form factor in Eq. (3.19) by

$$\tilde{f}_+^{K^-\eta^{(\prime)}}(s) = 1 + \frac{F_V G_V}{F^2} \frac{s}{M_{K^\star}^2 - s} + \frac{F_V' G_V'}{F^2} \frac{s}{M_{K^\star\prime}^2 - s} \,, \tag{3.25}$$

where the operators with couplings F_V' and G_V' are defined in analogy with the corresponding unprimed couplings in Eq. (1.76).

If we require that the $f_+^{K^-\eta^{(\prime)}}(s)$ and $f_0^{K^-\eta^{(\prime)}}(s)$ form factors vanish for $s \to \infty$ at least as $1/s$ [214], we obtain the short-distance constraints

$$F_V G_V + F_V' G_V' = F^2 \,, \quad 4c_d c_m = F^2 \,, \quad c_d - c_m = 0 \,, \tag{3.26}$$

which yield the form factors

$$\tilde{f}_+^{K^-\eta}(s) = \frac{M_{K^\star}^2 + \gamma s}{M_{K^\star}^2 - s} - \frac{\gamma s}{M_{K^\star\prime}^2 - s} = \tilde{f}_+^{K^-\eta'}(s) \,, \tag{3.27}$$
$$\tilde{f}_0^{K^-\eta}(s) = \frac{M_S^2}{M_S^2 - s} = \tilde{f}_0^{K^-\eta'}(s) \,,$$

---

[2]We point out that there is no limitation in the $R\chi T$ Lagrangians in this respect. In particular, a second multiplet of resonances has been introduced in the literature [134, 135] and bi- and tri-linear operators in resonance fields have been used [54, 136, 137, 138, 139, 140].

where $\gamma = -\frac{F'_V G'_V}{F^2} = \frac{F_V G_V}{F^2} - 1$ [14, 15, 103, 105]. We note that we are disregarding the modifications introduced by the heavier resonance states to the relation (3.26) and to the definition of γ.

3.3 Treatment of final-state interactions

The form factors in eqs. (3.27) diverge when the exchanged resonance is on-mass shell and, consequently, cannot represent the underlying dynamics that may peak in the resonance region but does not certainly show a singular behaviour. This is solved by considering a next-to-leading order effect in the large-N_C counting, as it is a non-vanishing resonance width [3]. Moreover, since the participating resonances are not narrow, an energy-dependent width needs to be considered. A precise formalism-independent definition of the off-shell vector resonance width within $R\chi T$ has been given in Ref. [141] and employed successfully in a variety of phenomenological studies. Its application to the $K^*(892)$ resonance gives

$$\Gamma_{K^*}(s) = \frac{G_V^2 M_{K^*} s}{64\pi F^4} \Big[\sigma^3_{K\pi}(s) + \cos^2\theta_P \sigma^3_{K\eta}(s) + \sin^2\theta_P \sigma^3_{K\eta'}(s)\Big], \qquad (3.28)$$

where $\sigma_{PQ}(s)$ was defined in Eq. (4.2). Several analyses of the $\pi\pi$ [96, 97, 134] and $K\pi$ [14, 15, 105] form factors where the $\rho(770)$ and $K^\star(892)$ prevail respectively, have probed the energy-dependent width of these resonances with precision. Although the predicted width [52] turns to be quite accurate, it is not optimal to achieve a very precise description of the data and, instead, it is better to allow the on-shell width to be a free parameter and write

$$\Gamma_{K^*}(s) = \Gamma_{K^*} \frac{s}{M_{K^*}^2} \frac{\sigma^3_{K\pi}(s) + \cos^2\theta_P \sigma^3_{K\eta}(s) + \sin^2\theta_P \sigma^3_{K\eta'}(s)}{\sigma^3_{K\pi}(M^2_{K^*})}, \qquad (3.29)$$

where it has been taken into account that at the M_{K^*}-scale the only absorptive cut is given by the elastic contribution.

In the case of the $K^\star(1410)$ resonance there is no warranty that the KP ($P = \pi, \eta, \eta'$) cuts contribute in the proportion given in Eqs. (3.28) and (3.29). We will assume that the lightest $K\pi$ cut dominates and use throughout that

$$\Gamma_{K^{\star\prime}}(s) = \Gamma_{K^{\star\prime}} \frac{s}{M^2_{K^{\star\prime}}} \frac{\sigma^3_{K\pi}(s)}{\sigma^3_{K\pi}(M^2_{K^{\star\prime}})}. \qquad (3.30)$$

---

[3]Other corrections at this order are neglected. Phenomenology seems to support that this is the predominant contribution.

The scalar resonance width can also be computed in $R\chi T$ similarly [48, 141]. In the case of the $K_0^\star(1430)$ it reads

$$\Gamma_S(s) = \Gamma_{S_0}\left(M_S^2\right) \left(\frac{s}{M_S^2}\right)^{3/2} \frac{g(s)}{g\left(M_S^2\right)}, \tag{3.31}$$

with

$$\begin{aligned}
g(s) &= \frac{3}{2}\sigma_{K\pi}(s) + \frac{1}{6}\sigma_{K\eta}(s)\left[\cos\theta_P\left(1 + \frac{3\Delta_{K\pi} + \Delta_{K\eta}}{s}\right) + 2\sqrt{2}\sin\theta_P\left(1 + \frac{\Delta_{K\eta}}{s}\right)\right]^2 \\
&+ \frac{4}{3}\sigma_{K\eta'}(s)\left[\cos\theta_P\left(1 + \frac{\Delta_{K\eta'}}{s}\right) - \frac{\sin\theta_P}{2\sqrt{2}}\left(1 + \frac{3\Delta_{K\pi} + \Delta_{K\eta'}}{s}\right)\right]^2. \tag{3.32}
\end{aligned}$$

At this point, different options for the inclusion of the resonances width arise. The most simple prescription is to replace $M_R^2 - s$ by $M_R^2 - s - iM_R\Gamma_R(s)$ in eqs. (3.27). We shall call this option 'dipole model', or simply 'Breit-Wigner (BW) model'. One should pay attention to the fact that analyticity of a quantum field theory imposes certain relations between the real and imaginary parts of the amplitudes. In particular, there is one between the real and imaginary part of the relevant two-point function. At the one-loop level its imaginary part is proportional to the meson width but the real part (which is neglected in this model) is non-vanishing. As a result, the Breit-Wigner treatment breaks analyticity at the leading non-trivial order.

Instead, one can try to devise a mechanism that keeps the complete complex two-point function. Ref. [52] used an Omnès resummation of final-state interactions in the vector form factor that was consistent with analyticity at next-to-leading order. The associated violations were small and consequently neglected in their study of the $\pi\pi$ observables. This strategy was also exported to the $K\pi$ decays of the τ in Refs. [103, 105] where it yielded remarkable agreement with the data. We will call this approach to the vector form factor 'the exponential parametrization' (since it exponentiates the real part of the relevant loop function) and refer to it by the initials of the authors who studied the $K\pi$ system along these lines, 'JPP'.

A decade after, a construction that ensures analyticity of the vector form factor exactly was put forward in Ref. [14] and applied successfully to the study of the $K\pi$ tau decays. It is a dispersive representation of the form factor where the input phaseshift, which resums the whole loop function in the denominator of Eq. (3.27), is proportional to the ratio of the imaginary and real parts of this form factor. This method also succeeded in its application to the di-pion system [97], where it was rephrased in a way which makes chiral symmetry manifest at next-to-leading order.

We will name this method 'dispersive representation' or 'BEJ', by the authors who pioneered it in the $K\pi$ system.

We would like to stress that the Breit-Wigner model is consistent with χPT only at leading order, while the exponential parametrization (JPP) and the dispersive representation (BEJ) reproduce the chiral limit results up to next-to-leading order and including the dominant contributions at the next order [142].

In the dispersive approach to the study of the di-pion and Kaon-pion systems it was possible to achieve a unitary description in the elastic region that could be extended up to $s_{inel} = 4m_K^2$ (the 4π cut, which is phase-space and large-N_C suppressed is safely neglected) and $s_{inel} = (m_K + m_\eta)^2$, respectively. Most devoted studies of these form factors neglect -in one way or another- inelasticities and coupled-channel effects beyond s_{inel} in them [4], an approximation that seems to be supported by the impressive agreement with the data sought. However, this overlook of the problem seems to be questionable in the case of the $\tau^- \to K^- \eta^{(\prime)} \nu_\tau$ decays where we are concerned with the first (second) inelastic cuts.

An advisable solution may come from the technology developed for the scalar form factors that were analyzed in a coupled channel approach in Refs. [56, 131, 143] (for the strangeness-changing form factors) [5] and [58, 144] (for the strangeness-conserving ones) unitarizing $SU(3)$ and $U(3)$ (respectively) χPT with explicit exchange of resonances [57]. However, given the large errors of the $\tau^- \to K^- \eta \nu_\tau$ decay spectra measured by the BaBar [107] and Belle [12] Collaborations and the absence of data on the $K^- \eta'$ channel we consider that it is not timely to perform such a cumbersome numerical analysis in the absence of enough experimental guidance [6]. For this reason we have attempted to obviate the inherent inelasticity of the $K\eta^{(\prime)}$ channels and tried an elastic description, where the form factor that defines the input phaseshift is given by Eq. (3.27) with $\Gamma_{K^\star}(s)$ defined analogously to $\Gamma_{K^{\star\prime}}(s)$, i.e., neglecting the inelastic cuts. We anticipate that the accord with data supports this procedure until more precise measurements demand a better approximation.

Regarding the scalar form factor accompanying the exponential and dispersive descriptions of the vector form factor, we will employ the form factors in three coupled

---

[4]See, however, Ref. [104], which includes coupled channels for the $K\pi$ vector form factor.

[5]We will use these unitarized scalar form factors instead of the one in Eq. (3.27) in the JPP and BEJ treatments (see above).

[6]One could complement this poorly known sector with the information from meson-meson scattering on the relevant channels [67]. Our research at next-to-leading order in the $1/N_C$ expansion treating consistently the $\eta - \eta'$ mixing [8, 69] is in progress.

channels ($K\pi$, $K\eta$, $K\eta'$ for $i = 1, 2, 3$ in Eq. (2.47)) solved in Ref. [56] and kindly provided by one of the authors[7].

Let us recapitulate the different alternatives for the treatment of final-state interactions that will be employed in sections 3.4-3.6 to study the $\tau^- \to K^- \eta^{(\prime)} \nu_\tau$ decays. The relevant form factors will be obtained from Eqs. (3.27) in each case by:

- Dipole model (Breit-Wigner): $M_R^2 - s$ will be replaced by $M_R^2 - s - iM_R\Gamma_R(s)$ with $\Gamma_{K^\star}(s)$ and $\Gamma_S(s)$ given by Eqs. (3.29) and (3.31). The from factors written in this way are not analytic, in the sense that the real part of the unitarity corrections is obviated, and only considers the absorptive (imaginary) part of these corrections.

- Exponential parametrization (JPP): The Breit-Wigner vector form factor described above is multiplied by the exponential of the real part of the loop function as illustrated in Ref. [52] devoted to the pion vector form factor. We will adopt here the discussion to the $K\pi$ case which determines the $K\eta^{(\prime)}$ processes. The key point in obtaining the Omnès solution is that in the elastic region Watson final-state theorem (cf. Eq. 2.31) relates the imaginary part of the vector form factor to the partial wave amplitude for $K\pi$ scattering with spin one and isospin one-half, $T_1^{1/2}(s)$. In fact, in this region both phases are equal, which allows to write an n-subtracted dispersion relation which has the well-known Omnès solution (cf. Eq. (2.44))

$$f_+^{K\pi}(s) = P_n(s) \exp\left\{ \frac{s^n}{\pi} \int\limits_{s_{\text{thr}}}^{\infty} ds' \frac{\delta_1^1(s')}{(s')^n(s' - s - i\epsilon)} \right\}, \qquad (3.33)$$

where

$$\log P_n(s) = \sum_{k=0}^{n-1} \alpha_k \frac{s^k}{k!} \qquad (3.34)$$

is the corresponding subtraction polynomial. The subtraction constants α_k are given by [8]

$$\alpha_k = \frac{d^k}{ds^k} \log f_+^{K\pi}(s)\Big|_{s=0}. \qquad (3.35)$$

Using the leading-order χPT result in the integral (3.33) generates the χPT one-loop function at the next order. In this way, the Omnès formula provides an exponentiation of the chiral logarithmic corrections. The ambiguity in the

---

[7]We thank Matthias Jamin on this point.

[8]More general formulae with subtractions at an arbitrary point $s = s_0$ can for example be found in Ref. [74].

non-logarithmic part of the Omnès relation can be resolved to a large extent by matching it to the $R\chi T$ result yielding

$$f_+^{K\pi}(s) = \frac{M_{K^\star}^2}{M_{K^\star}^2 - s}\exp\left\{\frac{3}{2}\left[\widetilde{H}_{K\pi}(s) + \widetilde{H}_{K\eta}(s)\right]\right\}, \qquad (3.36)$$

where $\widetilde{H}_{PQ}(s)$ subtracts the contribution of the local term at next-to-leading order in χPT from the untilded function [9] to avoid double counting, since this term is recovered upon integration of the vector resonances in the chosen formalism.

The problem, however, comes when the resonance width is included (as it should to avoid the divergent behaviour of the denominator at the resonance mass). In Ref. [52] the imaginary part of the loop function (giving the resonance width) was shifted to the denominator by hand, which resulted in an expression analogous to

$$f_+^{K\pi}(s) = \frac{M_{K^\star}^2}{M_{K^\star}^2 - s - iM_{K^\star}\Gamma_{K^\star}(s)}\exp\left\{\frac{3}{2}Re\left[\widetilde{H}_{K\pi}(s) + \widetilde{H}_{K\eta}(s)\right]\right\}. \qquad (3.37)$$

which strictly speaking is no yet analytic, in the sense that the real and imaginary parts of the unitarity corrections are resummed in two different functions, but both the absorptive (imaginary) and dispersive (real) part of the corrections are considered. If inelasticities were not important, the exponential resummation should be a suitable representation of the vector form factor. Although in our case we consider the $K\pi$ and $K\eta$ channels and, *strictu sensu*, elastic unitarity cannot be employed i.e. the vector form factor is neither totally unitary, Eq. (3.37) still could be a good representation. The unitarized scalar form factor [56] will be employed.

- Dispersive representation (BEJ): both the real and imaginary parts of the loop-function $H_{K\pi}(s)$ are resummed and accomodated in the resonance propagator as of

$$\widetilde{f}_+(s) = \frac{m_{K^\star}^2 - \kappa_{K^\star}\widetilde{H}_{K\pi}(0) + \gamma s}{D(m_{K^\star}, \gamma_{K^\star})} - \frac{\gamma s}{D(m_{K^{\star\prime}}, \gamma_{K^{\star\prime}})}, \qquad (3.38)$$

where the denominators read

$$D(m_n, \gamma_n) \equiv m_n^2 - s - \kappa_n Re\left[H_{K\pi}(s)\right] - im_n\gamma_n(s), \qquad (3.39)$$

---

[9]$H_{PQ}(s)$ is the standard Gasser and Leutwyler's two-particle loop function [6].

with

$$\kappa_n \;=\; \frac{192\pi F_K F_\pi}{\sigma^3(m_n^2)} \frac{\gamma_n}{m_n} \,, \quad \gamma_n(s) \;=\; \gamma_n \frac{s}{m_n^2} \frac{\sigma_{K\pi}^3(s)}{\sigma_{K\pi}^3(m_n^2)} \,, \tag{3.40}$$

and $\sigma(m_P^2) = \sigma_{PP}(s) = \sqrt{1 - \frac{4m_P^2}{s}}$ is the two-body phase-space factor.

The input phaseshift is obtained using the vector form factor in Eq. (3.38) including only the $K\pi$ cut as

$$\delta(s) \;=\; \tan^{-1} \left[\frac{\mathrm{Im} \widetilde{f}_+(s)}{\mathrm{Re} \widetilde{f}_+(s)} \right] , \tag{3.41}$$

which inserted into a three-times subtracted dispersion relation of the form factor leads [10] (cf. Eq. (2.44))

$$\widetilde{f}_+(s) \;=\; \exp \left[\alpha_1 \frac{s}{m_\pi^2} + \frac{1}{2} \alpha_2 \frac{s^2}{m_\pi^4} + \frac{s^3}{\pi} \int_{s_{K\pi}}^{s_{cut}} ds' \frac{\delta(s')}{(s')^3 (s' - s - i0)} \right] , \tag{3.42}$$

where $s_{K\pi} = (m_K + m_\pi)^2$ [11] and the two subtraction constants are related to the low-energy expansion of the $\widetilde{f}_+(s)$ form factor:

$$\widetilde{f}_+(s) \;=\; 1 + \lambda'_+ \frac{s}{m_\pi^2} + \frac{1}{2} \lambda''_+ \frac{s^2}{m_\pi^4} + ... \,, \tag{3.43}$$

while the value of the cut-off, s_{cut}, should in principle be varied to estimate the associated systematic error. The form factor representation as written as in Eq. (3.42) suppresses the weight of the high-energy contribution to the phase integral where possible inelastic effects, starting at the $K^* \pi$ threshold, are already present. This results in a transfer of the information into the two subtraction constants α_1 and α_2. Again, the unitarized scalar form factor [56] will be employed.

3.4 Predictions for the $\tau^- \to K^- \eta \nu_\tau$ decay

We note that Eqs. (3.27) also hold for the $\tilde{f}_{+,0}^{K^- \pi}(s)$ form factors (see Eq. (3.8) and comments below, as well). Therefore, in principle the knowledge of these form factors in the $K\pi$ system can be transferred to the $K\eta^{(\prime)}$ systems immediately, taking thus advantage of the larger statistics accumulated in the former and their sensitivity to the $K^\star(892)$ properties. This is certainly true in the case of the vector form factor

---

[10]The analyses of the $\pi\pi$ [96, 97] and $K\pi$ [14, 15] vector form factors within this framework shows an optimal description of the data with three subtractions.

[11]The values of the masses that are actually used in this relation are discussed in section 3.4.

in its assorted versions and in the scalar Breit-Wigner form factor. However, in the BEJ and JPP scalar form factor one has to bear in mind that the KP ($P = \pi^0$, η, η') scalar form factors are obtained solving the coupled channel problem which breaks the universality of the $\tilde{f}_0^{K^-P}(s)$ form factors as a result of the unitarization procedure. As a consequence, our application of the $\tilde{f}_0^{K^-\eta^{(\prime)}}(s)$ form factors to the $\tau^- \to K^-\eta^{(\prime)}\nu_\tau$ decays will provide a test of the unitarized results. Taking into account the explanations in Ref. [56] about the difficult convergence of the three-channel problem (mainly because of the smallness of the $K\eta$ contribution and its correlation with the $K\eta'$ channel) this verification is by no means trivial, specially regarding the $K\eta'$ channel, where the scalar contribution is expected to dominate the decay width.

In this way, we have predicted the $\tau^- \to K^-\eta\nu_\tau$ branching ratio and differential decay width using the knowledge acquired in the $\tau^- \to (K\pi)^-\nu_\tau$ decays. Explicitly:

- In the dipole model, we have taken the $K^\star(892)$, $K^\star(1410)$ and $K_0^\star(1430)$ mass and width from the PDG [124] -since this compilation employs Breit-Wigner parametrizations to determine these parameters- and estimated the relative weight of them using $\gamma = \frac{F_V G_V}{F^2} - 1$ (see discussion at the end of section 3.2) [48]. In this way, we have found $\gamma = -0.021 \pm 0.031$.

- In the JPP parametrization, we have used the best fit results of Ref. [105] for the vector form factor. The scalar form factor has been obtained from the solutions (6.10) and (6.11) of Ref. [56]. The scalar form factors have also been treated alike in the BEJ approach.

- In the BEJ representation, one would use the best fit results of Ref. [15] to obtain our vector form factor. However, we have noticed the strong dependence on the actual particle masses of the slope form factor parameters, λ'_+ and λ''_+. Ref. [15] used the physical masses in their study of $\tau^- \to K_S\pi^-\nu_\tau$ data. On the other hand we focus on the $\tau^- \to K^-P\nu_\tau$ decays. Consequently, the masses should correspond now to $K^-\pi^0$ instead of to $K_S\pi^-$. Noteworthy, both the K^- and π^0 are lighter than the K_S and π^- and the corresponding small mass differences, given by isospin breaking, are big enough to demand for a corresponding change in the $\lambda'^{(\prime)}_+$ parameters. Accepting this, the ideal way to proceed would be to fit the BaBar data on $\tau^- \to K^-\pi^0\nu_\tau$ decays [17]. Unfortunately, these data are not publicly available yet. For this reason, we have decided to fit Belle data on the $\tau^- \to K_S\pi^-\nu_\tau$ decay using the K^- and π^0 masses throughout. The results

can be found in table 3.1, where they are confronted to the best fit results of Ref. [14] [12], both of them yield $\chi^2/dof = 1.0$ and are given for $s_{cut} = 4$ GeV^2, although the systematic error due to the choice of this energy scale is included in the error estimation. We will use the results in the central column of table 3.1 to give our predictions of the $\tau^- \to K^- \eta \nu_\tau$ decays based on the $K\pi$ results.

Parameter	Best fit with fake masses	Best fit [14]
$\lambda'_+ \times 10^3$	22.2 ± 0.9	24.7 ± 0.8
$\lambda''_+ \times 10^4$	10.3 ± 0.2	12.0 ± 0.2
$M_{K^\star}$ (MeV)	892.1 ± 0.6	892.0 ± 0.9
$\Gamma_{K^\star}$ (MeV)	46.2 ± 0.5	46.2 ± 0.4
$M_{K^{\star\prime}}$ (GeV)	1.28 ± 0.07	1.28 ± 0.07
$\Gamma_{K^{\star\prime}}$ (GeV)	$0.16^{+0.10}_{-0.07}$	$0.20^{+0.06}_{-0.09}$
γ	-0.03 ± 0.02	-0.04 ± 0.02

Table 3.1: Results for the fit to Belle $\tau^- \to K_S \pi^- \nu_\tau$ data [100] with a three-times subtracted dispersion relation including two vector resonances in $\tilde{f}^{K\pi}_+(s)$, according to Eq. (3.27) and resumming the loop function in the denominator, as well as the scalar form factor [56]. The middle column is obtained using the masses of the K^- and π^0 mesons and the last column using the K_S and π^- masses actually corresponding to the data.

Proceeding this way we find the differential decay distributions for the three different approaches considered using Eq. (3.8). This one is, in turn, related to the experimental data by using

$$\frac{dN_{events}}{dE} = \frac{d\Gamma}{dE} \frac{N_{events}}{\Gamma_\tau BR(\tau^- \to K^- \eta \nu_\tau)} \Delta E_{bin} \,. \tag{3.44}$$

We thank the Belle Collaboration for providing us with their data [12]. This was not possible in the case of the BaBar Collaboration [107] because the person in charge of the analysis left the field and the data file was lost. We have, however, read the data points from the paper's figures and included this effect in the errors. The number of events after background subtraction in each data set are 611 (BaBar) and 1365 (Belle) and the corresponding bin widths are 80 and 25 MeV, respectively. In Fig. 3.2 we show our predictions based on the $K\pi$ system according to BW, JPP and BEJ. In this figure we have normalized the BaBar data to Belle's using Eq. (3.44). A look at the data shows some tension between both measurements and we notice

---

[12]We display the results of this reference instead of those in Ref. [15] because we are not using information from $K_{\ell 3}$ decays in this exercise. Differences are, nonetheless, tiny.

a couple of strong oscillations of isolated Belle data points which do not seem to correspond to any dynamics but rather to an experimental issue or to underestimation of the systematic errors [13]. In this plot there are also shown the corresponding one-sigma bands obtained neglecting correlations between the resonance parameters and also with respect to other sources of uncertainty, namely $|V_{us}f_+^{K^-\pi^0}(0)|$ and θ_P, whose errors are also accounted for. The corresponding branching ratios are displayed in table 3.2, where the χ^2/dof is also shown. We note that the error correlations corresponding to the fit results shown in table 3.1 have been taken into account in BEJ's branching ratio of table 3.2.

It can be seen that the BW model gives a too low decay width and that the function shape is not followed by this prediction, as indicated by the high value of the χ^2/dof that is obtained. On the contrary, the JPP and BEJ predictions yield curves that compare quite well with the data already. Moreover, the corresponding branching fractions are in accord with the PDG value within errors. Altogether, this explains the goodness of the χ^2/dof, which is $1.5 \leftrightarrow 1.9$. Besides, we notice that the error bands are wider in the dispersive representation than in the exponential parametrization, which may be explained by the larger number of parameters entering the former and the more complicated correlations between them that were neglected in obtaining Fig. 3.2 and the JPP result in table 3.2.

From these results we conclude that quite likely the BW model is a too rough approach to the problem unless our reference values for γ and the $K^\star(1410)$ resonance parameters were a bad approximation. We will check this in the next section. On the contrary, the predictions discussed above hint that JPP and BEJ are appropriate for the analysis of $\tau^- \to K^- \eta \nu_\tau$ data that we will pursue next.

Source	Branching ratio	χ^2/dof
Dipole Model (BW)	$\left(0.78^{+0.17}_{-0.10}\right) \cdot 10^{-4}$	8.3
JPP	$\left(1.47^{+0.14}_{-0.08}\right) \cdot 10^{-4}$	1.9
BEJ	$(1.49 \pm 0.05) \cdot 10^{-4}$	1.5
Experimental value	$(1.52 \pm 0.08) \cdot 10^{-4}$	-

Table 3.2: Predicted branching ratio of the $\tau^- \to K^- \eta \nu_\tau$ decays according to the different approaches used (see the items above Eq. (4.12) for details). The corresponding χ^2/dof values are also given and the PDG branching fraction is given for reference.

---

[13]We have also realized that the first two Belle data points, with non-vanishing entries, are below threshold, a fact which may indicate some problem in the calibration of the hadronic system energy or point to underestimation of the background.
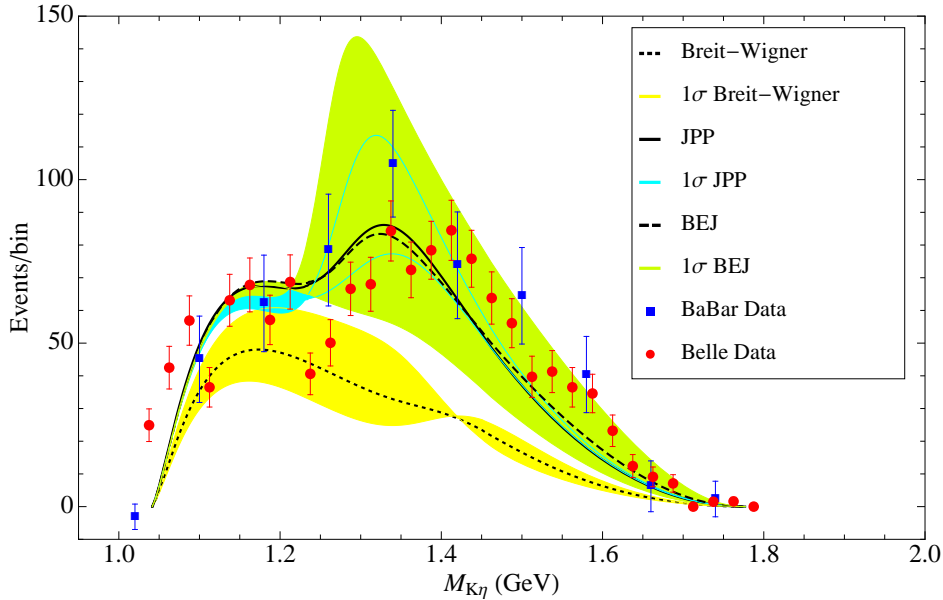
Figure 3.2: BaBar (blue) [107] and Belle (red) [12] data for the $\tau^- \to K^- \eta \nu_\tau$ decays are confronted to the predictions obtained in the BW (dotted), JPP (solid) and BEJ (dashed) approaches (see the main text for details) which are shown together with the corresponding one-sigma error bands in yellow, light blue and light green, respectively.

3.5 Fits to the $\tau^- \to K^- \eta \nu_\tau$ BaBar and Belle data

We have considered different fits to the $\tau^- \to K^- \eta \nu_\tau$ data. In full generality we have assessed that the data is not sensitive either to the low-energy region or to the $K^\star(892)$ peak region. This is not surprising, since the threshold for $K^- \eta$ production opens around 1041 MeV which is some 100 MeV larger than $M_{K^\star} + \Gamma_{K^\star}$, a characteristic energy scale for the $K^\star(892)$ region of dominance. This implies first that the fits are unstable under floating $M_{K^\star}$ and $\Gamma_{K^\star}$ (which affects all three approaches) and second that the slopes of the vector form factor, which encode the physics immediately above threshold, can not be fitted with $\tau^- \to K^- \eta \nu_\tau$ data (this only concerns BEJ). We have considered consequently fits varying only the $K^\star(1410)$ mass and width and γ and sticking to the reference values discussed in the previous section for the remaining parameters in every approach.

Our best fit results for the branching ratios are written in table 3.3, where the corresponding χ^2/dof can also be read. These are obtained with the best fit parameter values shown in table 3.4, which can be compared to the reference values, which were

used to obtain the predictions in the previous section, that are recalled in table 3.5. The corresponding decay distributions with one-sigma error bands attached are plotted in Fig. 3.3.

These results show that the BW model does not really provide a good approximation to the underlying physics for any value of its parameters and should be discarded. Oppositely, JPP and BEJ are able to yield quite good fits to the data with values of the χ^2/dof around one. This suggests that the simplified treatment of final state interactions in BW, which misses the real part of the two-meson rescatterings and violates analyticity by construction, is responsible for the failure.

A closer look to the fit results using JPP and BEJ in tables 3.3 and 3.4 shows that:

- Fitting γ alone is able to improve the quality of both approaches by $15 \leftrightarrow 20\%$. The fitted values are consistent with the reference ones (see table 3.5): in the case of BEJ at one sigma, being the differences in JPP slightly larger than that only. This is satisfactory because both the $\tau^- \to (K\pi)^- \nu_\tau$ and the $\tau^- \to K^- \eta \nu_\tau$ decays are sensitive to the interplay between the first two vector resonances and contradictory results would have casted some doubts on autoconsistency.

- When the $K^\star(1410)$ parameters are also fitted the results improve by $\sim 13\%$ in JPP and by $\sim 33\%$ in BEJ. This represents a reduction of the χ^2/dof by $\sim 26\%$ in JPP and by $\sim 50\%$ in BEJ. It should be noted that the three-parameter fits do not yield to physical results in BW. Specifically, $K^\star(1410)$ mass and width tend to the $K^\star(892)$ values and $|\gamma|$ happens to be one order of magnitude larger than the determinations in the literature. Therefore we discard this result. We also notice that although the branching ratios of both JPP and BEJ (which have been obtained taking into account the parameter fit correlations) are in agreement with the PDG value, the JPP branching ratios tend to be closer to its lower limit while BEJ is closer to the upper one. It can be observed that the deviations of the three-parameter best fit values with respect to the default ones lie within errors in BEJ, as it so happens with $\Gamma_{K^{\star\prime}}$ in JPP. However, there are small tensions between the reference and best fit values of $M_{K^{\star\prime}}$ and γ in JPP.

These results are plotted in Fig. 3.3. Although the BW curve has improved with respect to Fig. 3.2 and seems to agree well with the data in the higher-energy half of the spectrum, it fails completely at lower energies. On the contrary, JPP and BEJ provide good quality fits to data which are satisfactory along the whole phase

space. We note that JPP goes slightly below BEJ and its error band is again narrower possibly due to having less parameters. BEJ errors include the systematics associated to changes in s_{cut} which is slightly enhanced with respect to the $K\pi$ case.

Despite the vector form factor giving the dominant contribution to the decay width, the scalar form factor is not negligible and gives $\sim (3 \leftrightarrow 4)\%$ of the branching fraction in the JPP and BEJ cases. In the BW model this contribution is $\sim 7\%$.

Source	Branching ratio	χ^2/dof
Dipole Model (BW) (Fit γ)	$\left(0.96^{+0.21}_{-0.15}\right) \cdot 10^{-4}$	5.0
Dipole Model (BW) (Fit γ, $M_{K^{\star\prime}}$, $\Gamma_{K^{\star\prime}}$)	Unphysical result	-
JPP (Fit γ)	$\left(1.50^{+0.19}_{-0.11}\right) \cdot 10^{-4}$	1.6
JPP (Fit γ, $M_{K^{\star\prime}}$, $\Gamma_{K^{\star\prime}}$)	$(1.42 \pm 0.04) \cdot 10^{-4}$	1.4
BEJ (Fit γ)	$\left(1.59^{+0.22}_{-0.16}\right) \cdot 10^{-4}$	1.2
BEJ (Fit γ, $M_{K^{\star\prime}}$, $\Gamma_{K^{\star\prime}}$)	$(1.55 \pm 0.08) \cdot 10^{-4}$	0.8
Experimental value	$(1.52 \pm 0.08) \cdot 10^{-4}$	-

Table 3.3:   The branching ratios and χ^2/dof obtained in BW, JPP and BEJ fitting γ only and also the $K^\star(1410)$ parameters are displayed. Other parameters were fixed to the reference values used in section 3.4. The PDG branching fraction is also given for reference.

The JPP model values appearing in tables 3.4 and 3.5 can be translated to pole values along the lines discussed in Ref. [145]. This yields $M_{K^{\star\prime}} = 1332^{+16}_{-18}$, $\Gamma_{K^{\star\prime}} = 220^{+26}_{-24}$ for the best fit values and $M_{K^{\star\prime}} = 1286^{+26}_{-28}$, $\Gamma_{K^{\star\prime}} = 197^{+41}_{-45}$ for the reference values, where all quantities are given in MeV. Remarkable agreement is found between our best fit values in the JPP and BEJ cases, since the latter yields $M_{K^{\star\prime}} = 1327^{+30}_{-38}$, $\Gamma_{K^{\star\prime}} = 213^{+72}_{-118}$. From the detailed study of the $\pi\pi$, $K\pi$ (in the quoted literature) and $K\eta$ systems (in this paper) within JPP and BEJ, one can conclude generally that the dispersive form factors allow a better description of the data while

Fitted value \ Approach	Dipole Model (BW)	JPP	BEJ
γ	-0.174 ± 0.007	-0.063 ± 0.007	-0.041 ± 0.021
γ	Unphysical	$-0.078^{+0.012}_{-0.014}$	$-0.051^{+0.012}_{-0.036}$
$M_{K^{\star\prime}}$ (MeV)	best fit	1356 ± 11	1327^{+30}_{-38}
$\Gamma_{K^{\star\prime}}$ (MeV)	parameters	232^{+30}_{-28}	213^{+72}_{-118}

Table 3.4:   The best fit parameter values corresponding to the different alternatives considered in table 3.3 are given. These can be compared to the reference values, which are given in table 3.5. BEJ results for the mass and width of the $K^\star(1410)$ correspond to pole values, while JPP figures are given for the model parameter as in the original literature.

Approach / Reference value	Dipole Model (BW)	JPP	BEJ
γ	-0.021 ± 0.031	-0.043 ± 0.010	-0.029 ± 0.017
$M_{K^{\star\prime}}$ (MeV)	1414 ± 15	1307 ± 17	1283 ± 65
$\Gamma_{K^{\star\prime}}$ (MeV)	232 ± 21	206 ± 49	163 ± 68

Table 3.5:   Reference values (used in section 3.4) corresponding to the best fit parameters appearing in table 3.4. Again BEJ results are pole values and JPP ones are model parameters. The latter are converted to resonance pole values in section 4.3, where the determination of the $K^\star(1410)$ pole parameters is given.

the exponential parametrizations lead to the determination of the resonance pole values with smaller errors. Both things seem to be due to the inclusion of the subtraction constants as extra parameters in the fits within the dispersive representations.
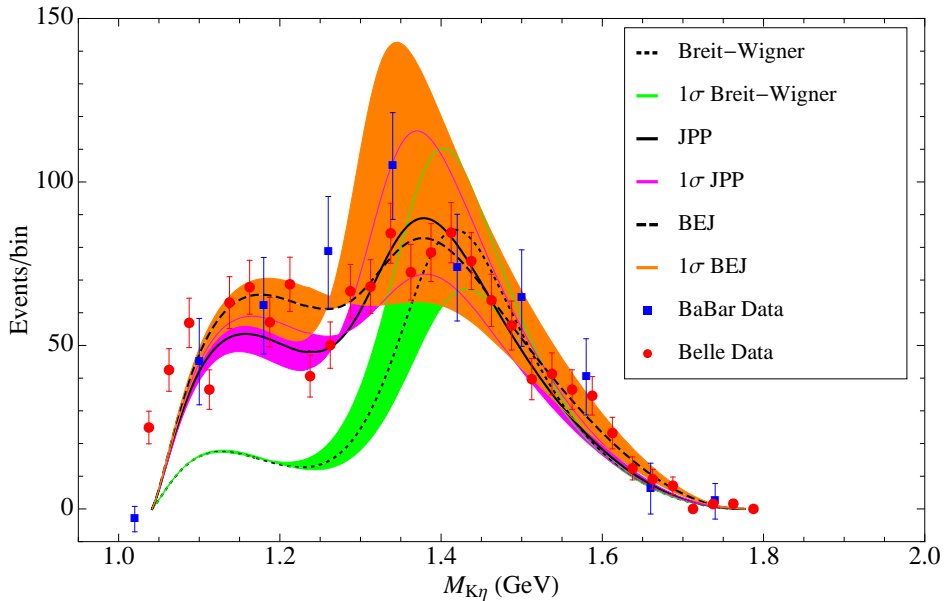
Figure 3.3:   BaBar (blue) [107] and Belle (red) [12] data for the $\tau^- \to K^- \eta \nu_\tau$ decays are confronted to the best fit results obtained in the BW (dotted), JPP (solid) and BEJ (dashed) approaches (see the main text for details) which are shown together with the corresponding one-sigma error bands in light green, pink and orange, respectively. The BW curve corresponds to the one-parameter fit while the JPP and BEJ ones correspond to three-parameter fits.

3.6 Predictions for the $\tau^- \to K^- \eta' \nu_\tau$ decay

We can finally profit from our satisfactory description of the $\tau^- \to K^- \eta \nu_\tau$ decays and predict the $\tau^- \to K^- \eta' \nu_\tau$ decay observables, where there is only the upper limit fixed at ninety percent confidence level by the BaBar Collaboration [110], $BR < 4.2 \cdot 10^{-6}$. We have done this for our best fit results in the BW (one-parameter fit) JPP and BEJ (three-parameter fits) cases. The corresponding results are plotted in Fig. 3.4 and the branching ratios can be read from table 3.6. In the figure we can see that the decay width is indeed dominated by the scalar contribution [14] [15]. In fact, the vector form factor contributes in the range $(9 \leftrightarrow 15)\%$ to the corresponding branching ratio. Although we keep the BW prediction for reference, we do not draw the associated (large) error band for the sake of clarity in the figure taking into account its wrong description of the $K\eta$ system shown in the previous section. As the scalar form factor dominates the decay width and we are using the same one in JPP and BEJ, the differences between them are tiny (and the errors, of order one third, are the same in table 3.6). As expected from the results in the $\tau^- \to K^- \eta \nu_\tau$ decays, BEJ gives the upper part of the error band while JPP provides the lower one. We are looking forward to the discovery of this decay mode to verify our predictions. A priori one may forecast some departure from it because of the effect of the poorly known elastic and $K\eta$ channels in meson-meson scattering, which affects the solution of the coupled system of integral equations and specially the value of the $K^- \eta'$ scalar form factor, that is anyway suppressed to some extent.

Source	Branching ratio
Dipole Model (BW) (Fit)	$(1.45^{+3.80}_{-0.87}) \cdot 10^{-6}$
JPP (Fit)	$(1.00^{+0.37}_{-0.29}) \cdot 10^{-6}$
BEJ (Fit)	$(1.03^{+0.37}_{-0.29}) \cdot 10^{-6}$
Experimental bound	$< 4.2 \cdot 10^{-6}$ at 90% C.L.

Table 3.6: Predicted branching ratios for the $\tau^- \to K^- \eta' \nu_\tau$ decays. The BaBar upper limit is also shown [110].

In Fig. 3.5 we also plot the correlation between the $\tau^- \to K^- \eta \nu_\tau$ and $\tau^- \to K^- \eta' \nu_\tau$ branching ratios according to the best fit JPP result at one sigma. The correlations

---

[14]In principle, both the scalar and vector $K\eta'$ form factors are suppressed since they are proportional to $\sin\theta_P$. However, the unitarization procedure of the scalar form factor enhances it sizeably [56] due to the effect of the coupled inelastic channels.

[15]The suppression of the vector contribution makes that the predicted values using information from the $K\pi$ system and the one-parameter fits with JPP and BEJ are very similar to the results in table 3.6. For this reason we do not show them.
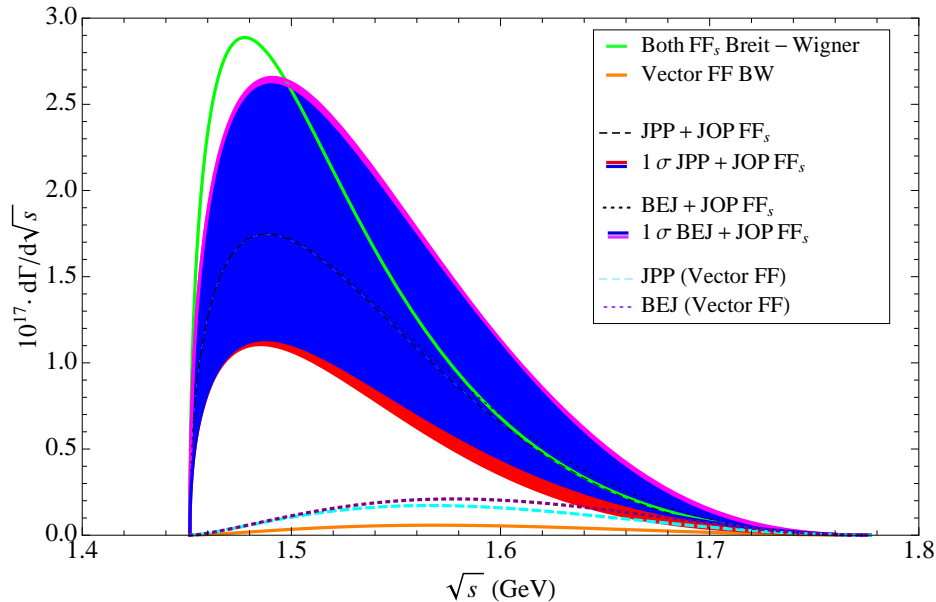
Figure 3.4:   The predicted $\tau^- \to K^- \eta' \nu_\tau$ decay width according to BW (green, its big uncertainty is not shown for clarity of the figure), JPP (blue with lower band in red) and BEJ (blue with upper part in pink) is shown. In these last two the scalar form factor corresponds to Ref. [131], which is represented by the author's initials, JOP, in the figure's legend. The corresponding vector form factor contributions, which are subleading are plotted in orange (solid), blue (dashed) and purple (dotted).

between the parameters are neglected. Since the vector (scalar) form factor dominates the former (latter) decays and their parameters are independent the plot does not show any sizeable correlation between both measurements, as expected. As a result, if new data on the $\tau^- \to K^- \eta' \nu_\tau$ decays demand a more careful determination of the $f_0^{K^-\eta'}(s)$ unitarized form factor this will leave almost unaffected the results obtained for the $\tau^- \to K^- \eta \nu_\tau$ channel.

3.7   Conclusions

Hadronic tau decays are an ideal scenario to learn about the non-perturbative character of the strong interactions in rather clean conditions. In this work, we have studied the $\tau^- \to K^- \eta^{(\prime)} \nu_\tau$ decays motivated by the recent measurements performed by the BaBar [107, 110] and Belle Collaborations [12]. These decays allow the application of the knowledge acquired in the study of $\tau^- \to (K\pi)^- \nu_\tau$ decays. In particular, the
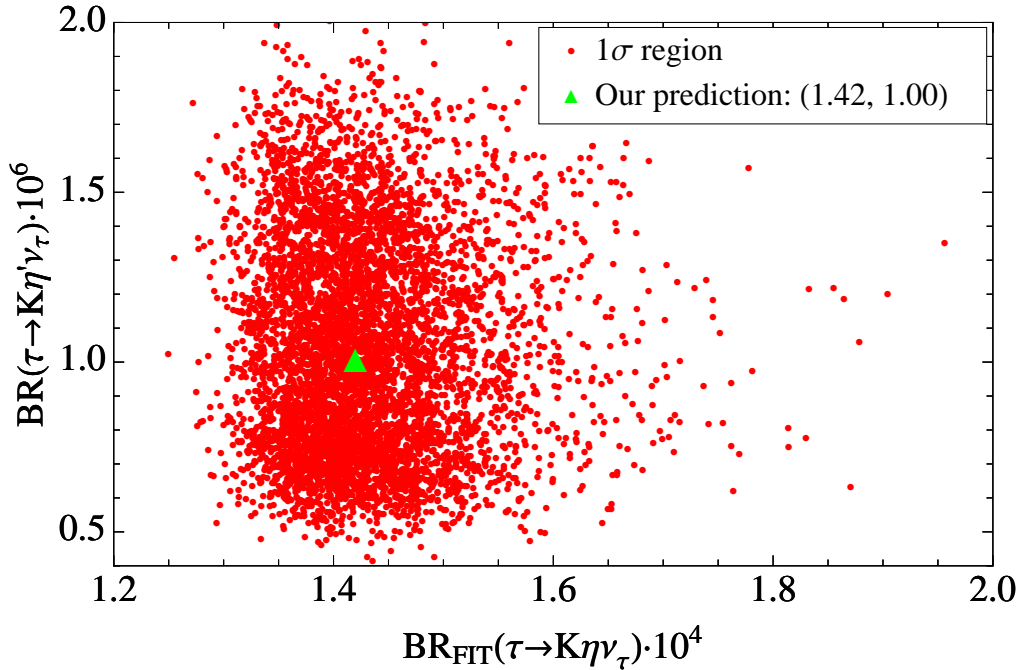
Figure 3.5: The correlation between the $\tau^- \to K^- \eta \nu_\tau$ and $\tau^- \to K^- \eta' \nu_\tau$ branching ratios is plotted according to the best fit JPP result at one sigma. Correlations between the parameters are neglected. According to expectations, no sizable correlation between both decay modes is observed.

$K\eta$ decay is sensitive to the parameters of the $K^\star(1410)$ resonance and to its interplay with the $K^\star(892)$ meson, while the $K\eta'$ decay is an appropriate place to test the unitarization of the strangeness-changing scalar form factors in three coupled-channel case.

We have defined with detail the (tilded) scalar and vector form factors and we have gone through the steps of their calculation within Chiral Perturbation Theory including the lightest resonances as explicit degrees of freedom and showed that the results are written in a more compact way using the tilded form factors. Then we have discussed different options according to the treatment of final-state interactions. Specifically, there is the dipole Breit-Wigner (BW) model, which neglects the real part of the two-meson loop function violating analyticity at next-to-leading order; there is the exponential parametrization (JPP) where this real part of the loop is resummed through an Omnès exponentiation, which violates analyticity at the next order; and there is the dispersive representation (BEJ), which resums the whole loop

function in the denominators, where analyticity holds exactly.

In our case, an additional difficulty is that the elastic approach is not valid in any region of the phasespace, since the $K\pi$ channel is open well below the $K\eta^{(\prime)}$ channels. In JPP this is not an issue, since one simply adds the corresponding contribution of these channels to the width and real part of the loop function. However, in BEJ it prevents an approach which does not include inelasticities and the effect of coupled channels. Being conscious of this, we have nevertheless attempted a dispersive representation of the $K\eta^{(\prime)}$ vector form factors were the input phaseshift is obtained using the elastic approximation and, to our surprise, it has done an excellent job in its confrontation to the $K\eta$ data. In the light of more accurate measurements it may become necessary to improve this treatment in the future. Very good agreement has also been found using JPP but BW has failed in this comparison. In the JPP and BEJ fits to the $K\eta$ channel the scalar form factor was obtained solving dispersion relations for the three-body problem.

We have checked that the $K\eta^{(\prime)}$ channels are not sensitive either to the $K^\star(892)$ parameters or to the slopes of the form factor, $\lambda_+^{\prime(\prime)}$ (BEJ). We have borrowed this information from the $K\pi$ system. This task was straightforward in BW and JPP although in BEJ we noticed that the $\lambda_+^{\prime(\prime)}$ parameters were sensitive to isospin breaking effects that we had to account for. Once this was done we could fit the $K^\star(1410)$ resonance pole parameters and its relative weight with respect to the $K^\star(892)$ meson, γ. Our results for these, with masses and widths in MeV, are

$$M_{K^{\star\prime}} = 1327^{+30}_{-38}, \quad \Gamma_{K^{\star\prime}} = 213^{+72}_{-118}, \quad \gamma = -0.051^{+0.012}_{-0.036}, \tag{3.45}$$

in the dispersive representation (BEJ) and

$$M_{K^{\star\prime}} = 1332^{+16}_{-18}, \quad \Gamma_{K^{\star\prime}} = 220^{+26}_{-24}, \quad \gamma = -0.078^{+0.012}_{-0.014}, \tag{3.46}$$

for the exponential parametrization (JPP). Our determination of these parameters has shown to be competitive with its extraction from the $\tau^- \to (K\pi)^- \nu_\tau$ decays. To illustrate this point, we average the JPP and BEJ determinations from the $K\pi$ [15, 105] and $K\eta$ systems, respectively, to find

$$M_{K^{\star\prime}} = 1277^{+35}_{-41}, \quad \Gamma_{K^{\star\prime}} = 218^{+95}_{-66}, \quad \gamma = -0.049^{+0.019}_{-0.016}, \tag{3.47}$$

from $K\pi$ and

$$M_{K^{\star\prime}} = 1330^{+27}_{-41}, \quad \Gamma_{K^{\star\prime}} = 217^{+68}_{-122}, \quad \gamma = -0.065^{+0.025}_{-0.050}, \tag{3.48}$$

from $K\eta$. We have thus open an alternative way of determining these parameters. New, more precise data on the $\tau^- \to (K\pi)^- \nu_\tau$ and $\tau^- \to K^- \eta \nu_\tau$ decays will make possible a more accurate determination of these parameters.

Finally we have benefited from this study of the $\tau^- \to K^- \eta \nu_\tau$ decays and applied it to the $\tau^- \to K^- \eta' \nu_\tau$ decays, were our predictions respect the upper limit found by BaBar and hint to the possible discovery of this decay mode in the near future.

In this way we consider that we are in position of providing TAUOLA with theory-based currents that can describe well the $\tau^- \to K^- \eta^{(\prime)} \nu_\tau$ decays, based on the exponential parametrization developed by JPP and the dispersive representation constructed by BEJ.

To conclude, differential distributions of hadronic tau decays provide important information for testing diverse form factors and extracting the corresponding parameters increasing our knowledge of hadronization in the low-energy non-perturbative regime of QCD. It will be interesting to see if our predictions for the $\tau^- \to K^- \eta' \nu_\tau$ decays are corroborated and if more precise data on the $\tau^- \to K^- \eta \nu_\tau$ decays demand a more refined treatment. Finally, we emphasize the need of giving pole resonance parameters irrespective of the approach employed, either in a theorists' article or in a publication by an experimental collaboration.

Chapter 4

Combined analysis of the decays $\tau^- \to K_S \pi^- \nu_\tau$ and $\tau^- \to K^- \eta \nu_\tau$

In this chapter, we re-analyze the experimental measurement of the invariant mass distribution of the decay $\tau^- \to K_S \pi^- \nu_\tau$ together with the most recent available spectrum of the $K^- \eta$ decay mode both released by the Belle Collaboration [12, 100]. The former has been studied in detail in Refs. [14, 15, 105], improving the determination of the resonance parameters of both the $K^*(892)$ and its first radial excitation $K^*(1410)$, while the later, with a threshold above the $K^*(892)$ dominance, has been tackled in chapter 3 obtaining the $K^*(1410)$ properties which appeared to be in accordance with those of the $K_S \pi^-$ decay channel. The main purpose of this chapter is to deepen our knowledge of the $K^\star(1410)$ resonance parameters by performing a combined analysis of both decays [16]. This study is presently limited by three facts: unfolding of detector effects has not been performed for the latter data, the associated errors of these are still relatively large and no measurement of the $K^- \pi^0$ spectrum has been published by the B-factories. We intend to demonstrate that an updated analysis of the $K_S \pi^-$ and/or $K^- \eta$ Belle spectrum including the whole Belle-I data sample could improve notably the knowledge of the $K^*(1410)$ pole position. Therefore, we hope that our work strengths the case for a (re)analysis of the $(K\pi)^-$ and $K^- \eta$ spectra at the first generation B-factories including a larger data sample and also for devoted analyses in the forthcoming Belle-II experiment. Turning to the low-energy parameters, we emphasise the importance of (independent) measurements of the two $\tau^- \to (K\pi)^- \nu_\tau$ charge channels with the target of disentangling isospin violations in forthcoming studies.

We have organised this chapter as follows: in section 4.1, the differential decay width of the $\tau^- \to K_S \pi^- \nu_\tau$ process is written as a function of the contributing $K\pi$ vector and scalar form factors. The vector form factors will be described according

to a dispersive representation along the lines of Refs. [14, 15] (cf. Eq. (3.42)), while the scalar form factors are taken from Refs. [56, 68], thereby resumming FSI which is crucial to describe the considered decay spectra. In the previous chapter, we showed that a simple Breit-Wigner parametrisation of the dominating vector form factor lead to a rather poor description of the data and we will not consider it anymore. In section 4.2, we describe our fits in detail and present the corresponding results for all parameters. It will be seen that we are able to improve the determination of the $K^*(1410)$ pole position. Furthermore, we discuss isospin violations on the slope parameters of the vector form factors and the prospects for improving them by analysing the full Belle-I data set or future measurements at Belle-II. Finally, we summarise our conclusions in section 4.3. A brief discussion of the so-called "exponential" parametrisation of the $K\pi$ vector form factor which was put forward in Refs. [103, 105] (cf. Eq. (3.37)) is relegated to Appendix C.

4.1 Form factor representations

The differential decay width of the transition $\tau^- \to K_S \pi^- \nu_\tau$ as a function of the invariant mass of the two-meson system can be written as

$$
\begin{aligned}
\frac{\mathrm{d}\Gamma(\tau^- \to K_S \pi^- \nu_\tau)}{\mathrm{d}\sqrt{s}} &= \frac{G_F^2 M_\tau^3}{96\pi^3 s} S_{EW} \left| V_{us} f_+^{K_S\pi^-}(0) \right|^2 \left(1 - \frac{s}{M_\tau^2}\right)^2 q_{K_S\pi^-}(s) \\
&\times \left\{ \left(1 + \frac{2s}{M_\tau^2}\right) q_{K_S\pi^-}^2(s) \left| \widetilde{f}_+^{K_S\pi^-}(s) \right|^2 + \frac{3\Delta_{K_S\pi^-}^2}{4s} \left| \widetilde{f}_0^{K_S\pi^-}(s) \right|^2 \right\},
\end{aligned}
\tag{4.1}
$$

where

$$
q_{PQ}(s) = \frac{\sqrt{s^2 - 2s\Sigma_{PQ} + \Delta_{PQ}^2}}{2\sqrt{s}}, \quad \Sigma_{PQ} = m_P^2 + m_Q^2, \quad \Delta_{PQ} = m_P^2 - m_Q^2, \tag{4.2}
$$

and

$$
\widetilde{f}_{+,0}^{PQ}(s) \equiv \frac{f_{+,0}^{PQ}(s)}{f_{+,0}^{PQ}(0)} \tag{4.3}
$$

are form factors normalised to unity at the origin. In this way, besides the global normalisation, all remaining uncertainties on the hadronization of the considered currents are encoded in the reduced form factors $\widetilde{f}_{+,0}^{PQ}(s)$. $S_{EW} = 1.0201$ [122] resums the short-distance electroweak corrections.[1] Eq. (4.1) corresponds to the definitions

---

[1]We have not included additional non-factorisable electromagnetic corrections. They have been estimated in Ref. [86] where it was found that at the current level of precision they can be safely neglected.

of the vector, $f_+^{PQ}(s)$, and scalar, $f_0^{PQ}(s)$, form factors that separate the P- and S-wave contributions according to the conventions of Ref. [121]. The corresponding formula for the $\tau^- \to K^-\eta\nu_\tau$ decay was been given in Eq. (3.8). Regarding the global normalisation, in the following we will employ $|V_{us}f_+^{K_S\pi^-}(0)| = 0.2163(5)$ [125], from a global fit to $K_{\ell 3}$ data, and $|V_{us}f_+^{K^-\eta}(0)| = |V_{us}f_+^{K_S\pi^-}(0)|\cos\theta_P$, with $\theta_P = -(13.3 \pm 1.0)°$ [123].

The required form factors cannot be computed analytically from first principles. Still, the symmetries of the underlying QCD Lagrangian are useful to determine their behaviour in specific limits, the chiral or low-energy limit and the high-energy behaviour, so that the model dependence is reduced to the interpolation between these known regimes. For our central fits, to be presented in the next section, we follow the dispersive representation of the vector form factors outlined in Ref. [14] (cf. Eq. (3.42)), and briefly summarised below for the convenience of the reader. For the case of the $K_S\pi^-$ system, including two resonances, the $K^* = K^*(892)$ and the $K^{*\prime} = K^*(1410)$, the reduced vector form factor is taken to be of the form [14]

$$\widetilde{f}_+^{K\pi}(s) = \frac{m_{K^*}^2 - \kappa_{K^*}\widetilde{H}_{K\pi}(0) + \gamma s}{D(m_{K^*}, \gamma_{K^*})} - \frac{\gamma s}{D(m_{K^{*\prime}}, \gamma_{K^{*\prime}})}, \tag{4.4}$$

where

$$D(m_n, \gamma_n) = m_n^2 - s - \kappa_n\widetilde{H}_{K\pi}(s), \tag{4.5}$$

and

$$\kappa_n = \frac{192\pi}{\sigma_{K\pi}(m_n^2)^3}\frac{\gamma_n}{m_n}. \tag{4.6}$$

The fit function for the vector form factor is expressed in terms of the unphysical "mass" and "width" parameters m_n and γ_n. They are denoted by small letters, to distinguish them from the physical mass and width parameters M_n and Γ_n, which will later be determined from the pole positions in the complex plane and are denoted by capital letters. The scalar one-loop integral function $\widetilde{H}_{K\pi}(s)$ is defined below Eq. (3) of Ref. [103], however removing the factor $1/f_\pi^2$ which cancels if κ_n is expressed in terms of the unphysical width γ_n. Finally, in Eq. (4.6), the phase space function $\sigma_{K\pi}(s)$ is given by $\sigma_{K\pi}(s) = 2q_{K\pi}(s)/\sqrt{s}$. Since the K^* resonances that are produced through the τ decay are charged, and can decay or rescatter into both $K^0\pi^-$ as well as $K^-\pi^0$ channels, in the resonance propagators described by Eqs. (4.4) to (4.6) we have chosen to employ the corresponding isospin average, that is

$$\widetilde{H}_{K\pi}(s) = \frac{2}{3}\widetilde{H}_{K^0\pi^-}(s) + \frac{1}{3}\widetilde{H}_{K^-\pi^0}(s), \tag{4.7}$$

and analogously for $\sigma_{K\pi}(s)$, such that the resonance width contains both contributions. Little is known about a proper description of the width of the second vector resonance $K^{*\prime}$. The complicated $K^*\pi \sim K\pi\pi$ cuts may yield relevant effects which however necessitates a coupled-channel analysis like in refs. [104, 106]. This is beyond the scope of the present paper, in which for simplicity also for the second resonance only the two-meson cut is included. Similar remarks apply to a proper inclusion of the $K\eta$ and $K\eta'$ channels into Eq. (4.7) which would also require a coupled-channel analysis as was done for the corresponding scalar form factors in refs. [56, 68].

Next, we further follow Ref. [14] in writing a three-times subtracted dispersive representation for the vector form factor (cf. Eq. (2.44))

$$\widetilde{f}_+^{K\pi}(s) = \exp\left[\alpha_1 \frac{s}{M_{\pi^-}^2} + \frac{1}{2}\alpha_2 \frac{s^2}{M_{\pi^-}^4} + \frac{s^3}{\pi} \int\limits_{s_{K\pi}}^{s_{\text{cut}}} \mathrm{d}s' \frac{\delta_1^{K\pi}(s')}{(s')^3(s' - s - i0)} \right], \qquad (4.8)$$

where $s_{K\pi} = (M_K + M_\pi)^2$ is the $K\pi$ threshold[2] and the two subtraction constants α_1 and α_2 are related to the slope parameters appearing in the low-energy expansion of the form factor:

$$\widetilde{f}_+^{K\pi}(s) = 1 + \lambda_+' \frac{s}{M_{\pi^-}^2} + \frac{1}{2}\lambda_+'' \frac{s^2}{M_{\pi^-}^4} + \frac{1}{6}\lambda_+''' \frac{s^3}{M_{\pi^-}^6} + \dots. \qquad (4.9)$$

Explicitly, the relations for the linear and quadratic slope parameters λ_+' and λ_+'' take the form:

$$\lambda_+' = \alpha_1, \qquad \lambda_+'' = \alpha_2 + \alpha_1^2. \qquad (4.10)$$

The incentive for employing a dispersive representation for the form factor is that in this way the influence of the less-well known higher energy region is suppressed. The associated error can be estimated by varying the cut-off s_{cut} in the dispersive integral. In order to obtain the required input phase $\delta_1^{K\pi}(s)$, like in [14] we use the resonance propagator representation Eq. (4.4) of the vector form factor. The phase can then be calculated from the relation

$$\tan\delta_1^{K\pi}(s) = \frac{\mathrm{Im}\widetilde{f}_+^{K\pi}(s)}{\mathrm{Re}\widetilde{f}_+^{K\pi}(s)}, \qquad (4.11)$$

which completes our representation of the vector form factor $\widetilde{f}_+^{K\pi}(s)$.

The scalar form factors that are required for a complete description of the decay spectra according to Eq. (4.1) will be taken from the coupled-channel dispersive representation of refs. [56, 68]. In particular, for the scalar $K\pi$ form factor, we employ

---

[2]Isospin breaking on the low-energy parameters, like the threshold of the dispersive integral or the slope parameters of the vector form factor, is discussed later on.

the update presented in Ref. [131]. For the scalar $K\eta$ form factor, the result of the three-channel analysis described in section 4.3 of [56] is used, choosing specifically the solution corresponding to fit (6.10) of Ref. [68]. As a matter of principle, this is not fully consistent, since the employed $K\pi$ form factor was extracted from a two-channel analysis, only including the dominant $K\pi$ and $K\eta'$ channels. But as our numerical analysis shows, anyway the influence of the scalar $K\eta$ form factor is insignificant so that this inconsistency can be tolerated.

4.2 Joint fits to $\tau^- \to K_S\pi^-\nu_\tau$ and $\tau^- \to K^-\eta\nu_\tau$ Belle data

The differential decay rate of Eq. (4.1) is related to the distribution of the measured number of events by means of

$$\frac{\mathrm{d}N_{\text{events}}}{\mathrm{d}\sqrt{s}} = \frac{\mathrm{d}\Gamma(\tau^- \to (PQ)^-\nu_\tau)}{\mathrm{d}\sqrt{s}} \frac{N_{\text{events}}}{\Gamma_\tau \bar{B}(\tau^- \to (PQ)^-\nu_\tau)} \Delta\sqrt{s_{\text{bin}}}, \qquad (4.12)$$

where N_{events} is the total number of events measured for the considered process, Γ_τ is the inverse τ lifetime and $\Delta\sqrt{s_{\text{bin}}}$ is the bin width. $\bar{B}(\tau^- \to (PQ)^-\nu_\tau) \equiv \bar{B}_{PQ}$ is a normalisation constant that, for a perfect description of the spectrum, would equal the corresponding branching fraction.

For the $\tau^- \to K_S\pi^-\nu_\tau$ decays, an unfolded distribution measured by Belle is available [100]. The corresponding number of events is 53113.21 (54157.59 before unfolding) and the bin width 11.5 MeV. As discussed in the earlier analyses, the data points corresponding to bins 5, 6 and 7 are difficult to bring into accord with the theoretical descriptions and have thus been excluded from the minimisation.[3] The first point has not been included either, since the centre of the bin lies below the $K_S\pi^-$ production threshold. Following a suggestion from the experimentalists, as in the previous analyses we have furthermore excluded data corresponding to bin numbers larger than 90.

On the other hand, the published $\tau^- \to K^-\eta\nu_\tau$ Belle data [12] are only available still folded with detector effects.[4] Lacking for a better alternative, we have assumed that the $K^-\eta$ unfolding function is reasonably estimated by the $K_S\pi^-$ one and we have extracted in this way pseudo-unfolded data that we employed in our analysis.

---

[3]Still, including them in the fits would just increase the χ^2 with only irrelevant changes in the fit parameters.

[4]Contrary to our previous analysis performed in chapter 3, here we have not included the BaBar data [107]. They only consist in ten data points, with rather large errors, which furthermore had to be digitised from the published plots.

The corresponding number of events turns out 1271.51 for a bin width of 25 MeV. In this case, we excluded the first three data points, which lie below the $K^- \eta$ production threshold, and discarded data above the τ mass.

The χ^2 function minimised in our fits was chosen to be

$$\chi^2 = \sum_{i,\,PQ=K_S\pi^-,\,K^-\eta}{}' \left(\frac{\mathcal{N}_i^{th} - \mathcal{N}_i^{exp}}{\sigma_{\mathcal{N}_i^{exp}}} \right)^2 + \sum_{PQ=K_S\pi^-,\,K^-\eta} \left(\frac{\bar{B}_{PQ}^{th} - B_{PQ}^{exp}}{\sigma_{B_{PQ}}^{exp}} \right)^2 , \quad (4.13)$$

where $\mathcal{N}_i^{exp}$ and $\sigma_{\mathcal{N}_i^{exp}}$ are, respectively, the experimental number of events and the corresponding uncertainties in the i-th bin.[5] The prime in the summation indicates that the points specified above have been excluded. Therefore, the number of fitted data points is 86 (28) for the $K_S \pi^-$ ($K^- \eta$) spectrum, together with the respective branching fractions: hence 116 data points in total. While it is possible to obtain stable fits without using the $K_S \pi^-$ branching fraction as a data point, this is not the case for the $K^- \eta$ channel. This is due to the fact that there are strong correlations between the branching ratio and the slope parameters of the vector form factor. While in the $K_S \pi^-$ case sufficiently many data points with small enough errors are available to determine all fit quantities from the spectrum, for the $K^- \eta$ decay mode this was not possible. As a consistency check, we will be comparing the fitted values of the respective branching ratios to the corresponding results obtained by directly integrating the spectrum in all our fits.

The fitted parameters within the dispersive representation of the form factors of Eq. (4.8) then include:

- the respective branching fractions $\bar{B}_{K\pi}$ and $\bar{B}_{K\eta}$. For consistency, as our inputs in Eq. (4.13) we employ the results obtained by Belle in correspondence with the employed decay distribution data: $(0.404 \pm 0.013)\%$ [100] as well as $(1.58 \pm 0.10) \times 10^{-4}$ [12], respectively. This may be compared to the averages by the Particle Data Group, $(0.420 \pm 0.020)\%$ and $(1.52 \pm 0.08) \times 10^{-4}$ [124] and Heavy Flavour Averaging Group values [146], $(0.410 \pm 0.009)\%$ and $(1.53 \pm 0.08) \times 10^{-4}$. The recent update by Belle [102] including a 669 fb^{-1} data sample was found to be $(0.416 \pm 0.008)\%$ for the former decay mode.

- The slope parameters: $\lambda_{K\pi}'^{(\prime)}$ and $\lambda_{K\eta}'^{(\prime)}$. As was noted in Ref. [13], while the former ones correspond to the $K_S \pi^-$ channel, the latter ones are related to the $K^- \pi^0$ system. Therefore, small differences in these parameters due to isospin

---

[5]While it is expected that bin-to-bin correlations due to unfolding should arise, a full covariance matrix for the spectral data is not available, whence we have to limit ourselves to the diagonal errors.

violations are expected, and in the most general fit we allow for independent parameters in the two channels. As consistency checks of our procedure, we have also considered some fits assuming $\lambda'_{K\eta} = \lambda'_{K\pi}$. The findings of Ref. [14], $\lambda'_{K\pi} = (24.66 \pm 0.77) \times 10^{-3}$ and $\lambda''_{K\pi} = (11.99 \pm 0.20) \times 10^{-4}$, should serve as a reference point for our present study, where however $\bar{B}_{K\pi}$ was fixed to the average $(0.418 \pm 0.011)\%$ at that time.

- The pole parameters of the $K^*(892)$ and $K^*(1410)$ resonances. The masses and widths of these resonances are extracted from the complex pole position s_R according to $\sqrt{s_R} = M_R - \frac{i}{2}\Gamma_R$ [145]. For the lowest-lying resonance our results for the pole mass and width should be compatible with (892.0 ± 0.2) MeV and (46.2 ± 0.4) MeV [15], respectively, where the quoted uncertainties are only statistical. We expect that the extraction of the $K^*(1410)$ pole position should benefit from our present combined fit for which (1273 ± 75) MeV and (185 ± 74) MeV were obtained in Ref. [14] when the uncertainties are symmetrised.

- The relative weight γ of the two resonances. In our isospin-symmetric way (4.4) of parametrising the resonance propagators in the form factor description, γ should be the same for the $K_S \pi^-$ and $K^- \eta$ channels, which we shall assume for our central fit. Still, we have also tried to fit them independently, as differences might indicate inelastic or coupled-channel effects. As is seen below, our various fit results do not show a sizeable preference for this possibility which supports our choice $\gamma_{K\eta} = \gamma_{K\pi}$. Our findings may be compared to the value $\gamma = -0.039 \pm 0.020$ of [14] indicating the influence of including the $\tau^- \to K^- \eta \nu_\tau$ mode into our analysis.

In the fits we have furthermore employed the following numerical inputs: $M_\tau = 1776.82$ MeV, $\Gamma_\tau = 2.265 \times 10^{-12}$ GeV and $G_F = 1.16637(1) \times 10^{-5}$ GeV^{-2} [124]. Pseudoscalar meson masses were also taken according to their PDG values [124]. Finally, the next-to-leading order χPT low-energy constants and the chiral logarithms depend on an arbitrary renormalisation scale μ (these dependencies cancel one another), which we have fixed to the physical mass scale of the problem, $M_{K^*} = 892$ MeV.

In Table 4.1, we display our results using slightly different settings, though in all of them Eq. (4.11) is employed to obtain the input phaseshift for the dispersion relation (4.8) and s_{cut} is fixed to 4 GeV^2 (the uncertainty associated to its variation is discussed later on): our reference fit (second column) corresponds to fixing $\gamma_{K\pi} = \gamma_{K\eta}$, fit A (third column) assumes $\lambda'_{K\pi} = \lambda'_{K\eta}$, fit B (fourth column) is the result of letting

Fitted value	Reference Fit	Fit A	Fit B	Fit C
$\bar{B}_{K\pi}(\%)$	0.404 ± 0.012	0.400 ± 0.012	0.404 ± 0.012	0.397 ± 0.012
$(B_{K\pi}^{th})(\%)$	(0.402)	(0.394)	(0.400)	(0.394)
M_{K^*}	892.03 ± 0.19	892.04 ± 0.19	892.03 ± 0.19	892.07 ± 0.19
Γ_{K^*}	46.18 ± 0.42	46.11 ± 0.42	46.15 ± 0.42	46.13 ± 0.42
$M_{K^{*\prime}}$	1305^{+15}_{-18}	1308^{+16}_{-19}	1305^{+15}_{-18}	1310^{+14}_{-17}
$\Gamma_{K^{*\prime}}$	168^{+52}_{-44}	212^{+66}_{-54}	174^{+58}_{-47}	184^{+56}_{-46}
$\gamma_{K\pi} \times 10^2$	$= \gamma_{K\eta}$	$-3.6^{+1.1}_{-1.5}$	$-3.3^{+1.0}_{-1.3}$	$= \gamma_{K\eta}$
$\lambda'_{K\pi} \times 10^3$	23.9 ± 0.7	23.6 ± 0.7	23.8 ± 0.7	23.6 ± 0.7
$\lambda''_{K\pi} \times 10^4$	11.8 ± 0.2	11.7 ± 0.2	11.7 ± 0.2	11.6 ± 0.2
$\bar{B}_{K\eta} \times 10^4$	1.58 ± 0.10	1.62 ± 0.10	1.57 ± 0.10	1.66 ± 0.09
$(B_{K\eta}^{th}) \times 10^4$	(1.45)	(1.51)	(1.44)	(1.58)
$\gamma_{K\eta} \times 10^2$	$-3.4^{+1.0}_{-1.3}$	$-5.4^{+1.8}_{-2.6}$	$-3.9^{+1.4}_{-2.1}$	$-3.7^{+1.0}_{-1.4}$
$\lambda'_{K\eta} \times 10^3$	20.9 ± 1.5	$= \lambda'_{K\pi}$	21.2 ± 1.7	$= \lambda'_{K\pi}$
$\lambda''_{K\eta} \times 10^4$	11.1 ± 0.4	11.7 ± 0.2	11.1 ± 0.4	11.8 ± 0.2
$\chi^2/\text{n.d.f.}$	$108.1/105 \sim 1.03$	$109.9/105 \sim 1.05$	$107.8/104 \sim 1.04$	$111.9/106 \sim 1.06$

Table 4.1: Fit results for different choices regarding linear slopes and resonance mixing parameters at $s_{\text{cut}} = 4\,\text{GeV}^2$. See the main text for further details. Dimensionful parameters are given in MeV. As a consistency check, for each of the fits we provide (in brackets) the value of the respective branching fractions obtained by integrating Eq. (4.1).

all parameters float independently and finally, fit C (fifth column) enforces both restrictions $\gamma_{K\pi} = \gamma_{K\eta}$ and $\lambda'_{K\pi} = \lambda'_{K\eta}$. It is seen that our approach is rather stable against these variations, as the $\chi^2/\text{n.d.f.}$ remains basically the same for the different scenarios. Also the values of the fitted parameters are always compatible across all fits. The largest modification is observed in fit A, where we fix $\lambda'_{K\pi} = \lambda'_{K\eta}$, but allow for independent resonance mixing parameters γ. This is partly expected since in the reference fit the former equality on the slope parameters is only fulfilled at the 2σ level. Letting all parameters float in fit B yields results which are nicely compatible with the reference fit, though for some parameters resulting in slightly larger uncertainties. Finally, enforcing both, the linear slopes as well as the mixing parameters to be equal also results in a compatible fit where now the largest shift by about 2σ is found in $\lambda''_{K\eta}$.

The theoretical uncertainty associated to the choice of s_{cut} is probed through the fits presented in Table 4.2 where, for the setting of our reference fit discussed previously, the values $3.24\,\text{GeV}^2$ (second column), $4\,\text{GeV}^2$ (third column), $9\,\text{GeV}^2$ (fourth column) and the $s_{\text{cut}} \to \infty$ limit (last column) are used ($s_{\text{cut}} = 4\,\text{GeV}^2$ corresponds to our reference fit in the second column of Table 4.1 and is repeated here for ease of comparison). The dependence of the fitted parameters on the integral cut-off is

similar to what was found in previous works (see, for instance refs. [14, 15]) and allows to estimate the corresponding systematic error. In order to corroborate our fits, we performed additional tests. We have also run fits considering two and four subtraction constants in order to test the stability of our results with respect to this choice. As in the previous analyses [14, 15] of the $\tau^- \to K_S \pi^- \nu_\tau$ spectrum, the changes in the results are well within our uncertainties. It is furthermore confirmed that regarding final uncertainties three subtractions appears to be an optimal choice. This may, however, change if the representation of the higher-energy region is improved, for example through a coupled-channel analysis, such that this region requires less suppression. As a second test, we have employed a variant of the form factor Ansatz (4.4) in which the real part of the loop function $\widetilde{H}_{K\pi}(s)$ is not resummed into the propagator denominator, but into an exponential, as was for example suggested in refs. [103, 105] for the description of $\tau \to K\pi\nu_\tau$ decays. This type of Ansatz is further discussed in Appendix C where also direct fits of the corresponding form factors are described. Our test here, however, consists in extracting the corresponding phase from this type of form factor according to Eq. (4.11) and plugging the respective phase into the dispersion relation (4.8). It is found that the corresponding fits are almost identical to the ones described before, providing additional faith on the robustness of the extracted parameters.

For presenting our final results, we have added to the statistical fit error a systematic uncertainty due to the variation of s_{cut}. To this end, we have taken the largest variation of central values while varying s_{cut} (which is always found at $s_{\text{cut}} = 3.24\,\text{GeV}^2$) and have added this variation in quadrature to the statistical uncertainty. We then obtain

$$\bar{B}_{K\pi} = (0.404 \pm 0.012)\,\%, \quad M_{K^*} = 892.03 \pm 0.19, \quad \Gamma_{K^*} = 46.18 \pm 0.44,$$

$$M_{K^{*\prime}} = 1305^{+16}_{-18}, \quad \Gamma_{K^{*\prime}} = 168^{+65}_{-59}, \quad \gamma_{K\pi} = \gamma_{K\eta} = \left(-3.4^{+1.2}_{-1.4}\right) \cdot 10^{-2},$$

$$\lambda'_{K\pi} = (23.9 \pm 0.9) \cdot 10^{-3}, \quad \lambda''_{K\pi} = (11.8 \pm 0.2) \cdot 10^{-4}, \quad \bar{B}_{K\eta} = (1.58 \pm 0.10) \cdot 10^{-4},$$

$$\lambda'_{K\eta} = (20.9 \pm 2.7) \cdot 10^{-3}, \quad \lambda''_{K\eta} = (11.1 \pm 0.5) \cdot 10^{-4}, \tag{4.14}$$

were like before all dimensionful quantities are given in MeV. Our final fit results are compared to the measured Belle $\tau^- \to K_S \pi^- \nu_\tau$ and $\tau^- \to K^- \eta \nu_\tau$ distributions [12, 100] in Figure 4.1. Satisfactory agreement with the experimental data, in accord with the observed $\chi^2/\text{n.d.f.}$ of order one, is seen for all data points. The $K\pi$ spectrum is dominated by the contribution of the $K^*(892)$ resonance, whose peak is neatly

$s_{\text{cut}}(\text{GeV}^2)$ / Fitted value	3.24	4	9	∞
$B_{K\pi}(\%)$	0.402 ± 0.013	0.404 ± 0.012	0.405 ± 0.012	0.405 ± 0.012
$(B_{K\pi}^{th})(\%)$	(0.399)	(0.402)	(0.403)	(0.403)
M_{K^*}	892.01 ± 0.19	892.03 ± 0.19	892.05 ± 0.19	892.05 ± 0.19
Γ_{K^*}	46.04 ± 0.43	46.18 ± 0.42	46.27 ± 0.42	46.27 ± 0.41
$M_{K^{*\prime}}$	1301^{+17}_{-22}	1305^{+15}_{-18}	1306^{+14}_{-17}	1306^{+14}_{-17}
$\Gamma_{K^{*\prime}}$	207^{+73}_{-58}	168^{+52}_{-44}	155^{+48}_{-41}	155^{+47}_{-40}
$\gamma_{K\pi}$	$= \gamma_{K\eta}$	$= \gamma_{K\eta}$	$= \gamma_{K\eta}$	$= \gamma_{K\eta}$
$\lambda'_{K\pi} \times 10^3$	23.3 ± 0.8	23.9 ± 0.7	24.3 ± 0.7	24.3 ± 0.7
$\lambda''_{K\pi} \times 10^4$	11.8 ± 0.2	11.8 ± 0.2	11.7 ± 0.2	11.7 ± 0.2
$\bar{B}_{K\eta} \times 10^4$	1.57 ± 0.10	1.58 ± 0.10	1.58 ± 0.10	1.58 ± 0.10
$(B_{K\eta}^{th}) \times 10^4$	(1.43)	(1.45)	(1.46)	(1.46)
$\gamma_{K\eta} \times 10^2$	$-4.0^{+1.3}_{-1.9}$	$-3.4^{+1.0}_{-1.3}$	$-3.2^{+0.9}_{-1.1}$	$-3.2^{+0.9}_{-1.1}$
$\lambda'_{K\eta} \times 10^3$	18.6 ± 1.7	20.9 ± 1.5	22.1 ± 1.4	22.1 ± 1.4
$\lambda''_{K\eta} \times 10^4$	10.8 ± 0.3	11.1 ± 0.4	11.2 ± 0.4	11.2 ± 0.4
$\chi^2/\text{n.d.f.}$	$105.8/105$	$108.1/105$	$111.0/105$	$111.1/105$

Table 4.2: Reference fit results obtained for different values of s_{cut} in the dispersive integral are displayed. Dimensionful parameters are given in MeV. As a consistency check, for each of the fits we give (in brackets) the value of the respective branching ratios obtained integrating Eq. (4.1).
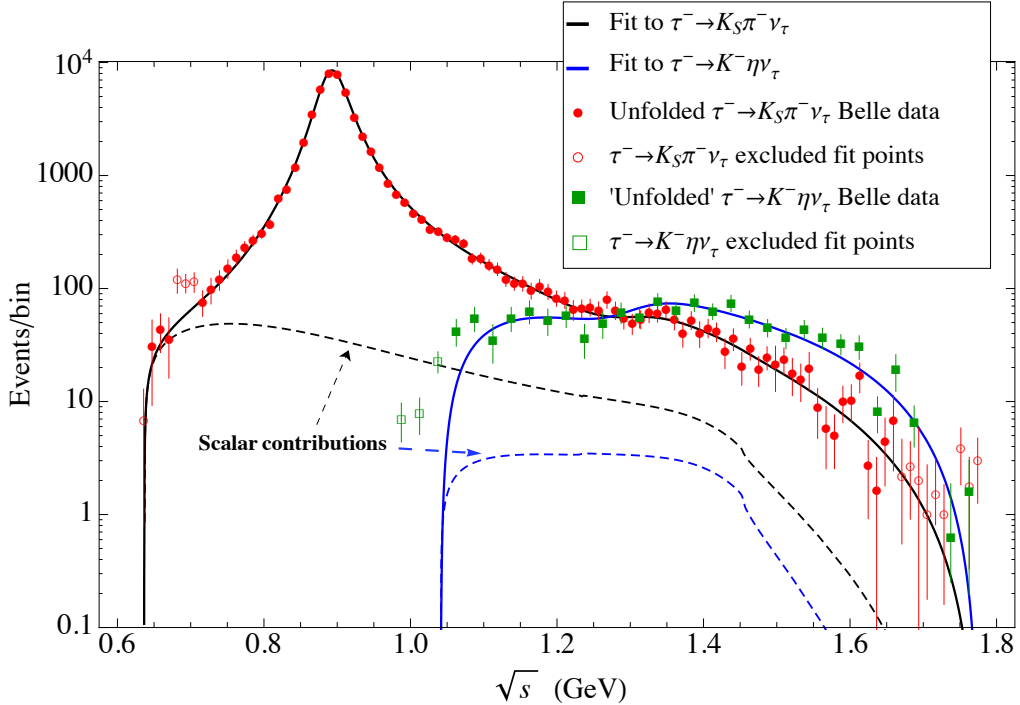
Figure 4.1:   Belle $\tau^- \to K_S\pi^-\nu_\tau$ (red solid circles) [100] and $\tau^- \to K^-\eta\nu_\tau$ (green solid squares) [12] measurements as compared to our best fit results (solid black and blue lines, respectively) obtained in combined fits to both data sets, as presented in Eq. (4.14). Empty circles (squares) correspond to data points which have not been included in the analysis. The small scalar contributions have been represented by black and blue dashed lines showing that while the former plays a role for the $K\pi$ spectrum close to threshold, the latter is irrelevant for the $K\eta$ distribution.

visible. The scalar form factor contribution, although small in most of the phase space, is important to describe the data immediately above threshold. There is no such clear peak structure for the $K\eta$ channel as a consequence of the interplay between both K^* resonances. The corresponding scalar form factor in this case is numerically insignificant.

The correlation coefficients corresponding to our reference fit with $s_{\mathrm{cut}} = 4$ GeV^2 can be read from Table 4.3. As anticipated, there is a large correlation between the set $\{\bar{B}_{K\pi}, \lambda'_{K\pi}, \lambda''_{K\pi}\}$ which enables stable fits removing one of these parameters (the fit then becomes somewhat less restrictive, though). Despite the correlation between $\lambda'_{K\eta}$ and $\lambda''_{K\eta}$ also being nearly maximal, these parameters are less correlated with $\bar{B}_{K\eta}$, implying that all three are needed to reach convergence in the minimisation.

	$\bar{B}_{K\pi}$	M_{K*}	Γ_{K*}	$M_{K*\prime}$	$\Gamma_{K*\prime}$	$\lambda'_{K\pi}$	$\lambda''_{K\pi}$	$\bar{B}_{K\eta}$	$\gamma_{K\eta}=\gamma_{K\pi}$	$\lambda'_{K\eta}$	$\lambda''_{K\eta}$
M_{K*}	−0.163	1									
Γ_{K*}	0.028	−0.060	1								
$M_{K*\prime}$	−0.063	−0.104	−0.142	1							
$\Gamma_{K*\prime}$	0.126	0.130	0.292	−0.556	1						
$\lambda'_{K\pi}$	0.800	−0.100	0.457	−0.244	0.432	1					
$\lambda''_{K\pi}$	0.928	−0.215	0.328	−0.166	0.304	0.942	1				
$\bar{B}_{K\eta}$	−0.003	−0.005	−0.010	0.003	−0.001	−0.015	−0.009	1			
$\gamma_{K\eta}=\gamma_{K\pi}$	−0.155	−0.173	−0.378	0.498	−0.878	−0.565	−0.373	0.019	1		
$\lambda'_{K\eta}$	0.058	0.028	0.117	0.050	0.337	0.182	0.128	0.434	−0.340	1	
$\lambda''_{K\eta}$	0.035	−0.017	0.037	0.106	0.218	0.080	0.064	0.561	−0.174	0.971	1

Table 4.3: Correlation coefficients corresponding to our reference fit with $s_{\mathrm{cut}} = 4 \text{ GeV}^2$, second column of Table 4.1. In the fits where $\gamma_{K\pi} = \gamma_{K\eta}$ is not enforced, their correlation coefficient turns out to be ≈ 0.67.

For this reason we prefer to keep $\bar{B}_{K\eta}$ as a data point in the joint analysis. Finally, we note a large correlation between the parameters $\gamma_{K\pi} = \gamma_{K\eta}$ and $\Gamma_{K*\prime}$ which seems to be enhancing the corresponding errors (this effect may in part be due to the three subtractions employed, which decrease the sensitivity to the higher-energy region). In the fits where $\gamma_{K\pi} = \gamma_{K\eta}$ is not enforced, their correlation coefficient is ≈ 0.67. This suggests that with more precise data in the future it might be possible to resolve the current degeneracy between both.

Several comments regarding our final results of Eq. (4.14) and the reference fit of Table 4.1 are in order:

- Concerning the branching fractions, we observe that in the $K_S\pi^-$ channel our fit value $\bar{B}_{K\pi}$, which is mainly driven by the explicit input, and the result when integrating the fitted spectrum $B^{th}_{K\pi}$, are in very good agreement, pointing to a satisfactory description of the experimental data. On the other hand, for the $K\eta$ case, one notes a trend that the integrated branching fraction $B^{th}_{K\eta}$ turns out about 10% smaller than the fit result $\bar{B}_{K\eta}$, which points to slight deficiencies in the theoretical representation of this spectrum. This issue should be investigated further in the future with more precise data.

- The $K_S\pi^-$ slope parameters are well compatible with previous analogous analysis [14, 15]. For the corresponding $K^-\eta$ slopes, we obtain somewhat smaller values, which are, however, compatible with the crude estimates in Ref. [13]. The fact that the $K^-\eta$ slopes are about 2σ lower than the $K_S\pi^-$ slopes could be an indication of isospin violations, or could be a purely statistical effect. (Or

a mixture of both.) To tackle this question and make further progress to disentangle isospin violations in the $K\pi$ form factor slopes, it is indispensable to study the related distribution for the $\tau^- \to K^-\pi^0\nu_\tau$ decay, and the experimental groups should make every effort to also publish the corresponding spectrum for this process.

- The pole parameters of the $K^*(892)$ resonance are in nice accord with previous values [14, 15] and have similar statistical fit uncertainties which is to be expected as these parameters are driven by the data of the $\tau^- \to K_S\pi^-\nu_\tau$ decay, which was the process analysed previously. Regarding the parameters of the $K^*(1410)$ resonance, adding the $\tau^- \to K^-\eta\nu_\tau$ spectral data into the fit results in a substantial improvement in the determination of the mass, while only a slight improvement in the width is observed. Part of the large uncertainty in the width of the second K^* resonance can be traced back to the strong fit correlation with the mixing parameter γ, which is also not very well determined. Future data of either $\tau^- \to (K\pi)^-\nu_\tau$ or $\tau^- \to K^-\eta\nu_\tau$ hadronic invariant mass distributions should enable a more precise evaluation. Prospects updating the Belle-I analyses with the complete data sample or studying Belle-II data are discussed next.

In Table 4.4, we have simulated the impact of future data on our fitted parameters. For this purpose we have kept the same central values of the data points and reduced the errors according to the expected increase in luminosity. Specifically, we have used that the $K_S\pi^-$ ($K^-\eta$) Belle analysis employed 351 (490) fb^{-1} for a complete data sample of 1000 fb^{-1} accumulated at Belle-I for general purpose studies (we have assumed the same resolution and efficiencies as in the published analyses following a suggestion from the Collaboration). Similarly, we have also compared our current results, Eq. (4.14), to the prospects for Belle-II at the end of its data taking, with 50 ab^{-1} neglecting again possible improvements in the detector response and data analysis. In the different columns of Table 4.4, we recall our results, Eq. (4.14), and compare them, in turn, to the cases where both decay modes are reanalysed using the whole Belle-I data sample, the same when only one of the analysis is updated and analogously for Belle-II.

The majority of the expected errors for Belle-II will make completely negligible the statistical error with respect to the theoretical uncertainties, which then will most likely demand more elaborated approaches than those considered here. This would also happen in the case of the $K^*(1410)$ parameters with any updated Belle-I

Data / Error	Current	Belle-I	Belle-I $K\pi$	Belle-I $K\eta$	Belle-II	Belle-II $K\pi$	Belle-II $K\eta$
$\bar{B}_{K\pi}(\%)$	0.404 ± 0.012	± 0.005	± 0.005	± 0.012	$^\dagger(0.001)$	$^\dagger(0.001)$	± 0.012
M_{K^*}	892.03 ± 0.19	± 0.09	± 0.09	± 0.19	$^\dagger(0.02)$	$^\dagger(0.02)$	± 0.19
Γ_{K^*}	46.18 ± 0.44	± 0.20	± 0.20	± 0.44	$^\dagger(0.02)$	$^\dagger(0.03)$	± 0.42
$M_{K^{*\prime}}$	1304 ± 17	$^\dagger(7)$	$^\dagger(9)$	$^\dagger(8)$	$^\dagger(1)$	$^\dagger(1)$	$^\dagger(1)$
$\Gamma_{K^{*\prime}}$	168 ± 62	$^\dagger(19)$	$^\dagger(24)$	$^\dagger(25)$	$^\dagger(3)$	$^\dagger(4)$	$^\dagger(11)$
$\lambda'_{K\pi} \times 10^3$	23.9 ± 0.9	$^\dagger(0.3)$	$^\dagger(0.3)$	± 0.8	$^\dagger(0.04)$	$^\dagger(0.04)$	± 0.8
$\lambda''_{K\pi} \times 10^4$	11.8 ± 0.2	± 0.07	± 0.07	± 0.2	$^\dagger(0.01)$	$^\dagger(0.01)$	± 0.2
$\bar{B}_{K\eta} \times 10^4$	1.58 ± 0.10	± 0.05	± 0.10	± 0.05	$^\dagger(0.01)$	± 0.10	$^\dagger(0.01)$
$\gamma_{K\eta}(= \gamma_{K\pi}) \times 10^2$	-3.3 ± 1.3	$^\dagger(0.3)$	$^\dagger(0.3)$	$^\dagger(0.4)$	$^\dagger(0.04)$	$^\dagger(0.04)$	$^\circ(0.3)$
$\lambda'_{K\eta} \times 10^3$	20.9 ± 2.7	$^\dagger(0.7)$	± 2.7	$^\dagger(0.8)$	$^\dagger(0.10)$	± 2.7	$^\circ(0.4)$
$\lambda''_{K\eta} \times 10^4$	11.1 ± 0.5	$^\dagger(0.2)$	± 0.5	$^\dagger(0.2)$	$^\dagger(0.02)$	± 0.5	$^\dagger(0.06)$

Table 4.4: The errors of our final results (4.14) are compared, in turn, to those achievable by analysing the complete Belle-I data sample, and updating only the $K_S\pi^-$ or $K^-\eta$ analyses. The last three columns show the potential of fitting all data collected by Belle-II and the same only for $K_S\pi^-$ or for $K^-\eta$ (assuming the other mode has not been updated to include the complete Belle-I data sample). Current Belle $K_S\pi^-$ ($K^-\eta$) data correspond to 351 (490) fb^{-1} for a complete data set of ~ 1000 fb$^{-1} = 1$ ab^{-1}. Expectations for Belle-II correspond to 50 ab^{-1}. All errors include both statistical and systematic uncertainties. † means that statistical errors (in brackets) will become negligible, while $^\circ$ signals a tension with the current reference best fit values. We thank Denis Epifanov for conversations on these figures and on expected performance of Belle-II at the detector and analysis levels. All errors have been symmetrised for simplicity.

study. The impact of $\tau^- \to K^- \pi^0 \nu_\tau$ on the $K^*(892)$ and $K^*(1410)$ meson parameters can be estimated by means of the $\tau^- \to K_S \pi^- \nu_\tau$ simulation. Such a measurement will be more significant in the determination of the $K^- \eta$ slope parameters than an updated study of this latter decay mode. In passing, we also mention that Belle-II statistics could be able to pinpoint possible inconsistencies between $\tau^- \to (K\pi)^- \nu_\tau$ and $\tau^- \to K^- \eta \nu_\tau$ data.

4.3 Conclusions

Hadronic decays of the τ lepton remain to be an advantageous tool for the investigation of the hadronization of QCD currents in the non-perturbative regime of the strong interaction. In this work we have explored the benefits of a combined analysis of the $\tau^- \to K_S \pi^- \nu_\tau$ and $\tau^- \to K^- \eta \nu_\tau$ decays. This study was motivated by (our) separate earlier works on the two decay modes considering them as independent data sets. In particular, it was noticed in [13] that the $K\eta$ decay channel was rather sensitive to the properties of the $K^*(1410)$ resonance as the higher-energy region is less suppressed by phase space.

Our description of the dominant vector form factor follows the work of Ref. [14], and proceeds in two stages. First, we write a Breit-Wigner type representation (4.4) which also fulfils constraints from χPT at low-energies. In Eq. (4.4), we have re-summed the real part of the loop function in the resonance denominators, but as was discussed above, employing the following dispersive treatment, this is not really essential. It mainly entails a shift in the unphysical mass and width parameters m_n and γ_n. Second, we extract the phase of the vector form factor according to Eq. (4.11) and plug it into the three-times subtracted dispersive representation of Eq. (4.8). This way, the higher-energy region of the form factor, which is less well know, is suppressed, and the form factor slopes emerge as subtraction constants of the dispersion relation. A drawback of this description is that the form factor does not automatically satisfy the expected $1/s$ fall-off at very large energies. Still, in the region of the τ mass (and beyond), our form-factor representation is a decreasing function such that the deficit should be admissible, thereby leaving more freedom for the slope parameters to assume their physical values.

In our combined dispersive analysis of the $(K\pi)^-$ and $K^- \eta$ decays we are currently limited by three facts: there are only published measurements of the $K_S \pi^-$ spectrum (and not of the corresponding $K^- \pi^0$ channel), the available $K^- \eta$ spectrum is not very precise and the corresponding data are still convoluted with detector effects.

The first restriction prevents us from cleanly accessing isospin violations in the slope parameters of the vector form factor. From our joint fits, we have however managed to get an indication of this effect. The second one constitutes the present limitation in determining the $K^*(1410)$ resonance parameters but one should be aware that our approach to avoid the last one (assuming that the $K_S \pi^-$ unfolding function gives a good approximation to the one for the $K^- \eta$ case) adds a small (uncontrolled) uncertainty to our results that can only be fixed by a dedicated study of detector resolution and efficiency. In this respect it would be most beneficial, if unfolded measured spectra would be made available by the experimental groups, together with the corresponding bin-to-bin correlation matrices.

In Table 4.1, we have compared slightly different options to implement constraints from isospin into the fits, and in Table 4.2, we studied the dependence of our fits on the cut-off s_{cut} in the dispersion integral. Our reference fit is given by the second column of Table 4.1 and adding together the statistical fit uncertainties with systematic errors from the variation of s_{cut}, our final results are summarised in Eq. (4.14). The pole position we find for the $K^*(892)$ resonance is in perfect agreement with previous studies. The main motivation of this work was, however, to exploit the synergy of the $K\pi$ and $K\eta$ decay modes in characterising the $K^*(1410)$ meson. According to our results, the relative weight γ of both vector resonances is compatible in the $K\pi$ and $K\eta$ vector form factors, which supports our assumption of their universality. With current data we succeed in improving the determination of the $K^*(1410)$ pole mass, but regarding the width, substantial uncertainties remain. Our central result for these two quantities is

$$M_{K^{*\prime}} = (1304 \pm 17)\ \text{MeV}\,, \quad \Gamma_{K^{*\prime}} = (171 \pm 62)\ \text{MeV}\,, \tag{4.15}$$

where we have symmetrised the uncertainties listed in Eq. (4.14). We provide a graphical account of this outcome in Fig. (4.2) compared with previous determinations from both channels separated.

We have then estimated the impact of future re-analyses including the complete Belle-I data sample and all expected data from Belle-II on these decay modes. This projection reveals (in both cases) that the increased statistics will most probably require a refined theoretical framework to match the experimental precision in the determination of the $K^*(1410)$ resonance parameters. While our description so far is purely elastic, this may include incorporation of coupled channels to take into account inelastic effects along the lines of refs. [104, 106], which would allow for a proper inclusion of higher channels in the resonance widths. Belle-II data would also lead to
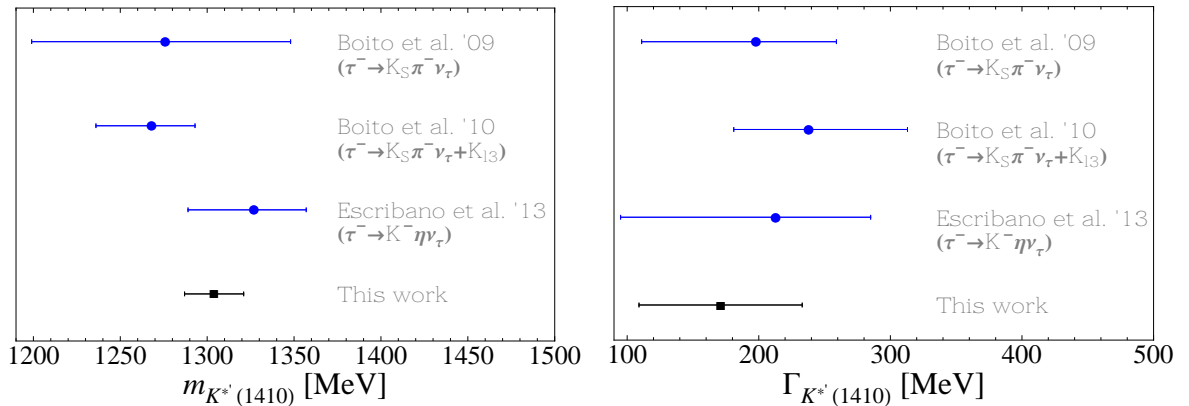
Figure 4.2: Our value for the pole parameters (black square) as given in Eq. (4.15), mass (left) and width (right), of the $K^*(1410)$ resonance obtained from a joint to both experimental Belle $\tau^- \to K_S \pi^- \nu_\tau$ and $\tau^- \to K^- \eta \nu_\tau$ decays spectra compared with previous determinations from both channels separated [13, 14, 15] (blue circles).

much improved tests of our low-energy description and the $K^*(892)$ dominance region. Knowledge of isospin breaking effects on the slope parameters could be drastically improved by measuring the hadronic invariant mass distribution in $\tau^- \to K^- \pi^0 \nu_\tau$ decays, which would by the way increase the accuracy in the extraction of the $K^*(892)$ pole position. We hope that this study will give additional motivation to the B-factory collaborations for performing the respective analyses.

Chapter 5

Study of the second-class current decays $\tau^- \to \pi^- \eta \nu_\tau$ and $\tau^- \to \pi^- \eta' \nu_\tau$

According to Weinberg [147], non-strange weak $(V - A)$ hadronic currents can be divided into two types depending on their G-parity: i) first class currents, with the quantum numbers $J^{PG} = 0^{++}, 0^{--}, 1^{+-}, 1^{-+}$; ii) second class currents (SCC), which have $J^{PG} = 0^{+-}, 0^{-+}, 1^{++}, 1^{--}$. The former completely dominate weak interactions since there has been no evidence of the later in Nature so far.

In the Standard Model (SM) SCC come up with an isospin violating term which heavily suppresses the interaction and the eventual sensitivity to new physics (*i.e.* by a charged Higgs contribution to the $\pi\eta^{(\prime)}$ scalar form factors) may be enhanced.

One tentative scenario to look for such kind of currents is through the rare hadronic decays of the τ lepton $\tau^- \to \pi^- \eta \nu_\tau$ and $\tau^- \to \pi^- \eta' \nu_\tau$ [148] for which some experimental upper bounds already exist. For the $\pi^- \eta$ decay mode, BaBar, Belle and CLEO collaborations have reported the branching ratio upper limits of $9.9 \cdot 10^{-5}$ at 95% CL [107], $7.3 \cdot 10^{-5}$ at 90% CL [149] and of $1.4 \cdot 10^{-4}$ at 95% CL [108], respectively. Actually, $\tau^- \to \pi^- \eta \nu_\tau$ belongs to the discovery modes list of the near future super-B factory Belle II [150] for which we advocate the measurement. Regarding the $\pi^- \eta'$ channel, BaBar obtained a new upper bound, $4.0 \cdot 10^{-6}$ at 90% CL [110], that slightly improved its previous value $7.2 \cdot 10^{-6}$ at 90% CL [151]. Also CLEO quoted the upper limit $7.4 \cdot 10^{-5}$ at 90% CL [152] in the nineties. Historically, $\tau^- \to \pi^- \eta \nu_\tau$ decays attracted a lot of attention at the end of the eighties when existing measurements hinted at abnormally large branching fractions into final states containing η mesons, and a preliminary announcement by the HRS Coll. advocated for an $\mathcal{O}(\%)$ decay rate into the $\pi^- \eta$ decay mode, which was against theoretical expectations [111]. Later on, the situation settled [80] and these decays remained undiscovered even at the first generation B-factories BaBar and Belle, where the background from other competing

modes such as $\tau^- \to \pi^- \pi^0 \eta \nu_\tau$ [12, 153] veiled the SCC signal. According to our results, their discovery (through either of the $\tau^- \to \pi^- \eta^{(\prime)} \nu_\tau$ decay channels) should be finally possible at Belle-II, thanks to the fifty times increased luminosity of Belle-II [154] with respect to its predecessor. The implementation of theory predictions for these modes in the TAUOLA version used by the Belle [119] Collaboration will help to accomplish this task.

From the theoretical perspective, the spin-parity of the $\pi^- \eta^{(\prime)}$ system, J^P, is 0^+ or 1^- depending whether the system is in S- or P-wave, respectively. However, the G-parity of the system is -1, which is opposed to the vector current that drives the decay in the SM. Therefore, the $S(P)$-wave of the $\pi^- \eta^{(\prime)}$ system gives $J^{PG} = 0^{+-}(1^{--})$, which can only be realized through a SCC independently of possible intermediate resonant states. Previous theoretical analysis estimated the branching ratio to be of the order of 10^{-5} and within the range 10^{-8} to 10^{-6} for the $\pi^- \eta$ and $\pi^- \eta'$ modes, respectively. In this work, we revisit these processes benefited from our previous experiences in describing dimeson τ decays data [13, 14, 15, 16, 97, 155, 156]. Here, the main subject of our study is the theoretical construction of the participant vector and scalar form factors. Our initial approach is carried out within the framework of the Chiral Perturbation Theory (χPT) [5, 6, 7] including resonances (RχT) [48]. On a second stage, we take advantage of the global analysis of the $U(3) \otimes U(3)$ one-loop meson-meson scattering in the frame of RχT performed in Ref. [57] to calculate the scalar form factors from dispersion relations based on arguments of unitarity and analyticity. In particular, we will first take into account elastic final state interactions through the Omnès solution [79] for describing the $\pi^- \eta$ and $\pi^- \eta'$ scalar form factors (SFF), respectively. Then, we consider the effect of coupled channels in the former system for studying inelasticities. Afterwards, we will also consider the $K^- K^0$ threshold, whose coupling to the intermediate scalar resonance is presumably large [57], and couple it to both $\pi^- \eta$ and $\pi^- \eta'$ SFFs independently. Finally, the three coupled-channels case will we addressed. Several ways of solving coupled channels form factors have been considered in literature; some use iterative methods [56, 157, 158, 159], while others employ closed algebraic expressions [130, 160, 161, 162, 163, 164, 165, 166]. The second alternative will be followed in this work. See also Ref. [167] for a recent description based on dispersive techniques.

This chapter is organized as follows. In Section 5.1, we define the hadronic matrix element in terms of the vector and scalar form factors and give the expression for the differential decay width. In Section 5.2, we derive the $\pi^- \eta^{(\prime)}$ vector form factor

(VFF) within RχT by considering mixing within the $\pi^0 - \eta - \eta'$ system. In our approach, the VFFs appear to be an isospin violating factor times the $\pi^- \pi^0$ form factor for which we will employ its experimental determination arising from the well-known first-class current $\tau^- \to \pi^- \pi^0 \nu_\tau$ decay. We devote Section 5.3 to the computation of the corresponding scalar form factors. We start with a simple Breit-Wigner parameterization and then consider a dispersion relation obeying unitarity, first in the elastic single channel case through the Omnès solution and then taking into account coupled-channel effects. The spectra and predictions for the branching ratios ($\mathcal{BR}$) are given in Section 5.4. Also in this section, we will briefly discuss the crossing symmetric $\eta_{\ell 3}^{(\prime)}$ decays, $\eta^{(\prime)} \to \pi^+ \ell^- \bar{\nu}_\ell \, (\ell = e, \mu)$, for which $\mathcal{BR}$ predictions will be given as well. Finally, we present our conclusions in Section 9.

5.1 Hadronic matrix element and decay width

The amplitude of the decay $\tau^- \to \pi^- \eta^{(\prime)} \nu_\tau$ in terms of the hadronic matrix element reads

$$\mathcal{M} = \frac{G_F}{\sqrt{2}} V_{ud} \bar{u}(p_{\nu_\tau}) \gamma_\mu (1 - \gamma_5) u(p_\tau) \langle \pi^- \eta^{(\prime)} | \bar{d} \gamma^\mu u | 0 \rangle \; , \tag{5.1}$$

where the $\pi^- \eta^{(\prime)}$ matrix element of the vector current follows the convention of Ref. [121],

$$\langle \pi^- \eta^{(\prime)} | \bar{d} \gamma^\mu u | 0 \rangle = c_{\pi^- \eta^{(\prime)}}^V \left[(p_{\eta^{(\prime)}} - p_{\pi^-})^\mu F_+^{\pi^- \eta^{(\prime)}}(s) - (p_{\eta^{(\prime)}} + p_{\pi^-})^\mu F_-^{\pi^- \eta^{(\prime)}}(s) \right] \; , \tag{5.2}$$

with $c_{\pi^- \eta^{(\prime)}}^V = \sqrt{2}$, $s = q^2 = (p_{\eta^{(\prime)}} + p_{\pi^-})^2$ and $F_{+(-)}^{\pi^- \eta^{(\prime)}}(s)$ the two Lorentz-invariant vector form factors. However, instead of $F_-^{\pi^- \eta^{(\prime)}}(s)$, the scalar form factor $F_0^{\pi^- \eta^{(\prime)}}(s)$ is usually employed, which arises as a consequence of the non-conservation of the vector current. That is, taking the divergence on the left-hand side of Eq. (5.2) we get

$$\langle \pi^- \eta^{(\prime)} | \partial_\mu (\bar{d} \gamma^\mu u) | 0 \rangle = i(m_d - m_u) \langle \pi^- \eta^{(\prime)} | \bar{d} u | 0 \rangle \equiv i \Delta_{K^0 K^+}^{\mathrm{QCD}} c_{\pi^- \eta^{(\prime)}}^S F_0^{\pi^- \eta^{(\prime)}}(s) \; , \tag{5.3}$$

with $c_{\pi^- \eta}^S = \sqrt{2/3}$, $c_{\pi^- \eta'}^S = 2/\sqrt{3}$ and $\Delta_{PQ} = m_P^2 - m_Q^2$, while on the right-hand side we have

$$iq_\mu \langle \pi^- \eta^{(\prime)} | \bar{d} \gamma^\mu u | 0 \rangle = i c_{\pi^- \eta^{(\prime)}}^V \left[(m_{\eta^{(\prime)}}^2 - m_{\pi^-}^2) F_+^{\pi^- \eta^{(\prime)}}(s) - s F_-^{\pi^- \eta^{(\prime)}}(s) \right] \; . \tag{5.4}$$

Then, by equating Eqs. (5.3) and (5.4), we link $F_-^{\pi^- \eta^{(\prime)}}(s)$ with $F_0^{\pi^- \eta^{(\prime)}}(s)$ through

$$F_-^{\pi \eta^{(\prime)}}(s) = -\frac{\Delta_{\pi^- \eta^{(\prime)}}}{s} \left[\frac{c_{\pi \eta^{(\prime)}}^S}{c_{\pi \eta^{(\prime)}}^V} \frac{\Delta_{K^0 K^+}^{\mathrm{QCD}}}{\Delta_{\pi^- \eta^{(\prime)}}} F_0^{\pi \eta^{(\prime)}}(s) + F_+^{\pi^- \eta^{(\prime)}}(s) \right] \; , \tag{5.5}$$

and the hadronic matrix element finally reads

$$\langle \pi^- \eta^{(\prime)} | \bar{d} \gamma^\mu u | 0 \rangle = c_{\pi\eta^{(\prime)}}^V \left[(p_{\eta^{(\prime)}} - p_\pi)^\mu + \frac{\Delta_{\pi^-\eta^{(\prime)}}}{s} q^\mu \right] F_+^{\pi\eta^{(\prime)}}(s) \\ + c_{\pi^-\eta^{(\prime)}}^S \frac{\Delta_{K^0 K^+}^{\text{QCD}}}{s} q^\mu F_0^{\pi^-\eta^{(\prime)}}(s) \ . \tag{5.6}$$

The advantage of the parameterization as given in Eq. (5.6) is that the vector(scalar) form factor $F_{+(0)}^{\pi^-\eta^{(\prime)}}(s)$ is in direct correspondence with the final $P(S)$-wave state, respectively. Moreover, the finiteness of the matrix element at the origin imposes[1]

$$F_+^{\pi^-\eta^{(\prime)}}(0) = -\frac{c_{\pi^-\eta^{(\prime)}}^S}{c_{\pi^-\eta^{(\prime)}}^V} \frac{\Delta_{K^0 K^+}^{\text{QCD}}}{\Delta_{\pi^-\eta^{(\prime)}}} F_0^{\pi^-\eta^{(\prime)}}(0) \ . \tag{5.7}$$

Therefore, the differential decay width of the $\tau^- \to \pi^- \eta^{(\prime)} \nu_\tau$ decay as a function of the invariant mass of the $\pi^- \eta^{(\prime)}$ system can be written as

$$\frac{d\Gamma\left(\tau^- \to \pi^- \eta^{(\prime)} \nu_\tau\right)}{d\sqrt{s}} = \frac{G_F^2 M_\tau^3}{24\pi^3 s} S_{\text{EW}} |V_{ud} F_+^{\pi^-\eta^{(\prime)}}(0)|^2 \left(1 - \frac{s}{M_\tau^2}\right)^2 \\ \times \left[\left(1 + \frac{2s}{M_\tau^2}\right) q_{\pi^-\eta^{(\prime)}}^3(s) |\widetilde{F}_+^{\pi^-\eta^{(\prime)}}(s)|^2 + \frac{3\Delta_{\pi^-\eta^{(\prime)}}^2}{4s} q_{\pi^-\eta^{(\prime)}}(s) |\widetilde{F}_0^{\pi^-\eta^{(\prime)}}(s)|^2 \right] , \tag{5.8}$$

where $q_{PQ}(s) = \sqrt{s^2 - 2s\Sigma_{PQ} + \Delta_{PQ}^2}/2\sqrt{s}$, $\Sigma_{PQ} = m_P^2 + m_Q^2$ and

$$\widetilde{F}_{+,0}^{\pi^-\eta^{(\prime)}}(s) = \frac{F_{+,0}^{\pi^-\eta^{(\prime)}}(s)}{F_{+,0}^{\pi^-\eta^{(\prime)}}(0)} \ , \tag{5.9}$$

are the two form factors normalised to unity at the origin. They encode the unknown strong dynamics occurring in the transition. Their descriptions will be given in Secs. 5.2 and 5.3, respectively. Regarding the global pre-factors, we employ $S_{\text{EW}} = 1.0201$ [122], accounting for short-distance electroweak corrections, and $V_{ud} = 0.97425(8)(10)(18)$ [37], while the normalisation $F_+^{\pi^-\eta^{(\prime)}}(0)$ is an isospin-violating quantity of $\mathcal{O}(m_d - m_u)$, whose value will be deduced in the next section, which brings an overall suppression explaining the smallness of the corresponding decay widths. In fact, in the limit of exact isospin, $m_u = m_d$ and $e = 0$, $F_+^{\pi^-\eta^{(\prime)}}(0) = 0$ and these processes would be forbidden in the SM.

---

[1]We will come back to Eq. (5.7) in Sect. 5.2 in order to derive our isospin violating input values.

5.2 $\pi^- \eta^{(\prime)}$ Vector Form Factor

We derive the $\pi^- \eta^{(\prime)}$ vector form factor within the context of resonance chiral theory (RChT) [48], which extends chiral perturbation theory [5, 6, 7] by adding resonances as explicit degrees of freedom. A short introduction to the topic can be found in Ref. [168], where references concerning its varied phenomenological applications are given. In Refs. [13, 155] we have also provided a short review of the theory as applied to the computation of the vector and scalar $K^- \eta^{(\prime)}$ form factors describing the decays $\tau^- \to K^- \eta^{(\prime)} \nu_\tau$. In the present analysis, we would occasionally refer the interested reader to the former references though some comments will be given in the following for consistency.

It is not straightforward to incorporate the dynamics of the η and η' mesons in a chiral framework [169]. The pseudoscalar singlet η_0 is absent in $SU(3)$ ChPT and their effects are encoded in the next-to-leading order low-energy constant L_7. To take into account consistently the effects of the singlet in an explicit way one must perform a simultaneous expansion not only in terms of momenta (p^2) and quark masses (m_q) but also in the number of colors ($1/N_c$). In this framework, known as Large-N_c ChPT [8], the singlet becomes a ninth pseudo-Goldstone boson and the η-η' mixing can be understood in a perturbative manner[2]. At lowest order, the physical states (η, η') are related to the mathematical states (η_8, η_0) in the so-called octet-singlet basis by a simple two-dimensional rotation matrix involving one single mixing angle (cf. Eq. 1.116). At the same order, the four different decay constants related to the η-η' system are all equal to the pion decay constant in the chiral limit. At next-to-leading order, however, besides mass-matrix diagonalisation one requires to perform first a wave-function renormalisation of the fields due to the non-diagonal form of the kinetic term of the Lagrangian (cf. Eq. 1.128). This two-step procedure makes the single mixing angle at lowest order to be split in two mixing angles at next-to-leading order[3]. The magnitude of this splitting is given in the octet-singlet basis by the difference of the F_K and F_π decay constants, that is, a $SU(3)$-breaking correction [170]. At this order, now, the decay constants are all different due to these wave-function–renormalisation corrections. Being this two-mixing angle scheme unavoidable at next-to-leading order in the large-N_c chiral expansion, one can express their associated

---

[2]In this simultaneous expansion the chiral loops are counted as next-to-next-to-leading order corrections and thus considered negligible [8]. This fact is in part corroborated numerically.

[3]For a detailed explanation of the two-mixing angle scheme in the large-N_c ChPT at next-to-leading order in the octet-singlet basis, see, for instance, the appendix B in Ref. [69]. Other comprehensive reviews using this basis or the so-called quark-flavour basis can be found in Refs. [169].

parameters either in the form of two mixing angles (θ_8, θ_0) and two decay constants (f_8, f_0) or one mixing angle, the one appearing at lowest order, and three wave-function–renormalisation corrections, appearing only at next-to-leading order. In this work, we will follow the second option (cf. Eq. 1.138). Needless to say, the mixing so far involves only the η and $\eta^\prime$ mesons in the isospin limit, but if isospin symmetry is broken, as it is our case, the π^0 is also involved, and instead of using one mixing angle and three wave-function–renormalisation corrections we will need to use three lowest order mixing angles, $\theta_{\eta\eta^\prime}$ for the η-$\eta^\prime$, $\theta_{\pi\eta}$ for the π-η and $\theta_{\pi\eta^\prime}$ for the π-$\eta^\prime$ systems, respectively, and the corresponding six wave-function–renormalisation corrections. Since we are in the context of RChT, these wave-function–renormalisation corrections are assumed to be saturated by the exchange of a nonet of scalar resonances and therefore expressed in terms of the associated c_d and c_m coupling constants (see below).

Because the size of isospin-breaking corrections due to the light-quark mass difference are given in terms of the ratio $(m_d - m_u)/m_s$ and hence very small, the two former mixing angles involving the π^0 can be well approximated by their Taylor expansion at first order. Then, the orthogonal matrix connecting the mathematical and physical states at lowest order can be written as

$$\begin{pmatrix} \pi^0 \\ \eta \\ \eta^\prime \end{pmatrix} = \begin{pmatrix} 1 & \varepsilon_{\pi\eta}\mathrm{c}\theta_{\eta\eta^\prime} + \varepsilon_{\pi\eta^\prime}\mathrm{s}\theta_{\eta\eta^\prime} & \varepsilon_{\pi\eta^\prime}\mathrm{c}\theta_{\eta\eta^\prime} - \varepsilon_{\pi\eta}\mathrm{s}\theta_{\eta\eta^\prime} \\ -\varepsilon_{\pi\eta} & \mathrm{c}\theta_{\eta\eta^\prime} & -\mathrm{s}\theta_{\eta\eta^\prime} \\ -\varepsilon_{\pi\eta^\prime} & \mathrm{s}\theta_{\eta\eta^\prime} & \mathrm{c}\theta_{\eta\eta^\prime} \end{pmatrix} \cdot \begin{pmatrix} \pi_3 \\ \eta_8 \\ \eta_0 \end{pmatrix} , \quad (5.10)$$

where $\varepsilon_{\pi\eta^{(\prime)}}$ are the approximated π^0-$\eta^{(\prime)}$ mixing angles and $(\mathrm{c}, \mathrm{s}) \equiv (\cos, \sin)$. Using this parametrization for the rotation matrix, we preserve the common η-$\eta^\prime$ mixing description, when both $\varepsilon_{\pi\eta^{(\prime)}}$ are fixed to 0, and the one for π-$\eta^{(\prime)}$ mixing, when both $\theta_{\eta\eta^\prime}$ and $\varepsilon_{\pi\eta^{\prime()}}$ are set to 0. A detailed illustration of this π^0-η-$\eta^\prime$ mixing can be found in Ref. [171], from where we borrow the numerical values $\hat\varepsilon_{\pi\eta} \equiv \varepsilon_{\pi\eta}(z = 0) = 0.017(2)$ and $\hat\varepsilon_{\pi\eta^\prime} \equiv \varepsilon_{\pi\eta^\prime}(z = 0) = 0.004(1)$ as a check of our results. For the η-$\eta^\prime$ mixing angle we take $\theta_{\eta\eta^\prime} = (-13.3 \pm 0.5)^\circ$ [172][4].

As stated before, the $\pi^-\eta^{(\prime)}$ VFFs will be calculated in the framework of RChT. There are four different types of contributions in total. At leading order, there is the contribution from the lowest order of large-N_c ChPT. At next-to-leading order, there are, in addition, the contribution from the exchange of explicit vector resonances, the so-called vacuum insertions and the wave-function–renormalisation contributions

---

[4]In Ref. [172], the value $\phi_{\eta\eta^\prime} = (41.4 \pm 0.5)^\circ$ is obtained in the quark-flavour basis. However, at lowest order, this value is equivalent in the octet-singlet basis to $\theta_{\eta\eta^\prime} = \phi_{\eta\eta^\prime} - \arctan\sqrt{2} = (-13.3 \pm 0.5)^\circ$.

(cf. Fig. 3.1). The latter two are written in terms of the explicit exchange of scalar resonances and seen to cancel each other [130]. As a result, we obtain

$$F_+^{\pi^-\eta^{(\prime)}}(s) = \varepsilon_{\pi\eta^{(\prime)}} \left(1 + \sum_V \frac{F_V G_V}{F^2} \frac{s}{M_V^2 - s} \right) , \qquad (5.11)$$

where the prefactor denotes it occurs via π^0-η-η' mixing and the parenthesis includes the direct contact term plus the exchange of an infinite number of vector resonances organized in nonets[5] (F_V and G_V are the two coupling constants of the Lagrangian of one nonet of vectors coupled to pseudoscalars, M_V the common nonet vector mass, and F the pion decay constant in the chiral limit).

Interestingly, the term in parenthesis appearing in Eq. (5.11) is nothing but what one would have obtained if the $\pi^-\pi^0$ VFF had been computed instead. Hence, written in this way, the $\pi^-\eta^{(\prime)}$ VFFs are given in terms of the well-known $\pi^-\pi^0$ VFF (see, for instance, Refs. [52, 97] for a review). Their value at the origin are $F_+^{\pi^-\eta^{(\prime)}}(0) = \varepsilon_{\pi\eta^{(\prime)}}$, and as a consequence the normalised form factors are both the same and equal to the normalised $\pi^-\pi^0$ one, that is

$$\widetilde{F}_+^{\pi^-\eta}(s) = \widetilde{F}_+^{\pi^-\eta'}(s) = \widetilde{F}_+^{\pi^-\pi^0}(s) . \qquad (5.12)$$

The above relation allows us to implement the well-known experimental data on the $\pi^-\pi^0$ VFF to describe the $\pi^-\eta^{(\prime)}$ decay modes we are interested in. In particular, we employ the latest experimental determination obtained by the Belle Collaboration from the measurement of the decay $\tau^- \to \pi^-\pi^0\nu_\tau$[6], which is shown in Fig. 5.1 (the set of data is borrowed from the Table VI of Ref. [19]). In this manner, we are not only taking into account the dominant vector resonant contribution given by the $\rho(770)$, whose effect is clearly seen from the neat peak around 0.6 GeV^2, but also the effects of higher radial excitations such as the $\rho'(1450)$ and $\rho''(1700)$ (see their manifestation in the form of a negative interference with the ρ in the energy region between 2 and 3 GeV^2). An interesting check would be then to compare these data with theoretical descriptions of this form factor, such as the ones given by dispersion relations, where the contributions of the different states can be switched on and off, to discern the number of participating resonances [97, 159].

---

[5]At leading order in $1/N_c$ at this stage, *i.e.*, with an infinite number of zero-width resonances [49].

[6]The contribution of the scalar form factor entering into the $\pi^-\pi^0$ decay mode is weighted by $\Delta_{\pi^-\pi^0}^2$, thus heavily suppressed by isospin [173] and usually neglected.
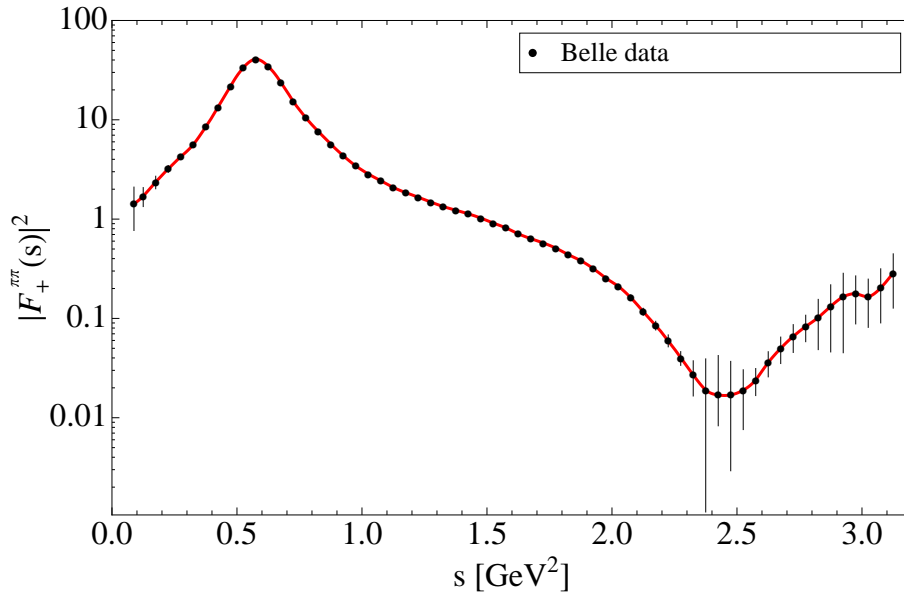
Figure 5.1: $\pi^-\pi^0$ vector form factor as obtained by the Belle Collaboration [19] (black circles). The red solid curve is an interpolation of these data.

5.3 $\pi^-\eta^{(\prime)}$ Scalar Form Factor

Any description of a physical observable involving light scalar mesons has been always controversial[7], and simple model parameterizations do not typically succeed. In this work, in order to construct a reasonable description of the participant scalar form factors we will basically exploit two powerful theoretical arguments: the required analytical structure of the form factor and the unitarity of the scattering matrix. In what follows, we will tackle three different parameterizations in increasing degree of completeness.

5.3.1 Breit-Wigner

Our initial approach for describing the required $\pi^-\eta^{(\prime)}$ scalar form factor (SFF) is, as in the case of the VFF, the RChT framework. In the large-N_c limit, the octet of scalar resonances and the singlet become degenerate in the chiral limit (with common mass M_S), and all them are collected in a nonet. The calculation of these SFFs is performed again at next-to-leading order in the simultaneous expansion in terms of momenta and the number of colors, and the different contributions to them are the lowest order one from large-N_c ChPT and the three next-to-leading order ones from RChT, which

---

[7]See *e.g.* the "Note on scalar mesons" in Ref. [37] for a review.

are, in order, the vacuum insertions, the explicit exchange of scalar resonances, and the wave-function–renormalisation contributions as shown in Fig. 5.2.
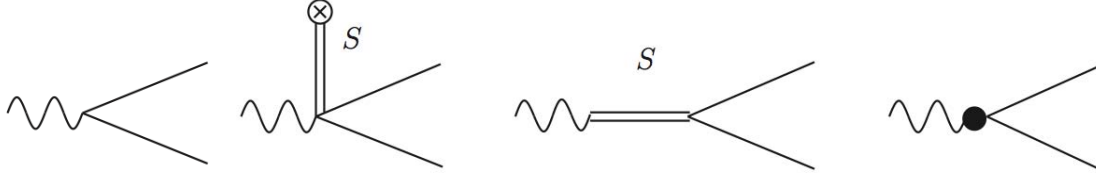
Figure 5.2:   Diagrams contributing for calculating the $\pi^- \eta^{(\prime)}$ scalar form factors. From left to right we have: contact term in χPT at lowest order; scalar resonance (S) exchange coupled to the vacuum; explicit exchange of scalar resonances, a_0 and excitations; $\mathcal{O}(p^4)$ contributions from the $\mathcal{O}(p^2)$ Lagrangian due to wave function and mass renormalizations.

The resulting SFFs are[8]

$$F_0^{\pi^- \eta^{(\prime)}}(s) = c_0^{\pi^- \eta^{(\prime)}} \left[1 - \frac{8 c_m (c_m - c_d)}{F^2} \frac{2 m_K^2 - m_\pi^2}{M_S^2} \right.$$
$$\left. + \frac{4 c_m}{F^2} \frac{(c_m - c_d) 2 m_\pi^2 + c_d \left(s + m_\pi^2 - m_{\eta^{(\prime)}}^2 \right)}{M_S^2 - s} \right] , \tag{5.13}$$

where $c_0^{\pi^- \eta} = \cos\theta_{\eta\eta'} - \sqrt{2}\sin\theta_{\eta\eta'}$ and $c_0^{\pi^- \eta'} = \cos\theta_{\eta\eta'} + \sin\theta_{\eta\eta'}/\sqrt{2}$ for the $\pi\eta$ and $\pi\eta'$ channels, respectively, and $c_{d(m)}$ are the couplings appearing in the derivative(mass) terms of the Lagrangian involving the nonets of scalar and pseudoscalar mesons. A similar analysis was done in Ref. [56] for the $K\pi$, $K\eta$ and $K\eta'$ SFFs. Once the QCD asymptotic behaviour of the form factors is imposed, that is, they are $\mathcal{O}(1/s)$ for large s, which implies $c_d - c_m = 0$ and $4 c_d c_m = F^2$, and hence $c_d = c_m = F/2$ [56], these can be finally written as [174]

$$F_0^{\pi^- \eta^{(\prime)}}(s) = c_0^{\pi^- \eta^{(\prime)}} \left(1 + \frac{\Delta_{\pi^- \eta^{(\prime)}}}{M_S^2} \right) \frac{M_S^2}{M_S^2 - s} , \tag{5.14}$$

and their value at the origin are

$$F_0^{\pi^- \eta^{(\prime)}}(0) = c_0^{\pi^- \eta^{(\prime)}} \left(1 + \frac{\Delta_{\pi^- \eta^{(\prime)}}}{M_S^2} \right) . \tag{5.15}$$

---

[8]As a starting point, we assume there is only a nonet of scalar resonances. Later on, we will include a second one. Moreover, we use in the calculation of the form factors isospin-averaged $\pi(K)$ masses $m_{\pi(K)}$ which will be in the following identified as their corresponding charged masses, being the differences higher-order isospin corrections.

These normalisations can now be incorporated into Eq. (5.7) to give a prediction of the normalisations of the related VFFs:

$$
\begin{aligned}
F_+^{\pi^- \eta}(0) &= -\frac{\cos\theta_{\eta\eta'} - \sqrt{2}\sin\theta_{\eta\eta'}}{\sqrt{3}} \frac{\Delta_{K^0 K^+}^{\mathrm{QCD}}}{\Delta_{\pi^- \eta}} \left(1 + \frac{\Delta_{\pi^- \eta}}{M_S^2}\right) \\
&= \cos\phi_{\eta\eta'} \frac{m_{K^0}^2 - m_{K^+}^2 - m_{\pi^0}^2 + m_{\pi^+}^2}{m_\eta^2 - m_{\pi^-}^2} \left(1 - \frac{m_\eta^2 - m_{\pi^-}^2}{M_S^2}\right),
\end{aligned}
\tag{5.16}
$$

and

$$
\begin{aligned}
F_+^{\pi^- \eta'}(0) &= -\frac{\sin\theta_{\eta\eta'} + \sqrt{2}\cos\theta_{\eta\eta'}}{\sqrt{3}} \frac{\Delta_{K^0 K^+}^{\mathrm{QCD}}}{\Delta_{\pi^- \eta'}} \left(1 + \frac{\Delta_{\pi^- \eta'}}{M_S^2}\right) \\
&= \sin\phi_{\eta\eta'} \frac{m_{K^0}^2 - m_{K^+}^2 - m_{\pi^0}^2 + m_{\pi^+}^2}{m_{\eta'}^2 - m_{\pi^-}^2} \left(1 - \frac{m_{\eta'}^2 - m_{\pi^-}^2}{M_S^2}\right),
\end{aligned}
\tag{5.17}
$$

where the η-η' mixing has been expressed for simplicity in the quark-flavour basis, $\cos\phi_{\eta\eta'} = (\cos\theta_{\eta\eta'} - \sqrt{2}\sin\theta_{\eta\eta'})/\sqrt{3}$ and $\sin\phi_{\eta\eta'} = (\sin\theta_{\eta\eta'} + \sqrt{2}\cos\theta_{\eta\eta'})/\sqrt{3}$, and $\Delta_{K^0 K^+}^{\mathrm{QCD}} = m_{K^0}^2 - m_{K^+}^2 - \Delta m_{K\,\mathrm{elm}}^2 = m_{K^0}^2 - m_{K^+}^2 - m_{\pi^0}^2 + m_{\pi^+}^2$ has been estimated from the K^0-K^+ mass difference corrected for mass contributions of electromagnetic origin according to Dashen's theorem [175, 176]. Comparing these VFFs normalitzations with those obtained after Eq. (5.11), one finally gets

$$
\varepsilon_{\pi\eta^{(\prime)}} = \cos\phi_{\eta\eta'}(\sin\phi_{\eta\eta'}) \frac{m_{K^0}^2 - m_{K^+}^2 - m_{\pi^0}^2 + m_{\pi^+}^2}{m_{\eta^{(\prime)}}^2 - m_{\pi^-}^2} \left(1 - \frac{m_{\eta^{(\prime)}}^2 - m_{\pi^-}^2}{M_S^2}\right), \tag{5.18}
$$

for the $\pi\eta$ and $\pi\eta'$ cases, respectively. It is worth noticing that the former equation is equivalent up to higher-order isospin corrections to Eq. (31) in Ref. [171] after the identification $z \equiv (f_u - f_d)/(f_u + f_d) = -(m_{K^0}^2 - m_{K^+}^2 - m_{\pi^0}^2 + m_{\pi^+}^2)/M_S^2$. The former equality allows for an estimate of this parameter, $z \simeq -5 \times 10^{-3}$ for $M_S = 980$ MeV, in agreement with the conclusion in Ref. [171] that $z < 0.015$. From Eq. (5.18), we can also provide the numerical determination of the $\pi\eta^{(\prime)}$ mixing angles we are employ in this work, $\varepsilon_{\pi\eta} = (9.8 \pm 0.3) \times 10^{-3}$ and $\varepsilon_{\pi\eta'} = (2.5 \pm 1.5) \times 10^{-4}$, which are far, specially in the latter case, from their infinite scalar mass limit, $\hat{\varepsilon}_{\pi\eta} \equiv \varepsilon_{\pi\eta}(M_S \to \infty) = 0.014$ and $\hat{\varepsilon}_{\pi\eta'} \equiv \varepsilon_{\pi\eta'}(M_S \to \infty) = 0.0038$, in accordance with Ref. [177]. These values were calculated using $\phi_{\eta\eta'} = (41.4 \pm 0.5)°$ [172]. As seen, $\varepsilon_{\pi\eta'}$ is one order of magnitude smaller than $\hat{\varepsilon}_{\pi\eta'}$ caused by the strong suppression due to $m_{\eta'} \simeq M_S$.

The description of the SFFs in the form of Eq. (5.14) begins to fail in the vicinity of the resonance region. It breaks down for $s = M_S^2$ which corresponds to an on-shell intermediate scalar resonance. A common and simple way to cure this limitation is

by promoting the scalar propagator $1/(M_S^2 - s)$ to $1/(M_S^2 - s - iM_S\Gamma_S(s))$, where the corresponding energy-dependent width computed within RChT in this case reads

$$\Gamma_S(s) = \Gamma_S(M_S^2) \left(\frac{s}{M_S^2}\right)^{3/2} \frac{h(s)}{h(M_S^2)} \ , \tag{5.19}$$

with ($\sigma_{PQ}(s) = 2q_{PQ}(s)/\sqrt{s} \times \Theta(s - (m_P + m_Q)^2)$ is a kinematical factor)

$$
\begin{aligned}
h(s) = {} & \sigma_{K^- K^0}(s) + 2\cos^2\phi_{\eta\eta'} \left(1 + \frac{\Delta_{\pi^- \eta}}{s}\right)^2 \sigma_{\pi^- \eta}(s) \\
& + 2\sin^2\phi_{\eta\eta'} \left(1 + \frac{\Delta_{\pi^- \eta'}}{s}\right)^2 \sigma_{\pi^- \eta'}(s) \ ,
\end{aligned}
\tag{5.20}
$$

for the $a_0(980)$ resonance case coupling dominantly to the $\pi\eta$ system[9]. In this way, we have incorporated into our description some elastic and inelastic unitarity corrections through resumming the imaginary part of the $\pi^- \eta^{(\prime)}$ and $K^- K^0$ self-energy loop insertions into the propagator, accounting for rescattering effects of the final state hadrons. Nonetheless, this description is not strictly unitary neither in its elastic form (since we have accommodated inelasticities into the description) nor in an inelastic fashion which would require to couple the channels in a more elaborated way. In addition, this description is neither fully analytic in the sense that the real part of the loop functions has been neglected. Usually, this option, known as the Breit-Wigner (BW) representation, is widely used in the literature even though it might not be an appropriate choice for describing data (as we have pointed out in Refs. [13, 179]). Notwithstanding, we have considered interesting to discuss it as a starting point. Using the values $M_S = (980 \pm 20)$ MeV and $\Gamma_S = (75 \pm 25)$ MeV [37] for the BW-mass and -width of the $a_0(980)$ resonance, the SFFs at the origin, see Eq. (5.15), are predicted to be $F_0^{\pi\eta}(0) = 0.92 \pm 0.02$ and $F_0^{\pi\eta'}(0) = 0.05 \pm 0.03$, respectively. Once these normalisations are taken into account, the resulting normalised SFFs are identical in the RChT framework, that is, $\widetilde{F}_0^{\pi^- \eta}(s) = \widetilde{F}_0^{\pi^- \eta'}(s)$. In Fig. 5.3, we provide their graphical account by considering $a_0(980)$ as the mediated scalar resonance.

The above description can be generalised to take into consideration further resonances with the same quantum numbers of the $a_0(980)$. In particular, we will also include the $a_0(1450)$ resonance whose effects, in spite of its mass, could be noticeable within the available phase space. For the same reason, however, no more resonances

---

[9]Current understanding favours that the meson multiplet including this resonance does not survive in the large-N_c limit (see e.g. Ref. [178]). However, since this Breit-Wigner–like model is only considered for illustrative purposes this fact will be ignored as it is usually done in this approach.
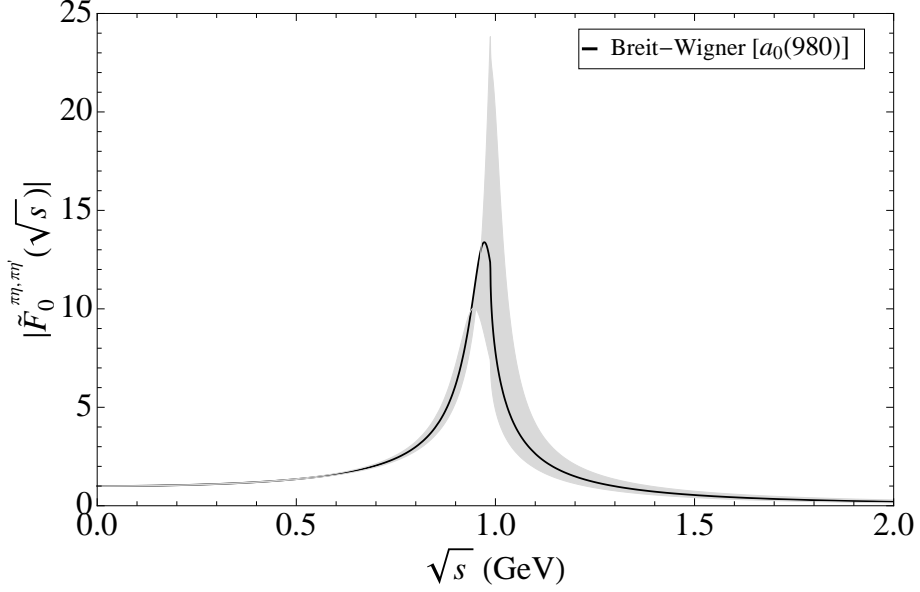
Figure 5.3: Normalised $\pi^-\eta^{(\prime)}$ scalar form factors as obtained from the Breit-Wigner approach described in Sec. 5.3.1. The gray error band accounts for the (uncorrelated) uncertainty on the mass and width of the $a_0(980)$ resonance.

will be considered henceforth. The SFFs in the framework of RChT including two resonances then read as

$$
F_0^{\pi^-\eta^{(\prime)}}(s) = c_0^{\pi^-\eta^{(\prime)}}
$$

$$
\times \left[1 - \frac{8c_m(c_m - c_d)}{F^2} \frac{2m_K^2 - m_\pi^2}{M_S^2} + \frac{4c_m}{F^2} \frac{(c_m - c_d)2m_\pi^2 + c_d\left(s + m_\pi^2 - m_{\eta^{(\prime)}}^2\right)}{M_S^2 - s} \right.
$$

$$
\left. - \frac{8c_m'(c_m' - c_d')}{F^2} \frac{2m_K^2 - m_\pi^2}{M_{S'}^2} + \frac{4c_m'}{F^2} \frac{(c_m' - c_d')2m_\pi^2 + c_d'\left(s + m_\pi^2 - m_{\eta^{(\prime)}}^2\right)}{M_{S'}^2 - s} \right],
$$

$$(5.21)$$

where S and S' correspond to the $a_0(980)$ and $a_0(1450)$ resonances, respectively. The short-distance requirement that the form factors go to zero for $s \to \infty$ then implies the constraints [56]:

$$
4c_d c_m + 4c_m' c_d' = F^2 , \qquad \frac{c_m}{M_S^2}(c_m - c_d) + \frac{c_m'}{M_{S'}^2}(c_m' - c_d') = 0 . \tag{5.22}
$$

Not so much is known on the exact values of the couplings $c_{d,m}'$ (and, to some extent, on $c_{d,m}$). The estimate with only one scalar resonance led to $c_d = c_m$ and thus it seems plausible to keep this constraint in the case of two resonances. One immediate consequence of the constraint and the second relation in Eq. (5.22) is $c_d' = c_m'$. Then,
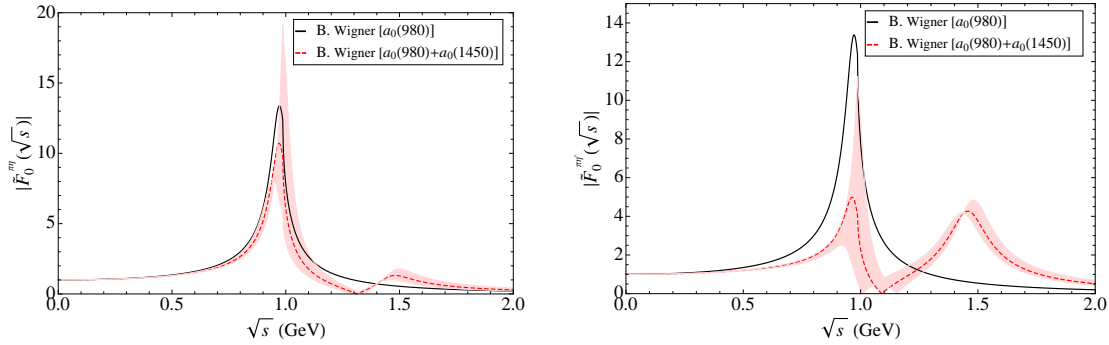
Figure 5.4: Normalised $\pi^- \eta^{(\prime)}$ (left plot) and $\pi^- \eta'$ (right plot) scalar form factors as obtained from the Breit-Wigner approach described in Sec. 5.3.1 including two resonances (red dashed curves) or a single resonance (solid black curves). The red error bands account for the (uncorrelated) uncertainty on the mass and width of the $a_0(980)$ and $a_0(1450)$ resonances.

the SFFs can be expressed, with c_m and c'_m fulfilling $c_m^2 + c_m'^2 = F^2/4$, as

$$F_0^{\pi^-\eta^{(\prime)}}(s) = c_0^{\pi^-\eta^{(\prime)}} \left[1 + \frac{4}{F^2} \left(\frac{c_m^2}{M_S^2 - s} + \frac{c_m'^2}{M_{S'}^2 - s} \right) \left(s + m_\pi^2 - m_{\eta^{(\prime)}}^2 \right) \right]$$

$$\longrightarrow \frac{c_0^{\pi^-\eta^{(\prime)}}}{\left(M_S^2 - s - iM_S\Gamma_S(s) \right) \left(M_{S'}^2 - s - iM_{S'}\Gamma_{S'}(s) \right)} \left\{ \left(M_S^2 - s \right) \left(M_{S'}^2 - s \right) \quad (5.23) \right.$$

$$\left. + \frac{4}{F^2} \left[c_m^2 \left(M_{S'}^2 - s \right) + c_m'^2 \left(M_S^2 - s \right) \right] \left(s + m_\pi^2 - m_{\eta^{(\prime)}}^2 \right) \right\},$$

once the energy-dependent widths have been incorporated into the scalar propagators. Regarding the numerical values, we employ $c_m = 41.9$ MeV [58] for the scalar coupling, and $M_{S'} = (1474 \pm 19)$ MeV and $\Gamma_{S'} = (265 \pm 13)$ MeV [37] for the $a_0(1450)$ mass and width, respectively. In Fig. 5.4, the normalised $\pi\eta^{(\prime)}$ SFFs obtained from Eq. (5.23) in the approximation of considering two resonances are shown and compared with the single-resonance case. Notice now that the normalised expressions depend on the mode. While in the $\pi\eta$ case, one clearly sees a dominant peak corresponding to the $a_0(980)$ followed by a second smaller one in association with the $a_0(1450)$, in the $\pi\eta^{(\prime)}$ case, two similar peaks located around both resonances are found.

5.3.2 Elastic dispersion relation: Omnès integral

A two-meson form factor is an analytic function in the whole complex plane except for the branch cut originated as soon as the energy reaches the threshold for producing the first intermediate state where an imaginary part is then developed. The case in

which the intermediate states are exactly the same as the final one is known as elastic and the corresponding cut is called unitary or elastic cut. For the case that concerns us the associated cut starts at $s = (m_{\pi^-} + m_{\eta^{(\prime)}})^2$ and the corresponding (elastic) unitarity relation for the scalar form factor reads (cf. Eq. (2.27))

$$\mathrm{Im}F_0^{\pi^-\eta^{(\prime)}}(s) = \sigma_{\pi^-\eta^{(\prime)}}(s)F_0^{\pi^-\eta^{(\prime)}}(s)t_{1,0}^{\pi^-\eta^{(\prime)}*}(s)\,, \tag{5.24}$$

where $t_{1,0}^{\pi^-\eta^{(\prime)}}(s)$ is the unitarized elastic $\pi^-\eta^{(\prime)}$ partial wave of the scattering amplitude of $I = 1$ and $J = 0$ to be discussed later. Analyticity, which relates the real and the imaginary part of the form factor in Eq. (5.24), is ensured through the use of a dispersion relation which after some algebra leads to the well-known Omnès representation [79]. In the case where one subtraction is allowed, it reads (up to a polynomial ambiguity given by $P(s)$ Eq. (2.36))

$$F_0^{\pi^-\eta^{(\prime)}}(s) = P(s)\exp\left[\frac{s - s_0}{\pi}\int_{s_{th}}^{\infty}ds'\frac{\delta_{1,0}^{\pi^-\eta^{(\prime)}}(s')}{(s' - s_0)(s' - s - i\varepsilon)}\right]\,, \tag{5.25}$$

where s_0 is the subtraction point chosen at 0 in our analysis. The dispersive representation has been wide and successfully employed for describing lots of phenomena and in particular data on exclusive hadronic tau decays [13, 14, 15, 16, 97, 106, 159, 180]. Unfortunately, the $\pi^-\eta^{(\prime)}$ decay modes lack of any kind of experimental data either on the phase shifts or the decays spectra. However, in the elastic region Watson's final state theorem [78] states that the phase of the elastic scattering amplitude equals that of the corresponding form factor. Thus, we can access the form factor phase shift $\delta_{1,0}^{\pi^-\eta^{(\prime)}}(s)$ through the identification

$$\phi_{\pi^-\eta^{(\prime)}}(s) \equiv \delta_{1,0}^{\pi^-\eta^{(\prime)}}(s) = \arctan\frac{\mathrm{Im}t_{1,0}^{\pi^-\eta^{(\prime)}}(s)}{\mathrm{Re}t_{1,0}^{\pi^-\eta^{(\prime)}}(s)}\,. \tag{5.26}$$

Regarding the scattering amplitudes $\pi^-\eta \to \pi^-\eta$ and $\pi^-\eta' \to \pi^-\eta'$, we have considered convenient for our analysis to employ the expressions obtained within the global analysis of the $U(3) \otimes U(3)$ one-loop meson-meson scattering amplitudes in χPT including resonances, carried out in Ref. [57], to have better control on the input values of the theory (couplings, masses etc.). In that work, the partial wave amplitudes have been properly deduced and unitarized through the N/D method [181, 182], whose general simplified perturbative solution reads

$$t_{I,J}^{PQ}(s) = \frac{\sigma_{PQ}(s)N_{I,J}^{PQ}(s)}{\left(1 + g^{PQ}(s)N_{I,J}^{PQ}(s)\right)}\,, \tag{5.27}$$

and finally employed to fit the available scattering amplitudes' phaseshifts. In Eq. (5.27), PQ refers to the interacting meson-meson system in question, $g^{PQ}(s)$ are the dimeson one-loop scalar functions defined in Eq. (33) of Ref. [57] and $N_{I,J}^{PQ}(s)$ contains the expressions of the partial wave amplitudes up to $\mathcal{O}(p^4)$.

The polynomial ambiguity $P(s)$ in Eq. (5.25) needs to be fixed from theory. In principle, it could depend on s, but if the form factor is "well-behaved" at high-energies, that is $\lim_{s\to\infty} F_0(s) = 0$, it can be set to a constant. Our analysis confirms, *a posteriori*, that this is a good assumption. We have chosen it to be $F_0^{\pi^-\eta}(0) = 0.92$ and $F_0^{\pi^-\eta'}(0) = 0.05$ from Eq. (5.14) [10]. In Fig. 5.5 we represent the elastic SFFs obtained by employing Eq. (5.25) using the results from the updated analysis of Ref. [58] as input values here and hereafter by neglecting error correlations since we ignore them (specifically we are using the values in Eq. (45) of this reference). From the figure, we see a resonant region at around 1.4 GeV which may be attributed to the effect of the $a_0(1450)$. This presence and the absence of a corresponding peak for the $a_0(980)$ is explained because the former resonance appears in the s-channel of the scattering amplitude while the latter only in the crossed t and u channels.

It can be verified that the form factor can also be written in a closed expression as [56, 161, 183]

$$F_0^{\pi^-\eta^{(\prime)}}(s) = \prod \frac{1}{\left(1 - s/s_{z_j}\right)} \frac{F_0^{\pi^-\eta^{(\prime)}}(0)}{\left(1 + g^{\pi^-\eta^{(\prime)}}(s) N_{1,0}^{\pi^-\eta^{(\prime)}}(s)\right)}. \tag{5.28}$$

The s_{z_j} are the locations of the zeros of the inverse of the denominator function $D(s) = (1 + g^{\pi^-\eta^{(\prime)}}(s) N_{1,0}^{\pi^-\eta^{(\prime)}}(s))$ which have to be removed in the form factor. In our specific case, the zero is placed at $s_{z_1} = 1.9516$ GeV^2 corresponding to the bare (squared) mass of the scalar octet, S_8 [58]. As a consistency check, we have verified that the results obtained with Eq. (5.25) are reproduced using the closed expression from Eq. (5.28). Inspired by the works of Refs. [160, 161, 162, 163, 164, 165, 166, 130, 184, 185, 186, 187, 188], we propose to mimic the analogous expression of Eq. (5.28) for describing the coupled-channels case. In this respect, our closed form solution for the coupled-channels problem giving the participant scalar form factors (instead of the more common iterative solution of the coupled integro-differential set of equations) appears numerically advantageous for the Monte Carlo event generator performance [115] specially if our expressions are to be used for fitting the resonance parameters appearing in the SFFs. The method is detailed in the appendix D.

---

[10]These inputs could be checked with lattice QCD simulations incorporating isosping breaking.
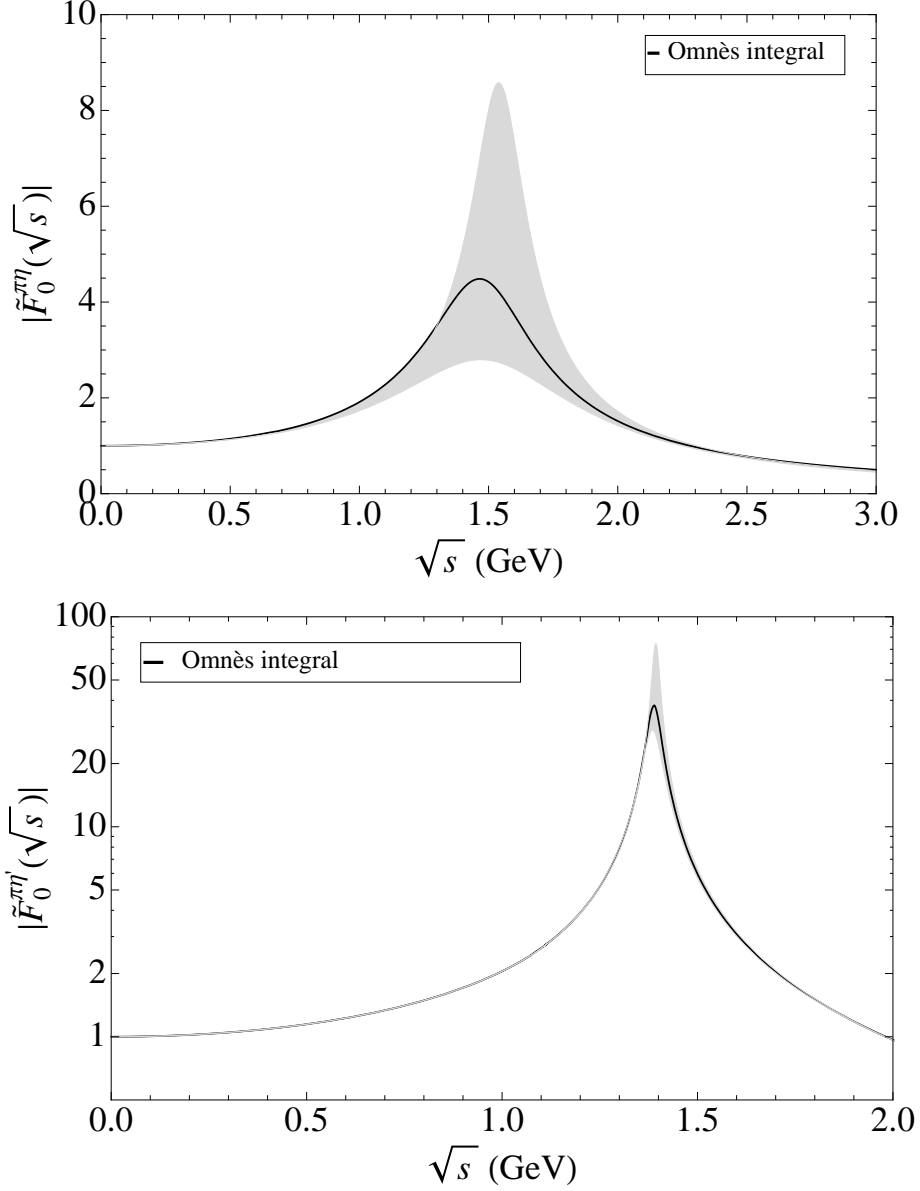
Figure 5.5: Scalar $\pi^-\eta$ (up) and $\pi^-\eta'$ (down) form factors considering elastic final-state interactions of the di-meson system as obtained from Eq. (5.25). The gray error bands account for the (uncorrelated) uncertainty on the input values from Ref. [58].

5.3.3 Two coupled channels

We first consider the two coupled channels case involving the $\pi^-\eta$ and $\pi^-\eta'$ cuts. The two-meson loop function and the required partial-wave scattering amplitudes are organized in symmetric matrices given, in this specific case, by

$$g(s) = \begin{pmatrix} g_{\pi^-\eta} & 0 \\ 0 & g_{\pi^-\eta'} \end{pmatrix}, \qquad N_{1,0}(s) = \begin{pmatrix} N_{\pi^-\eta\to\pi^-\eta} & N_{\pi^-\eta\to\pi^-\eta'} \\ N_{\pi^-\eta'\to\pi^-\eta} & N_{\pi^-\eta'\to\pi^-\eta'} \end{pmatrix}, \qquad (5.29)$$

where each entry of the matrix $N(s)$ (omitting the I, J quantum numbers) reads $N_{ij}(s) = T_{ij}^{\mathcal{O}(p^4)}(s) - g_i(s)\left(T_{ij}^{\mathcal{O}(p^2)}(s)\right)^2$ $(i, j = 1, 2)$ with $T_{ij}^{\mathcal{O}(p^4)}(s)$ referring to the corresponding partial wave amplitude at $\mathcal{O}(p^4)$ which includes the $\mathcal{O}(p^2)$ term, $\mathcal{O}(p^4)$ contributions arising from wave-function renormalization of the fields and, finally, the explicit $\mathcal{O}(p^4)$ resonance exchange and one-loop diagrams in the s as well as in the crossed t and u channels. Written in this way, we avoid double counting of loop contributions in the s-channel. For sake of clarity, Eq. (D.18) applied to this particular case would read

$$
\begin{pmatrix} F_0^{\pi^-\eta}(s) \\ F_0^{\pi^-\eta'}(s) \end{pmatrix} = \frac{1}{\text{Det}[\text{D}_{\text{IJ}}(\text{s})]} \times \tag{5.30}
$$
$$
\begin{pmatrix} 1 + g_{\pi^-\eta'}(s)N_{\pi^-\eta'\to\pi^-\eta'}(s) & -g_{\pi^-\eta}(s)N_{\pi^-\eta\to\pi^-\eta'}(s) \\ -g_{\pi^-\eta'}(s)N_{\pi^-\eta'\to\pi^-\eta}(s) & 1 + g_{\pi^-\eta}(s)N_{\pi^-\eta\to\pi^-\eta}(s) \end{pmatrix} \begin{pmatrix} 1 & 0 \\ 0 & 1 \end{pmatrix} \begin{pmatrix} F_0^{\pi^-\eta}(0) \\ F_0^{\pi^-\eta'}(0) \end{pmatrix},
$$

where we have considered the subtraction point to be $s_0 = 0$ for simplicity and in analogy with Refs. [14, 13, 16] where it appeared to be a good choice. The matrix $D_{IJ}(s)$ entering Eq. (5.30) is defined in Eq. (D.19) of appendix D whose determinant, $\text{Det}[\text{D}_{\text{IJ}}(\text{s})]$, may vanish for some values of s. We get rid of these possible zeros by factorizing them in the matrix $D_{IJ}(s)$ as has already been done in Eq. (5.28) for the single-channel elastic case. In this manner, these singularities can be seen as dynamically generated resonances from the matrix $D_{IJ}(s)$ after the rescattering of the pseudoscalars. In our particular case, $\text{Det}[\text{D}_{\text{IJ}}(\text{s})]$ vanishes, again, at $s_{z_1} = 1.9516$ GeV^2 for the same reason given for the single elastic case.

Regarding the input values at the origin of energies, their values are not precisely known and for our study we have employed $F_0^{\pi\eta}(0) = 0.92$ and $F_0^{\pi\eta'}(0) = 0.05$ as obtained from Eq. (5.14). These values, since need to be fixed from external theoretical arguments, enter as a source of model-dependency (see [10]). In Fig. 5.6 we show the results of solving Eq. (5.30) for the $\pi^-\eta$ SFF coupled to $\pi^-\eta'$ and *viceversa* (red dashed curves), compared to the respective elastic cases (black lines). On the upper plot of Fig. 5.6 it is seen that the $\pi^-\eta$ scalar form factor coupled to $\pi\eta'$ develops a thin peak at around 1.4 GeV followed by a hard drop. We can also observe that, in general terms, the neat effect of coupling the $\pi^-\eta'$ channel on the $\pi^-\eta$ SFF is small. On the contrary, the impact of the $\pi^-\eta$ cut onto the description of the $\pi^-\eta'$ SFF is large as one can see from the down panel of Fig. 5.6 where, in this case, the resonance region is highly enhanced. One interesting thing to notice is that the coupled-channels effects start, respectively, at the $\pi^-\eta$ and $\pi^-\eta'$ thresholds and if these inelasticities are switched off, one would recover the elastic description.
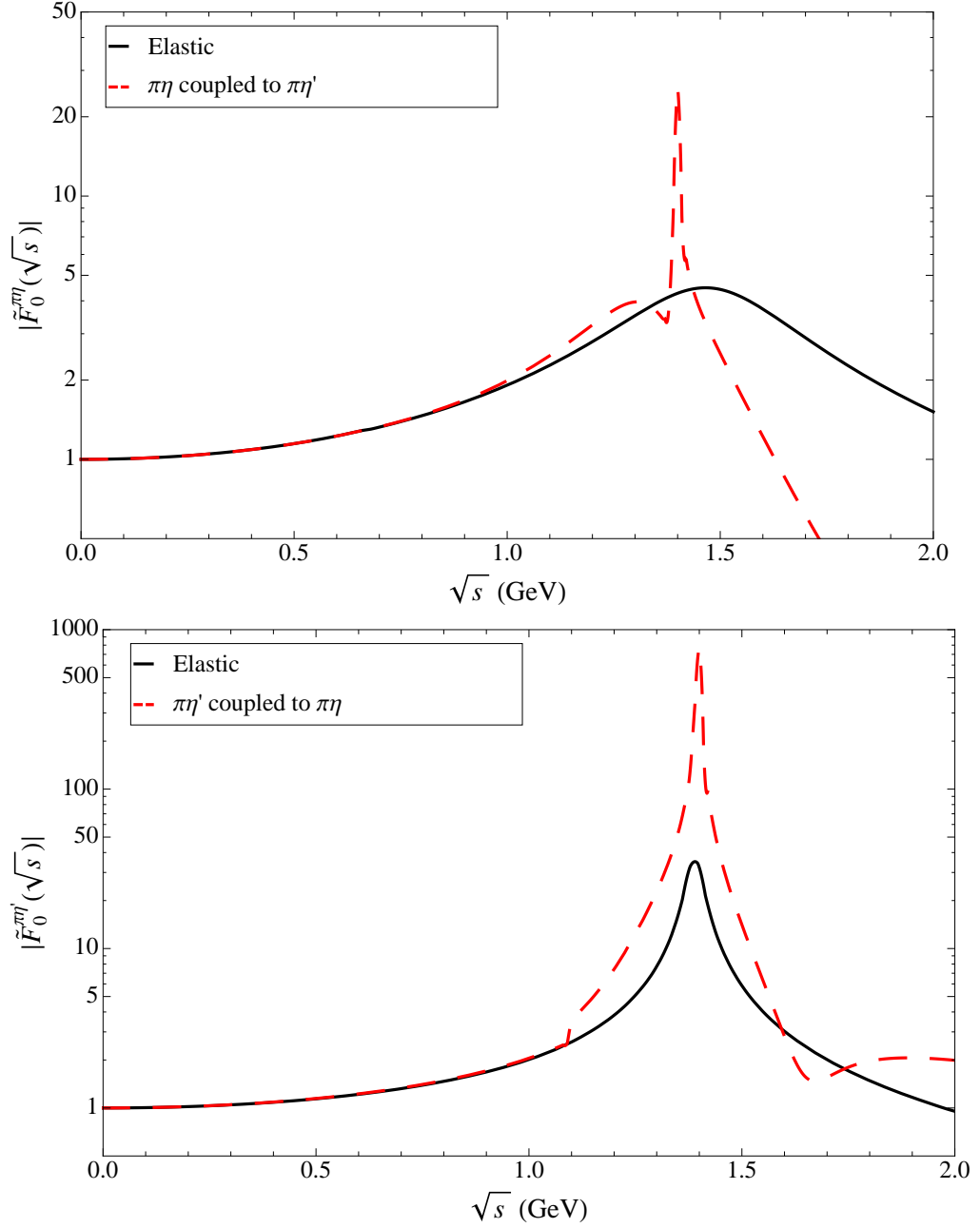
Figure 5.6: $\pi^-\eta$ SFF coupled to $\pi^-\eta'$ (up) and $\pi^-\eta'$ SFF coupled to $\pi^-\eta$ (down) as calculated from Eq. (5.30) (red dashed curves) compared to the corresponding elastic case (black solid curve). All the expressions are normalized to unity at the origin.

Analogously, we play the same game by considering the K^-K^0 cut which is located between $\pi^-\eta$ and $\pi^-\eta'$. *A priori* one may expect the intermediate $\bar{u}d$-like scalar to strongly couple to the K^-K^0 system [189]. One important thing we would like to emphasize is that the value at the origin of the energies of the K^-K^0 SFF, as

computed from RχT in analogy with Eq. (5.14) for $\pi^- \eta^{(\prime)}$, is $F_0^{K^- K^0}(0) = 1$ (this can be easily understood observing that the kaon mass difference is very small compared to the chiral symmetry breaking scale), and therefore its weight may be relevant. This is corroborated in Fig. 5.7, where we show the $\pi^- \eta^{(\prime)}$ SFF coupled to $K^- K^0$ (blue dotted curves in the up and down panels respectively). Notice that this time the effect on the $\pi^- \eta$ SFF is sizable. After a small dip at the $\pi \eta$ threshold, we see a small peak at the $K^- K^0$ threshold and a significant enhancement between $1.3 - 1.45$ GeV respect to the elastic case. This is one interesting result which may help to unveil the somehow "exotic" nature of scalar resonances which couple to the $\bar{u}d$ operator. Suggestions like tetraquark interpretation as well as molecular $K\bar{K}$ threshold states exist in literature [11].

5.3.4 Three coupled channels

Let us now turn to the case in which the $\pi^- \eta, K^- K^0$ and $\pi^- \eta'$ cuts are considered at the same time [12]. This requires to perform an evaluation where the three channels are coupled to each other. In this case, the matrices encoding the corresponding scalar loop function and partial-wave amplitudes read

$$g(s) = \begin{pmatrix} g_{\pi^- \eta} & 0 & 0 \\ 0 & g_{KK} & 0 \\ 0 & 0 & g_{\pi^- \eta'} \end{pmatrix}, \tag{5.31}$$

$$N_{1,0}(s) = \begin{pmatrix} N_{\pi^- \eta \to \pi^- \eta} & N_{\pi^- \eta \to \pi^- \eta'} & N_{\pi^- \eta \to K^- K^0} \\ N_{\pi^- \eta' \to \pi^- \eta} & N_{\pi^- \eta' \to \pi^- \eta'} & N_{\pi^- \eta' \to K^- K^0} \\ N_{K^- K^0 \to \pi^- \eta} & N_{K^- K^0 \to \pi^- \eta'} & N_{K^- K^0 \to K^- K^0} \end{pmatrix}. \tag{5.32}$$

From the corresponding analogous expression of Eq. (5.30) for three coupled channels (which now we do not explicitly quote), we obtain the $\pi^- \eta$ SFF coupled to $K^- K^0$ and $\pi^- \eta'$ as well as $\pi^- \eta'$ SFF coupled to $K^- K^0$ and $\pi^- \eta$. In Fig. 5.8 we provide a graphical account of these results (green dot-dashed curves) compared with all previous cases. In addition, we get the $K^- K^0$ SFF coupled to the $\pi^- \eta^{(\prime)}$ system as shown in Fig. 5.9. In the case of the $\pi \eta$ SFF, the three coupled channels solution follows closely the one obtained coupling $\pi \eta$ and KK cuts, except for the region between 1.2 and 1.3 GeV where a dip first appears. For the KK SFF, the three coupled channels solution resembles very much the KK coupling to $\pi \eta$ apart from

---

[11]See e.g. the note on scalar mesons at the PDG [37].

[12]The $\pi^- \pi^0$ cut is safely neglected, because no resonance contributions to this channel are allowed at first order in isospin breaking. However, its low-energy limit has been derived in Ref. [190] in a model-independent way because of its importance in producing a sizable CP-violating asymmetry in the di-pion tau decays, albeit only very close to the $\pi\pi$-threshold.
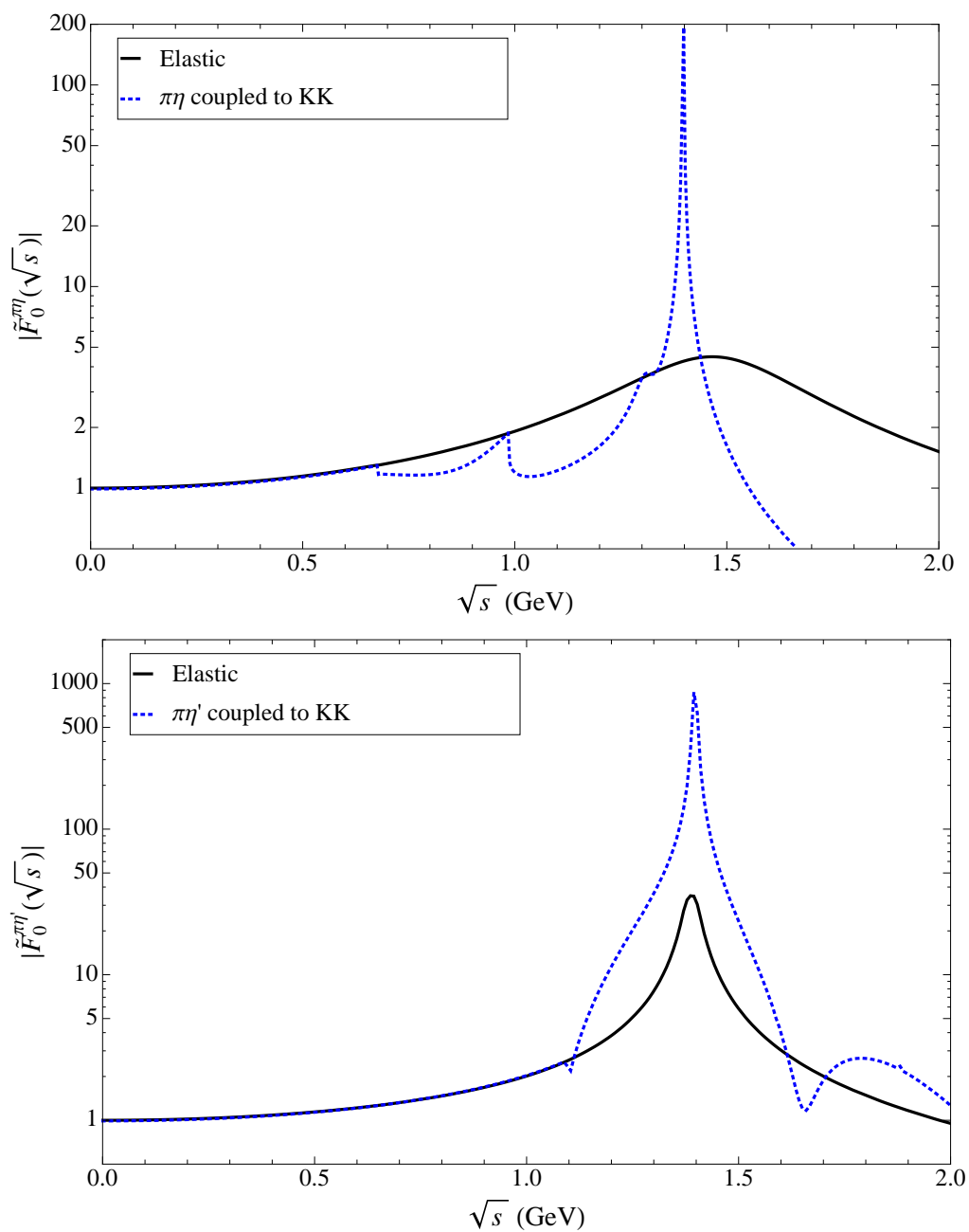
Figure 5.7: $\pi^-\eta$ (up) and $\pi^-\eta'$ (down) SFF coupled to K^-K^0 as calculated from Eq. (D.18) (blue dotted curves) compared to the corresponding elastic case (black solid curve). All the expressions are normalized to unity at the origin.

the 1.3 to 1.4 GeV region, where the peak in the two-channels case almost disappears in the three-channel solution. Finally, in the $\pi\eta'$ case, the three coupled channels solution does not appear to be significantly dominated by any of the two-channels results in the inelastic region.
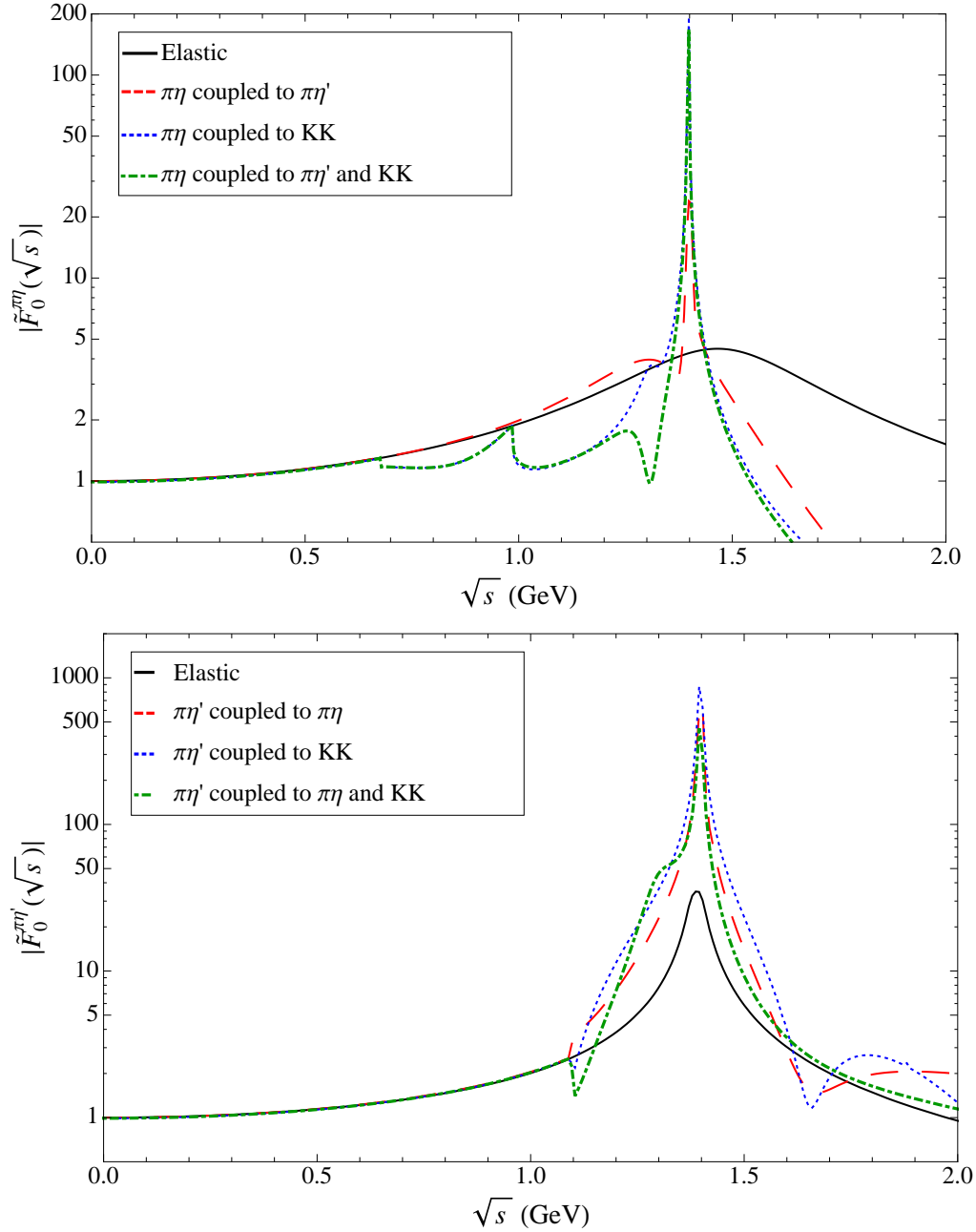
Figure 5.8: $\pi^- \eta$ SFF coupled to $K^- K^0$ and $\pi^- \eta'$ (up) and $\pi^- \eta'$ SFF coupled to $\pi^- \eta$ and $K^- K^0$ (right) as calculated from Eq. (D.18) (green dot-dashed curve) compared to both the elastic case (black solid curve) and to the two coupled-channels cases (red dashed and blue dotted curves). All the expressions are normalized to unity at the origin.

A last explanation is in order: the effect of the $\pi \eta^{(\prime)} \to \pi(\pi)\gamma$ channels should, in principle, be considered as well. The devoted discussion of these contributions in
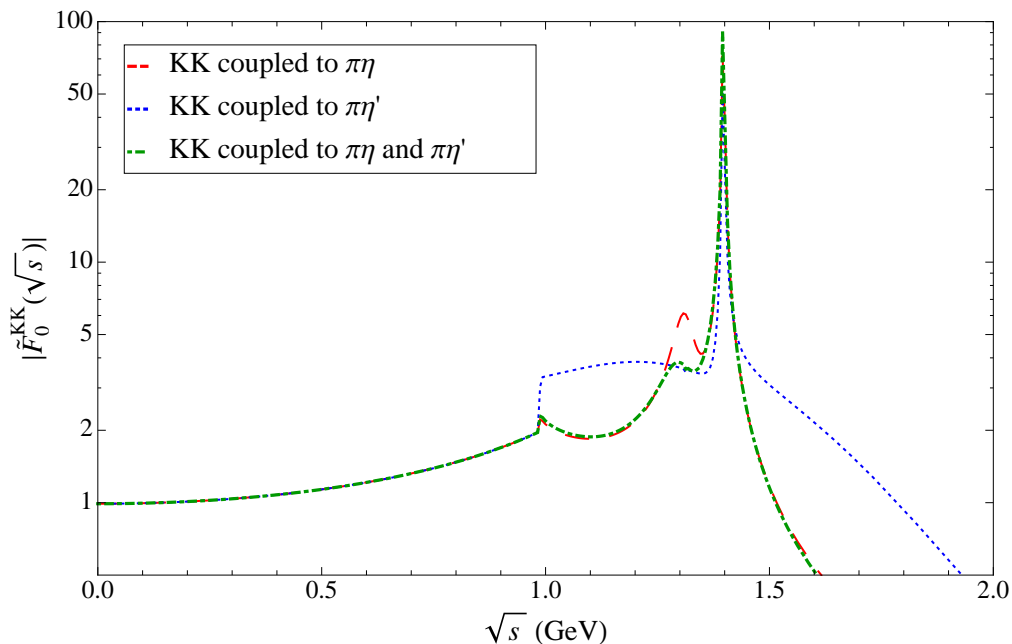
Figure 5.9: KK SFF coupled to $\pi^-\eta^{(\prime)}$ normalized to unity at the origin. The green dot-dashed curve refers to the three coupled-channels case while the red-dashed and blue-dotted curves refer to KK coupled to $\pi^-\eta$ and $\pi^-\eta'$, respectively.

Ref. [190] shows that either the subleading isospin breaking of the ρ contribution to the one-pion final state, or phase space considerations in the two-pion channel suppress enough these channels so as to neglect them given the current level of uncertainty.

5.4 Spectra and branching ratio predictions

5.4.1 $\tau^- \to \pi^-\eta\nu_\tau$

The vector and scalar form factors as described in Sections 5.2 and 5.3 finally enter Eq. (5.8) in order to predict the partial width of the decay $\tau^- \to \pi^-\eta\nu_\tau$. The corresponding distributions are plotted in Fig. 5.10 and the predicted branching ratios are given and compared with other authors results in Table 5.1. In the figure, we display the vector contribution alone (red dashed curve) as well as the full decay width distribution. The latter is shown in three different ways depending on the employment of the Breit-Wigner formula (blue dotted curve), the elastic Omnès formula (solid black curve), or the three coupled channels description (green dot-dashed curve) for the parameterization of the scalar form factor as presented in the main text.

On one hand, we can see that the low-energy region of the spectrum, which ranges

from the $\pi^-\eta$ threshold to 1 GeV, is mainly dominated by the vector contribution with a neatly visibly effect associated to the $\rho(770)$ resonance. Only in the case of the Breit-Wigner description of the SFF the low-energy region is instead dominated by the $a_0(980)$ scalar resonance whose manifestation is clearly seen at around 0.90 GeV, and then suppressed. On the other hand, the scalar contribution as obtained from a dispersion relation through the single channel Omnès integral, or from coupling three channels, dominates the energy region of the distribution above 1.2 GeV. For the elastic single channel case the distribution falls off smoothly, while a sizable peak at around 1.4 GeV appears if the three coupled channels description is employed. This peak appears due to considering the K^-K^0 intermediate state, and it is associated with the octet of the scalar multiplet, S_8, appearing in the resonance chiral lagrangian our work is based on, and may be attributed to the effect of the $a_0(1450)$ resonance. Also, in the upper part of the distribution, although suppressed, we can see the trace of other vector contributions, such as ρ' and ρ'', and the corresponding interferences among them.

We would like to note that our predictions respect the current experimental upper bounds as can be seen from the results presented in Table 5.1. From the table, we can also observe that our prediction for the vector contribution is quite in accordance with previous results while the scalar contributions show some scatter. The latter may be one interesting consequence of the effect of coupling channels for the parameterization of the scalar form factor. Our description is pretty sensitive to the isospin violating $\pi^0 - \eta$ mixing angle $\varepsilon_{\pi\eta} = 9.8(3) \cdot 10^{-3}$ whose error becomes an important source of uncertainty for our predictions together with the intrinsic error associated to the scalar form factor. The latter arise from the (uncorrelated) errors on the resonance parameters for the Breit-Wigner description and from the (uncorrelated) errors on the input values of Ref. [58] for the Omnès solution as explained in Section 5.3.2. On the contrary, it is very important to emphasize that for the coupled-channels description we do not provide an uncertainty associated to the SFF since our forced guess of uncorrelated parameters gives large uncertainties resulting in predictions compatible with zero [13]. This happens because our parameterization is rather sensitive to the value of the mass of the scalar resonance entering in s-channel, which appears moved away from the central value enhancing their contribution when trying to cover the

---

[13]In Ref. [190], it is pointed out that an uncertainty smaller than 20% in the $f_0^{\pi\eta}$ at 1 GeV would allow to improve the bounds on a charged Higgs obtained from $B \to \tau\nu_\tau$. The previous remark in the main text makes clear that this is not currently possible.

band within the uncertainty. Regarding the effect of the error from the measured $\pi^-\pi^0$ VFF on the $\pi^-\eta$ VFF, this is very tiny and hence neglected in our predictions.

Accurate predictions would demand precise values for $\varepsilon_{\pi\eta}$ and as soon as $\tau^- \to \pi^-\eta\nu_\tau$ becomes measured we will be in a position to infer the input values we have employed in our analysis ($\varepsilon_{\pi\eta}$, couplings, masses, $F_0^{\pi^-\eta^{(\prime)}}(0)$, etc.) from fitting data, check their consistency with the corresponding fit results of the global analysis of meson-meson scattering [57] and with [58], and present more accurate results.
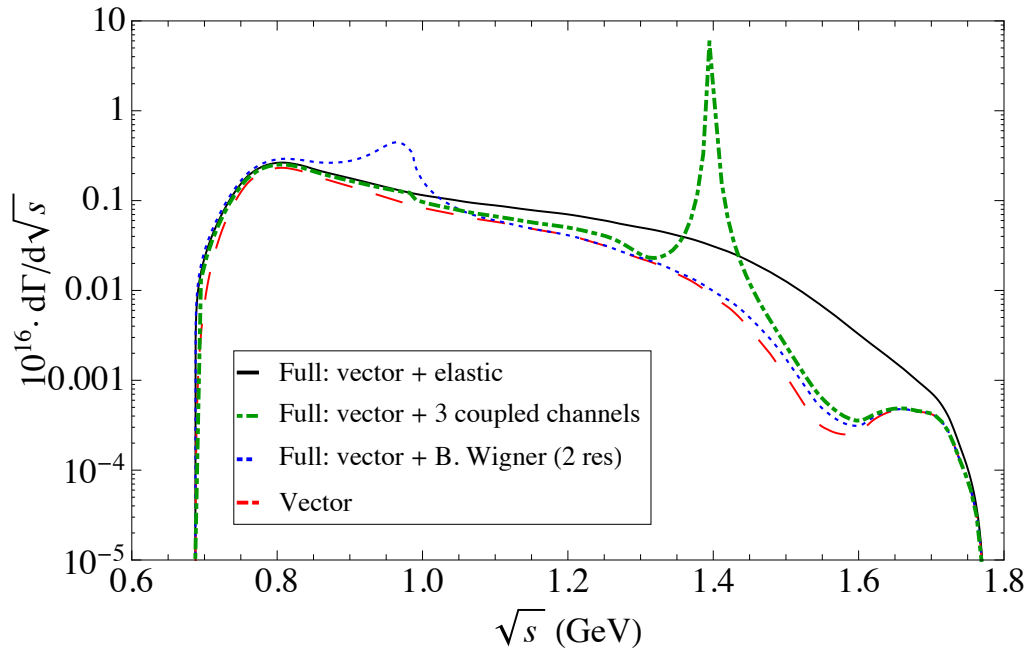
Figure 5.10: Decay distribution for $\tau^- \to \pi^-\eta\nu_\tau$ as obtained from Eq. (5.8). Red-dashed curve describes the contribution corresponding to the vector form factor while the other three curves represent the full distribution by employing the scalar form factor in its elastic version (black solid curve), in the three coupled-channels analysis (green dot-dashed curve) and using the Breit-Wigner formula with two resonances (blue dotted curve).

5.4.2 $\quad \tau^- \to \pi^-\eta'\nu_\tau$

Regarding $\tau^- \to \pi^-\eta'\nu_\tau$, we show the decay width distribution in Fig. 5.11 and our branching ratio estimates in Table 5.2. In this case, the large mass of the η' considerably reduces the available phase space with respect to the $\pi^-\eta$ mode. As a consequence of that, the vector contribution (red dashed curve in the plot) is suppressed since the effect of the $\rho(770)$ appears before the $\pi^-\eta'$ production threshold.

$BR_V \cdot 10^5$	$BR_S \cdot 10^5$	$BR \cdot 10^5$	Reference
0.25	1.60	1.85	Tisserant, Truong [191]
0.12	1.38	1.50	Bramón, Narison, Pich [192]
0.15	1.06	1.21	Neufeld, Rupertsberger [193]
0.36	1.00	1.36	Nussinov, Soffer [194]
[0.2, 0.6]	[0.2, 2.3]	[0.4, 2.9]	Paver, Riazuddin [195]
0.44	0.04	0.48	Volkov, Kostunin [196]
0.13	0.20	0.33	Descotes-Genon, Moussallam [190]
$BR_V \cdot 10^5$	$BR_S \cdot 10^5$	$BR \cdot 10^5$	Our analysis
0.26 ± 0.02	$0.72^{+0.46}_{-0.22}$	0.98 ± 0.51	Breit-Wigner [$a_0(980)$]
0.26 ± 0.02	$0.48^{+0.29}_{-0.14}$	0.74 ± 0.32	Breit-Wigner [$a_0(980) + a_0(1450)$]
0.26 ± 0.02	$0.10^{+0.02}_{-0.03}$	0.36 ± 0.04	Elastic Omnès solution
0.26 ± 0.02	0.15 ± 0.09	0.41 ± 0.09	2 coupled channels ($\pi^- \eta$ to $\pi^- \eta'$)
0.26 ± 0.02	1.86 ± 0.11	2.12 ± 0.11	2 coupled channels ($\pi^- \eta$ to $K^- K^0$)
0.26 ± 0.02	1.41 ± 0.09	1.67 ± 0.09	**3 coupled channels**
		$BR \cdot 10^5$	Experimental collaboration
		< 14 (95% CL)	CLEO [108]
		< 7.3 (90% CL)	Belle [149]
		< 9.9 (95% CL)	BaBar [107]

Table 5.1: Branching ratio predictions for $\tau^- \to \pi^- \eta \nu_\tau$ as obtained as from Eq. (5.8) with the vector and scalar form factors described in the text. We name our predictions depending on the scalar form factor description we have employed. A comparison with current experimental status and with other authors' estimates is also provided. The source of the uncertainty arises from the errors on $\varepsilon_{\pi\eta}$ (only source on the vector form factor) and from the (uncorrelated) errors on the scalar form factor input values. For the coupled channels cases, the uncertainty arises from $\varepsilon_{\pi\eta}$ only. The total branching ratio is obtained after symmetrizing and adding in quadrature all uncertainties.

Therefore, the decay is mainly driven by the scalar form factor. Again, we show three different curves for the full distribution named depending on the scalar form factor we have employed. The Breit-Wigner contribution (blue dotted curve) is, in this case, small since the effect of the $a_0(980)$ appears before the $\pi^- \eta'$ threshold and only the peak of the $a_0(1450)$ is relevant. The coupled channels description (green dot-dashed curve) shows a clear peak at around 1.4 GeV which vastly dominates the decay. This effect may be attributed to the $a_0(1450)$ resonance as we argued in the $\pi^- \eta$ mode. The same argument is valid for the elastic Omnès description (solid black curve) though the peak, in this case, is not as pronounced.

While our estimate for the vector contribution, of the order of 10^{-10}, is smaller than previous predictions, our values for the scalar contribution lie within the window $10^{-7} - 10^{-6}$, respecting the current upper bounds in any case. Regarding the numerical

calculations, we have found this process much more sensitive to the isospin violating input value $\varepsilon_{\pi\eta'}$ than the $\pi^-\eta$ mode. This is so because they are combined is such a way that the value at the origin of the energies, $F_0^{\pi^-\eta'}(0)$ given in Eq. (5.7), becomes a small quantity, whose square enters Eq. (5.8) for the description of the width. The upper and lower values of the windows given in the predictions of Table 5.2 are due to the associated errors to $\varepsilon_{\pi\eta'} = 2.5(1.5) \cdot 10^{-4}$. We find that this decay could be of the order of the current experimental bound 10^{-6}. It is really interesting to see whether future experimental information can soon shed light on this mode. Taking into account the current upper bounds as well as our predictions either of the decay modes $\tau^- \to \pi^-\eta^{(\prime)}\nu_\tau$ is likely to allow the discovery of SCC at Belle-II.
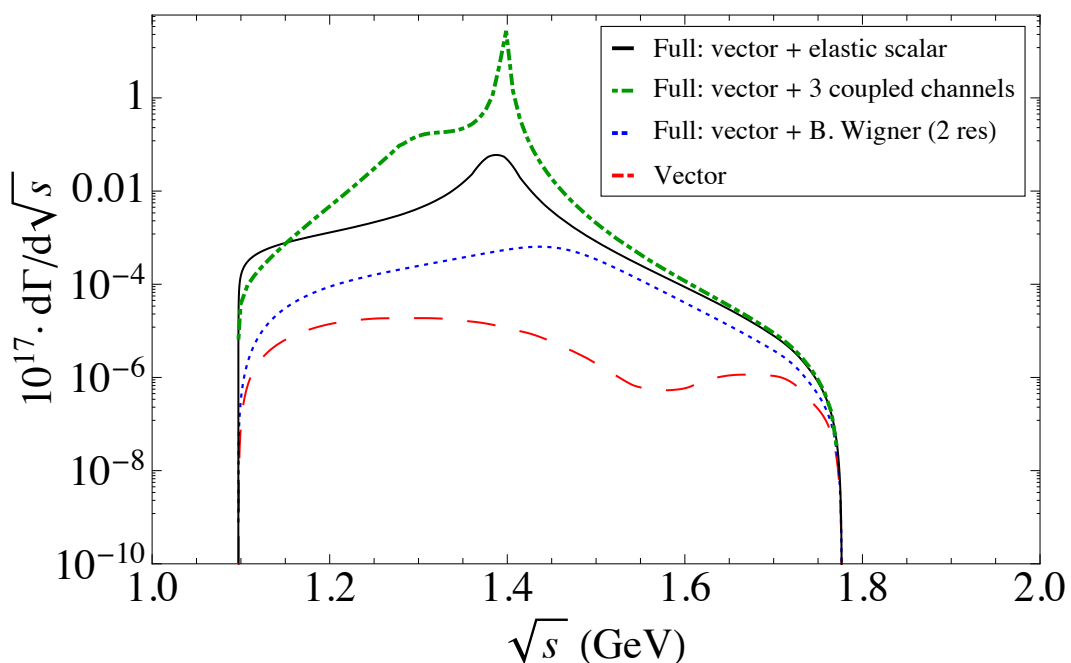
Figure 5.11: Decay distribution for $\tau^- \to \pi^-\eta'\nu_\tau$ as obtained as from Eq. (5.8). Red-dashed curve describes the contribution corresponding to the vector form factor while the other three curves represent the full distribution by employing the scalar form factor in its elastic version (black solid curve), in the three coupled-channels analysis (green dot-dashed curve) and finally using the Breit-Wigner formula with two resonances (blue dotted curve).

5.4.3 $\eta^{(\prime)} \to \pi^+\ell^-\nu_\tau$ $(\ell = e, \mu)$

The form factors required for describing $\tau^- \to \pi^-\eta^{(\prime)}\nu_\tau$ and the semileptonic decays $\eta^{(\prime)} \to \pi^+\ell^-\nu_\tau$ are the same since the hadronic matrix element $\langle\eta^{(\prime)}|\bar{d}\gamma^\mu u|\pi^+\rangle$ is related

BR$_V$	BR$_S$	BR	Reference
$< 10^{-7}$	$[0.2, 1.3] \cdot 10^{-6}$	$[0.2, 1.4] \cdot 10^{-6}$	Nussinov, Soffer [197]
$[0.14, 3.4] \cdot 10^{-8}$	$[0.6, 1.8] \cdot 10^{-7}$	$[0.61, 2.1] \cdot 10^{-7}$	Paver, Riazuddin [198]
$1.11 \cdot 10^{-8}$	$2.63 \cdot 10^{-8}$	$3.74 \cdot 10^{-8}$	Volkov, Kostunin [196]
BR$_V$	BR$_S$	BR	Our analysis
$[0.3, 5.7] \cdot 10^{-10}$	$[2 \cdot 10^{-11}, 7 \cdot 10^{-10}]$	$[0.5 \cdot 10^{-10}, 1.3 \cdot 10^{-9}]$	Breit-Wigner (1 res)
$[0.3, 5.7] \cdot 10^{-10}$	$[5 \cdot 10^{-11}, 2 \cdot 10^{-9}]$	$[0.8 \cdot 10^{-10}, 2.6 \cdot 10^{-9}]$	Breit-Wigner (2 res)
$[0.3, 5.7] \cdot 10^{-10}$	$[2 \cdot 10^{-9}, 4 \cdot 10^{-8}]$	$[2.6 \cdot 10^{-9}, 4 \cdot 10^{-8}]$	Elastic Omnès solution
$[0.3, 5.7] \cdot 10^{-10}$	$[2 \cdot 10^{-7}, 2 \cdot 10^{-6}]$	$[2 \cdot 10^{-7}, 2 \cdot 10^{-6}]$	2 cc ($\pi^- \eta'$ to $\pi^- \eta$)
$[0.3, 5.7] \cdot 10^{-10}$	$[3 \cdot 10^{-7}, 3 \cdot 10^{-6}]$	$[3 \cdot 10^{-7}, 3 \cdot 10^{-6}]$	2 cc ($\pi^- \eta'$ to $K^- K^0$)
$[0.3, 5.7] \cdot 10^{-10}$	$[1 \cdot 10^{-7}, 1 \cdot 10^{-6}]$	$[1 \cdot 10^{-7}, 1 \cdot 10^{-6}]$	**3 coupled channels**
		BR	Experimental collaboration
		$< 4 \cdot 10^{-6}$ (90% CL)	BaBar [110]
		$< 7.2 \cdot 10^{-6}$ (90% CL)	BaBar [151]

Table 5.2: Branching ratio predictions for $\tau^- \to \pi \eta' \nu_\tau$ as obtained as from Eq. (5.8) with the vector and scalar form factors described in the text. We name our predictions depending on the scalar form factor description we have employed. A comparison with current experimental status and with other author estimates is also provided. Our best theoretical estimate, corresponding to the three-coupled channel SFF analysis, is highlighted in boldface.

by crossing with Eq. (5.6). In $\eta_{\ell 3}^{(\prime)}$ decays the available kinematical energy range is, however, $m_\ell^2 < s < (m_{\eta^{(\prime)}} - m_\pi)^2$ instead of $(m_{\eta^{(\prime)}} + m_\pi)^2 < s < m_\tau^2$ for the τ decays. Consequently, the form factors entering $\eta_{\ell 3}$ decays are real functions of s. The differential decay width is given in this case by

$$
\frac{d\Gamma}{d\sqrt{s}} = \frac{G_F^2 |V_{ud} F_+(0)|^2 (c_V^{\pi\eta^{(\prime)}})^2 (s - m_l^2)^2}{24\pi^3 M_\eta^3 s}
$$
$$
\left\{ (2s + m_\ell^2) q_{\pi\eta^{(\prime)}}^3 \widetilde{F}_+(s)^2 + \frac{3}{4s} \Delta_{\pi\eta^{(\prime)}}^2 m_\ell^2 q_{\pi\eta^{(\prime)}} \widetilde{F}_0(s)^2 \right\} . \qquad (5.33)
$$

Notice that the width is mainly given by the contribution of the vector form factor since the scalar form factor is weighted by the squared mass of the final state lepton, hence suppressing its contribution.

In Fig. 5.12, we show the decay distributions while in Table 5.3 we present our branching ratios estimates. The rareness of these modes may enhance the sensitivity to new types of interactions and any clear deviation from the branching ratio of order $\mathcal{O}(10^{-13} - 10^{-12})$ may probe physics beyond the SM. At present, BESIII has reported $\mathcal{B}(\eta \to \pi^+ e^- \bar{\nu}_e + c.c.) < 1.7 \cdot 10^{-4}$ and $\mathcal{B}(\eta' \to \pi^+ e^- \bar{\nu}_e + c.c.) < 2.2 \cdot 10^{-4}$, both at the

90% C.L., which means the firsts upper bounds ever for η and η' semileptonic weak decays [199], but still extremely far from our values. These are in agreement with those in Ref. [190]. This can be understood from the fact that, although the analysis of the VFF dominating $\eta_{\ell 3}^{(')}$ decays is quite different in our analysis and theirs [14] both are consistent with the chiral limit of QCD and incorporate information on the off-shell $\rho(770)$ meson contribution, which is of paramount important in the available phase space. However, we note that our predictions are slightly lower than theirs. Predictions in [193] are in turn a factor two smaller than in Ref. [190] because their pure χPT result at NLO lacking the explicit $\rho(770)$ exchange effect.

Decay	Descotes-Genon, Moussallam [190]	Our estimate
$\eta \to \pi^+ e^- \bar{\nu}_e + c.c.$	$\sim 1.40 \cdot 10^{-13}$	$0.6 \cdot 10^{-13}$
$\eta \to \pi^+ \mu^- \bar{\nu}_\mu + c.c.$	$\sim 1.02 \cdot 10^{-13}$	$0.4 \cdot 10^{-13}$
$\eta' \to \pi^+ e^- \bar{\nu}_\mu + c.c.$		$1.7 \cdot 10^{-17}$
$\eta' \to \pi^+ \mu^- \bar{\nu}_\mu + c.c.$		$1.7 \cdot 10^{-17}$

Table 5.3: Branching ratio estimates for $\eta^{(')} \to \pi^+ \ell^- \nu_\ell \quad (\ell = e, \mu)$ obtained after employing $\varepsilon_{\pi\eta} = 9.8(3) \cdot 10^{-3}$, $\varepsilon_{\pi\eta'} = 2.5(1.5) \cdot 10^{-4}$ for the $\eta_{\ell 3}$ and $\eta'_{\ell 3}$ respectively.

---

[14]We recall that in our case is given by the corresponding $\eta^{(')} - \pi^0$ mixing factor times the $\pi^- \pi^0$ VFF taken from data, while in Ref. [190] it is basically built upon the unitarized $\eta\pi \to \pi\pi$ χPT amplitudes taking into account $\eta \to 3\pi$ information.
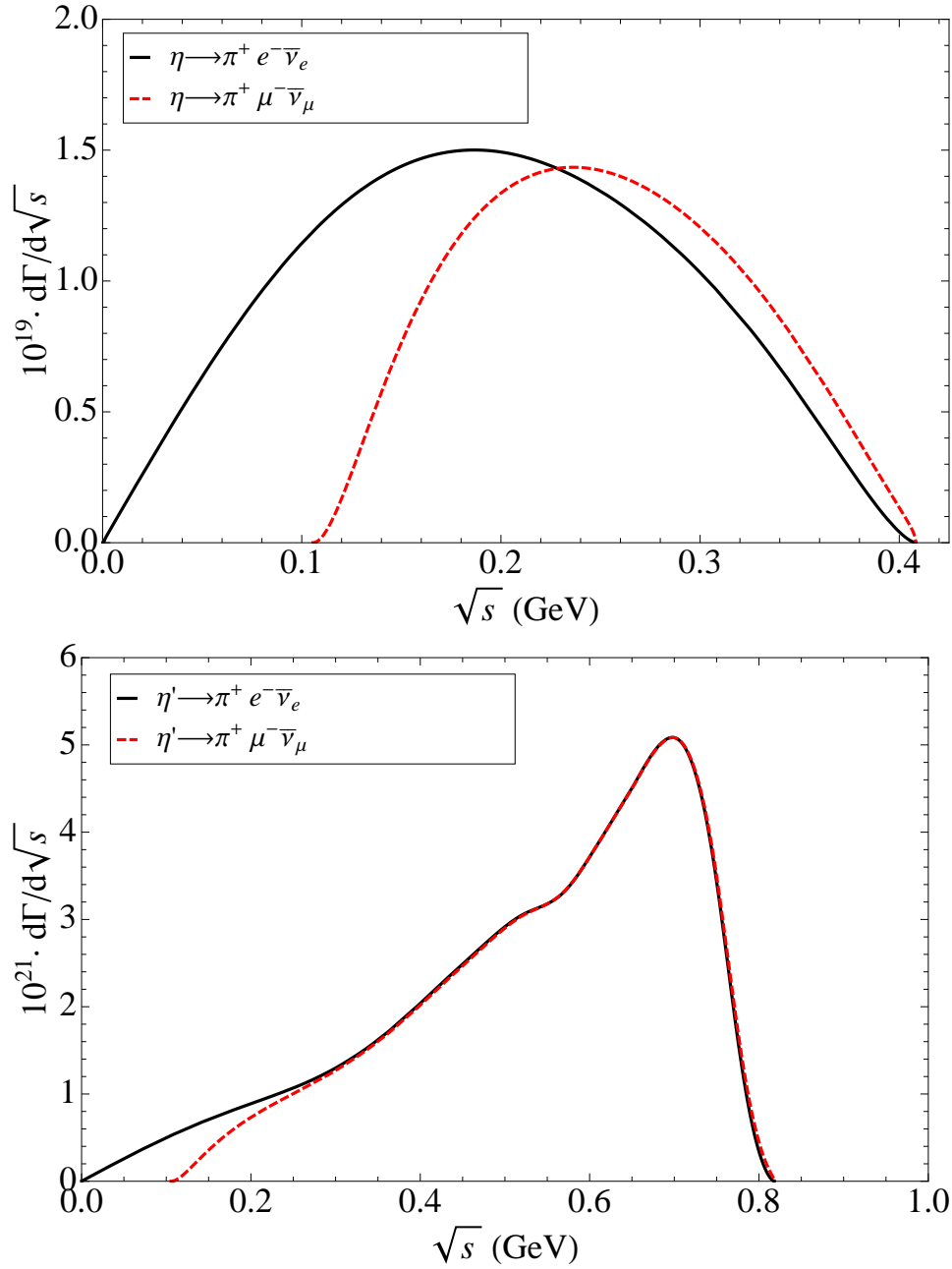
Figure 5.12: Decay distribution for $\eta \to \pi^+ \ell^- \nu_\tau$ (up panel) and $\eta' \to \pi^+ \ell^- \nu_\tau$ (black solid and red dashed curves for the electronic, $\ell = e$, and muonic, $\ell = \mu$, cases respectively) as obtained as from Eq. (5.33).

5.5 Conclusions

Hadronic decays of the τ lepton constitute an ideal scenario for studying the hadronization of QCD currents in its non-perturbative regime. In this work, we examine the

$\tau^- \to \pi^- \eta \nu_\tau$ and $\tau^- \to \pi^- \eta' \nu_\tau$ decays which –while being allowed, though isospin-suppressed, SM processes– belong to the so-called SCC processes unseen in Nature so far.

We focus on the Standard Model prediction of these decays by describing the participant vector and scalar form factors. These have been calculated within Chiral Perturbation Theory including resonances as explicit degrees of freedom as an initial setup approach. In this framework, we have encoded the $\pi^0 - \eta - \eta'$ mixing by means of three Euler angles ($\varepsilon_{\pi\eta}$, $\varepsilon_{\pi\eta'}$, and $\theta_{\eta\eta'}$), where $\varepsilon_{\pi\eta^{(\prime)}}$ is an isospin violating quantity entering the expression for decay width which explains the smallness of these decays. We have determined $\varepsilon_{\pi\eta}$ and $\varepsilon_{\pi\eta'}$ to be $9.8(3) \cdot 10^{-3}$ and $2.5(1.5) \cdot 10^{-4}$, respectively, calculated at next-to-leading order in the RChT framework (cf. Eq. (5.18)). One nice and interesting consequence which emerges neatly in this parameterization is that the corresponding $\pi^- \eta$ and $\pi^- \eta'$ vector from factors in its normalized version are found to be proportional to the well-known $\pi^- \pi^0$ vector form factor. For our study, we have implemented the experimental determination of the latter, obtained from the Belle collaboration [19] in the analysis of $\tau^- \to \pi^- \pi^0 \nu_\tau$ decays, for describing the former in a model-independent way.

Regarding the scalar form factor description, we have discussed different parameterizations according to their increasing fulfilment of unitarity and analyticity. We started considering a Breit-Wigner representation by resumming inelastic width effects into the resonance propagator(s) but neglecting the real part of the corresponding loop function, hence inducing a violation of unitarity and analyticity. This case has been tackled by considering, first, the contribution of the $a_0(980)$ as the only resonant state and, second, by including the nearest radial excitation $a_0(1450)$ into the representation. Then, we moved to a completely analytic description, respecting elastic unitarity, by the use of a dispersion relation through the well-known Omnès integral. This solution requires as an input the elastic phase of the form factor which has been obtained from Ref. [57], after invoking Watson's theorem. Finally, we have illustrated a method for solving coupled-channels form factors (see appendix D) by using closed algebraic expressions after exemplifying the equivalence with the Omnès solution for the single channel elastic case. In this way, the lowest-lying scalar resonances are generated dynamically after considering final-state interactions of meson-meson systems.

Several comments are in order concerning our branching ratios predictions:

i) We have found the $\pi^- \eta$ decay branching ratio to be of order 10^{-5}, in agreement with previous estimates and respecting the current experimental upper bound [107];

121

ii) both vector and scalar contributions are comparable;

iii) the Breit-Wigner descriptions are both in agreement at one sigma level independently of considering one or two scalar resonances;

iv) the effect of coupling the $\pi^- \eta'$ channel to the $\pi^- \eta$ description of the scalar form factor is small since it does not differ so much from the elastic dispersive representation (obtained after Omnès);

v) the effect of including the KK threshold is, however, sizable. This may be due to the exotic nature of the scalars coupled to the $\bar{u}d$ operator;

vi) accurate predictions demand precise value for the isospin violating parameter $\varepsilon_{\pi\eta}$ which factor out in the decay width;

vii) the $\pi^- \eta'$ is basically driven by the scalar contribution because of phase space considerations;

viii) the latter mode is much more sensitive to the isospin violating parameters, $\varepsilon_{\pi\eta'}$, as well as to the SFF description;

ix) inelastic channels may increase the branching ratio of the $\pi^- \eta'$ mode by one or two orders of magnitude up to order of 10^{-6};

x) the errors of our scalar form factors contributions are underestimated since correlations between the participating parameters are unknown. This important limitation shall be improved once these decay modes are first measured. Ideally, through a joint analysis of meson-meson scattering and $\tau^- \to \pi^- \eta^{(\prime)} \nu_\tau$ decays data.

Therefore, considering the tighter bounds on the $\pi^- \eta'$ channels, both $\tau^- \to \pi^- \eta' \nu_\tau$ decay modes have good prospects for discovering SCC soon at Belle-II. While the $\rho(770)$ meson shoulder should be an unambiguous signature of this discovery in the $\pi^- \eta$ mode, the thin peak of the $a_0(1450)$ resonance would be very much helpful in both cases. Finally, we have given estimates for the semileptonic crossing symmetric decays $\eta^{(\prime)} \to \pi^+ \ell^- \nu_\ell$ ($\ell = e, \mu$) for which we do not foresee detection in the near future. We hope our work to serve as a motivation for the experimental collaborations to measure these decays in the near future at Belle-II, BESIII and forthcoming facilities.

Part II

Phenomenological applications of Padé approximants

Chapter 6

Introduction to Padé approximants

When perturbation methods are considered to solve a problem, the answer usually emerges as an infinite series given in terms of the perturbation parameter ε. If the perturbation series converge rapidly, summing up the few calculated terms provides a realistic approximation to the exact solution. As a matter of example in physics, perturbative tools have been applied to QED leading a successful description of the interactions among fermions and photons. However, it is more common for the series to converge slowly, if it converges at all. Fortunately, there are powerful methods for recovering an accurate approach to the exact answer from a few terms of a slowly convergent or divergent series. In this chapter we will briefly discuss the Padé method which, in some instances, has been proven to be a successful summation method. We will not provide a formal and rigorous mathematical discussion on the method[1], which is out of the scope of this thesis, but rather a general overview with explanatory and easy going examples.

Let us consider the power series expansion of a function $f(z)$ around the origin on the complex plane $(z \to 0)$ as of

$$f(z) = \sum_{n=0}^{\infty} c_n z^n \, , \tag{6.1}$$

with a certain radius of convergence r. The idea of Padé approximants is to replace the power series as given in Eq. (6.1) by a sequence of rational functions. Strictly speaking a PA to $f(z)$ is a polynomial of order N over a polynomial of order M

$$P_M^N(z) = \frac{\sum_{j=0}^{N} a_j(z)^j}{\sum_{k=0}^{M} b_k(z)^k} = \frac{a_0 + a_1 z + \cdots + a_N(z)^N}{1 + b_1 z + \cdots + b_M(z)^M} \, , \tag{6.2}$$

---

[1]The interested reader is referred to Refs. [200, 201] to deepen on the subject.

constructed such that[2] the Taylor series expansion of $P_M^N(z)$ matches the power series $f(z)$ up to the highest possible order

$$f(z) - P_M^N(z) = \mathcal{O}(z)^{M+N+1}.$$ (6.3)

For example, to determine the $P_1^0(z)$ Padé we expand this approximant in a Taylor series

$$P_1^0(z) = \frac{a_0}{1 + b_1 z} = a_0 - a_0 b_1 z + \mathcal{O}(z^2),$$ (6.4)

and compare with the first two terms in the power series representation of Eq. (6.1) $f(z) = c_0 + c_1 z + \mathcal{O}(z)$. This leads two equations

$$c_0 = a_0,$$ (6.5)

$$c_1 = -a_0 b_1,$$ (6.6)

thus

$$P_1^0(z) = \frac{c_0}{1 - \frac{c_1}{c_0} z}.$$ (6.7)

As we will see in the following, the main advantage of the use Padé approximants respect to Taylor series expansion is that they often enlarge their proven range of applicability and accelerate the rate of convergence though, sometimes, the improvement is not astounding. Actually, the convergence of Padé approximants is not a simple extension of the convergence theory of Taylor series and one can find situations where Taylor series converge while Padé approximants do not [201]. However, the real power of Padé approximants arises when applying the method to divergent series as we will illustrate with the next example. Let us consider the function

$$f(z) = \frac{1}{z} \ln(1 + z),$$ (6.8)

whose Taylor expansion

$$f(z) = \sum_{n=0} \frac{(-z)^n}{n+1} = 1 - \frac{z}{2} + \frac{z^2}{3} - \frac{z^3}{4} + \frac{z^4}{5} + \mathcal{O}(z^5),$$ (6.9)

converges for $|z| < 1$ and diverges elsewhere.

As a matter of example, in Fig. 6.1 we provide a graphical account of the PAs $P_1^0(z)$ (short-dashed blue curve), $P_1^1(z)$ (dot-dashed red curve), $P_2^1(z)$ (long-dashed

---

[2]With any loos of generality, we take $b_0 = 1$ for definitiness.

orange curve) and $P_2^2(z)$ (dotted green curve) Padé approximants to the function Eq. (6.8) (black solid curve),

$$P_1^0(z) = \frac{1}{1 + \frac{z}{2}} \,, P_1^1(z) = \frac{1 + \frac{z}{6}}{1 + \frac{2z}{3}} \,, P_2^1(z) = \frac{1 + \frac{z}{2}}{1 + z + \frac{z^2}{6}} \,, P_2^2(z) = \frac{1 + \frac{7z}{10} + \frac{z^2}{30}}{1 + \frac{6z}{5} + \frac{3z^2}{10}} \,. \quad (6.10)$$

We see that the sequence converge rapidly and even beyond the radius of convergence of the Taylor series $|z| < 1$.
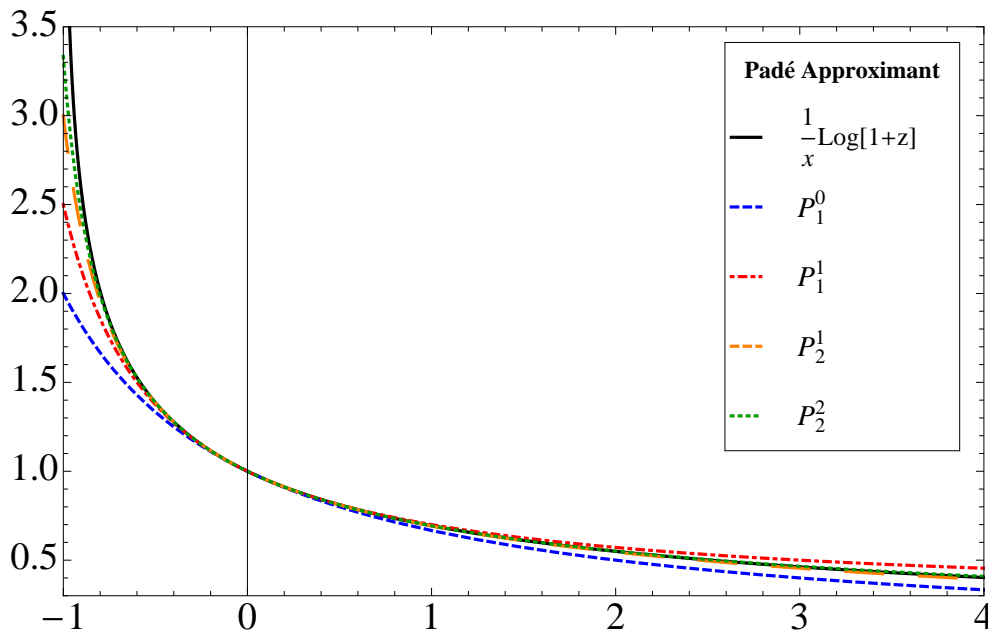
Figure 6.1: $P_1^0(z)$ (blue curve), $P_1^1(z)$ (red curve), $P_2^1(z)$ (orange curve) and $P_2^2(z)$ (green curve) Padé approximants to the function to $\frac{1}{z}\ln(1 + z)$ (black curve).

Convergence properties of PA to a given function are far from trivial and is an active field of research in applied mathematics. The convergence of the sequence of PA to the function we want to approximate is only ensured for special kind of functions such as Stieltjes or meromorphic functions. A function $f(z)$ is called Stieltjes if obeys a dispersion relation given in terms of a positive definite spectral function. In this case, the Padé sequence is convergent everywhere on the complex plane, except on the branch cut. The function Eq. (6.8) that concerns us is of Stieltjes-type and can be proved that Padé approximants converge to $\frac{1}{z}\ln(1 + z)$ for all z in the cut plane $|\arg| < \pi$ (See Ref. [201] for a detailed demonstration).

The reason why PA are able to provide a better description of Eq. (6.8) than the Taylor series Eq. (6.9) lies on the inability of a polynomial to reproduce singularities

such as branch-cuts or poles. The PA $P^N_M(z)$, however, place all the poles and zeros on the negative real axis which, in turn, tend to reproduce the effect of the branch-cut singularity of the function, $(-\infty, -1]$. This feature can be seen in Fig. 6.2, where we observe that effectively the poles and zeros all lie on the negative real axis and as $N \to \infty$ the poles become dense mimicking, in some sense, the branch cut.
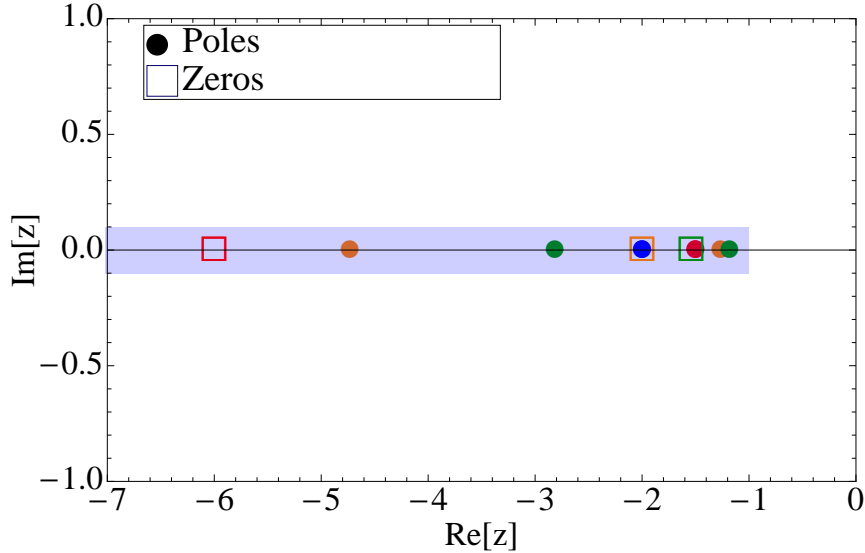
Figure 6.2: Poles (circles) and zeroes (squares) of the PA shown in Fig. 6.1.

The Padé sequence of a Stieltjes series has some interesting convergence properties such that: i) the diagonal Padé sequence $P^N_N(z)$ decreases monotonically as N increases; ii) the Padé sequence $P^{N-1}_N(z)$ increases monotonically as N increases; iii) The sequence $P^N_N(z)$ has a lower bound, while the sequence $P^{N-1}_N(z)$ has an upper bound. It is proven that all Stieltjes functions $F(z)$ with the same finite series representation used in the Padé summation satisfy [201]

$$\lim_{N \to \infty} P^{N-1}_N(z) \leq F(z) \leq \lim_{N \to \infty} P^N_N(z). \tag{6.11}$$

Canterbury approximants

Let us briefly introduce the so-called Canterbury approximants [200, 202, 203], a bivariate generalization of PAs defined as $C^N_N(x, y) = \frac{R_N(x,y)}{Q_N(x,y)}$. The coefficients of $R_N(x, y) = \sum^N_{i,j} a_{i,j} x^i y^j$, $(i, j) \in \mathcal{N}$, and $Q_N(x, y) = \sum^N_{i,j} b_{i,j} x^i y^j$, $(i, j) \in \mathcal{D}$ are determined by the accuracy-through-order conditions up to $\mathcal{O}(x^{2N} y^{2N})$, and $\mathcal{O}(x^{2N+1-\alpha} y^\alpha)$ with $\alpha = 0, 1, \dots 2N$. The Canterbury group [202] demonstrated that for Stieltjes and meromorphic bivariate functions, the convergence of $C^{N+J}_N(Q^2_1, Q^2_2)$ is guaranteed

for $J = -1, 0$ and resemble those of the PAs. This convergence properties will be exploited in section 7.1.4.

Quadratic approximants

Thus far we have seen the powerfulness of PA to approximate our test function, Eq. (6.8), away from the branch cut and the failure for describing the branch cut region. Nonetheless, we would also like to illustrate a method which might be able to approximate the branch cut region as well.

In the same spirit than Padé approximants, Quadratic approximants [204] (QA) arise by squaring Eq. (6.3), the contact term of PA with the function $f(z)$ we want to approximate. This yields the quadratic equation

$$Q(z)f^2(z) + 2R(z)f(z) + S(z) = \mathcal{O}(z^{q+r+s+2}),\qquad(6.12)$$

where $Q(z), R(z)$ and $S(z)$ are polynomials of order q, r, s, respectively. The solution of Eq. (6.12) leads to

$$QA_q^{r,s}(z) = \frac{-R(z) \pm \sqrt{R^2(z) - Q(z)S(z)}}{Q(z)},\qquad(6.13)$$

with the special feature of generating a branch cut thanks to the square root. Notice that the are two solutions, being the ones that picks up the phase of the function to approximate the correct ones. With QA at hand, we reassess the logarithm function evaluated in the previous section. Convergence of QA to Stieltjes functions is well proven and documented and in most cases, the rate of convergence is faster than for PAs [200]. Even better is their ability to reproduce order by order the analytic structure of the branch cut and incorporate, at once, the correct behavior for $z \to \infty$ [200, 204]. To illustrate their performance, we start with single pole QAs of the type $QA_1^{r,s}(z)$ allowing r and s to run from 0 to 1. The sequence with two poles converge much faster and is less illustrative for our pedagogical discussion. The $QA_1^{0,0}(z)$ requires 3 coefficients, while the $QA_1^{1,1}(z)$ requires up to five. As examples,

$$QA_1^{0,0}(z) = \frac{-1 \pm \sqrt{9 - 6z}}{4 - 3z}, \quad QA_1^{1,1}(z) = \frac{(\frac{21}{2} - 5z) \pm \frac{3}{2}\sqrt{225 - 240z + 14z^2}}{12 - 13z}.$$
$$(6.14)$$

The result is shown in Fig. 6.3 from where we realize that we are not only able to approximate the region away from the cut, for which PA already worked well (cf. Fig. 6.1), but also the branch-cut region. The higher the order r and s, the better
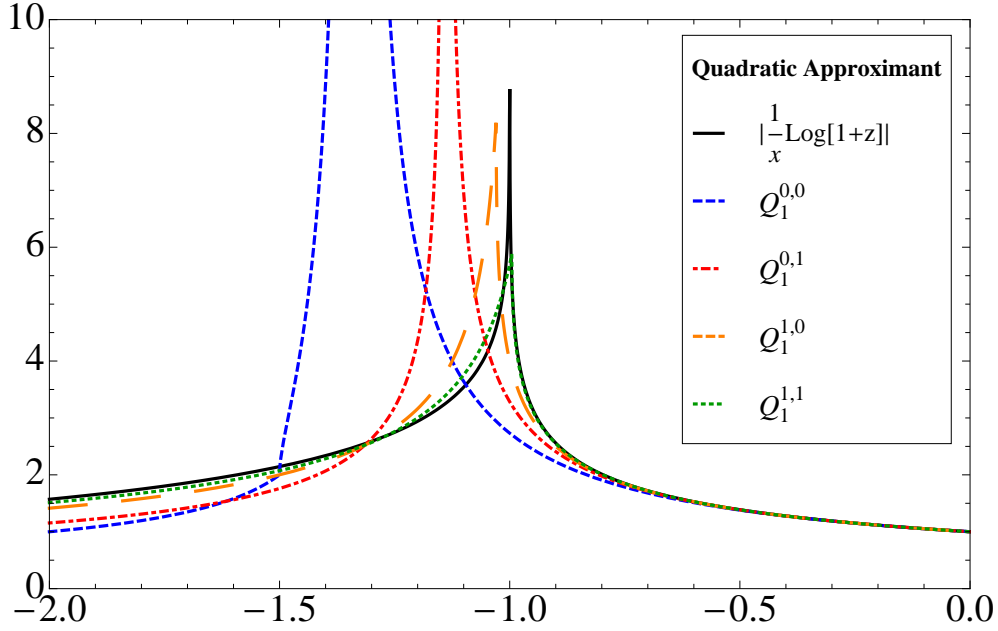
Figure 6.3: $QA_1^{0,0}(z)$ (short dashed blue), $QA_1^{0,1}(z)$ (dot-dashed red), $QA_1^{1,0}(z)$ (long dashed orange) and $QA_1^{1,1}(z)$ (dotted green) QAs to the function $\frac{1}{z}\ln(1+z)$ (black).

the approximation of both branch cut and the region out of the cut. The $QA_1^{1,1}(z)$ requires the same amount of information than the $P_2^2(z)$ but performs better not only along the cut but also below.

Phenomenological applications

With all the insights from the Padé method and convergence theorems at hand, we can venture a trip towards phenomenological studies. In some cases, the direct application of the convergence theorem might guarantee in advance our success. In other cases, specially when the analytical properties of the function to approximate are unknown and the local information scarce, we will pursue a convergence pattern to satisfy our criterium of systematic study.

In the forthcoming sections 7 and 8, we will apply Padé approximants to describe meson transition form factors. It is worth to say once more, that there is no *a priori* probe assuring the convergence of the Padé sequence to them since we do not know the explicit analytical structure behind the form factor i.e we can not probe that these form factor are not Stieltjes or pure meromorphic functions, but we can neither probe the contrary. Therefore, one can always try the approximation and learn from what happens.

Chapter 7

Single and double Dalitz decays of π^0, η and η' mesons

Anomalous decays of the neutral pseudoscalar mesons $\mathcal{P}$ ($\mathcal{P} = \pi^0, \eta, \eta'$) are driven through the chiral anomaly of QCD (cf. Eq. (1.147)). Of historical importance is the process $\mathcal{P} \to \gamma\gamma$, which apart from being the main decay channel of the π^0 and the η, its experimental discovery confirmed, for the first time, the existence of anomalies. In this case, the two final state photons are real and the transition form factor (TFF) encoding the effects of the strong interactions of the decaying meson is predicted to be a mere constant, the value of the axial anomaly in the chiral and large-N_c limits of QCD, $F_{\pi^0\gamma\gamma}(0) = 1/(4\pi^2 F_\pi)$ in the case of neutral pion, where $F_\pi \simeq 92$ MeV is the pion decay constant. On the contrary, if one of the two photons is virtual, the corresponding TFF is no longer a constant but a function of the transferred momentum to the virtual photon $F_{\mathcal{P}\gamma\gamma^*}(q^2)$, whereas when both photons are virtual the TFF depends on both photon virtualities and it is represented by $F_{\mathcal{P}\gamma^*\gamma^*}(q_1^2, q_2^2)$. A single Dalitz decay occurs through the single-virtual TFF after the conversion of the virtual photon into a lepton pair, while double Dalitz decays proceed with the TFF of double virtuality involving two dilepton pairs in the final state. Dalitz decays are attractive processes to improve our knowledge of the not yet exactly known TFFs of the $\mathcal{P}\gamma^{(*)}\gamma^*$ vertices. This is the main motivation of this work together with predicting the invariant mass spectra and the branching ratios ($\mathcal{BR}$) of the decays $\mathcal{P} \to \ell^+\ell^-\gamma$ and $\mathcal{P} \to \ell^+\ell^-\ell^+\ell^-$ with $\mathcal{P} = \pi^0, \eta, \eta'$ and $\ell = e$ or μ.

From the experimental side, the current status is the following. The PDG reported value for the branching ratio of the decay $\pi^0 \to e^+e^-\gamma$ is $(1.174 \pm 0.035)\%$ [37], which is obtained from the PDG fits of the ratio $\Gamma(\pi^0 \to e^+e^-\gamma)/\Gamma(\pi^0 \to \gamma\gamma) = (1.188 \pm 0.035)\%$ (the latest measurement of this ratio, $(1.140 \pm 0.041)\%$, was performed by ALEPH in 2008 [205]) and $B(\pi^0 \to \gamma\gamma) = (98.823 \pm 0.034)\%$. It is worth commenting

that this is the second most important decay mode of the π^0. The branching ratio for the decay $\eta \to e^+e^-\gamma$ has been recently measured by the A2 Collaboration at MAMI [206], $(6.6 \pm 0.4 \pm 0.4) \times 10^{-3}$ (see also the most recent Ref. [207]), and the CELSIUS/WASA Collaboration [208], $(7.8 \pm 0.5 \pm 0.8) \times 10^{-3}$, whilst the PDG quoted value is $(6.9 \pm 0.4) \times 10^{-3}$ [37], in accordance with the preliminary result, $(6.72 \pm 0.07 \pm 0.31) \times 10^{-3}$, from the WASA@COSY Collaboration [209]. The decay $\eta \to \mu^+\mu^-\gamma$ has been studied by the NA60 Collaboration at CERN SPS [210], though they do not provide a value for the branching ratio. The PDG fit reports the value $(3.1 \pm 0.4) \times 10^{-4}$ [37]. The branching fraction for the decay $\eta' \to e^+e^-\gamma$ has been recently measured for the first time by the BESIII Collaboration [25] obtaining a value of $(4.69 \pm 0.20 \pm 0.23) \times 10^{-4}$. To end, the decay $\eta' \to \mu^+\mu^-\gamma$ was measured long ago at the SERPUKHOV-134 experiment with a value of $(1.08 \pm 0.27) \times 10^{-4}$ [211]. Regarding the double Dalitz decays, the KTeV Collaboration measured the branching ratio of the decay $\pi^0 \to e^+e^-e^+e^-$, $(3.46 \pm 0.19) \times 10^{-5}$ [212], thus averaging the PDG result to $(3.38 \pm 0.16) \cdot 10^{-5}$ [37]. The KLOE Collaboration reported the first experimental measurement of $\eta \to e^+e^-e^+e^-$ [213], $(2.4 \pm 0.2 \pm 0.1) \times 10^{-5}$, which is in agreement with the preliminary result, $(3.2 \pm 0.9 \pm 0.5) \times 10^{-5}$, provided by the WASA@COSY Collaboration [209]. In Ref. [208], upper bounds for the branching ratios of $\eta \to \mu^+\mu^-\mu^+\mu^-$, $< 3.6 \times 10^{-4}$, and $\eta \to e^+e^-\mu^+\mu^-$, $< 1.6 \times 10^{-4}$, both at 90% CL, are reported. Finally, no experimental evidence for $\eta' \to e^+e^-e^+e^-$, $\eta' \to \mu^+\mu^-\mu^+\mu^-$ and $\eta' \to e^+e^-\mu^+\mu^-$ exists.

On the theory side, the effort is focused on encoding the QCD dynamical effects in the anomalous $\mathcal{P}\gamma^{(*)}\gamma^*$ vertices through the corresponding TFF functions. The exact momentum dependence of these TFFs over the whole energy region is not known, we only possess theoretical predictions from chiral perturbation theory (ChPT) and perturbative QCD (pQCD), thus constraining the low- and space-like large-momentum transfer regions, respectively. The TFF at zero-momentum transfer can be inferred either from the measured two-photon partial width,

$$|F_{\mathcal{P}\gamma\gamma}(0)|^2 = \frac{64\pi}{(4\pi\alpha)^2} \frac{\Gamma(\mathcal{P} \to \gamma\gamma)}{M_{\mathcal{P}}^3} \ , \tag{7.1}$$

or the prediction from the axial anomaly in the chiral and large-N_c limits of QCD, as mentioned before, while the asymptotic behavior of the TFF at $Q^2 \equiv -q^2 \to \infty$ should exhibit the right falloff as $1/Q^2$ [214][1]. Furthermore, the operator product

---

[1] Perturbative QCD predicts $\lim_{Q^2 \to \infty} Q^2 F_{\pi^0\gamma\gamma^*}(Q^2) = 2F_\pi$. Alternative values to this result exist, see for instance refs. [215, 216], though they seem to be disfavored, as pointed out in refs. [217, 218]. For the η and η', see the asymptotic values obtained in refs. [22, 23].

expansion (OPE) predicts the behaviour of the double-virtual TFF in the limit $Q_1^2 = Q_2^2 \equiv Q^2 \to \infty$ to be the same as for the single one, that is, $1/Q^2$ [219][2]. For the intermediate-momentum transfer region, the most common parameterization of the TFF, widely used by experimental analyses, is provided by the Vector Meson Dominance model (VMD). The dispersive representation of the TFF in terms of q^2, where q^2 is the photon virtuality in the time-like momentum region, can be written as

$$F_{\mathcal{P}\gamma\gamma^*}(q^2) = \int_{s_0}^{\infty} ds \frac{\rho(s)}{s - q^2 - i\epsilon} \ , \tag{7.2}$$

where s_0 is the threshold for the physical intermediate states imposed by unitarity and $\rho(s) = \mathrm{Im} F_{\mathcal{P}\gamma\gamma^*}(s)/\pi$ is the associated spectral function. To approximate this intermediate-energy part of the spectral function one usually employs one or more single-particle states. As an illustration, the contribution to the spectral function of a narrow-width resonance of mass M_{eff} reduces to $\rho(s) \propto \delta(s - M_{\mathrm{eff}}^2)$, which yields

$$F_{\mathcal{P}\gamma\gamma^*}(q^2) = \frac{F_{\mathcal{P}\gamma\gamma}(0)}{1 - q^2/\Lambda^2} \ , \tag{7.3}$$

where $F_{\mathcal{P}\gamma\gamma}(0)$ serves as a normalization constant and $\Lambda(= M_{\mathrm{eff}})$ is a real parameter which fixes the position of the resonance pole on the real axis. However, this simple and successful single-pole approximation given in Eq. (7.3) breaks down for $q^2 = \Lambda^2$. One may cure this limitation by taking into account resonant finite-width effects as proposed by Landsberg in Ref. [220] when considering the transitions $\mathcal{P} \to \ell^+\ell^-\gamma$ in a VMD framework. According to this model, these transitions occur through the exchange of the lowest-lying ρ, ω and ϕ vector resonances and their contributions to the TFF are written as

$$\widetilde{F}_{\mathcal{P}\gamma\gamma^*}(q^2) = \left(\sum_{V=\rho,\omega,\phi} \frac{g_{V\mathcal{P}\gamma}}{2g_{V\gamma}} \right)^{-1} \sum_{V=\rho,\omega,\phi} \frac{g_{V\mathcal{P}\gamma}}{2g_{V\gamma}} \frac{M_V^2}{M_V^2 - q^2 - iM_V\Gamma_V(q^2)} \ , \tag{7.4}$$

where $\widetilde{F}_{\mathcal{P}\gamma\gamma^*}(q^2) = F_{\mathcal{P}\gamma\gamma^*}(q^2)/F_{\mathcal{P}\gamma\gamma}(0)$ is defined as the normalized TFF, $g_{V\mathcal{P}\gamma}$ and $g_{V\gamma}$ are the $V\mathcal{P}\gamma$ and $V\gamma$ couplings, respectively, M_V the vector masses, and $\Gamma_V(q^2)$ the energy-dependent widths.

Despite the notorious success of VMD in describing lots of phenomena at low and intermediate q^2, particularly useful for the decays we consider in this work, this model can be seen as a first step in a systematic approximation. Padé approximants are used to go beyond VMD in a simple and model-independent manner also incorporating information from higher energies, allowing an improved determination of

---

[2]The OPE predicts for the case of the pion $\lim_{Q^2 \to \infty} Q^2 F_{\pi^0\gamma^*\gamma^*}(Q^2, Q^2) = 2F_\pi/3$.

the low-energy constants relative to other methods [20]. For this reason, we make use in our study of the works in refs. [22, 21], where all current measurements of the space-like TFFs $\gamma^*\gamma \to \mathcal{P}$ [24], produced in the reactions $e^+e^- \to e^+e^-\mathcal{P}$, have been accommodated in nice agreement with experimental data using these rational approximants. We benefit from these parameterizations valid in the space-like region to predict the transitions $\mathcal{P}\gamma^{(*)}\gamma^*$ used in the time-like region for the Dalitz decays we are interested in, with the primary aim of achieving accurate results for these decays. Different parameterizations existing in the literature are based on resonance chiral theory [221, 222] and dispersive techniques [223, 224], among others [225, 226, 227, 233, 228, 229, 230, 232, 231, 234].

This chapter is structured as follows. In section 7.1, we introduce our description for the π^0, η and η' transition form factors using the mathematical method of Padé approximants. Sections 7.2 and 7.3 are devoted to the analysis of single and double Dalitz decays, respectively, and predictions for the several invariant mass spectra and branching ratios are given. Finally, in section 7.4, we present our conclusions.

7.1 Transition Form Factors

The usefulness of Padé approximants (PAs) as fitting functions for different form factors have been extensively illustrated [20, 21, 22, 23, 235]. The reader is referred to these references for details on the method though here we cover some important aspects for consistency. The PAs to a given function are ratios of two polynomials (with degree L and M, respectively),[3]

$$P^L_M(q^2) = \frac{\sum_{j=0}^{L} a_j(q^2)^j}{\sum_{k=0}^{M} b_k(q^2)^k} = \frac{a_0 + a_1 q^2 + \cdots + a_L(q^2)^L}{1 + b_1 q^2 + \cdots + b_M(q^2)^M} \ , \tag{7.5}$$

constructed such that the Taylor expansion around the origin exactly coincides with that of $f(q^2)$ up to the highest possible order, i.e., $f(q^2) - P^L_M(q^2) = \mathcal{O}(q^2)^{L+M+1}$. We would like to point out that the previous VMD ansatz for the form factor (7.3) can be viewed as the first element in a sequence of PAs which can be constructed in a systematic way. By considering higher-order terms in the sequence, one may be able to describe the experimental space-like data with an increasing level of accuracy. The important difference with respect to the traditional VMD approach is that, as a Padé sequence, the approximation is well-defined and can be systematically improved upon. Although polynomial fitting is more common, in general, rational approximants are

---

[3]With any loss of generality, we take $b_0 = 1$ for definiteness.

able to approximate the original function in a much broader range in momentum than a polynomial [200].

Yet the success of PAs as fitting functions for space-like TFFs, some important remarks are in order. First, there is no *a priori* mathematical proof ensuring the convergence of a Padé sequence to the unknown TFF function, though a pattern of convergence may be inferred from the data analysis *a posteriori*[4]. For instance, the excellent performance of PAs in Ref. [23] (see figures 2 and 7 there) seems to indicate that the convergence of the η TFF normalization and low-energy constants is assured (see also Ref. [236] for the η' case). Second, unlike the space-like TFF data analyses [22, 21], one should not expect to reproduce the time-like TFF data since a Padé approximant contains only isolated poles and cannot reproduce a time-like cut[5]. However, if this right-hand cut is approximated by one or more single-particle states in the form of one or several narrow-width resonances, as stated before, then the Padé method may be still used up to the first resonance pole, indeed, up to neighbourhoods of the pole. The size of the region which is affected by the presence of the pole, a disk of radius ε, is not known but, as we will see later, may be deduced, thus fixing the range of application of the PAs for the time-like data. Third and last, the poles found in the PAs fitting the TFFs can not be directly associated to physical resonance poles in the second Riemann sheet of the complex plane. These, in turn, may be obtained following the prescriptions of Ref. [237], which is beyond the scope of the present work.

We would like to emphasize that the use of PAs as fitting functions for some set of experimental data can be viewed as an effective mathematical method which intrinsically contains relevant physical information of the function represented by the data set. In this work, we benefit from the findings of refs. [22, 21], where the π^0, η and η' TFFs were fixed in the space-like region from the analysis of the intermediate process $\gamma\gamma^* \rightarrow \mathcal{P}$ by several experimental collaborations, to predict the time-like region of the same TFFs needed for the description of the reaction $\mathcal{P} \rightarrow \gamma\gamma^*$ and therefore for the single and double Dalitz decays studied here. The extrapolated version of the TFFs, from the space-like region to the time-like one, used in this analysis are discussed case by case in the following.

---

[4]For a detailed discussion of Padé convergence applied to form factors, see for instance Ref. [20].

[5]The TFF function is unknown but expected to be analytical in the entire q^2-complex plane except for a branch cut along the real axis for $q^2 \geq 4M_\pi^2$.

7.1.1 $\pi^0 \to \gamma\gamma^*$

Given the small phase-space available in this transition, $4m_\ell^2 \leq q^2 \leq M_\pi^2$, the π^0 TFF can be expressed in terms of its Taylor expansion,

$$F_{\pi^0\gamma\gamma^*}(q^2) = F_{\pi^0\gamma\gamma}(0) \left(1 + b_\pi \frac{q^2}{M_\pi^2} + c_\pi \frac{q^4}{M_\pi^4} + \cdots \right) , \tag{7.6}$$

where $F_{\pi^0\gamma\gamma}(0)$ is fixed from Eq. (7.1) and the values of the low-energy constants (LECs), slope and curvature, b_π and c_π, respectively, are borrowed from eqs. (12,13) in Ref. [21][6],

$$b_\pi = -3.24(12)_{\text{stat}}(19)_{\text{sys}} \times 10^{-2} , \quad c_\pi = 1.06(9)_{\text{stat}}(25)_{\text{sys}} \times 10^{-3} , \tag{7.7}$$

where the statistical error is the result of a weighted average of several fits using different types of PAs to the same joint set of π^0 TFF space-like data and the systematic error is attributed to the model dependence of the PA's method. In this way, the values obtained for the LECs can be considered as model-independent. It is worth mentioning that the systematic errors ascribed to the LECs are quite conservative, in the sense that they are obtained from a comparison of the constants predicted by several well-established phenomenological models for the TFF and their counterparts extracted using various types of PAs from fits to pseudo-data sets generated by the different models. For each LEC, the systematic error is chosen to be the largest difference among these comparisons, making the whole approach reliable and with a stamp of model independence [21].

The Taylor expansion in Eq. (7.6) can be safely used for the description of the π^0 TFF in the time-like region within the range of available phase-space since the first pole seems to appear, for all types of PAs considered, inside the region of ρ-dominance [21], thus well beyond the phase-space end point. Finally, we would like to remark that this expansion of the single-virtual π^0 TFF will be used for predicting both $\pi^0 \to e^+e^-\gamma$ and $\pi^0 \to e^+e^-e^+e^-$ decays, the latter by means of a factorisation of the double-virtual π^0 TFF in terms of a product of the single-virtual one (see subsection 7.1.4 for details).

7.1.2 $\eta \to \gamma\gamma^*$

In order to describe the time-like region of the η TFF from the space-like data analysis in Ref. [22], we will employ two PAs, the $P_1^5(q^2)$ and the $P_2^2(q^2)$. These are the

---

[6]In Ref. [21], the value of the slope parameter appears with a positive sign due to the different definition used for the Taylor expansion of the π^0 TFF.
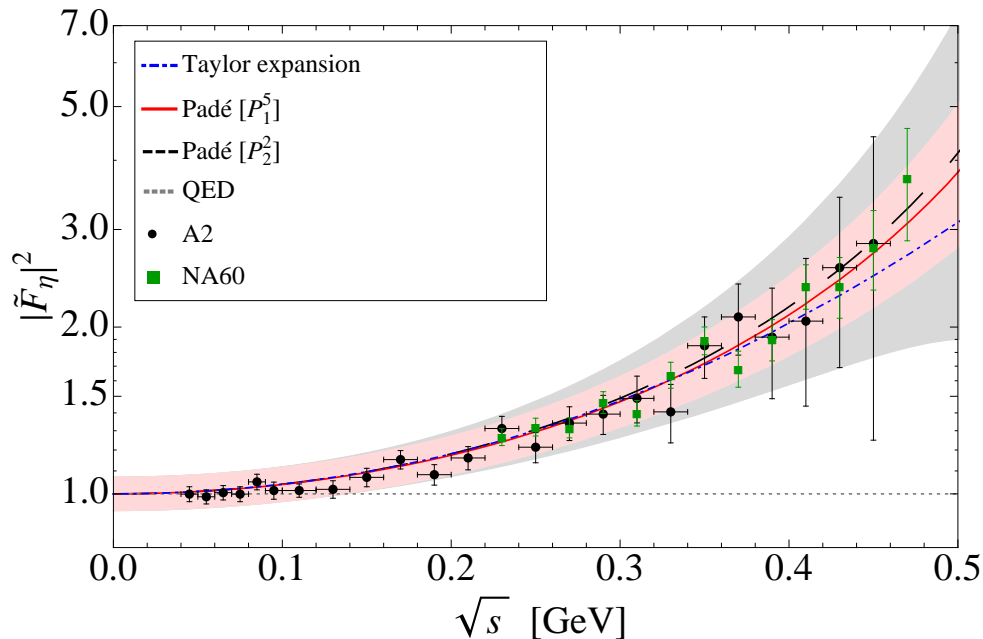
Figure 7.1: Modulus square of the normalized time-like η TFF, $\widetilde{F}_{\eta\gamma^*}(q^2)$, as a function of the invariant dilepton mass, $\sqrt{s} \equiv m_{\ell\ell}$. The predictions coming from the $P_1^5(q^2)$ (red solid line) and $P_2^2(q^2)$ (black long-dashed line) PAs, and the Taylor expansion (blue dot-dashed line) are compared to the experimental data from $\eta \to e^+e^-\gamma$ [207] (black circles) and $\eta \to \mu^+\mu^-\gamma$ [210] (green squares). The one-sigma error bands associated to $P_1^5(q^2)$ (light-red) and $P_2^2(q^2)$ (light-gray) PAs, and the QED prediction (gray short-dashed line) are also displayed.

highest-order PAs one can achieve when confronted with the joint sets of space-like experimental data. The sequence $P_1^L(q^2)$ is used when the TFF is believed to be dominated by a single resonance, while the $P_N^N(q^2)$ one is appropriate for the case the TFF fulfils the asymptotic behaviour[7]. A Taylor expansion equivalent to Eq. (7.6), with $b_\eta = 0.60(6)_{\text{stat}}(3)_{\text{sys}}$ and $c_\eta = 0.37(10)_{\text{stat}}(7)_{\text{sys}}$ for the slope and curvature parameters, respectively, is better not to be used in this case because of the larger phase-space available, $4m_\ell^2 \leq q^2 \leq M_\eta^2$. From the analysis in Ref. [22], we also obtained that the fitted poles for the $P_1^L(q^2)$ sequence are seen in the range $(0.71, 0.77)$ GeV, beyond the phase-space end point, thus making again our approach applicable and the predictions reliable.

Our predictions for the modulus square of the normalized time-like η TFF, $\widetilde{F}_{\eta\gamma^*}(q^2)$, as a function of the invariant dilepton mass, $\sqrt{s} \equiv m_{\ell\ell}$, are shown in figure 7.1, to-

---

[7]In Ref. [22], the fit to space-like data is done for $Q^2|F(Q^2)|$ and not for the TFF itself. As a consequence, PAs satisfying the correct asymptotic limit, that is, $\lim_{Q^2\to\infty} Q^2 F(Q^2) = \text{const.}$, are represented by the sequence $P_N^N(q^2)$.

gether with the experimental data points from the A2 Collaboration on the decay $\eta \to e^+ e^- \gamma$ [207] (black circles) and the NA60 experiment on $\eta \to \mu^+ \mu^- \gamma$ [210][8] (green squares). The predictions from the $P_1^5(q^2)$ (red solid line) and $P_2^2(q^2)$ (black long-dashed line) are almost identical and in nice agreement with the experimental data, whereas the Taylor expansion (blue dot-dashed line) is not so precise in the upper part of the spectrum. For this reason, we will use in our analysis both PAs indistinctly. The one-sigma error bands associated to $P_1^5(q^2)$ and $P_2^2(q^2)$ PAs are displayed in light-red and light-gray, respectively. These error bands are built from the uncertainty in the coefficients of the PAs[9] and the normalization factor extracted from the two-photon decay width. To these bands, we have also ascribed a conservative systematic error coming from the propagation of the systematic errors associated to b_η and c_η. Therefore, the η TFF has also a stamp of model independence as explained for the case of the π^0 TFF.

7.1.3 $\eta' \to \gamma \gamma^*$

The description of the whole time-like η' TFF by means of PAs is cumbersome. The available phase space, $4m_\ell^2 \leq q^2 \leq M_{\eta'}^2$, includes now an energy region where poles associated to these PAs can emerge. The analysis of the η' TFF space-like data performed in Ref. [22] revealed the appearance of a pole in the range $(0.83, 0.86)$ GeV for the cases of a $P_1^L(q^2)$ sequence. Consequently, we cannot employ the method of PAs for describing the time-like TFF in the entire phase-space region and a complementary approach must be used. Then, we propose to match the description based on PAs to that given by Eq. (7.4) at a certain energy point[10]. Given the mass and the width of the ρ meson, the first of the resonances included in the VMD description, the region of influence due to its presence may be defined using the half-width rule as $M_\rho \pm \Gamma_\rho/2$ [238], thus deducing the value of the radius ε mentioned earlier. The particular energy point located at $\sqrt{s} \simeq 0.70$ GeV, the lowest value of the former

---

[8]We thank S. Damjanovic from the NA60 experiment for providing us with the time-like TFF data points obtained from $\eta \to \mu^+ \mu^- \gamma$.

[9]The coefficients of the PAs along with their errors and the correlation matrix can be obtained from the authors upon request.

[10]To proceed with the matching, we have considered an energy-dependent width for the ρ resonance,

$$\Gamma_\rho(q^2) = \Gamma_\rho \frac{q^2}{M_\rho^2} \frac{\sigma^3(q^2)}{\sigma^3(M_\rho^2)} \ ,$$

with $\sigma(q^2) = \sqrt{1 - 4M_\pi^2/q^2}$, and a constant width for the ω and ϕ narrow resonances. Input values for the masses and widths as well as for the rest of the couplings entering Eq. (7.4) are taken from Ref. [37].
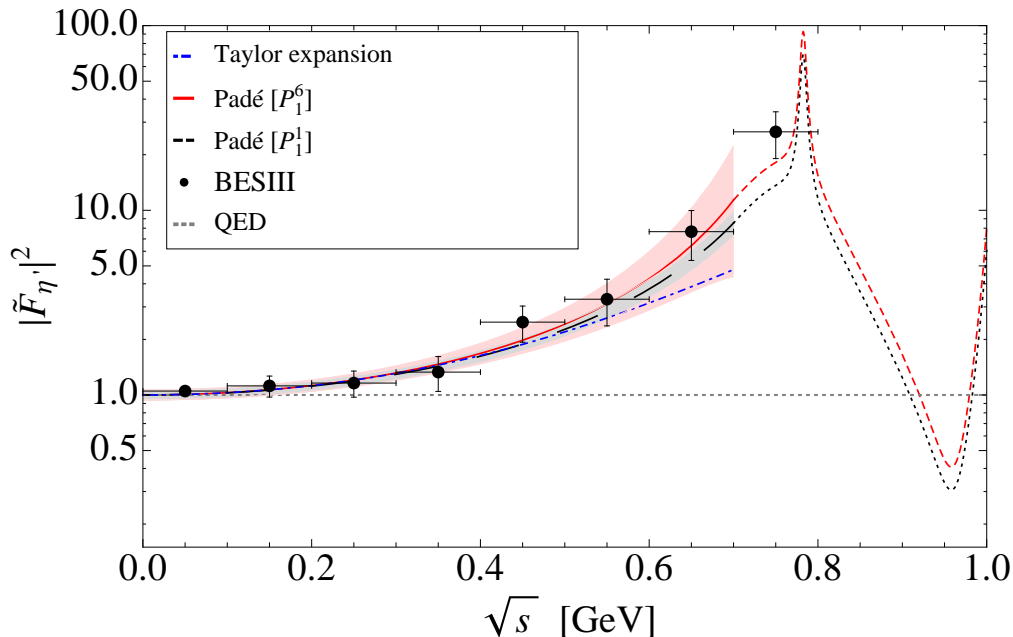
Figure 7.2: Modulus square of the normalized time-like η' TFF, $\widetilde{F}_{\eta'\gamma\gamma^*}(q^2)$, as a function of the invariant dilepton mass, $\sqrt{s} \equiv m_{\ell\ell}$. The predictions up to the matching point located at $\sqrt{s} = 0.70$ GeV coming from the $P_1^6(q^2)$ (red solid line) and $P_1^1(q^2)$ (black long-dashed line) PAs, and the Taylor expansion (blue dot-dashed line) are compared to the experimental data from $\eta' \to e^+e^-\gamma$ [25] (black circles). From the matching point on, rescaled versions of the VMD description in Eq. (7.4) are used. The one-sigma error bands associated to $P_1^6(q^2)$ (light-red) and $P_1^1(q^2)$ (light-gray) PAs, and the QED prediction (gray short-dashed line) are also displayed.

region for $M_\rho \simeq 775$ MeV and $\Gamma_\rho \simeq 150$ MeV, fixes the optimal matching point[11]. Fixed this value, a representation valid in the whole phase-space domain is that given by the PA below the matching point an Eq. (7.4) above it. In order to match both descriptions of the form factor at the matching point we have to rescale the VMD result accordingly. In this manner, we keep track of the resonant behaviour in the upper part of the spectrum where PAs cannot be applied, while the low-energy region is predicted in a more systematic way as compared to VMD by PAs established uniquely from space-like data. This will allow us to integrate the whole spectrum and predict the branching ratio of the several η' Dalitz decays considered here.

Our predictions for the time-like η' TFF together with the experimental data points from the BESIII Collaboration on the decay $\eta' \to e^+e^-\gamma$ [25] (black circles) are displayed in figure 7.2. The results from the $P_1^6(q^2)$ (red solid line) and $P_1^1(q^2)$

---

[11]The region of influence attributed to the ω and ϕ poles is negligible since these are narrow resonances and are placed far from the matching point.

(black long-dashed line) are shown up to the matching point. The corresponding error bands are in light-red and light-gray, respectively. These bands include, as for the case of the η TFF, the uncertainty in the coefficients of the PAs, the normalization factor extracted from the two-photon decay width and a systematic error arising from $b_{\eta'}$ and $c_{\eta'}$. From the matching point on our predictions are replaced by a rescaled VMD representation based on the three lowest-lying vector resonances. Our PAs-based predictions are again in fine agreement with experiment. A Taylor expansion with $b_{\eta'} = 1.30(15)_{\text{stat}}(7)_{\text{sys}}$ and $c_{\eta'} = 1.72(47)_{\text{stat}}(34)_{\text{sys}}$ [22] is also included for comparison. It is worth mentioning that an extrapolation of the $P_1^6(q^2)$ PA beyond the matching point nicely passes through the last experimental point. This can be understood in the following terms. The VMD description includes three resonances whose poles are located at different places, while the $P_1^L(q^2)$ PAs include only one. Making use of the single pole approximation in Eq. (7.3) and the Taylor expansion in Eq. (7.6) for the case of the η', the slope parameter is identified as $b_{\eta'} = m_{\eta'}^2/\Lambda^2$. Using the $b_{\eta'}$ value deduced from Eq. (7.4) one gets $\Lambda = M_{\text{eff}} = 0.822(58)$ GeV, where the error is due to the half-width rule and can be utilized as a measure of the region of influence of the pole. The former value is very similar to the one obtained from the pole position of the $P_1^6(q^2)$ PA, located at $\sqrt{s} = 0.833$ GeV. Therefore, the region of influence of this pole can be estimated to be in the interval $(0.77, 0.89)$ GeV. It is for this reason that the last experimental point would be also in agreement with the $P_1^6(q^2)$ prediction [236]. This is not so for the $P_1^1(q^2)$ PA, thus showing that increasing the Padé order allows for a better description of the data. In any case, for the numerical analysis of the different decays involving the η' we also keep both PAs for the sake of comparison.

7.1.4 $\mathcal{P} \to \gamma^*\gamma^*$

The double-virtual TFF, $F_{\mathcal{P}\gamma^*\gamma^*}(q_1^2, q_2^2)$, depends on both photon virtualities, q_1 and q_2. Due to Bose symmetry, it must satisfy $F_{\mathcal{P}\gamma^*\gamma^*}(q_1^2, q_2^2) = F_{\mathcal{P}\gamma^*\gamma^*}(q_2^2, q_1^2)$. Its normalization is obviously the same as the single virtual TFF, $F_{\mathcal{P}\gamma^*\gamma^*}(0, 0) = F_{\mathcal{P}\gamma\gamma^*}(0)$, and can be extracted either from the two-photon partial width by means of Eq. (7.1) or from the axial anomaly. It must also satisfy that when one of the photons is put on-shell the double-virtual TFF becomes the single-virtual one, i.e. $\lim_{q_i^2 \to 0} F_{\mathcal{P}\gamma^*\gamma^*}(q_1^2, q_2^2) = F_{\mathcal{P}\gamma\gamma^*}(q^2)$ for $i = 1, 2$. In addition, the double-virtual TFF can fulfil the following asymptotic space-like constraints, $\lim_{Q^2 \to \infty} F_{\mathcal{P}\gamma^*\gamma^*}(-Q^2, 0) \propto 1/Q^2$ [?] and $\lim_{Q^2 \to \infty} F_{\mathcal{P}\gamma^*\gamma^*}(-Q^2, -Q^2) \propto 1/Q^2$ [219].

Due to the lack of experimental information in the case of double-virtual TFFs, our initial ansatz will be to use the standard factorisation approach, which in terms of normalized form factors reads $\widetilde{F}_{\mathcal{P}\gamma^*\gamma^*}(q_1^2, q_2^2) = \widetilde{F}_{\mathcal{P}\gamma\gamma^*}(q_1^2, 0)\widetilde{F}_{\mathcal{P}\gamma\gamma^*}(0, q_2^2)$ [239, 240, 241]. This double-virtual TFF description may or may not satisfy the high-energy constraints above. For instance, the PA $P_1^0(q^2) = a_0/(1 - a_1 q^2)$, corresponding to the single pole approximation in Eq. (7.3) motivated by VMD, would induce a $1/q^4$ term in the double-virtual TFF, which violates the last of the asymptotic constraints mentioned before (OPE prediction) [219, 242, 243, 244]. For this reason, we also use for our study the lowest order bivariate approximant

$$P_1^0(q_1^2, q_2^2) = \frac{a_{0,0}}{1 - \frac{b_{1,0}}{M_{\mathcal{P}}^2}(q_1^2 + q_2^2) + \frac{b_{1,1}}{M_{\mathcal{P}}^4}q_1^2 q_2^2} \, , \tag{7.8}$$

which consists in a generalization of the univariate PAs named Chisholm approximants (CAs) [200]. The analysis of the $\pi^0 \to e^+e^-$ decay is a recent example that illustrates the application of these CAs [203]. In Eq. (7.8), $a_{0,0}$ is identified as the normalization $F_{\mathcal{P}\gamma^*\gamma^*}(0,0)$ and then fixed from Eq. (7.1), $b_{1,0}$ is the slope of the single-virtual TFF obtained in refs. [21, 22], that is, b_π from Eq. (7.7) for the pion and $b_{\eta^{(\prime)}}$ from Eq. (5) in Ref. [22] for the η and η', respectively, and $b_{1,1}$ would correspond to the double-virtual slope which may be extracted in the future as soon as experimental data for the double-virtual TFFs become available. For the numerical analysis, we consider, as a conservative estimate, to vary $b_{1,1}$ from the value respecting the OPE prediction, $b_{1,1} = 0$, to $b_{1,1} = 2b_{1,0}^2$, far from the factorisation result $b_{1,1} = b_{1,0}^2$. In this manner, we can test the sensitivity of our predictions to the double-virtual slope. We also encourage experimental groups to perform double-virtual TFF measurements in order to fix this parameter. In this work, we employ both descriptions indistinctly, the factorisation ansatz and the bivariate approximant in Eq. (7.8). See also Ref. [245] for a recent approach to the double-virtual TFF of the η meson based on the standard factorisation approach.

7.2 Single Dalitz Decays

Single Dalitz decays involve the single virtual TFF as described in section 7.1. The amplitude of the decays reads

$$\mathcal{A}(\mathcal{P}(p) \to \ell^+\ell^-\gamma) = -ie^2 F_{\mathcal{P}\gamma\gamma^*}(s)\varepsilon^{\alpha\beta\mu\nu}p_\alpha q_\beta \epsilon_\mu^*(k)\frac{-ig_{\nu\rho}}{s}\bar{u}(p_{\ell^-})(-ie)\gamma^\rho v(p_{\ell^+}) \, , \tag{7.9}$$

Source	$\mathcal{BR}(\pi^0 \to e^+e^-\gamma) \cdot 10^2$
this work	1.169(2)
QED	1.172
Experimental	1.174(35) [37]
measurements	1.140(41) [205]

Table 7.1: Comparison betwen our $\mathcal{BR}$ prediction for $\pi^0 \to e^+e^-\gamma$ and experimental measurements.

while the corresponding differential decay rate is given by

$$\frac{d\Gamma_{\mathcal{P}\to\ell^+\ell^-\gamma}}{d\sqrt{s}\,\Gamma^{\exp}_{\mathcal{P}\to\gamma\gamma}} = \frac{4\alpha}{3\pi\sqrt{s}}|\widetilde{F}_{\mathcal{P}\gamma\gamma^*}(s)|^2 \left(1 - \frac{s}{M_\mathcal{P}^3}\right)^3 \sqrt{1 - \frac{4m_\ell^2}{s}}\left(1 + \frac{2m_\ell^2}{s}\right), \qquad (7.10)$$

where the TFF appears in its helpful normalized version in order to avoid misunderstandings due to different conventions on the definition of $F_{\mathcal{P}\gamma\gamma^*}(0)$ existing in the literature. Notice that the experimental measurement of the partial width to two photons appears as a normalization in any case. For our numerical calculations we employ the PrimEx Collaboration result $\Gamma_{\pi^0\to\gamma\gamma} = 7.82(14)(17) \cdot 10^{-6}$ MeV [246] and the values collected in the PDG $\Gamma_{\eta\to\gamma\gamma} = 5.16(18) \cdot 10^{-4}$ MeV and $\Gamma_{\eta'\to\gamma\gamma} = 4.35(14) \cdot 10^{-3}$ MeV [37].

7.2.1 $\pi^0 \to e^+e^-\gamma$

The decay $\pi^0 \to e^+e^-\gamma$ was suggested for the first time by Dalitz in 1951 [247]. The first $\mathcal{BR}$ prediction arose from a pure QED radiative correction calculation neglecting the momentum dependence of the TFF [248] (radiative corrections have recently been revisited in Ref. [249]). By looking at figure 7.3 where we compare, as a function of the invariant mass of the dielectron pair, our description of the decay rate distribution (green solid curve) with the QED result (gray dashed curve), this seems to be a reasonable approximation since the main contribution to the decay rate comes from the very low-energy part of the spectrum where the effect of the TFF is almost negligible. In fact, there is an almost perfect overlap between the two curves and only really tiny differences appear on the second half of the spectrum. Numerical results for the $\mathcal{BR}$ are presented in table 7.1. Our prediction is in very good agreement with the experimental measurements. The main source of the error we have quoted arise from the uncertainty associated to the low energy constants, Eq. (7.7), which include also the error associated to the measured decay width to two photons [246]. Our results are also in agreement with other theoretical predictions existing in literature,
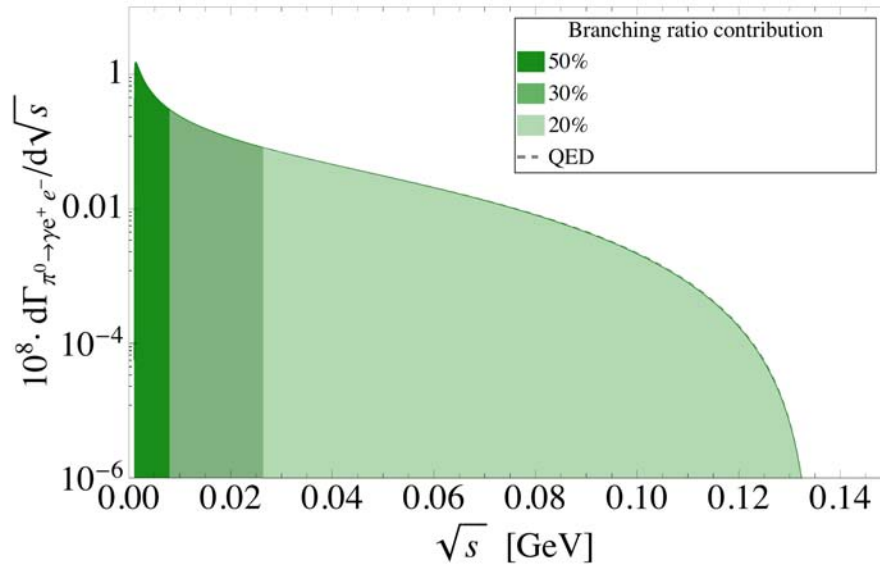
Figure 7.3: Differential decay rate distribution for $\pi^0 \to e^+e^-\gamma$ as a function of the invariant mass of the dielectron pair. Green solid curve corresponds to our description while the gray dashed curve accounts for the QED prediction.

refs. [220, 226, 233, 224], as well as with the QED estimates of refs. [224, 250, 251]. The dimuon mode in the final state is not kinematically allowed in this case.

7.2.2 $\eta \to \ell^+\ell^-\gamma$ $(\ell = e, \mu)$

Qualitatively, this is the same process as the π^0 Dalitz decay, with the novelty that a dimuon pair in the final state is also allowed since the larger mass of the η increases the upper kinematic limit. *A priori*, these decays are expected to be more challenging for testing the momentum dependence of the TFF because the energy released in the process is now larger, expecting higher deviations from the QED estimates. This is precisely what our predictions reflect in figure 7.4 where the decay rate distribution of $\eta \to e^+e^-\gamma$ (blue solid curve) and $\eta \to \mu^+\mu^-\gamma$ (black solid curve) are compared to the QED estimates (gray dotted and dashed curves, respectively). As a matter of example we have employed the $P_1^L(q^2)$ Padé type in the figure, here and hereafter. Diagonal PAs, $P_N^N(q^2)$, would produce very similar description in accordance with the transition form factors descriptions given in sections 7.1.2 and 8. One interesting feature of both decays modes is that, in absolute terms, the effect of the TFF is much more sizable in the muonic case than in the electronic one. The reason is because the shape of the distribution of the latter shows, as occurred in $\pi^0 \to e^+e^-\gamma$, a strong peak in the low-momentum transferred region of the spectrum, where the effect of the TFF is small, which provides the main contribution to the $\mathcal{BR}$. Noticeably, the high
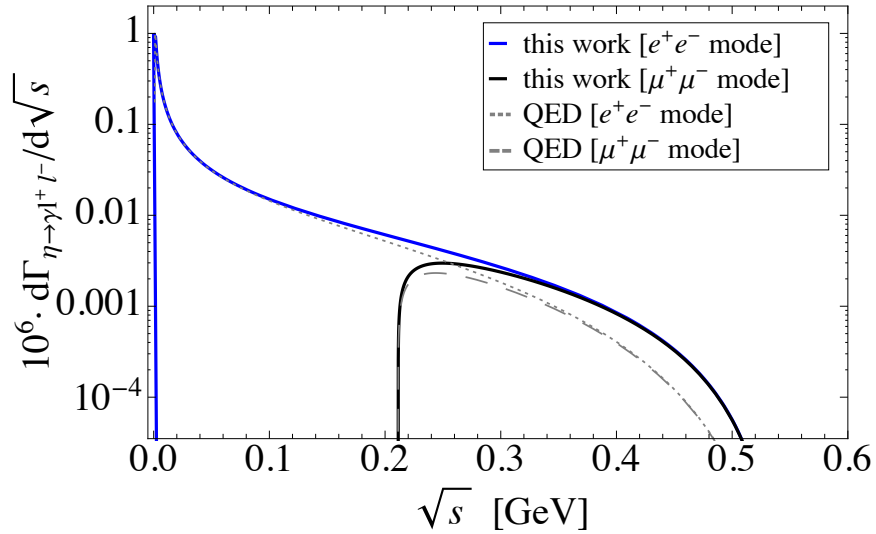
Figure 7.4: Decay rate distribution for $\eta \to e^{+} e^{-} \gamma$ (blue solid curve) and $\eta \to \mu^{+} \mu^{-} \gamma$ (black solid curve). The corresponding QED estimates are also displayed (gray dotted and long-dashed curves, respectively).

Source	$\mathcal{BR}(\eta \to e^{+}e^{-}\gamma) \cdot 10^{3}$	$\mathcal{BR}(\eta \to \mu^{+}\mu^{-}\gamma) \cdot 10^{4}$
this work $[P_1^5]$	$6.60^{+0.50}_{-0.47}$	$3.25^{+0.40}_{-0.36}$
this work $[P_2^2]$	$6.61^{+0.53}_{-0.49}$	$3.30^{+0.65}_{-0.56}$
QED	6.38	2.17
Experimental measurements	$6.9(4)$[37] $6.6(4)_{\text{stat}}(4)_{\text{syst}}$ [206] $6.72(7)_{\text{stat}}(31)_{\text{syst}}$ [209]	$3.1(4)$ [37]

Table 7.2: Comparison between our $\mathcal{BR}$ predictions for $\eta \to \ell^{+}\ell^{-}\gamma$ and experimental measurements.

energy part of the spectrum of both modes is overlapped as it may be since the only difference between them is the dilepton threshold production. Numerically, we see from table 7.2 that the $\mathcal{BR}$ involving muons in the final state has increased by 50% with respect to the QED prediction while the effect is much less considerable when dealing with electrons ($\sim 3.5\%$) where, predictions with and without considering TFF effects are compatible within errors at the current level of accuracy. The source of the associated errors arise from the error bands shown in figure 7.1. In all, our predictions are in good agreement with present experimental measurements. Comparing with other authors results, we agree with: the QED estimates of Ref. [251], the predictions of Ref. [233] and the values of Ref. [225], while tiny differences with Ref. [226] are noticed.
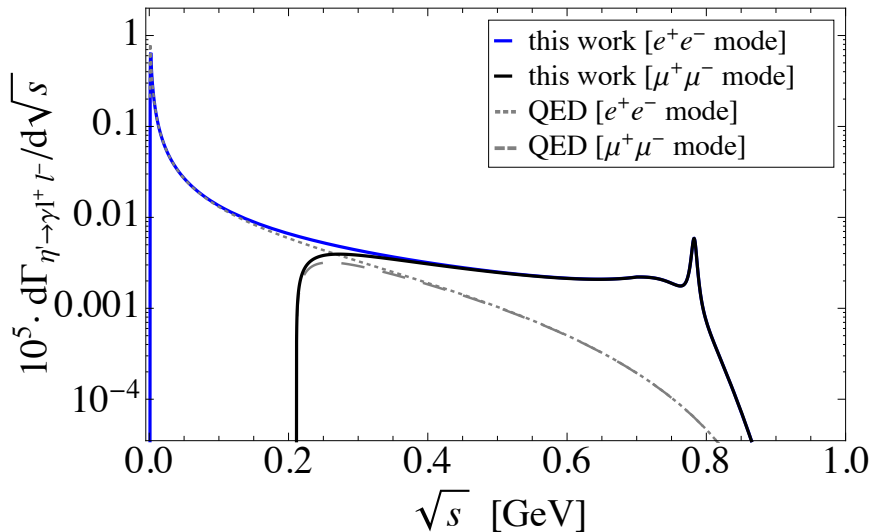
Figure 7.5: Decay distributions for $\eta' \to e^+ e^- \gamma$ (blue solid curve) and $\eta' \to \mu^+ \mu^- \gamma$ (black solid curve). The QED estimates are also shown (gray dotted and long-dashed curves, respectively).

7.2.3 $\quad \eta' \to \ell^+ \ell^- \gamma \ (\ell = e, \mu)$

The large mass of the η' increases the upper kinematical limit by ~ 410 MeV with respect to the case of the η. The TFF description is given in section 8, where the effect of the intermediate vector resonances ρ, ω and ϕ is included. As shown in figure 7.5, the distribution of the decay $\eta' \to e^+ e^- \gamma$ (blue solid curve) evidences again a marked peak at low-energies which, despite the contribution coming from the resonance region, dominates the decay as occurred in $\pi^0(\eta) \to e^+ e^- \gamma$. On the contrary, the effect of the TFF on the decay $\eta' \to \mu^+ \mu^- \gamma$ (black solid curve) is larger than in $\eta \to \mu^+ \mu^- \gamma$, increasing the $\mathcal{BR}$ by a factor of about 2. This is so because both phase space considerations and the effect of passing through a q^2 region where resonances may be produced on-shell. Interestingly, the contribution due to the ρ resonance bends the distribution while the inclusion of the ω resonance accounts for the sharp peak at around 0.8 GeV. Numerical results are presented in table 7.3, where the source of the error comes from the error bands associated to the TFF. From the theory side, our predictions are in accordance with those of Ref. [233], while they are slighlty below respect to both the recent experimental measurement of $\eta' \to e^+ e^- \gamma$ [25] and the old measurement of $\eta' \to \mu^+ \mu^- \gamma$ [211], though in agreement within errors in both cases. To sum up, the pattern of both η and η' single Dalitz decays is notably similar: the impact of the TFF on the muonic channel is much larger than in the electronic ones as discussed in section 7.2.2.

Source	$\mathcal{BR}(\eta' \to e^+e^-\gamma) \cdot 10^4$	$\mathcal{BR}(\eta' \to \mu^+\mu^-\gamma) \cdot 10^4$
this work $[P_1^6]$	$4.42^{+0.39}_{-0.35}$	$0.81^{+0.16}_{-0.13}$
this work $[P_1^1]$	$4.35^{+0.29}_{-0.27}$	$0.74(6)$
QED	3.94	0.38
Experimental measurements	$4.69(20)_{\text{stat}}(23)_{\text{sys}}$ [25]	$1.08(27)$ [211]

Table 7.3: Comparison between our $\mathcal{BR}$ predictions for $\eta' \to \ell^+\ell^-\gamma$ and experimental measurements.

7.3 Double Dalitz Decays

Double Dalitz decays involve the TFF of double virtuality as described in section 7.1. They implicate four particles in the final state which makes the phase space integration much more tedious. In case of having two pairs of non-identical particles, that is $\eta^{(\prime)} \to e^+e^-\mu^+\mu^-$, the required diagram is shown in figure 7.6 (left diagram) and the amplitude of the decay reads

$$\mathcal{A}(\eta^{(\prime)} \to e^+e^-\mu^+\mu^-) = -i2! \frac{e^4}{q^2 k^2} F_{\mathcal{P}\gamma^*\gamma^*}(q^2, k^2) \varepsilon^{\mu\nu\alpha\beta} q_\mu k_\nu \bar{u}(q_{e^-})\gamma_\alpha v(q_{e^+}) \bar{u}(q_{\mu^-})\gamma_\beta v(q_{\mu^+}) \,. \tag{7.11}$$

The corresponding decay rate distribution can be reduced to[12]

$$\frac{d^2\Gamma}{dM^2_{e^+e^-}M^2_{\mu^+\mu^-}\Gamma^{\text{exp}}_{\eta^{(\prime)}\to\gamma\gamma}} = \quad \mathcal{S}\frac{8\alpha^2}{9\pi^2 m^6_{\eta^{(\prime)}}}|\widetilde{F}(q^2,k^2)|^2\sqrt{1-\frac{4m_e^2}{k^2}}\sqrt{1-\frac{4m_\mu^2}{q^2}}\frac{\left(1+\frac{2m_e^2}{k^2}\right)\left(1+\frac{2m_\mu^2}{q^2}\right)}{k^2 q^2}$$
$$\left[\frac{1}{4}(m^2_{\eta^{(\prime)}} - (k^2+q^2))^2 - k^2 q^2\right]^{3/2} \,, \tag{7.12}$$

where, in this case, $\mathcal{S} = 2$ in agreement with the expression given in Ref. [234]. The TFF appears again normalized to unity at the origin.

On the contrary, in case of having two pairs of identical particles in the final state, that is $\mathcal{P} \to e^+e^-e^+e^-$ or $\eta^{(\prime)} \to \mu^+\mu^-\mu^+\mu^-$, one should consider both the direct and exchange diagrams of figure 7.6 (left and right diagrams). Therefore, the total amplitude of the process reads

$$\mathcal{A} = \mathcal{A}_{\text{dir}} - \mathcal{A}_{\text{exch}} \,, \tag{7.13}$$

where the appearance of the minus sign is due to the exchange of two indistinguishable fermions in the final state. Then, squaring the amplitude of Eq. (7.13) we arrive at

$$|\mathcal{A}|^2 = |\mathcal{A}_{\text{dir}}|^2 + |\mathcal{A}_{\text{exch}}|^2 - 2(\Re\mathcal{A}_{\text{dir}}\mathcal{A}^*_{\text{exch}}) \,, \tag{7.14}$$

---

[12]See, for instance, Ref. [252] for reducing distributions of four body-final-state decays into two invariant masses.
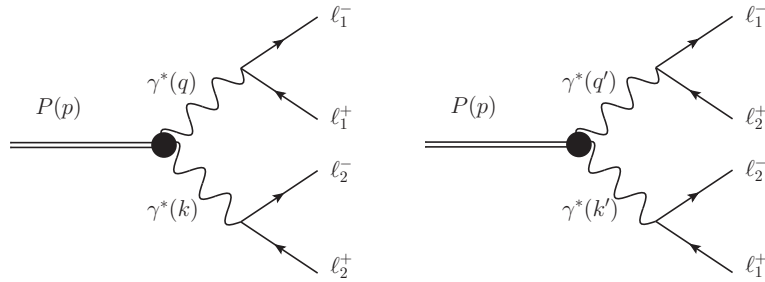
Figure 7.6: Double Dalitz direct (left) and exchange (right) diagrams.

where not only appear the contributions from both the direct and exchange diagrams but an interference term. We notice that the contribution to the partial decay width coming from the first and the second term of Eq. (7.14) is obviously the same, that is $\Gamma_{\text{dir}} = \Gamma_{\text{exch}}$, because the integration variables are nothing more than dummy indices. In this way, the contribution coming from the sum of the direct and exchange diagrams, $\Gamma_{\text{dir+ex}}$, is obtained through the use of Eq. (7.12), of course after permuting $\mu \to e$ (or equivalently $e \to \mu$), now with $\mathcal{S} = 1$ once the factor of $\frac{1}{2!2!}$, accounting for the two pairs of two identical particles in the final state, has been taken into account. Regarding the interference term, its computation is much more cumbersome. We have relegated to appendix E the detailed expression due to its length but it is worth to comment that we have obtained an expression in terms of five invariant masses which has required a Monte Carlo (MC) simulation to be integrated.

7.3.1 $\pi^0 \to e^+e^-e^+e^-$

The only possible double Dalitz decay of the neutral pion is $\pi^0 \to e^+e^-e^+e^-$, other possibilities are not kinematically allowed. In view of the results from $\pi^0 \to\to e^+e^-\gamma$, one may expect that the overall effect of the TFF will be again small. In figure 7.7, we show our results for the different contributions to the decay rate distribution as a function of the invariant mass of one dielectron pair of the direct diagram. Concretely, we display the curve corresponding to the direct diagram (green solid line), the curve of the contribution of the exchange diagram expressed in terms of the former dielectron invariant mass of the direct diagram[13] (red dotted line), the interference term (blue dotted line) and finally the total distribution (black dotted line). We want to note that the contribution from both direct and exchange diagrams

---

[13]The curve of the exchange diagram expressed in its own variables would look equal as the green solid line of figure 7.7. In this work, we have opted to show, in just one figure, all the contributions as a function of one dielectron invariant mass of the direct diagram. In this convention, the exchange diagram as expressed in figure 7.7 has also required a MC integration.
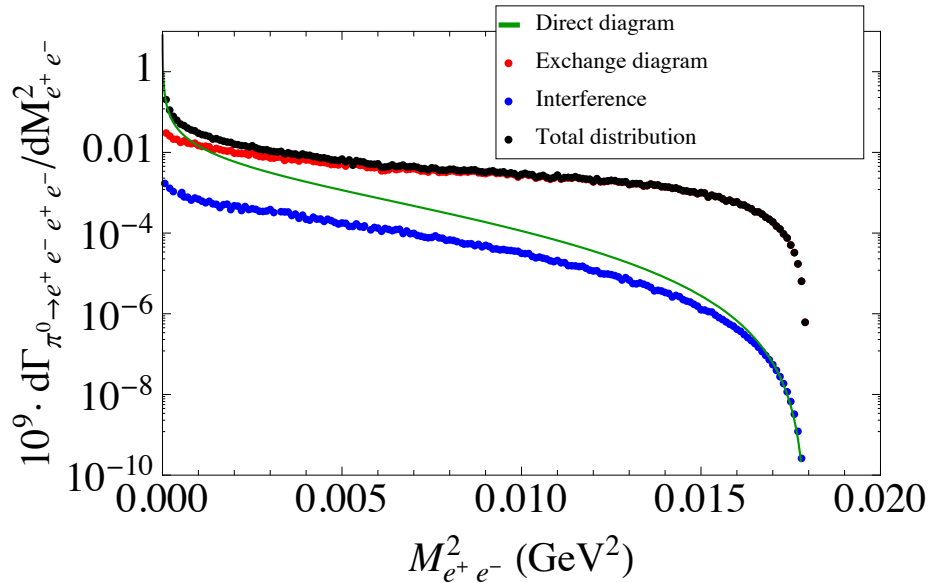
Figure 7.7: Different contributions to the $\pi^0 \to e^+e^-e^+e^-$ decay distribution. Direct diagram (green solid curve), exchange diagram (red dotted curve), interference term (blue dotted curve) and total distribution (black dotted curve) are shown as a function of one dielectron invariant mass of the direct diagram.

integrates obviously the same and that the interference is small and destructive. Our $\mathcal{BR}$ predictions are shown in table 7.4 from which we corroborate that the effect of the TFF is small because the main contribution to the $\mathcal{BR}$ proceeds from the very low-momentum transferred region where we a peak emerges, as already occurred in $\pi^0 \to e^+e^-\gamma$. Our results are well in accordance with current experimental measurements. The source of the associated error comes from the uncertainty on the low-energy parameters Eq. (7.7). Notice that the sensitivity of this decay to the variations of the double virtual slope parameter, $b_{1,1}$, is at the fifth decimal number. In this sense,

Source	Double virtual TFF		$\mathcal{BR}(\pi^0 \to e^+e^-e^+e^-) \cdot 10^5$	
			direct+exchange	interference
This work	Chisholm approximants	$b_{1,1} = 0$	3.40287(9)	-0.03602
		$b_{1,1} = b_{1,0}$	3.40286(9)	-0.03602
		$b_{1,1} = 2b_{1,0}$	3.40286(9)	-0.03602
	factorisation approach	Eq.(7.6)	3.40295(9)	-0.03602
	QED		3.41607	-0.03484
Experimental measurements			3.38(16) [37] 3.46(19) [212]	

Table 7.4: Branching ratio predictions for $\pi^0 \to e^+e^-e^+e^-$ compared with experimental measurements.
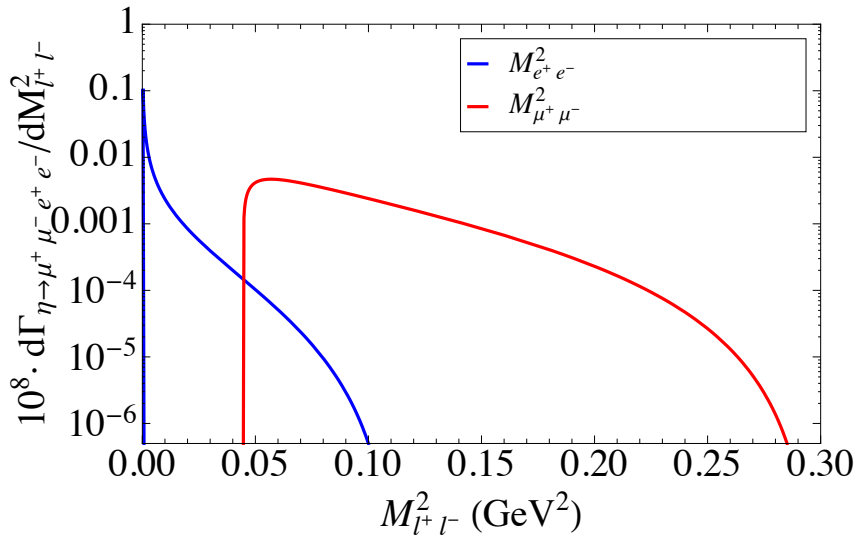
Figure 7.8: Decay distribution for $\eta \to e^+e^-\mu^+\mu^-$ with respect to the dielectron (blue curve) and to the dimuon (red curve) invariant mass.

the high level of accuracy demanded to infer its value is unthinkable at the current precision level. It is also interesting to compare with other authors results. We are in good agreement with the results given in refs. [239, 233, 234] for the direct and exchange contributions while the result of Ref. [226] is about 5% lower than our predictions. Regarding the interference term we have, a perfect agreement with refs. [239, 233] and a value about 30% higher than Ref. [234] while Ref. [226] did not consider this term. Comparing with previous QED estimates we agree with refs. [250, 251] for the direct and exchange contributions. For the interference term the former did not consider it and the later gave a result 5 times larger than us.

7.3.2 $\eta \to \ell^+\ell^-\ell^+\ell^- \ (\ell = e, \mu)$

The double Dalitz decays of the η meson, $\eta \to e^+e^-e^+e^-$, $\eta \to \mu^+\mu^-\mu^+\mu^-$, and $\eta \to e^+e^-\mu^+\mu^-$, are now kinematically allowed. Let us first analyze the latter for simplicity. In this case, the two dilepton pairs are different and consequently there is no interference phenomenon. Hence, the distribution rate is just given by Eq. (7.12) and shown in figure 7.8 in two different manners, one expressed in terms of the dielectron invariant mass and the other in the dimuon variable (blue and red solid lines respectively), where, of course, both curves integrate the same. Our predictions are shown in table 7.5, where the source of the associated errors comes from the error bands associated to the TFF for the case of the factorisation approach, and from the uncertainty on the single virtual slope for the description employing CAs.

Source	Double virtual TFF		$\mathcal{BR}(\eta \to e^+e^-\mu^+\mu^-) \cdot 10^6$
This work	Chisholm approximants	$b_{1,1} = 0$	2.39(12)
		$b_{1,1} = b_{1,0}$	2.39(12)
		$b_{1,1} = 2b_{1,0}$	2.38(12)
	factorisation approach	P_1^5	$2.35^{+0.47}_{-0.40}$
		P_2^2	$2.39^{+0.66}_{-0.53}$
	QED		1.57
Experimental measurement			$< 1.6 \cdot 10^{-4}$ (90% CL) [208]

Table 7.5: Branching ratio predictions for $\eta \to \mu^+\mu^-e^+e^-$ compared to the current experimental upper bound.

From the experimental side, we respect the current upper limit, while from the theory side, because of the appearance of a dimuon pair in the final state, the effect of the TFF increases the $\mathcal{BR}$ about 50% for the same arguments as explained in $\eta \to \ell^+\ell^-\gamma$. This decay, though much more sensitive than $\pi^0 \to e^+e^-e^+e^-$ to the double virtual slope, $b_{1,1}$, would require accurate measurements as well as demanding a very precise description of the TFF, in order to diminish its associated error, for deducing $b_{1,1}$, far from the present situation. Comparing with other authors, we agree with the predictions of Ref. [233], while we have found discrepancies with the value $5.83 \cdot 10^{-7}$ of Ref. [226], with the prediction $2 \cdot 10^{-7}$ of Ref. [225] and with the estimate $7.84 \cdot 10^{-7}$ of Ref. [251]. In the later case, the reason seems to be a typographical fault of a factor of 2 missing as pointed out in both refs. [239, 233]. In such case, it would reproduce the QED result of table 7.5 as it should be, because they did not consider the momentum dependence of the TFF.

The decays involving two identical dilepton pairs in the final state, $\eta \to e^+e^-e^+e^-$ and $\eta \to \mu^+\mu^-\mu^+\mu^-$, require to consider Eq. (7.14). Their distributions are given in figure 7.9 (left and right panels respectively) as a function of one dilepton invariant mass of the direct diagram. We explicitly show the contribution from the direct diagram (green solid curve), the curve of the exchange diagram expressed in terms of the former dielectron (dimuon) invariant mass of the direct diagram (red dotted curve), the interference term (blue dotted curve) and the total decay rate distribution (black dotted line). The integrated $\mathcal{BR}$ results are shown in table 7.6 where the error comes again from the error bands of the TFF description as given in figure 7.1, for the factorisation approach, and from the uncertainty associated to the slope, b_η, for the description using CAs.

Comparing with present experimental status, our prediction for $\eta \to e^+e^-e^+e^-$ is compatible at less than 1σ with the KLOE measurement [213] as well as with
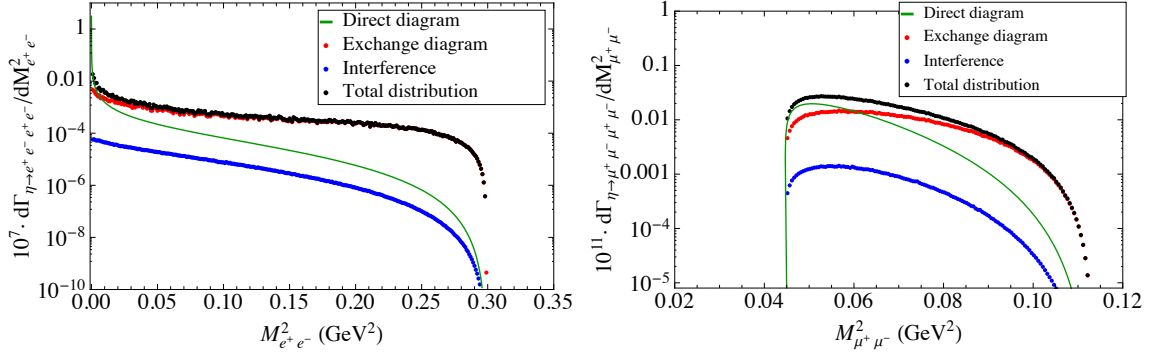
Figure 7.9: Different contributions to the decay distributions of $\eta \to e^+e^-e^+e^-$ (left) and $\eta \to \mu^+\mu^-\mu^+\mu^-$ (right), respectively. Direct diagram (green solid curve), exchange diagram (red dotted curve), interference term (blue dotted curve) and the total distribution (black dotted curve) are displayed with respect to one dilepton invariant mass of the direct diagram.

Source		TFF	$\mathcal{BR}(\eta \to e^+e^-e^+e^-) \cdot 10^5$		$\mathcal{BR}(\eta \to \mu^+\mu^-\mu^+\mu^-) \cdot 10^9$	
			dir+exch	inter	dir+exch	inter
This work	CAs	$b_{1,1}=0$	2.74(3)	-0.02	4.47(33)	-0.32
		$b_{1,1}=b_{1,0}$	2.73(3)	-0.03	4.31(31)	-0.32
		$b_{1,1}=2b_{1,0}$	2.73(3)	-0.03	4.15(30)	-0.32
	fact.	P_1^5	$2.72^{+0.43}_{-0.70}$	-0.03	$4.23^{+0.83}_{-0.70}$	-0.43
		P_2^2	$2.73^{+0.45}_{-0.39}$	-0.03	$4.30^{+1.12}_{-0.91}$	-0.47
	QED		2.56	-0.02	2.59	-0.19
Exp. measurements			$3.2(9)_{\text{stat}}(5)_{\text{sys}}$ [209] $2.4(2)_{\text{stat}}(1)_{\text{sys}}$ [213]		$< 3.6 \cdot 10^{-4}$ (90% CL) [208]	

Table 7.6: Branching ratio predictions for $\eta \to e^+e^-e^+e^-$ and $\eta \to \mu^+\mu^-\mu^+\mu^-$ confronted to current experimental status.

the recent measurement value of the WASA@COSY collaboration [209], while our estimate for $\eta \to \mu^+\mu^-\mu^+\mu^-$ respects the current upper bound of Ref. [208]. We have found the same trend as in $\eta \to \ell^+\ell^-\gamma$ that is, while the overall effect of the TFF on the electronic mode is small, increasing the $\mathcal{BR}$ of $\eta \to e^+e^-e^+e^-$ by 6% respect to the QED estimate, the impact on the muonic channel, $\eta \to \mu^+\mu^-\mu^+\mu^-$, becomes important increasing the $\mathcal{BR}$ by a factor ranging $(1.6 - 1.7)$ respect to the QED calculation. As a consequence of that, the sizable sensitivity of $\eta \to \mu^+\mu^-\mu^+\mu^-$ to the TFF of double virtuality makes it a good candidate to improve our knowledge on it. Interestingly, a precise experimental measurement of this mode at the per cent level of precision leaves us in position to estimate the value of $b_{1,1}$. For that purpose, it is also required to diminish the associated uncertainty to the TFF. Here enters the ability of the Padé method we use for accommodating new experimental data as soon as released by experimental groups. On the contrary, this same exercise for $\eta \to e^+e^-e^+e^-$ would demand accurate measurements at the per mil level to unveil this quantity, far from the present situation. Our predictions are in good agreement with the results of Ref. [233] for the electronic mode, while a $(10 - 15)\%$ over the muonic prediction. Comparing with Ref. [226] (who did not considered the interference term) we are a 10% over for the electronic case while his result for $\eta \to \mu^+\mu^-\mu^+\mu^-$ is 60% smaller. We are also in accordance with the estimate of Ref. [225] for $\eta \to e^+e^-e^+e^-$. Regarding the pure QED calculation of Ref. [251], we are in perfect agreement for the electronic channel while tiny differences are found in the muonic decay, probably caused by the updated values of our inputs values.

7.3.3 $\eta' \to \ell^+\ell^-\ell^+\ell^-$ ($\ell = e, \mu$)

Regarding the double Dalitz decays of the η', we have the same three possible final states as for the η. However, in this case we have only adopted the factorisation approach ansatz for describing the double virtual TFF of the η'. The reason is because the use of Chisholm approximants, which may respect the appropriate asymptotic behavior q^{-2}, would only apply at low energies, concretely up to the matching point where PAs are applicable, while beyond, we are somehow forced to employ the factorisation approximation, through a VMD description, which induces a q^{-4} term. So, there is no gain respecting the high-energy behavior in the low-energy region if we violate it at high energies. We compute first $\eta' \to e^+e^-\mu^+\mu^-$ again through Eq. (7.12). Noticeably, it follows the same trend as $\eta \to e^+e^-\mu^+\mu^-$, with the difference that this case is sensitive to the resonance region as can be read off from figure 7.10. Once more, the low-momentum region basically dominates the distribution when working
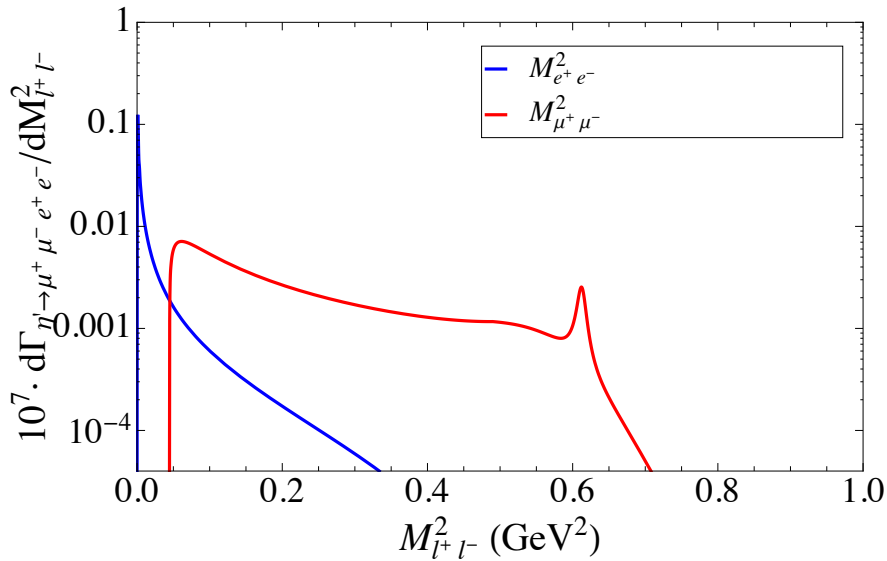
Figure 7.10: Decay distribution for $\eta' \to \mu^+\mu^-e^+e^-$ shown as a function of the dielectron and of the dimuon invariant masses (blue and red solid curves respectively).

Source	$\mathcal{BR}(\eta' \to \mu^+\mu^-e^+e^-) \cdot 10^7$
this work $[P_1^6]$	$6.80^{+1.39}_{-1.17}$
this work $[P_1^1]$	$6.25^{+0.83}_{-0.72}$
QED	3.21
Experimental measurements	not seen

Table 7.7: Branching ratio predictions for $\eta' \to \mu^+\mu^-e^+e^-$.

with the electronic variable (blue solid curve) while it is a smooth falling function of the dimuonic momentum with a small bump and a sharp peak accounting for the effect of the ρ and the ω, respectively (red solid curve). Indistinguishable, both curves integrate the same $\mathcal{BR}$. Our predictions are presented in table 7.7 without, in this case, any experimental reference to compare with. The effect of the TFF increases by a factor of about 2 the $\mathcal{BR}$ respect to the QED estimate, which is much notorious than in $\eta \to e^+e^-\mu^+\mu^-$.

The decay spectra for $\eta' \to e^+e^-e^+e^-$ and $\eta' \to \mu^+\mu^-\mu^+\mu^-$ shown in figure 7.11 (left and right panels respectively) have been computed by taking Eq. (7.14) into account. We have represented the contributions of the direct diagram (green solid curve), the exchange diagram expressed in terms of the variable of the direct diagram (red dotted curve), the interference term (blue dotted curve) and lastly the total distribution (black dotted line). One interesting feature concerning phase space is that the electronic mode (left panel) is clearly sensitive to the intermediate vector resonances while the muonic (right panel) is basically not. Our predictions are
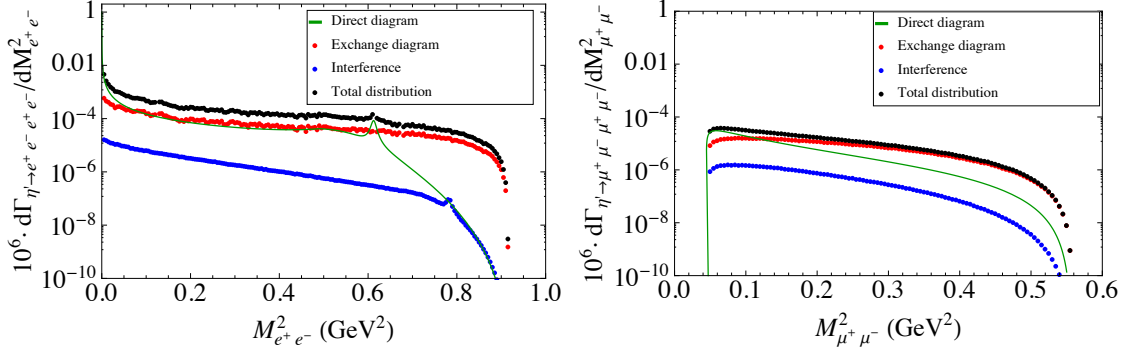
Figure 7.11: Different contributions to the dielectron and the dimuon invariant masses distribution for $\eta' \to e^+e^-e^+e^-$ (left) and $\eta' \to \mu^+\mu^-\mu^+\mu^-$ (right), respectively. Direct diagram (green solid curve), exchange diagram (red dotted curve), interference term (blue dotted curve) and the total distribution (black dotted curve) are displayed with respect to one invariant mass of the direct diagram.

Source	TFF		$\mathcal{BR}(\eta' \to e^+e^-e^+e^-) \cdot 10^6$		$\mathcal{BR}(\eta' \to \mu^+\mu^-\mu^+\mu^-) \cdot 10^8$	
			direct+exch	inter	direct+exch	inter
This work	factorisation	P_1^6	$2.15^{+0.35}_{-0.29}$	-0.03	$2.19^{+0.23}_{-0.19}$	-0.44
		P_1^1	$2.09^{+0.28}_{-0.24}$	-0.01	$2.06^{+0.17}_{-0.15}$	-0.41
	QED		1.75	-0.01	0.98	-0.11
Exp. measurements			not seen		not seen	

Table 7.8: Branching ratio predictions for $\eta' \to e^+e^-e^+e^-$ and $\eta' \to \mu^+\mu^-\mu^+\mu^-$.

presented in table 7.8 which also reflect the tendency that the effect of the TFF is sizable and larger than for the case of the η. In particular, the $\mathcal{BR}$ of $\eta' \to e^+e^-e^+e^-$ and $\eta' \to \mu^+\mu^-\mu^+\mu^-$ have increased by 20% and by a factor of 2, respectively. On the experimental side, we neither have an observation to compare with, while on the theory side we have only found the predictions given in Ref. [233] with which we are in good agreement for the cases of having two identical dilepton pairs in the final state, while we are slightly below for $\eta' \to \mu^+\mu^-e^+e^-$.

7.4 Conclusions

The single and double Dalitz decays $\mathcal{P} \to \ell^+\ell^-\gamma$ and $\mathcal{P} \to \ell^+\ell^-\ell^+\ell^-$ ($\mathcal{P} = \pi^0, \eta, \eta'$; $\ell = e$ or μ) have been analysed by means of a data-driven model-independent description of the transition $\mathcal{P} \to \gamma^{(*)}\gamma^*$. We have benefited from (our) previous findings on the space-like single-virtual TFF $\gamma\gamma^* \to \mathcal{P}$ obtained through the use of Padé approximants to represent these transitions in the time-like energy region where they are applicable. We have shown that this extrapolation from the space-like to the time-like

Decay	This work	Experimental value [37]	n_σ
$\pi^0 \to e^+e^-\gamma$	$1.169(1)\%$	$1.174(35)\%$	0.15
$\eta \to e^+e^-\gamma$	$6.61(50) \cdot 10^{-3}$	$6.90(40) \cdot 10^{-3}$	0.45
$\eta \to \mu^+\mu^-\gamma$	$3.26(46) \cdot 10^{-4}$	$3.1(4) \cdot 10^{-4}$	0.26
$\eta' \to e^+e^-\gamma$	$4.38(32) \cdot 10^{-4}$	$4.69(20)(23) \cdot 10^{-4}$	0.70
$\eta' \to \mu^+\mu^-\gamma$	$0.75(6) \cdot 10^{-4}$	$1.08(27) \cdot 10^{-4}$	1.19
$\pi^0 \to e^+e^-e^+e^-$	$3.36689(5) \cdot 10^{-5}$	$3.34(16) \cdot 10^{-5}$	0.17
$\eta \to e^+e^-e^+e^-$	$2.71(2) \cdot 10^{-5}$	$2.4(2)(1) \cdot 10^{-5}$	1.38
$\eta \to \mu^+\mu^-\mu^+\mu^-$	$3.98(15) \cdot 10^{-9}$	$< 3.6 \cdot 10^{-4}$	
$\eta \to e^+e^-\mu^+\mu^-$	$2.39(7) \cdot 10^{-6}$	$< 1.6 \cdot 10^{-4}$	
$\eta' \to e^+e^-e^+e^-$	$2.10(45) \cdot 10^{-6}$	not seen	
$\eta' \to \mu^+\mu^-\mu^+\mu^-$	$1.69(36) \cdot 10^{-8}$	not seen	
$\eta' \to e^+e^-\mu^+\mu^-$	$6.39(91) \cdot 10^{-7}$	not seen	

Table 7.9: Central final branching ratio predictions as a combined weighted average of the results presented. Errors are symmetrised. n_σ stands for the number of standard deviations the measured results are from our predictions.

is supported by current experimental data η and η' TFFs obtained from $\eta^{(\prime)} \to e^+e^-\gamma$ and $\eta \to \mu^+\mu^-\gamma$ decays. This nice behaviour proves that these TFFs are well approximated by meromorphic functions. Regarding the TFF of double virtuality, besides the standard factorisation approach, we have motivated the use of bivariate approximants, which would satisfy the high-energy constraints and whose coefficients may be determined as soon as experimental data become available. From the phenomenological point of view, we have found that the invariant mass distributions involving electrons in the final state show strong peaks at the very low-momentum transfer region, which mainly dominate the contribution to the branching ratios, hence suppressing the effect of the TFFs. On the contrary, distributions implicating muons in the final state are much more homogeneously distributed and clearly manifest the neat effect of the TFF, which, in particular, is enhanced for the η' decays due to phase space considerations. Our central final branching ratio predictions are summarised in table 7.9, where a combined weighted average of the results shown in the different tables have been considered and the uncertainties symmetrised. The values of n_σ in the table account for the number of standard deviations the experimental measurements are from our predictions. All these predictions are seen to be in accordance with present experimental measurements, only $\eta' \to \mu^+\mu^-\gamma$ and $\eta \to e^+e^-e^+e^-$ appear slightly in tension. To end, we would like to encourage once more experimental groups to measure these TFFs.

Chapter 8

The η' transition form factor from space-and time-like data

Padé approximants (PAs) have been shown recently to be very useful for the description of meson transition form factors from the analysis of space-like (SL) experimental data [21, 22, 255, 256, 257][1]. Such parameterisations based on the measurement of SL data have been used to extrapolate our knowledge of the form factors down to the low-energy limit ($Q^2 \to 0$), thus extracting the low-energy parameters (LEPs), and up to the high-energy limit ($Q^2 \to \infty$), then predicting the asymptotic behavior. Moreover, they have been employed to reconstruct the double-virtual transition form factor [203, 258]. PAs are now regarded as a valuable tool for incorporating available data into problems requiring a precise error estimation. They conform a data-driven approach that can be considered as simple, systematic and model independent, the latter because one can provide a systematic error which can be reduced as soon as more experimental data is included. These PAs applied to the pseudoscalar transition form factors (TFFs) are utilised in the evaluation of the lightest pseudoscalar mesons contributions to the hadronic light-by-light piece of the anomalous magnetic moment of the muon [21, 22, 203, 256, 257], the calculation of the $\pi^0 \to e^+e^-$ rare decay [203], the extraction of the η-η' mixing parameters [22, 23], the analysis of π^0, η and η' single and double Dalitz decays [258], and in the quest for dark photons [?]. In all cases, they provide an excellent laboratory for synergic studies between theory and experiment.

The PAs $P^L_M(Q^2)$ to a given function $f(Q^2)$ are ratios of two polynomials (with degree L and M, respectively), constructed such that the Taylor expansion around the origin exactly coincides with that of the function up to the highest possible order,

---

[1]See also the seminal work in [20] for the application of PAs to the case of the pion vector form factor.

i.e., $f(Q^2) - P_M^L(Q^2) = \mathcal{O}(Q^2)^{L+M+1}$ [200, 235]. They often provide a means of obtaining information about the function outside its circle of convergence, and of more rapidly evaluating the function within its circle of convergence. However, in spite of being flexible and user friendly, PAs reconstructed from their power series at the origin are rational functions with a simple analytical structure given by a set of poles. Therefore, they do not possess branch cuts and cannot be used to predict the position of resonance poles, which are hidden in the second Riemann sheet of the complex plane. Similarly, PAs reconstructed using information on the branch cut, which allow for a precise determination of the resonance pole parameters [237, 259], are not suitable for the extraction of the LEPs, i.e., PAs cannot access different Riemann sheets. Nonetheless, for special kind of functions, such as Stieltjes [260, 261] or non-Stieltjes but meromorphic functions [133], convergence theorems for PAs are known. To apply these theorems, an understanding of the analytical properties of the functions is required in advance. When this knowledge is missing, the practitioner would explore a sequence of PAs and expect a pattern of convergence. The question is whether observing this behaviour one could infer, within some uncertainties, the approximate analytical structure of the function under consideration.

In this work, we will explore this last insight taking the η' TFF as a proof of concept. We will try to learn and extract from the sequence of PAs employed details on the analytical properties of this TFF in the energy regime covered by experimental data. In our previous analyses of the TFFs from SL data, we have always carefully expressed the limits on the range of applicability of PAs [21, 22]. Initially, PAs could be analytically continued from the SL region to the time-like (TL) one but only up to the first singularity, usually a branch cut in the form of a production threshold. For instance, in the case of the single Dalitz decay $\pi^0 \rightarrow e^+e^-\gamma$ PAs can be safely extended into the TL region up to the pion mass since no branch cuts are present. On the contrary, for the $\eta \rightarrow \ell^+\ell^-\gamma$ decays, with $\ell = e, \mu$, the presence of the $\pi\pi$ branch cut could in principle limit the application of PAs in the TL region. However, the $\eta \rightarrow e^+e^-\gamma$ decay and its associated TFF in the TL region was recently measured with great accuracy by the A2 Collaboration [207]. The authors compared their measurement with several theoretical predictions, among them ours, based on SL parameterisations of the TFF in terms of PAs [22], and found that these PAs show the best agreement with data for the full range of e^+e^- invariant masses reached in the experiment. This nice result challenged our understanding of the PAs method and triggered, for the first time, a combined analysis of the η TFF from both SL and TL experimental data [23]. The reason for that agreement can be understood

by the fact that the branch cut in this decay ($\pi\pi$ unitary cut) is not resonant inside the available phase-space region since the ρ resonance is well beyond the η mass. The PAs will fail for sure at the first pole encountered on the real axis, or, to be more precise, will start failing at some point near the pole[2]. In any case, for the η TFF, this pole on the real axis is found to be at $\sqrt{s} \simeq 720$ MeV for the single-pole parameterisation used frequently by the experimental collaborations [23]. Therefore, for the $\eta \to \ell^+\ell^-\gamma$ decays the PAs can also be extended into the TL region up to the η mass. The case of the $\eta' \to \ell^+\ell^-\gamma$ Dalitz decays is more cumbersome since the available phase-space this time includes the resonant region. However, the analysis performed in [22] on the η' TFF using only SL data revealed that the pole on the real axis for the single-pole parameterisation is located at $\sqrt{s} \simeq 830$ MeV. In order to estimate the region of influence of this pole one can make use of the half-width rule [238]. In this case, the ρ and ω resonances are within the phase-space region and the ϕ is not far from its end point. Taking the values of their masses and widths from the PDG [37], the application of this rule gives $M_{\text{eff}} \pm \Gamma_{\text{eff}}/2 = 822 \pm 58$ MeV [22]. This value of the effective pole is compatible with the result obtained before from the single-pole parameterisation, thus showing that the pole found at 830 MeV is somewhat a kind of weighted average of the three existing resonance poles. The range given by the half-width rule above implies that the region of influence of the former pole is from 770 MeV to 900 MeV. Consequently, for the η' TFF the PAs can also be used in a safe manner up to around 770 MeV in the TL region[3]. Recently, the BESIII Collaboration reported the first measurement of the e^+e^- invariant-mass distribution for the $\eta' \to e^+e^-\gamma$ decay up to 750 MeV [25]. As discussed, our prediction for the TL region of the η' TFF based solely on SL data should be able to describe this new measurement. In Figure 8.1, the BESIII experimental extraction of the modulus square of the η' TFF as a function of the e^+e^- invariant-mass is compared with our theoretical prediction. It is worth remarking that this is not a fit but a prediction and the agreement is seen to be excellent.

The main purpose of the present work is to further improve our determination of the η' TFF taking into consideration not only the existing SL experimental data but also the new set of TL data from the recent BESIII measurement. This combined analysis will allow us to better determine the LEPs of the TFF, its normalization and the

---

[2]The question is how close the PAs can approach the pole without failing. A detailed discussion on this issue for the case of η' Dalitz decays can be obtained from [258].

[3]In [258], we were more conservative and the half-width rule was applied taking only into account the ρ resonance. As a result, we obtained that the lowest value of the region of influence in that case was around 700 MeV.
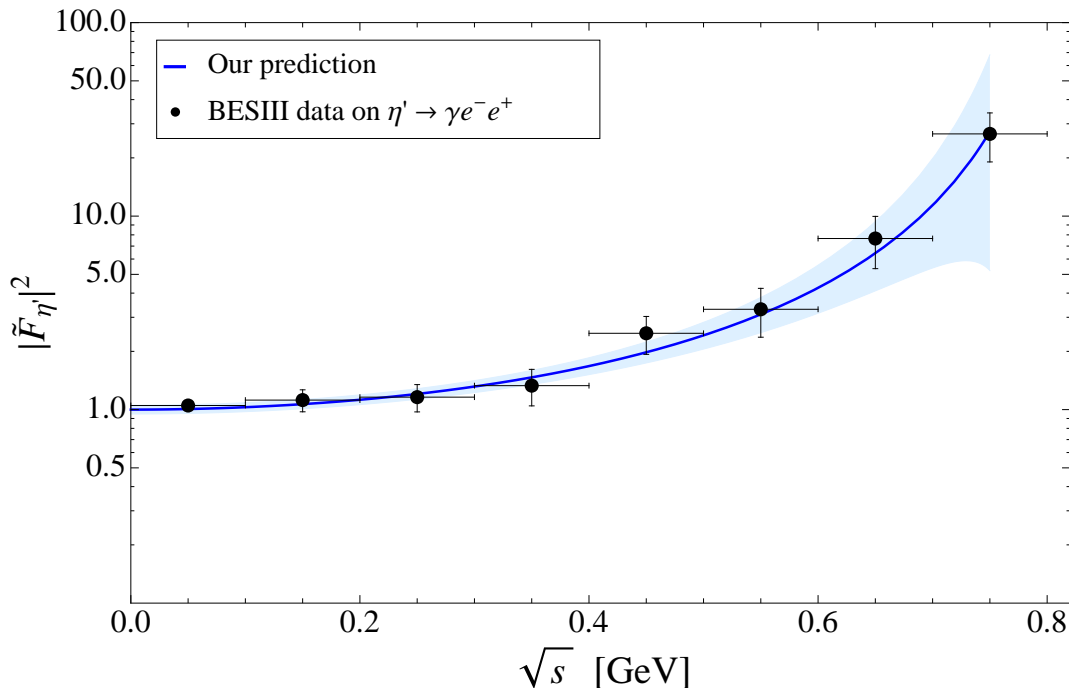
Figure 8.1: Our prediction for the η' transition form factor in the time-like region obtained from the $P_1^6(\sqrt{s})$ fit to space-like data performed in [22]. Experimental points are from the BESIII measurement in [25].

asymptotic limit. Such an enhancement permits to reconsider the η-η' mixing scheme, with special emphasis on the OZI-rule–violating parameters and the $J/\psi(Z) \to \eta^{(\prime)}\gamma$ decays. In Section 8.1, we provide a detailed discussion on the reasons for the success of PAs when applied to the TL region. In Section 8.2, we include the TL data in the analysis, present the new results and comment the improvements achieved. Section 8.3 is devoted to the reassessment of the η-η' mixing parameters and their consequences for the J/ψ and Z radiative decays. Finally, in Section 8.4, we conclude and mention the future prospects.

8.1 Padé approximants in the time-like region

When the original function to be approximated is Stieltjes with a finite radius of convergence about the origin, R, it is a well-known result in the theory of Padé approximants that the sequence $P_N^{N+J}(z)$ (with $J \geq -1$) converges to the original function, as $N \to \infty$, on any compact set in the complex plane, excluding the cut at $R \leq z < \infty$ [200]. In other words, even though the $\pi\pi$ unitary cut driving the decay is of Stieltjes nature, there is no *a priori* reason why the PA should work
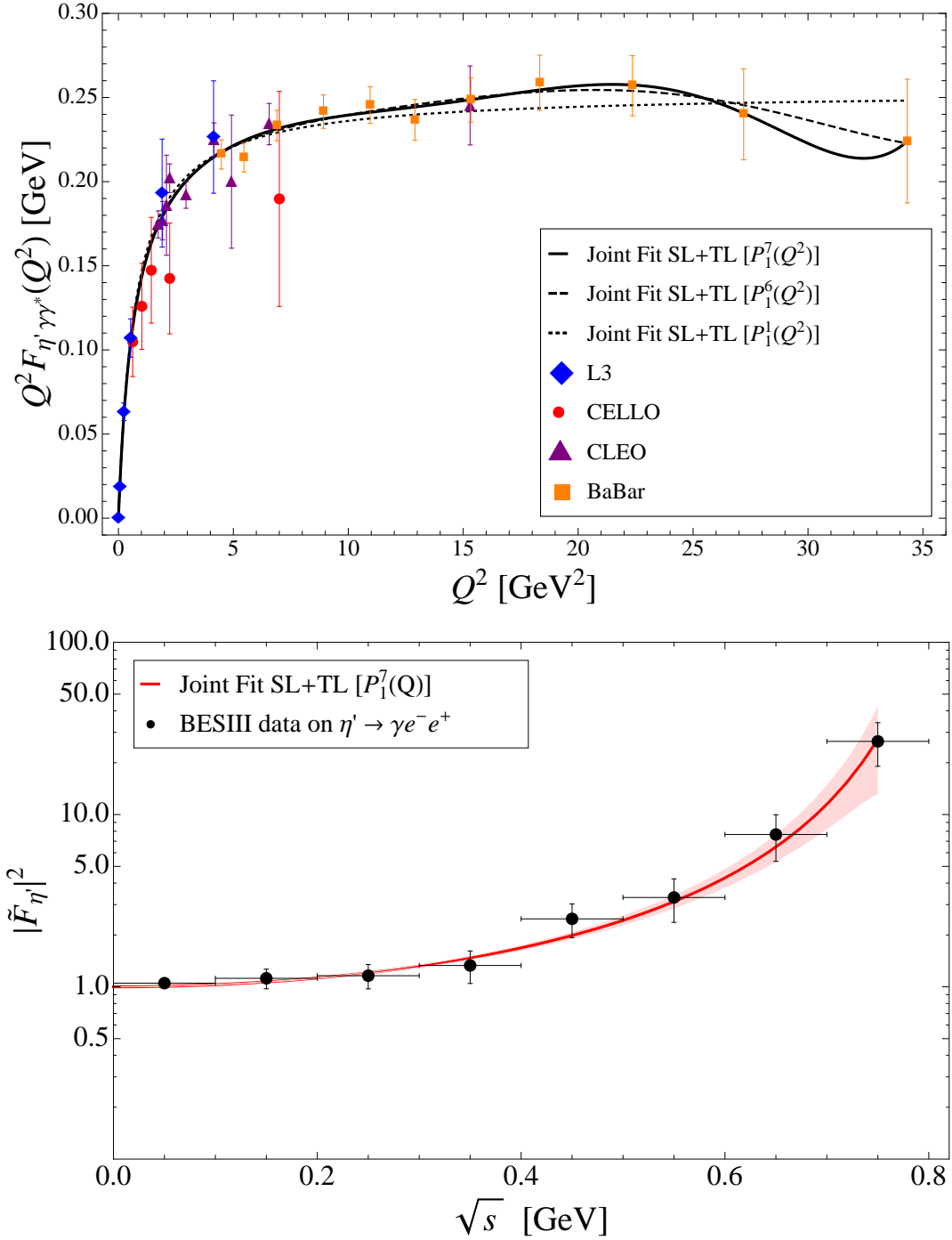
Figure 8.2: η' TFF in the SL (up) and TL (down) regions after a joint fit to the SL and TL sets of experimental data. The dotted, dashed and solid black lines represent the fits using $P_1^1(Q^2)$, $P_1^6(Q^2)$ and $P_1^7(Q^2)$, respectively, on the left panel, while the red solid line represents $P_1^7(\sqrt{s})$ on the right panel.

above the branch cut. The cumbersome situation is, however, that at least the $P_1^L(s)$ sequence does work well above the cut (cf. Figure 8.1). And the unanswered question is, then, whether one could have anticipated this success and how general is for any arbitrary situation. A fair statement would be to say that, approximately, the TFF is a meromorphic function which has nothing but a set of single and isolated poles within the data range. In this scenario, PA are an excellent approximation tool [133]. Moreover, they tell us about the underlying physical phenomena driving the decay without the need to assume any model.

To better understand this situation from a qualitative point of view, let us discuss the following. As we have said, in the zero-width approximation, the TFF becomes a meromorphic function. If the TFF contains a single and isolated pole, the $P_1^L(s)$ sequence reproduces the pole of the TFF with infinite precision. As soon as the width is again switched on, the $\pi\pi$ threshold opens a branch cut responsible for that width. Then, at first, no mathematical theorem will guarantee convergence on this scenario. On the contrary, if the convergence theorem is to be satisfied, one would expect the single pole of the $P_1^L(s)$ to be located closer and closer to the threshold point as soon as $L \to \infty$, since this is the first singular point the PA is going to find. However, the behavior of this $\pi\pi$ branch cut at threshold is well known. This knowledge comes from the P-wave $\pi\pi$ scattering amplitude (the opened cut yields vector states) together with the Fermi-Watson theorem that relates the phase of the scattering amplitude with the phase of the form factor below the first inelastic threshold. The $\pi\pi$ P-wave scattering amplitude $t_1^1(s)$ at threshold behaves like [262]:

$$
\begin{aligned}
\mathrm{Im}[t_1^1(s)] &= q^4\sqrt{q^2}\left(\frac{a^2}{m_\pi} + \frac{4a\,b\,m_\pi^2 - a^2}{2m_\pi^3}q^2 + \mathcal{O}((q^2)^3)\right) , \\
\mathrm{Re}[t_1^1(s)] &= q^2\left(a + b\,q^2 + \mathcal{O}(q^2)^2\right) ,
\end{aligned}
\tag{8.1}
$$

with q^2 the center-of-mass momentum $4q^2 = s - 4m_\pi^2$ and where for the imaginary part we used the unitary relation $\mathrm{Im}[t_1^1(s)^{-1}] = -\sigma(s)$, where $\sigma(s) = \sqrt{1 - 4m_\pi^2/s}$. The absolute value of the threshold expansion of the amplitude $t_1^1(s)$ is basically a polynomial in $(s - 4m_\pi^2)$ with the influence of the imaginary part starting only at $(s - 4m_\pi^2)^4$. Following the previous equation, if the threshold parameters a and b are of order 1 (with the appropriate units) [262], then the real part dominates near threshold and the absolute value is given basically by the real part. By virtue of the unitary relation for the TFF, $\mathrm{Im}F(s) = \sigma(s)F(s)t_1^1(s)^*$, and the expansion in Eq. (8.1), one concludes that while the real part of the threshold expansion of the TFF starts at order $(s - 4m_\pi^2)^0$, its imaginary part, coming from $\sigma(s)\mathrm{Re}[t_1^1(s)]$, only

starts showing up at order $(s - 4m_\pi^2)^{3/2}$. If this is the case and the offset of the threshold is that smooth, the $P_1^L(s)$ sequence will be an excellent tool to reproduce the TFF near and above the threshold and its pole will not be located at the starting point of the threshold since it is not singular. Actually, taking the definition of a $P_1^L(s)$ given by

$$P_1^L(s) = \sum_{k=0}^{L-1} a_k s^k + \frac{a_L s^L}{1 - \frac{a_{L+1}}{a_L} s} \ , \tag{8.2}$$

the polynomial part will reproduce the threshold and the PA pole part will account in an effective manner for the pole of the TFF far away from the threshold. This simple consideration already shows the ability of PAs to go above the threshold for functions with smooth threshold offset. In our current case, the discrepancies can be further reduced if the object to be approximated is the absolute value squared of the TFF, $|F|^2$. Then, the $P_1^L(s)$ will reproduce $|F|^2$ in an even larger energy range, going further above the opening of the branch cut.

The present discussion already anticipates that for the η-TFF our PAs will yield an excellent result, since the $\pi\pi$ invariant mass can only reach the η mass where the threshold expansion reproduces the absolute value of the TFF with great precision. Consequently, a $P_1^L(s)$ with large enough L will reproduce the TFF accurately. The last question is, then, up to what energy one can go above the threshold before failing. The threshold expansion itself must fail at some point because it breaks unitarity by powers of $(s - 4m_\pi^2)$. A quantitative answer to this question would demand to study this problem using a particular model. To make a general statement, model independent, and qualitative, we notice that the threshold expansion should break down when the presence of the resonance pole is large enough and cannot be approximated by a polynomial in $(s - 4m_\pi^2)$. This happens basically at a distance of the pole given by the half-width rule [238] which, as argued in the Introduction, provides a simple estimate of the PA range.

In a realistic situation with multiple cuts, the picture will develop new features but the final result would be similar. The PA pole becomes an effective pole resulting from the combination of the absolute values of the different resonances entering the process, closer to the one with larger coupling in the particular reaction, with shifts produced by the different widths of the resonances. The role of the $\pi\pi$ branch cut is intertwined with the particular particle for which the cut is opened. For example, if one expects the ρ, ω and ϕ vectors to play a role, since the ρ width is the largest, the TFF line shape will basically be dominated by that meson and its $\pi\pi$ opening. The fact that a single-pole PA works so well in the η' TFF is a clear indication that the 3π

	Constraining $F_{\eta'\gamma\gamma}(0)$		**Predicting $F_{\eta'\gamma\gamma}(0)$**	
	P_1^7	P_1^1	P_1^6	P_1^1
$b_{\eta'}$	1.31(4)	1.25(3)	1.30(4)	1.27(4)
$c_{\eta'}$	1.74(9)	1.56(6)	1.73(9)	1.62(11)
$d_{\eta'}$	2.30(19)	1.94(12)	2.29(19)	2.06(22)
$F_{\eta'\gamma\gamma}(0)$	0.344(5)	0.345(5)	0.342(13)	0.351(10)
$Q^2 F_{\eta'\gamma^*\gamma}^{\mathrm{asym}}(Q^2)$	—	0.254(3)	—	0.253(3)
χ_{dof}^2	0.65	0.67	0.66	0.68

Table 8.1: Low-energy parameters as obtained after a joint fit to both space- and time-like data with and without including the measured two-photon partial width as a restriction in the χ^2 function of (8.4), second and third multicolumn, respectively. The leading coefficient of the TFF asymptotic limit and the χ_{dof}^2 are also shown.

cut is very small and its presence is already captured by the approximant. PAs cannot differentiate among the different weights of the different contributions appearing in the TFF, though. However, being fitted to experimental data, all the possible pieces are included —as they are in the data. An interesting exercise would be, then, to compare with other parameterizations existent in literature [222, 223, 227, 228, 229, 230, 231, 263, 264] and, eventually, to help to understand model dependencies. This statement already excludes the generalization of our results for any arbitrary Stieltjes function since one can immediately conclude that the clue feature of the function that would allow the PA to access the branch cut is its behavior around the threshold point. That is, for a form factor with an abrupt threshold offset, the range of applicability within the time-like region will be more limited.

8.2 Incorporation of the low-energy time-like data

Since our goal is to provide a parameterization of the TFF as accurate as possible and we have shown in the previous section that the TL experimental data up to 0.75 GeV can be well described with our old parameterization based on SL data, in this section we will include the TL data as a new data set to be fitted, following [23]. At low-momentum transfer, the TFF can be described by the expansion

$$
\begin{aligned}
F_{\eta'\gamma^*\gamma}(Q^2) \quad &= F_{\eta'\gamma\gamma}(0) \times \\
&\times \left(1 - b_{\eta'} \frac{Q^2}{m_{\eta'}^2} + c_{\eta'} \frac{Q^4}{m_{\eta'}^4} - d_{\eta'} \frac{Q^6}{m_{\eta'}^6} + \cdots \right),
\end{aligned} \tag{8.3}
$$

where $F_{\eta'\gamma\gamma}(0)$ is the normalization (the TFF at zero momentum transfer) while the LEPs parameters $b_{\eta'}$, $c_{\eta'}$ and $d_{\eta'}$ are, respectively, the slope, the curvature and the third derivative of the TFF. By reassessing our SL fits [22] through including TL data, we will update the results for the LEPs of the η' TFF. The χ^2 function minimized in our fit is given by ($\widetilde{F}(\sqrt{s}) = F(\sqrt{s})/F(0)$)

$$
\chi^2 = \sum_{i=1}^{50} \left(\frac{Q^2 \left| P_M^L(Q^2) \right|_i - Q^2 \left| F_{\eta'\gamma^*\gamma}^{\exp}(Q^2) \right|_i}{\sigma_{Q^2 \left| F_{\eta'\gamma^*\gamma}^{\exp}(Q^2) \right|_i}} \right)^2 +
$$

$$
\sum_{i=1}^{8} \left(\frac{\left| \widetilde{P}_M^L(\sqrt{s}) \right|_i^2 - \left| \widetilde{F}_{\eta'\gamma^*\gamma}^{\exp}(\sqrt{s}) \right|_i^2}{\sigma_{\left| \widetilde{F}_{\eta'\gamma^*\gamma}^{\exp}(\sqrt{s}) \right|_i^2}} \right)^2 + \left(\frac{P_M^L(0) - \left| F_{\eta'\gamma\gamma}^{\exp}(0) \right|}{\sigma_{\left| F_{\eta'\gamma\gamma}^{\exp}(0) \right|}} \right)^2 , \tag{8.4}
$$

where the first and second terms correspond to SL [24] and TL [25] data, respectively, while the last term encodes information from the TFF at zero momentum transfer and introduces an additional restriction. For the experimental value we use $F_{\eta'\gamma\gamma}^{\exp}(0) = 0.3437(55)$ GeV^{-1}, inferred from the partial width to two photons, $\Gamma_{\eta'\rightarrow\gamma\gamma} = 4.35(14)$ keV [37], through the relation

$$
\left| F_{\eta'\gamma\gamma}(0) \right|^2 = \frac{64\pi}{(4\pi\alpha)^2} \frac{\Gamma(\eta' \rightarrow \gamma\gamma)}{m_{\eta'}^3} . \tag{8.5}
$$

The value $\Gamma_{\eta'\rightarrow\gamma\gamma} = 4.35(14)$ keV cited in [37] is not a measured quantity, rather a fit inferred from the branching ratio and using the current η' total width. The average experimental determination for such decay reads 4.28(19) keV. It will be interesting to see whether this 0.3σ difference would affect our results at the precision we are working.

We start fitting with a Padé approximants' sequence of the type $P_1^L(Q^2)$, and current data allow us to reach $L = 7$. The coefficients of our best $P_1^L(Q^2)$ fit for the $Q^2 F_{\eta'\gamma^*\gamma}(Q^2)$ defined as

$$
P_1^L(Q^2) = \frac{T_N(Q^2)}{R_1(Q^2)} = \frac{t_1 Q^2 + t_2 Q^4 + \cdots + t_N (Q^2)^N}{1 + r_1 Q^2} , \tag{8.6}
$$

are gathered in table 8.2.

With these coefficients one can extract the slope of the TFF by expanding (8.6) and normalizing the result as

$$
b_{\eta'} = m_{\eta'}^2 (t_1 \cdot r_1 - t_2)/t_1 = 1.312 , \tag{8.7}
$$

with $m_{\eta'} = 0.95778$ GeV. We provide a graphical account of our fits as compared to both SL and TL in Figure 8.2, from where one can see that the one sigma error

Table 8.2: Fitted coefficients for the best Padé approximant, $P_1^7(Q^2)$, associated to $Q^2 F_{\eta'\gamma^*\gamma}(Q^2)$.

Coefficient	Value
t_1	0.3437
t_2	$3.847 \cdot 10^{-3}$
t_3	$0.550 \cdot 10^{-3}$
t_4	$-1.621 \cdot 10^{-4}$
t_5	$1.338 \cdot 10^{-5}$
t_6	$-4.495 \cdot 10^{-7}$
t_7	$5.261 \cdot 10^{-9}$
r_1	1.4413

band associated to the time-like η' TFF has considerably decreased as compared to Figure 8.1. The LEPs obtained from the fit are collected in Table 8.1 and their corresponding convergence pattern in Figures 8.3 and 8.4 (red circles) reflect the impact of the inclusion of TL compared with the old results.

Comments on these results are in order.

1. The precision gained on the LEPs determination is remarkable as compared to our previous results (blue triangles) when only SL were fitted [22];

2. We enlarge our PA sequence by one element (reducing then the systematic uncertainty);

3. The new LEPs sequence reaches faster the stability value manifesting the excellent performance of the method as new experimental data is included;

4. Including $F_{\eta'\gamma\gamma}^{\text{exp}}(0)$ as an additional datum in the fit reduces significantly the uncertainty associated to this quantity. Regarding to this constraint, it is noticed that while LEPs obtained from the $P_1^L(Q^2)$ sequence are basically insensitive to this effect, the LEPs obtained from the $P_1^1(Q^2)$ element are not and suffer small distortions.

After the first combined analysis of both SL and TL data, our central value results for $F_{\eta'\gamma\gamma}(0)$ and LEPs are

$$F_{\eta'\gamma\gamma}(0) = 0.344(5)(0) \text{ GeV}^{-1} , \quad b_{\eta'} = 1.31(4)(1) ,$$
$$c_{\eta'} = 1.74(9)(3) , \quad d_{\eta'} = 2.30(19)(21) , \tag{8.8}$$

where the first error is statistic and the second systematic, the latter being 0% for the value at the origin, and 1%, 2%, and 9% for the slope, curvature, and third derivative,
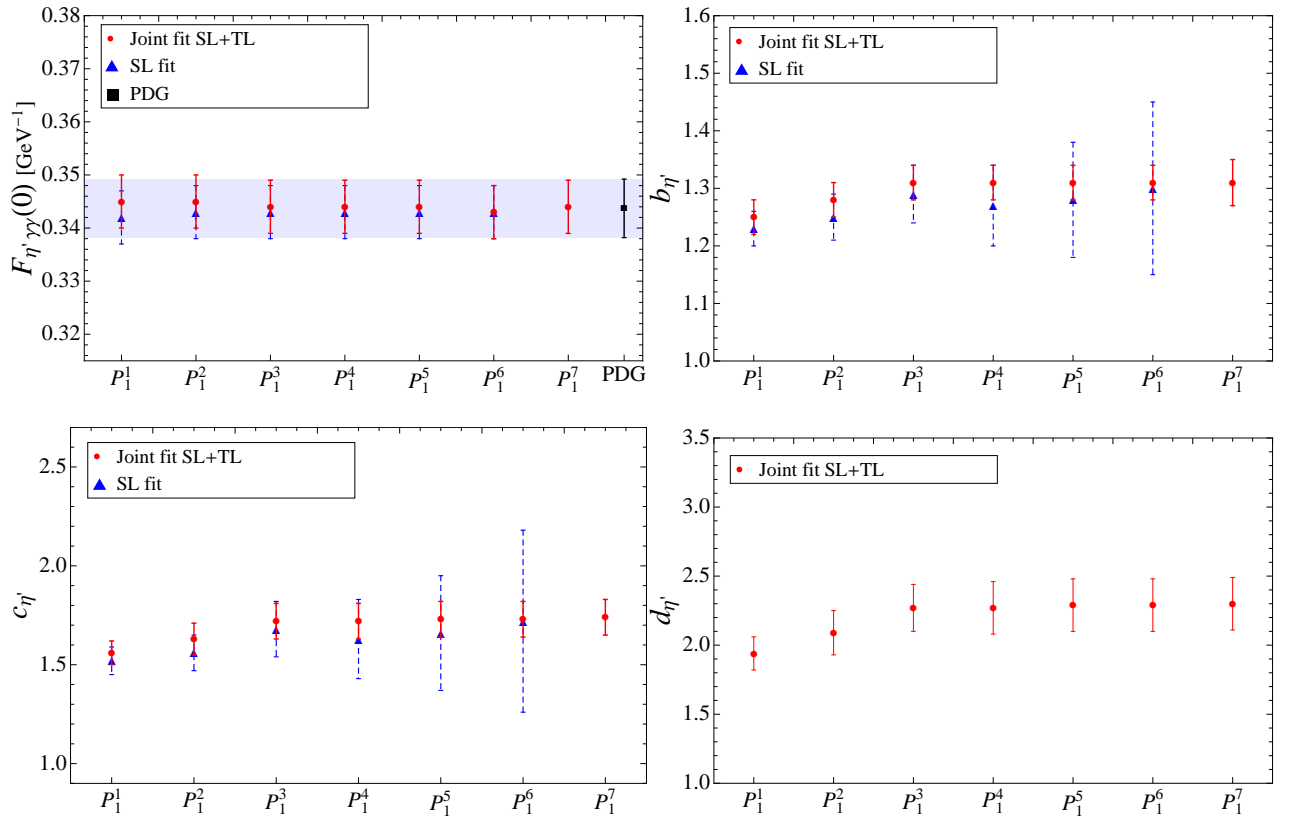
Figure 8.3: Convergence pattern of the P_1^L sequence for $F_{\eta'\gamma\gamma}(0)$, $b_{\eta'}$, $c_{\eta'}$, and $d_{\eta'}$ as obtained from fitting experimental SL and TL data together with $F_{\eta'\gamma\gamma}(0)$ from the PDG [37].
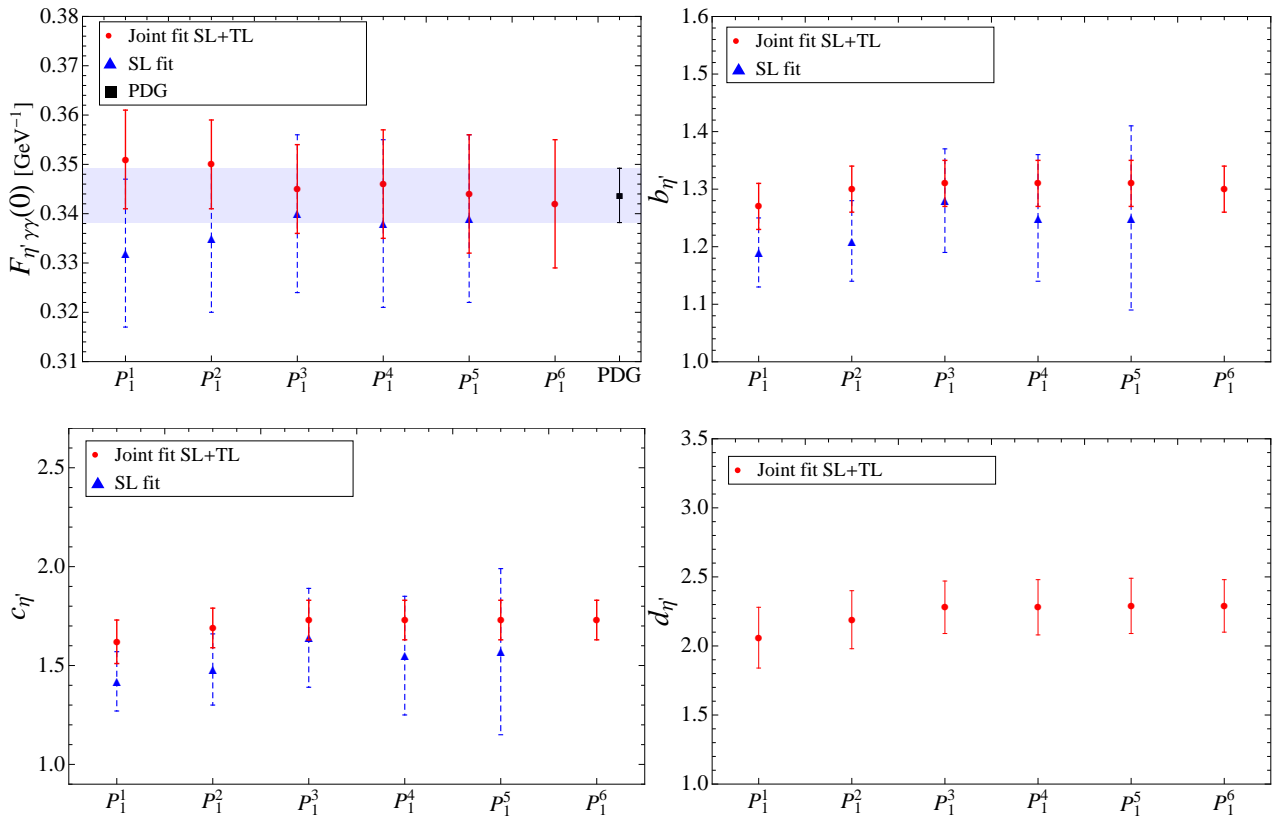
Figure 8.4: Convergence pattern as in Fig. 8.3 without including information on the $\Gamma_{\eta'\to\gamma\gamma}$.

respectively [22]. The results above can be compared with the ones obtained by the $P_N^N(Q^2)$ sequence in Table 8.1. Since this second sequence stops at its first element (which is actually the first element on the $P_1^L(Q^2)$ sequence), we do not consider its results for a combined weighted average. The systematic error is at the level of the statistical one. To reduce it, we would need more precise high-energy data on the one hand, and enlarge, on the other hand, the $P_N^N(Q^2)$ sequence which is limited in this analysis to its first element. Notice that the $P_N^N(Q^2)$ has systematic errors dramatically smaller than the ones considered here (see the Appendix in [23] for details). It turns out that the η' TFF is very much dominated by a single hadronic scale that gives to the TFF its characteristic vector meson dominance-like shape (VMD). A $P_2^2(Q^2)$ fit cannot be accommodated at the current level, and we hope that more data from BESIII, MAMI, and Belle-II will help to improve the present values. These results can be compared with $F_{\eta'\gamma\gamma}(0) = 0.344(4)(0)$ GeV^{-1}, $b_{\eta'} = 1.30(15)(7)$ and $c_{\eta'} = 1.72(47)(34)$, obtained using SL data only [22]. Clearly, the statistical uncertainty of the LEPs has considerably diminished as a consequence of including TL data to the analysis, being that one of the main results of this work. Our slope, $b_{\eta'} = 1.31(4)$, can be compared with the values 1.46(23), 1.24(8) and 1.6(4), quoted by the CELLO and CLEO in Ref. [24] and Lepton-G (cited in [220]), respectively. One should notice that all the previous collaborations used a single-pole model, VMD, to extract the slope, which is nothing but the simplest $P_1^1(Q^2)$ element from our approach (which we neglected). Other theoretical predictions existent in the literature are $b_{\eta'} = 1.47$ predicted by chiral perturbation theory for $\sin\theta_P = -1/3$, being θ_P the η-η' mixing angle, $b_{\eta'} = 1.30$ from constituent-quark loops, both values taken from [265], $b_{\eta'} = 1.33$ from VMD [266], and $b_{\eta'} = 2.11$ from the Brodsky-Lepage interpolation formula [267]. More recently, one can find $b_{\eta'} = 1.323(4)$ from resonance chiral theory [221], $b_{\eta'} = 1.45^{+0.17}_{-0.12}$ using dispersive techniques [223], and $b_{\eta'} = 1.06$ or 1.16 from anomaly sum rules [230].

The main difference between Figure 8.1 and Figure 8.2 is the width of the uncertainty band, specially at large $\sqrt{s}$, which is the region where we expect the PA to eventually fail. To control on the quality of the fits at this large $\sqrt{s}$, we have repeated the fits by first enlarging artificially the errors of the last energy points and secondly eliminating subsequently the last data points. We have observed a completely stable fit even under these manipulations which only slightly enlarge the slope error but always keeping the same χ^2_{dof} (degrees of freedom). We conclude, then, that our final results in (8.8) are robust enough and independent of an eventual failure of the PA method at the highest TL energy point.

We benefit from our results $F_{\eta'\gamma\gamma}(0) = 0.344(5)$ GeV^{-1} and $F_{\eta'\gamma\gamma}(0) = 0.342(13)$ GeV^{-1} (constrained and unconstrained cases, respectively) to predict the η' partial decay width to two photons. For the constrained fit, i.e. including the value at the origin in our data set, the fit returns $\Gamma_{\eta'\to\gamma\gamma} = 4.35(13)$ keV, slightly better than the PDG fitted value and at 0.3 standard deviations off its averaged result. For the unconstrained case, we find $\Gamma_{\eta'\to\gamma\gamma} = 4.30(33)$ keV, which lies 0.1 standard deviations off the experimental value. Regarding the asymptotic behavior of the TFF, we have considered the $P_N^N(Q^2)$ sequence since they have the right asymptotic fall-off $1/Q^2$ built-in. We reached $N = 1$ and then predicted the leading coefficient

$$\lim_{Q^2\to\infty} Q^2 F_{\eta'\gamma^*\gamma}(Q^2) = 0.254(3) \text{ GeV} , \qquad (8.9)$$

which is in very good agreement with the value $0.254(21)$ GeV[4] measured at $Q^2 = 112$ GeV^2 by the BABAR collaboration [268]. This prediction is basically the same one obtained in [22] when only the SL data were considered. Therefore, the effect of including the TL data is negligible in this respect. Ideally, it would be desirable to extract such value from the $N = 2$ element, which allows for diminishing the intrinsic systematic error as well as for checking convergence. This should be possible in the future if new precise Belle-II data becomes available.

8.3 A reassessment of the η-η' mixing

In this section we reanalyze the η-η' mixing as we did in [22, 23]. In these works, we took advantage of the flavor basis, where the η and η' pseudoscalar decay constants, defined in terms of the axial currents $J_{5\mu}^a = \bar{q}\gamma_\mu\gamma_5 \frac{\lambda^a}{\sqrt{2}} q$, with $\lambda^q = \text{diag}(1,1,0)$ and $\lambda^s = \text{diag}(0,0,\sqrt{2})$, as $\langle 0|J_{5\mu}^a|P\rangle = i\sqrt{2}F_P^a p_\mu$, where $a = (q,s)$ refers to light and strange quarks, respectively, can be expressed as

$$(F_P^{qs}) \equiv \begin{pmatrix} F_\eta^q & F_\eta^s \\ F_{\eta'}^q & F_{\eta'}^s \end{pmatrix} = \begin{pmatrix} F_q\cos\phi_q & -F_s\sin\phi_s \\ F_q\sin\phi_q & F_s\cos\phi_s \end{pmatrix} . \qquad (8.10)$$

This basis has become popular since large-N_c chiral perturbation theory (ChPT) next-to-leading order (NLO) predictions yield [269, 270]

$$F_q F_s \sin(\phi_q - \phi_s) = \frac{\sqrt{2}}{3} F_\pi^2 \Lambda_1 , \qquad (8.11)$$

---

[4]Such value is obtained from the BABAR result $0.251(19)(8)$ GeV after taking into account kinematical corrections [22].

where $F_\pi \simeq 92.2$ MeV is the pion decay constant and Λ_1 an OZI-rule–violating parameter expected to be small. Assuming Λ_1 to be negligible, (8.11) implies $\phi_q = \phi_s \equiv \phi$, an approximation which has been shown to be successful in phenomenological applications [269, 270]. Large-N_c ChPT also predicts

$$F_q^2 = F_\pi^2 + \frac{2}{3}F_\pi^2\Lambda_1 \ . \tag{8.12}$$

Here, phenomenological studies [22, 23, 269, 270] do not support $\Lambda_1 = 0$ since they clearly find $F_q > F_\pi$. Therefore, to be consistent, we will consider the most general case $\phi_q \neq \phi_s$ and work in the so-called octet-singlet basis, where the decay constants are defined as

$$(F_P^{80}) \equiv \begin{pmatrix} F_\eta^8 & F_\eta^0 \\ F_{\eta'}^8 & F_{\eta'}^0 \end{pmatrix} = \begin{pmatrix} F_8\cos\theta_8 & -F_0\sin\theta_0 \\ F_8\sin\theta_8 & F_0\cos\theta_0 \end{pmatrix} \ . \tag{8.13}$$

In this basis, large-N_c ChPT at NLO predicts [269, 270]

$$F_8^2 = \frac{4F_K^2 - F_\pi^2}{3} \ , \quad F_0^2 = \frac{2F_K^2 + F_\pi^2}{3} + F_\pi^2\Lambda_1 \ , \tag{8.14}$$

$$F_8 F_0 \sin(\theta_8 - \theta_0) = -\frac{2\sqrt{2}}{3}(F_K^2 - F_\pi^2) \ , \tag{8.15}$$

where $F_K \simeq 1.20F_\pi$ is the kaon decay constant.

At this point we call the attention that F_0 is renormalization group (RG) dependent. This is connected to the $J_{5\mu}^0$ anomalous dimension implying [231, 271]

$$\mu\frac{dF_0}{d\mu} = -N_F\left(\frac{\alpha_s(\mu)}{\pi}\right)^2 F_0 + \mathcal{O}(\alpha_s^3) \ , \tag{8.16}$$

where N_F is the number of active flavors at scale μ. Solving this equation up to order α_s, the singlet decay constant at a different scale can be expressed as

$$\begin{aligned} F_0(\mu) &= F_0(\mu_0)\left[1 + \frac{2N_F}{\beta_0}\left(\frac{\alpha_s(\mu)}{\pi} - \frac{\alpha_s(\mu_0)}{\pi}\right)\right] \\ &\equiv F_0(1 + \delta) \ , \end{aligned} \tag{8.17}$$

with $\beta_0 = 11 - 2N_F/3$. In the octet-singlet basis, the different limiting behaviors of the TFF, $F_{P\gamma\gamma} \equiv F_{P\gamma^*\gamma}(0)$ and $P_\infty \equiv \lim_{Q^2 \to \infty} Q^2 F_{P\gamma^*\gamma}(Q^2)$, take the simple form

$$F_{\eta\gamma\gamma} = \frac{1}{4\pi^2}\frac{\hat{c}_8 F_{\eta'}^0 - \hat{c}_0(1 + \Lambda_3)F_{\eta'}^8}{F_{\eta'}^0 F_\eta^8 - F_{\eta'}^8 F_\eta^0} \ , \tag{8.18}$$

$$F_{\eta'\gamma\gamma} = \frac{1}{4\pi^2}\frac{\hat{c}_8 F_\eta^0 - \hat{c}_0(1 + \Lambda_3)F_\eta^8}{F_\eta^0 F_{\eta'}^8 - F_\eta^8 F_{\eta'}^0} \ , \tag{8.19}$$

$$\eta_\infty = 2(\hat{c}_8 F_\eta^8 + \hat{c}_0(1 + \delta_\infty)F_\eta^0) \ , \tag{8.20}$$

$$\eta'_\infty = 2(\hat{c}_8 F_{\eta'}^8 + \hat{c}_0(1 + \delta_\infty)F_{\eta'}^0) \ , \tag{8.21}$$

169

Table 8.3: Predictions for the mixing parameters. $\theta_{8,0}$ are expressed in degrees.

F_8/F_π	F_0/F_π	θ_8	θ_0	Λ_3	χ^2_{dof}
1.32(7)	1.25(3)	$-22.8(1.1)$	$-7.6(2.2)$	0.05(3)	1.0

where $\hat{c}_8 = 1/\sqrt{3}$ and $\hat{c}_0 = \sqrt{8/3}$ are charge factors and $\delta_\infty = -0.17$ [23] accounts for the F_0 running from $\mu_0 = 1$ GeV up to $\mu \to \infty$ [231]. In addition, we have included the OZI-rule–violating parameter Λ_3, which has been neglected in our previous studies since it enters at the same level as Λ_1.

The set (8.18-8.21) form a system of 4 equations with 5 unknowns $(F^{(8,0)}_{\eta^{(\prime)}}, \Lambda_3)$. Then it could seem that, at least taking $\Lambda_3 = 0$, we may solve the system. However, as explained in [22], such a system is underdetermined as there is the relation

$$\eta_\infty F_{\eta\gamma\gamma} + \eta'_\infty F_{\eta'\gamma\gamma} = \frac{3}{2\pi^2} \left(1 + \frac{8}{9}(\delta_\infty + \Lambda_3 + \delta_\infty \Lambda_3) \right) , \qquad (8.22)$$

which is free of mixing parameters. Indeed, (8.22) fixes Λ_3 once its left-hand side is (experimentally) known. However, we still have to face the fact that our system is underdetermined. In order to overcome this problem, we notice that at NLO in large-N_c ChPT (8.14,8.15) provide a clean prediction for both F_8 and $(\theta_8 - \theta_0)$ in terms of the well-known value for F_K/F_π [37]. Taking either F_8 or $(\theta_8 - \theta_0)$ as a constraint, one would add an additional equation to the previous system, which would provide a unique solution. Taking both, would lead to an overdetermined system, which in general has no solution. For this reason, we adopt a democratic procedure in which we perform a fit including both, F_8 and $(\theta_8 - \theta_0)$ constraints, together with (8.18-8.21). In addition, we include the theoretical uncertainties from large-N_c ChPT predictions, (8.14,8.15), by noticing that F_K/F_π typically receives 5% corrections from the NNLO. Consequently, we add this error in quadrature on top of the one from [37] for our fitting procedure.

The solution is collected in Table 8.3 and is the main result of this section. The value for χ^2_{dof} is excellent, which indicates a good agreement with large-N_c ChPT but with non-negligible NNLO corrections accounted here as a 5%. Without this 5%, the χ^2_{dof} would grow up to 1.5. In addition, we can use (8.14) to predict the value $\Lambda_1 = 0.21(5)$. In Figure 8.5 we collect our results (orange crosses) and compare them to different predictions in the literature [269, 270, 271, 272] (red dots), as well with our previous results [23] in blue-empty squares. We see that the main difference with respect to our previous work [23], where we did not use the η′ TFF asymptotic value and assumed $\phi_q = \phi_s$, appears in F_0. This is to be expected as the inclusion of Λ_1 and Λ_3 affects the singlet part exclusively. In addition, we have reduced our errors
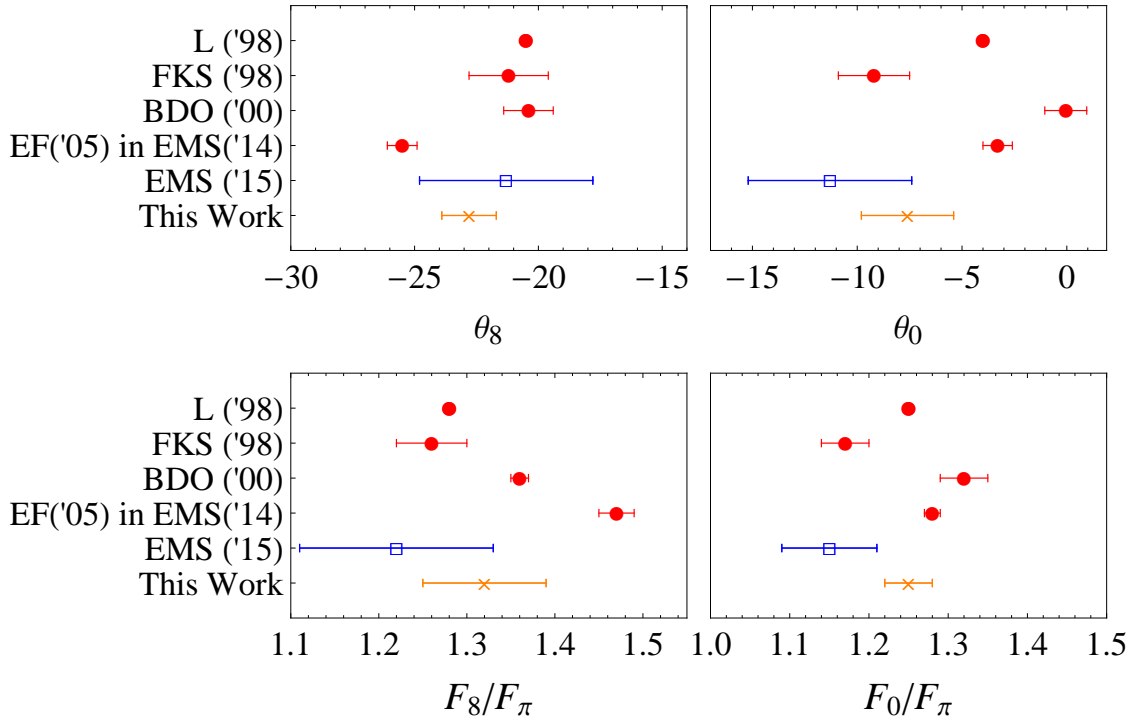
Figure 8.5: η-η' mixing parameters in the octet-singlet basis from L [271], FKS [270], BDO [272], EF [269], EMS(14) [22], and EMS(15) [23].

thanks to the constraints from large-N_c ChPT with respect to our previous work. Our prediction for Λ_3 may be compared with the one in [272], $\Lambda_3 = -0.03(2)$. Both of them point towards a small value for this parameter, though they differ in sign. We find that Λ_3 actually plays an important role not only in fulfilling the degeneracy condition (8.22), but in the $\eta(\eta') \to \gamma\gamma$ decays as well. In addition, the Λ_1 term is rather important and affects specially the η' results, where deviations of order 10% appear if this is omitted. Finally, we stress that the use of the RG equation for F_0 is fundamental, whereas most of the theoretical and experimental analysis do not account for this effect, which —to our best knowledge— was included for the first time in [231]. This effect increases η_∞ and diminishes η'_∞, bringing in agreement experiment and theory.

Our results may be translated to the quark-flavor basis through the use of the rotation matrix [270] (see appendix A)

$$U(\theta_{\text{ideal}}) = \frac{1}{\sqrt{3}} \begin{pmatrix} 1 & -\sqrt{2} \\ \sqrt{2} & 1 \end{pmatrix} , \qquad (8.23)$$

relating the pseudoscalar decay constants

$$(F_P^{qs}) = (F_P^{80}) U(\theta_{\text{ideal}}) . \qquad (8.24)$$

From the above equation, together with the values from the first row of Table 8.3, we obtain

$$F_q = 1.10(3)F_\pi , \qquad F_s = 1.45(8)F_\pi ,$$
$$\phi_q = 40.6(1.8)° , \qquad \phi_s = 38.4(1.2)° . \tag{8.25}$$

In addition, we can predict the ratio $R_{J/\psi} \equiv \Gamma_{J/\psi \to \eta'\gamma}/\Gamma_{J/\psi \to \eta\gamma}$, which is given in terms of ϕ_q alone [269] as

$$R_{J/\psi} = \tan^2 \phi_q \left(\frac{m_{\eta'}}{m_\eta} \right)^4 \left(\frac{M_{J/\psi}^2 - m_{\eta'}^2}{M_{J/\psi}^2 - m_\eta^2} \right)^3 . \tag{8.26}$$

With (8.25), $R_{J/\psi} = 5.6(7)$, just at 1.2σ from the experimental value $R_{J/\psi} = 4.7(2)$ [37]. It may be that, as precision improves, the deviation grows, which would be a hint of novel phenomena in the η-η' system, as gluonium component, which has long been debated, but not found so far [273]. We recall in this sense that large-N_c ChPT implicitly assumes that such component is not present in the η'. Moreover, the 3-gluon annihilation amplitude, not included in our framework, may need to be included to account for this 10% discrepancy [274]. Alternatively, we could include $R_{J/\psi}$ in our fitting procedure. The results would then be $F_8 = 1.37(6)$, $F_0 = 1.26(2)$, $\theta_8 = -23.5(0.9)$, $\theta_0 = -8.8(2.0)$, and $\Lambda_3 = 0.07(3)$, with $\chi_{\text{dof}}^2 = 1.3$, being very similar to those in Table 8.3. With respect to the $VP\gamma$ couplings calculated in our previous work [23], the new results yield more precise errors and very similar central values, with the exception of the ϕ cases, which get slightly closer to the experimental results. With the set of parameters in Table 8.3, together with (8.13), we can also predict the ratio $R_Z \equiv \Gamma_{Z \to \eta'\gamma}/\Gamma_{Z \to \eta\gamma}$, which is given by [177]

$$R_Z = \left| \frac{F_{\eta'\gamma Z}}{F_{\eta\gamma Z}} \right|^2 \left(\frac{M_Z^2 - m_{\eta'}^2}{M_Z^2 - m_\eta^2} \right)^3 , \tag{8.27}$$

where $M_Z^2 F_{P\gamma Z}(M_Z^2) = 6\sqrt{2}(C_{8\gamma Z}F_P^8 + C_{1\gamma Z}F_P^0(1+\delta_\infty))$ with $C_{8\gamma Z} = (1-4\sin^2\theta_W)/6\sqrt{6}$, $C_{1\gamma Z} = (2 - 4\sin^2\theta_W)/3\sqrt{3}$ and θ_W the Weinberg angle at M_Z^2 [37]. Since $C_{8\gamma Z} \ll C_{1\gamma Z}$, one may expect $R_Z \simeq \cot^2\theta_0$ [177], an observable quite sensitive, then, to the singlet angle. However, since $F_\eta^8 \gg F_\eta^0$, the denominator of (8.27) should not be approximated and all the terms should be retained. In this respect, we find $R_Z = 8.4(2.1)$, indicating a large singlet component in R_Z.

Finally, we comment on possible venues to improve our errors. On the one hand, it would be desirable to improve not only on η_∞, which now is the input with the largest error, but also to obtain η'_∞ from a P_2^2, which would reassess both the central value and the error of this parameter. This would be possible from future Belle-II data.

On the other hand, it would be interesting to have a more precise $\mathcal{O}(\alpha_s)^2$ calculation for δ as well as NNLO predictions for the mixing parameters and $\eta(\eta') \to \gamma\gamma$ decays, which would allow to check the stability and accuracy of the results. In addition, future lattice analysis may play an important role in this field [275] and a combined analysis using the PA method will be highly desirable.

8.4 Conclusions

In this work we have shown the excellent performance of the Padé approximants method developed in [21, 22, 255, 23] for the description of the recently reported first observation of the Dalitz decay $\eta' \to \gamma e^+ e^-$ by the BESIII collaboration [25]. This experimental analysis studies the time-like region of the η' transition form factor up to the resonance region.

Unlike our previous works, we have explored in the present one the limits of application of PAs in the TL region finding that, beyond expectations, PAs can be extended to energies very close to the location of poles. We have nicely described the behaviour of the modulus square of the η' TFF thus showing that this form factor has a simple analytical structure in the complex plane made of an isolated branch cut due to the $\pi\pi$ production threshold, the unitary cut, which disappears as soon as the TFF is modulus squared, and a set of single poles.

The careful analysis of the PA sequence $P_1^L(Q^2)$ reveals, however, more effects than those of the ρ resonance emerging here from $\pi\pi$ rescattering. Subleading effects caused by additional branch cuts or the influence of higher resonances' tails are also captured by PAs and are indeed responsible for the shift of the PA-pole location with respect to the naive projection of the ρ resonant pole onto the real axis. Since this shift is not known with precision it is difficult to extract from the PA pole the exact position of the resonance pole. This limitation of the method, already mentioned at the beginning of this work, does not prevent the PAs from guiding us about the underlying analytical structure of the TFF. One can take advantage of this highly non-trivial knowledge to further use the PAs method in other approaches such as $B \to \pi$ semileptonic form factors or the extraction of the proton charge radius from electron scattering. A last remark concerns the role of VMD in experimental analyses, now that the meaning of the PA pole on the real axis is understood. As pointed out in [20], VMD should be interpreted as a first step in a systematic approximation, that is, the P_1^0 element belonging to a more general and exhaustive P_1^N sequence. Although

it is common to report on such fit for ease of comparison, the range of application of VMD in the TL region is much shorter than the P_1^7 we used here.

In summary, PAs are not only useful for fitting and extrapolating data within the SL region but also give us information about the analytical structure of the TFF. On the one hand, they justify the use of elaborated dispersion relations with a single $\pi\pi$ elastic branch cut for the isovector part of the TFF and a more simple Breit-Wigner model for the isoscalar one [223, 263]. On the other hand, since no information on the analytical structure of the TFF must be given in advance, PAs are an excellent tool for testing other approaches decomposing the TFF into cuts and resonance poles. PAs are also capable of accommodating the SL region high-energy QCD constraints while still providing accurate predictions of the $\Gamma_{\eta(\eta')\to\gamma\gamma}$ decay widths. Moreover, they allowed us to update the η-η' mixing parameters within the context of the most general large-N_c ChPT scenario, thus superseding the values obtained in our previous works. Yet another issue is the lack of an imaginary part in the TFF when analysed by means of PAs. Nevertheless, due to the indication of a simple analytical structure of the TFF and its almost meromorphic nature as soon as it is modulus squared, a PA constructed from a complex-conjugated Taylor expansion would locate the poles of this TFF in a convergence sequence. This idea opens the door to such extensions which are postponed for future work.

Chapter 9

Conclusions

In this thesis we have studied several processes involving η and η' mesons. In particular, we have first investigated the hadronic decays of the tau lepton $\tau^- \to K^-\eta^{(\prime)}\nu_\tau$ and $\tau^- \to K_S\pi^-\nu_\tau$ in sections 3, 4 and then $\tau^- \to \pi^-\eta^{(\prime)}\nu_\tau$ in section 5. Our analyses have been focused in the description of the participant hadronic form factors encoding the effects of the strong interactions. The corresponding parameterizations have been carried out by means of Chiral Perturbation Theory including resonances supplemented by arguments of analyticity and unitarity through dispersion relations. Benefited from the experimental measurement of the $\tau^- \to K^-\eta\nu_\tau$ decay spectrum released by the BaBar and Belle collaborations [107, 12], we have determined the pole parameters in the complex plane of the $K^{*-}(1410)$ vector resonance to be $M_{K^*(1410)} = 1330^{+27}_{-41}$ MeV and $\Gamma_{K^*(1410)} = 217^{+68}_{-122}$ MeV for the mass and width (cf. Eq. (3.48)), respectively. Subsequently, we predicted the branching ratio of the decay $\tau^- \to K^-\eta'\nu_\tau$ to be $\sim 1 \cdot 10^{-6}$ (cf. table 3.4), respecting the upper limit, $4.2 \cdot 10^{-6}$ at 90% CL, found by BaBar [110], and advocated its measurement in near future B-factories.

On a second stage, we have performed a simultaneous fit to both Belle data [12, 100] on the decays $\tau^- \to K^-\eta\nu_\tau$ and $\tau^- \to K_S\pi^-\nu_\tau$, that has led the determination of the $K^*(1410)$ resonance with improved precision. We find $M_{K^*(1410)} = 1304 \pm 17$ MeV and $\Gamma_{K^*} = 171 \pm 62$ MeV, Eq. (4.15), that supersede previous determinations from both channels separated (cf. Fig. 4.2). We have also discussed prospects of improvement for Belle-II and motivated experimental groups to measure the distribution for the $\tau^- \to K^-\pi^0\nu_\tau$ decay in order to disentangle possible isospin violations in the $K\pi$ low-energy parameters.

We closed the first part of the thesis by studying the second-class current decays $\tau \to \pi^-\eta^{(\prime)}\nu_\tau$. These processes occur via isospin violation and have not been evidenced in Nature so far. We discussed different parameterizations of the scalar form

factor ordered according to their increasing fulfillment of analyticity and unitarity constraints while the vector form factor has been extracted using existing data on the well known $\pi^-\pi^0$ one. We conclude that, according to our predictions (cf. tables 5.1 and 5.2), both decays have good prospects for discovering at Belle-II. The crossing symmetric semileptonic $\eta^{(\prime)} \to \pi^- \ell^+ \nu_\ell$ ($\ell = e, \mu$) decays have been also been tackled.

In the second part of the thesis, we have examined several processes driven by the anomalous vertex $\mathcal{P}\gamma^*\gamma^{(*)}$ ($\mathcal{P} = \pi^0, \eta, \eta'$). The transition form factor in the space-like region has been accessed via the two-photon fusion reaction $e^+e^- \to e^+e^-\mathcal{P}$ by different experimental groups which have reported the corresponding data. These data have been suitably parameterized, in a model-independent way, by means of Padé approximants [22]. This allowed us to predict the time-like region as shown in Figs. 7.1 and 7.2 proving the remarkable ability of PA in describing also this regime. Since data is nicely supported by our description, we then proceeded to describe the single and double Dalitz decays $\mathcal{P} \to \ell^+\ell^-\gamma$ and $\mathcal{P} \to \ell^+\ell^-\ell^+\ell^-$ ($\ell = e, \mu$). We find that the effect of the TFF is much notorious when muons are involved and enhanced for η' decays. Regarding our predictions on the different branching ratios given in table 7.9, they are not only in accordance with the measured decays but rather we also hope them to serve as a guide to the experimental collaborations to measure the unseen one.

Finally, we have benefited from the recent experimental measurement of the single Dalitz decay $\eta' \to e^+e^-\gamma$ released by the BESIII collaboration [25], to perform, for the first time, a combined analysis of both space-and time-like data of the TFF through the method of PA. In the study, we have addressed the issue of why Padé approximants work so well in reproducing time-like data concluding that the clue feature is the small effect of the $\pi\pi$ cut at threshold. From our combined fit, we succeeded in extracting both the low-energy form factor parameters as well as the $\eta - \eta'$ mixing parameters, Eq. (8.8) and table. (8.3), respectively, with improved degree of accuracy than our previous determinations.

Appendix A

Bases of the $\eta - \eta'$ mixing

In section 1.5, we have seen that the mixing phenomenon among the eigenstates η_8 and η_1 occurs due to an explicit $SU(3)$ flavor symmetry breaking. However, these states are not the physical η and η' mesons we observe in nature (see table 1.2) but rather linear combinations of them. This admixture is parameterized by the so-called mixing angle and can be described in two different bases:

- the octet-singlet basis, which uses $|\eta_8\rangle = \frac{1}{\sqrt{6}}|u\bar{u} + d\bar{d} - 2s\bar{s}\rangle$ and $|\eta_1\rangle = \frac{1}{\sqrt{3}}|u\bar{u} + d\bar{d} + s\bar{s}\rangle$ as the basis states

$$\begin{pmatrix} \eta \\ \eta \end{pmatrix} = \begin{pmatrix} \cos\theta_P & -\sin\theta_P \\ \sin\theta_P & \cos\theta_P \end{pmatrix} \begin{pmatrix} \eta_8 \\ \eta_1 \end{pmatrix}, \tag{A.1}$$

- the quark-flavor basis, with $|\eta_q\rangle = \frac{1}{\sqrt{2}}$ and $|\eta_s\rangle = |s\bar{s}\rangle$ as the relevant basis states

$$\begin{pmatrix} \eta \\ \eta \end{pmatrix} = \begin{pmatrix} \cos\phi_P & -\sin\phi_P \\ \sin\phi_P & \cos\phi_P \end{pmatrix} \begin{pmatrix} \eta_q \\ \eta_s \end{pmatrix}. \tag{A.2}$$

In order to find a relation between the mixing angle θ_P and ϕ_P we compare the mixing pattern of the η and η' states for both mixing schemes as

$$|\eta\rangle = \cos\theta_P|\eta_8\rangle - \sin\theta_P|\eta_1\rangle = \cos\phi_P|\eta_q\rangle - \sin\phi_P|\eta_s\rangle\,,$$
$$|\eta'\rangle = \sin\theta_P|\eta_8\rangle + \cos\theta_P|\eta_1\rangle = \sin\phi_P|\eta_q\rangle + \cos\phi_P|\eta_s\rangle\,. \tag{A.3}$$

Then, using the change of basis

$$\begin{pmatrix} \eta_8 \\ \eta_1 \end{pmatrix} = \begin{pmatrix} 1/\sqrt{3} & -\sqrt{2/3} \\ \sqrt{2/3} & 1/\sqrt{3} \end{pmatrix} \begin{pmatrix} \eta_q \\ \eta_s \end{pmatrix}. \tag{A.4}$$

and equating both sides of Eq. (A.3) we arrive at

$$\cos\theta_P = \frac{1}{\sqrt{3}}\left(\cos\phi_P + \sqrt{2}\sin\phi_P\right)\,, \quad \sin\theta_P = \frac{1}{\sqrt{3}}\left(\sin\phi_P - \sqrt{2}\cos\phi_P\right)\,. \tag{A.5}$$

In the $SU(3)$ flavor symmetry limit i.e. no mixing in the octet-singlet basis ($\theta_P = 0$), from Eq. (A.5) one can define an ideal mixing angle ϕ_{ideal} in the quark-flavor basis

$$\cos\phi_{\text{ideal}} = \frac{1}{\sqrt{3}}, \quad \sin\phi_{\text{ideal}} = \sqrt{\frac{2}{3}}, \tag{A.6}$$

which leads

$$\phi_{\text{ideal}} = \arctan\sqrt{2}. \tag{A.7}$$

Thus, the first term in Eq. (A.5) can be written as

$$\cos\theta_P = \cos\phi_{\text{ideal}}\cos\phi_P + \sin\phi_{\text{ideal}}\sin\phi_P = \cos(\phi_P - \phi_{\text{ideal}}), \tag{A.8}$$

which allow us to get the well-known relation between the octet-singlet mixing angle θ_P and the quark-flavor ones ϕ_P

$$\theta_P = \phi_P - \phi_{\text{ideal}} = \phi_P - \arctan\sqrt{2} \simeq \phi_P - 54.7°. \tag{A.9}$$

Appendix B

G-parity and second class currents: the case of $\tau^- \to \pi^- \eta^{(\prime)} \nu_\tau$

The concept of G-parity is defined as a rotation of the wave function by 180° around the y-axis in the isospin space followed by the application of the charge conjugation operator C. The general G-parity operator applied over a state $|X\rangle$ reads

$$G|X\rangle = \exp[i\theta I_y]C|X\rangle\,, \tag{B.1}$$

though, in short, is equivalent to

$$G|X\rangle = (-1)^I C|X\rangle\,, \tag{B.2}$$

as we will demonstrate in the following (cf. Eq. (B.14)).

B.1 Isospin rotation

A general isospin rotation of a field ϕ is given by $U\phi(x)U^{-1} = S(\theta)\phi(x)$ where U is a unitary operator $U = \exp[i\theta I]$ and $S(\theta) = \exp[-i\theta T]$ its representation in a three-dimensional isospin space with $T = (T_x, T_y, T_z)$ being the rotation matrix generators given by

$$T_x = \begin{pmatrix} 0 & 0 & 0 \\ 0 & 0 & -i \\ 0 & i & 0 \end{pmatrix}, T_y = \begin{pmatrix} 0 & 0 & i \\ 0 & 0 & 0 \\ -i & 0 & 0 \end{pmatrix}, T_z = \begin{pmatrix} 0 & -i & 0 \\ i & 0 & 0 \\ 0 & 0 & 0 \end{pmatrix}. \tag{B.3}$$

These matrices, the generators of isospin rotations, are obtained from the standard rotation matrices around x, y and z axes

$$R_x = \begin{pmatrix} 1 & 0 & 0 \\ 0 & \cos\theta & \sin\theta \\ 0 & -\sin\theta & \cos\theta \end{pmatrix}, R_y = \begin{pmatrix} \cos\theta & 0 & -\sin\theta \\ 0 & 1 & 0 \\ \sin\theta & 0 & \cos\theta \end{pmatrix}, R_z = \begin{pmatrix} \cos\theta & \sin\theta & 0 \\ -\sin\theta & \cos\theta & 0 \\ 0 & 0 & 1 \end{pmatrix},$$
$$\tag{B.4}$$

by considering an infinitesimal rotation as of

$$R_{x,y,z} = \mathbb{1}_{3\times3} + iT_{x,y,z}\theta. \tag{B.5}$$

For our purpose, we are interested in isospin rotations of an angle θ around the y-axis whose general form reads

$$
\begin{aligned}
S(\theta) &= \exp[-i\theta T_y] = \mathbb{1}_{3\times3} + \sum_{n=1,3..}^{\infty} \frac{1}{n!}(-i\theta T_y)^n + \sum_{n=2,4..}^{\infty} \frac{1}{n!}(-i\theta T_y)^n \\
&= \mathbb{1}_{3\times3} - iT_y \sum_{n=1}^{\infty}(-1)^{n-1}\frac{\theta^{2n-1}}{(2n-1)!} + (T_y)^2 \sum_{n=1}^{\infty}(-1)^n \frac{\theta^{2n}}{(2n)!} \\
&= \mathbb{1}_{3\times3} - iT_y \sin\theta - (1-\cos\theta)(T_y)^2,
\end{aligned}
\tag{B.6}
$$

where we have used $T_y^3 = T_y$.

In particular, the matrix for an isospin rotation of an angle $\theta = \pi$ is given by

$$S(\theta) = \mathbb{1}_{3\times3} - 2\begin{pmatrix} 1 & 0 & 0 \\ 0 & 0 & 0 \\ 0 & 0 & 1 \end{pmatrix} = \begin{pmatrix} -1 & 0 & 0 \\ 0 & 1 & 0 \\ 0 & 0 & -1 \end{pmatrix}, \tag{B.7}$$

whose application on the cartesian pion triplet,

$$\pi^1 = \frac{1}{\sqrt{2}}(\pi^+ + \pi^-), \quad \pi^2 = \frac{i}{\sqrt{2}}(\pi^+ - \pi^-), \quad \pi^3 = \pi^0, \tag{B.8}$$

flips the sign of π^1 and π^3 leaving π^2 unchanged

$$S(\theta = \pi)\begin{pmatrix} \pi^1 \\ \pi^2 \\ \pi^3 \end{pmatrix} = \begin{pmatrix} -1 & 0 & 0 \\ 0 & 1 & 0 \\ 0 & 0 & -1 \end{pmatrix}\begin{pmatrix} \pi^1 \\ \pi^2 \\ \pi^3 \end{pmatrix} = \begin{pmatrix} -\pi^1 \\ \pi^2 \\ -\pi^3 \end{pmatrix}. \tag{B.9}$$

In other words, because of this rotation the following replacements are in order $\pi^\pm \to -\pi^\mp$ and $\pi^0 \to -\pi^0$.

B.2 Charge conjugation

The charge conjugation operator applied to the cartesian pion triplet Eq. (B.8) flips the sign of π^2

$$C \begin{pmatrix} \pi^1 \\ \pi^2 \\ \pi^3 \end{pmatrix} = \begin{pmatrix} 1 & 0 & 0 \\ 0 & -1 & 0 \\ 0 & 0 & 1 \end{pmatrix} \begin{pmatrix} \pi^1 \\ \pi^2 \\ \pi^3 \end{pmatrix} = \begin{pmatrix} \pi^1 \\ -\pi^2 \\ \pi^3 \end{pmatrix}, \tag{B.10}$$

where we have taken into account that $C|\pi^\pm\rangle = |\pi^\mp\rangle$ and $C|\pi^0\rangle = |\pi^0\rangle$.

B.3 G-parity

Regarding G-parity transformations, let us consider the cartesian pions Eq. (B.8) and apply first an isospin rotation of an angle $\theta = \pi$ around the y-axis followed by a charge conjugation operation as of

$$\begin{aligned}
G \begin{pmatrix} \pi^1 \\ \pi^2 \\ \pi^3 \end{pmatrix} &= S(\theta = \pi)C \begin{pmatrix} \pi^1 \\ \pi^2 \\ \pi^3 \end{pmatrix} \\
&= \begin{pmatrix} -1 & 0 & 0 \\ 0 & 1 & 0 \\ 0 & 0 & -1 \end{pmatrix} \begin{pmatrix} 1 & 0 & 0 \\ 0 & -1 & 0 \\ 0 & 0 & 1 \end{pmatrix} \begin{pmatrix} \pi^1 \\ \pi^2 \\ \pi^3 \end{pmatrix} = - \begin{pmatrix} \pi^1 \\ \pi^2 \\ \pi^3 \end{pmatrix},
\end{aligned} \tag{B.11}$$

which lead the mass eigenstates of the isospin pion triplet suffer the following transformation

$$G|\pi^{\pm 0}\rangle = -|\pi^{\pm 0}\rangle. \tag{B.12}$$

Regarding G-parity applied to the η and η' mesons we have

$$G|\eta^{(\prime)}\rangle = |\eta^{(\prime)}\rangle, \tag{B.13}$$

since they are neutral isospin singlets i.e. they do no rotate under isospin transformation and are invariant under charge conjugation.

Finally, the G-parity of the final state hadronic system, $\pi\eta^{(\prime)}$, is given by

$$G|\pi^{\pm,0}\eta^{(\prime)}\rangle = G|\pi^{\pm,0}\rangle|\eta^{(\prime)}\rangle = -|\pi^{\pm,0}\eta^{(\prime)}\rangle. \tag{B.14}$$

Notice that we would have arrived at this same result by applying Eq. (B.2) with $I = 1$, the isospin of the $\pi^-\eta^{(\prime)}$ system.

For the case that concerns us, the G-parity of the vector current entering the description of $\tau^- \to \pi^-\eta^{(\prime)}\nu_\tau$ is

$$G|\bar{u}\gamma d\rangle = +|\bar{u}\gamma d\rangle, \tag{B.15}$$

which is opposite to what we have derived in Eq. (B.14) for the final state hadronic system. Therefore, the decay $\tau^- \to \pi^- \eta^{(\prime)} \nu_\tau$ occurs via G-parity violation leading $J^{PG} = 0^{+-}$ or 1^{--} for the spin-parity-G-parity quantum numbers of the $\pi \eta^{(\prime)}$ system which, in the SM, can only proceed through the unseen second class currents.

Appendix C

Exponential parametrisation of the vector form factor

The exponential parametrisation of $f_+^{K\pi}(s)$ is a variant of the form factor Ansatz (4.4) in which the real part of $\tilde{H}_{K\pi}(s)$ is resummed into an exponential function [103, 105, 52],

$$f_+^{K\pi}(s) = \left[\frac{m_{K^*}^2 + \gamma s}{D(m_{K^*}, \gamma_{K^*})} - \frac{\gamma s}{D(m_{K^{*\prime}}, \gamma_{K^{*\prime}})} \right] e^{\frac{3}{2}\mathrm{Re}\tilde{H}_{K\pi}(s)} , \tag{C.1}$$

where now $D(m_n, \gamma_n) = m_n^2 - s - i\, m_n \gamma_n(s)$ and the energy-dependent resonance widths, defined as

$$\gamma_n(s) = \gamma_n \frac{s}{m_n^2} \frac{\sigma_{K\pi}^3(s)}{\sigma_{K\pi}^3(m_n^2)} , \tag{C.2}$$

are equal to the imaginary part of the propagator in eq. (4.5) through the identification $\kappa_n \,\mathrm{Im}\widetilde{H}_{K\pi}(s) = m_n \gamma_n(s)$. This representation of $f_+^{K\pi}(s)$ in the elastic limit was used beyond this approximation in refs. [103, 105] including the $K\eta$ channel and ref. [13] also incorporating the $K\eta'$ effects. However, in order to perform a fair comparison of the results obtained from this parametrisation and the dispersive representation in eq. (4.8) we work in the elastic limit and use for $\widetilde{H}_{K\pi}(s)$ the isospin average of eq. (4.7). Needless to say, the unphysical "mass" and "width" parameters m_n and γ_n in this parametrisation will be different from their analogues in the dispersive treatment but the corresponding pole parameters should not differ significantly. It is worth mentioning, however, that when the normalised version of the form factor in eq. (C.1) is directly confronted with experimental data the slope parameters are not fitted but deduced from the Taylor expansion of the form factor (unlike the test proposed in the main text where the phase of the form factor is calculated first and then plugged into the dispersive relation).

In Table C.1, we display the results of the direct application of the exponential vector form factor in eq. (C.1) using three different settings: a combined fit of the two sets of data with $\gamma_{K\pi} = \gamma_{K\eta}$ (Fit I, which implies $\lambda'^{(\prime)}_{K\pi} = \lambda'^{(\prime)}_{K\eta}$); the same but $\gamma_{K\pi} \neq \gamma_{K\eta}$ (Fit II); and fitting the data sets separately (Fit III). In the last case, the pole position of the $K^*(892)$ resonance is obtained from the fit to $K\pi$ data and then plugged into the $K\eta$ fit. On the contrary, the $K^*(1410)$ pole position is kept free in both fits (in brackets the results from the fit to $K\eta$ data alone). Looking at the various χ^2/n.d.f. of Table C.1, one immediately realises the meagre performance exhibited by the exponential parametrisation as compared to the dispersive representation achievements shown in Table 4.1. In the $K\eta$ part of Fit III (fourth column) the χ^2/n.d.f.~ 2. Particularly inept are the values obtained for the $K\eta$ branching ratio which are in all cases far from the experimental measurement. Therefore, a combined analysis of the $\tau^- \to K_S\pi^-\nu_\tau$ and $K^-\eta\nu_\tau$ decays clearly disfavours the direct exponential treatment as compared to the dispersive approach, a conclusion which was already hinted at by the independent analysis of $K\eta$ data in ref. [13]. Now comparing, for instance, Fit II in Table C.1 with its analogue Fit B in Table 4.1, it is seen that the pole positions of both resonances are quite in agreement in the two approximations as also happens with their relative weights. However, somewhat larger values with smaller errors are obtained for all the different slope parameters, in accord this time with the previous analyses in refs. [103, 105].

Fitted value	Fit I	Fit II	Fit III
$\bar{B}_{K\pi}(\%)$	0.394 ± 0.008	0.398 ± 0.009	0.401 ± 0.009
$(B_{K\pi}^{th})(\%)$	(0.391)	(0.394)	(0.398)
M_{K^*}	892.35 ± 0.25	892.31 ± 0.25	892.39 ± 0.23
Γ_{K^*}	47.19 ± 0.51	47.21 ± 0.49	47.15 ± 0.46
$M_{K^{*\prime}}$	1318 ± 10	1318 ± 11	$1265 \pm 16 \, (1340 \pm 19)$
$\Gamma_{K^{*\prime}}$	146 ± 31	165 ± 36	$145 \pm 42 \, (218 \pm 65)$
$\gamma_{K\pi} \times 10^2$	$= \gamma_{K\eta}$	-4.1 ± 0.9	-3.8 ± 1.0
$\lambda'_{K\pi} \times 10^3$	25.02 ± 0.13	25.08 ± 0.14	25.16 ± 0.14
$\lambda''_{K\pi} \times 10^4$	12.56 ± 0.10	12.61 ± 0.10	12.66 ± 0.11
$\bar{B}_{K\eta} \times 10^4$	1.34 ± 0.07	1.35 ± 0.08	1.25 ± 0.11
$(B_{K\eta}^{th}) \times 10^4$	(1.15)	(1.16)	(1.06)
$\gamma_{K\eta} \times 10^2$	-4.6 ± 0.8	-6.2 ± 1.6	-8.4 ± 2.7
$\lambda'_{K\eta} \times 10^3$	$= \lambda'_{K\pi}$	24.80 ± 0.23	24.47 ± 0.40
$\lambda''_{K\eta} \times 10^4$	$= \lambda''_{K\pi}$	12.40 ± 0.17	12.18 ± 0.29
χ^2/n.d.f.	$188.4/109 \sim 1.72$	$184.0/108 \sim 1.70$	$(117.9 + 49.5)/(81 + 25) \sim 1.58$

Table C.1: Fit results obtained using the exponential parametrisation for different settings: a combined fit of $K\pi$ and $K\eta$ data with $\gamma_{K\pi} = \gamma_{K\eta}$ (Fit I), the same but $\gamma_{K\pi} \neq \gamma_{K\eta}$ (Fit II); and fitting the data separately (Fit III). See the main text for further details. Dimensionful parameters are given in MeV. As a consistency check, for each of the fits we provide (in brackets) the value of the respective branching ratios obtained by integrating eq. (4.1)

Appendix D

Form factors in coupled-channels

Let us write the scalar form factor on general grounds through the once-subtracted dispersion relation

$$F(s) = F(s_0) + \frac{s - s_0}{\pi} \int_{s_{th}}^{\infty} ds' \frac{\text{Im}F(s')}{(s - s_0)(s' - s - i\epsilon)}, \tag{D.1}$$

where $F(s)$ is now a n-entries column vector. Eq. (D.1) comes together with the unitarity relation $\text{Im}F(s) = \Sigma(s)t_{IJ}^*(s)F(s)$, with $\Sigma(s)$ a diagonal matrix of kinematical factors given by

$$\Sigma(s) = \begin{pmatrix} \sigma_1(s) & 0 & ... & 0 \\ 0 & \sigma_2(s) & ... & 0 \\ ... & ... & ... & 0 \\ 0 & 0 & 0 & \sigma_n(s) \end{pmatrix}, \tag{D.2}$$

and $t_{IJ}(s)$ a $n \times n$ matrix defined as

$$t_{IJ}(s) = \begin{pmatrix} t^{11}(s) & t^{12}(s) & ... & t^{1n}(s) \\ t^{21}(s) & t^{22}(s) & ... & t^{2n}(s) \\ ... & ... & ... & ... \\ t^{n1}(s) & t^{n2}(s) & .. & t^{nn}(s) \end{pmatrix} \tag{D.3}$$

encoding the required unitarized partial-wave amplitudes. Then, Eq. (D.1) can be rewritten as

$$F(s + i\varepsilon) = F(s_0) + \frac{s - s_0}{\pi} \int_{s_{th}}^{\infty} ds' \frac{\Sigma(s')t_{IJ}^*(s')F(s')}{(s' - s_0)(s' - s - i\varepsilon)} = F(s_0) + \widetilde{F}(s + i\varepsilon), \tag{D.4}$$

where $F(s_0)$ is a real term and the discontinuity of $\widetilde{F}(s + i\varepsilon)$ is given by

$$\widetilde{F}(s + i\varepsilon) - \widetilde{F}(s - i\varepsilon) = 2i \lim_{\varepsilon \to 0} \text{Im}F(s + i\varepsilon) = 2i\text{Im}F(s) = 2i\Sigma(s)t_{IJ}^*(s)F(s). \tag{D.5}$$

We introduce the N/D method for unitarizing the partial wave scattering amplitude by

$$t_{I,J}(s) = \frac{N_{I,J}(s)}{D_{I,J}(s)}, \tag{D.6}$$

where the matrix functions (we omit the I and J indices hereafter) N and D contain the left- and right-hand cuts of the partial-wave amplitude respectively, and satisfy the dispersion relations

$$N(s) = \frac{s - s_0}{\pi} \int_{-\infty}^{s_L} ds' \frac{\mathrm{Im}N(s')}{(s' - s_0)(s' - s - i\varepsilon)} \tag{D.7}$$

and

$$D(s) = D(s_0) + \frac{s - s_0}{\pi} \int_{s_{th}}^{\infty} ds' \frac{\mathrm{Im}D(s')}{(s' - s_0)(s' - s - i\varepsilon)}. \tag{D.8}$$

One nice consequence of unitarity is the that the inverse of the (unitarized) partial wave amplitude fulfills

$$\mathrm{Im}t^{-1}(s) = -\Sigma(s), \tag{D.9}$$

or, equivalently,

$$\mathrm{Im}D(s) = -N\Sigma(s). \tag{D.10}$$

By inserting Eq. (D.10) into Eq. (D.6) we deduce

$$t^*(s) = \frac{N^*(s)}{D^*(s)} = \frac{-(\mathrm{Im}D(s)/\Sigma(s))^*}{D^*(s)} = \frac{-\mathrm{Im}D(s)/\Sigma(s)}{D(s - i\varepsilon)}. \tag{D.11}$$

Then, using Eq. (D.11) we can rewrite Eq. (D.5) as

$$\widetilde{F}(s + i\varepsilon) - \widetilde{F}(s - i\varepsilon) = 2i\mathrm{Im}F(s) = 2i\Sigma(s)\left[\frac{-\mathrm{Im}D(s)/\Sigma(s)}{D(s - i\varepsilon)}\right]\left[F(s_0) + \widetilde{F}(s + i\varepsilon)\right] \tag{D.12}$$

which further reduces to

$$\widetilde{F}(s + i\varepsilon)\left[D(s - i\varepsilon) + 2i\mathrm{Im}D(s)\right] - \widetilde{F}(s - i\varepsilon)D(s - i\varepsilon) = -2i\mathrm{Im}D(s)F(s_0). \tag{D.13}$$

The term in square brackets in Eq. (D.13) can be rewritten as $D(s + i\varepsilon)$ because its discontinuity across the cut. Then, we arrive at the following expression

$$\widetilde{F}(s + i\varepsilon)D(s + i\varepsilon) - \widetilde{F}(s - i\varepsilon)D(s - i\varepsilon) = -2i\mathrm{Im}D(s)F(s_0), \tag{D.14}$$

whose once subtraced solution, by virtue of the Cauchy integral, reads

$$\widetilde{F}(s + i\varepsilon)D(s + i\varepsilon) = \frac{s - s_0}{2\pi i} \int_{s_{th}}^{\infty} ds' \frac{F(s' + i\varepsilon)D(s' + i\varepsilon) - F(s' - i\varepsilon)D(s' - i\varepsilon)}{(s' - s_0)(s' - s)}, \tag{D.15}$$

and the desired solution is

$$\widetilde{F}(s + i\varepsilon) = \frac{1}{D(s + i\varepsilon)} \frac{-(s - s_0)}{\pi} \int_{s_{th}}^{\infty} ds' \frac{\mathrm{Im}D(s')F(s_0)}{(s' - s_0)(s' - s)}, \tag{D.16}$$

which, by employing Eq. (D.8), reduces to

$$\widetilde{F}(s + i\varepsilon) = -D(s + i\varepsilon)^{-1} \left(D(s + i\varepsilon) - D(s_0) \right) F(s_0).$$ (D.17)

Finally, Eq. (D.4) reads up to a polynomial indetermination [1]

$$F(s) = \left[1 + D(s)^{-1} \left(- \left[D(s) - D(s_0) \right] \right) \right] F(s_0) = D(s)^{-1} D(s_0) F(s_0).$$ (D.18)

As written in Eq. (D.18), the coupled-channels form factors problem reduces to finding a suitable parameterization for the $D(s)$ matrix in analogy with Eq. (5.28) for the single channel case. In the N/D method our work is based on, the $D(s)$ matrix is associated to

$$D_{IJ}(s) = \left(\mathbb{1} + g(s) N_{IJ}(s) \right),$$ (D.19)

where the matrices $N_{I,J}(s)$ and $g(s)$ encode, respectively, the scattering amplitudes and the meson-meson one-loop scalar function defined in Eq. (33) of Ref. [57].

---

[1] As for the single channel case, the solution is not unique since the appearance of a polynomial may encode information on the solution. This ambiguity, known as the polynomial ambiguity, can not be fixed without invoking external information such as experimental data and/or with the help of theoretical arguments. We argue that if the form factor has a proper high-energy fall-off behavior, this term may be ignored, without loss of generality, as a first approximation. Although, as soon as data becomes available in the future this term shall be accounted for and its weight would be inferred from fitting data.

Appendix E

Interference term in double Dalitz decays

E.1 Four-body decay width in invariant variables

The partial decay width of a particle P of mass M_P decaying into four particles $p_1 p_2 p_3 p_4$ reads [37]

$$\Gamma(P \to p_1 p_2 p_3 p_4) = \int d\Phi(p_P; q_{p_1}, q_{p_2}, q_{p_3}, q_{p_4}) \frac{(2\pi)^4}{2M_P} \overline{|\mathcal{M}(P \to p_1 p_2 p_3 p_4)|^2} , \quad \text{(E.1)}$$

where $d\Phi(p_P; q_{p_1}, q_{p_2}, q_{p_3}, q_{p_4})$ is the four-body phase-space element given by

$$d\Phi(p_P; q_{p_1}, q_{p_2}, q_{p_3}, q_{p_4}) = \delta^4 \left(p_P - \sum_{i=1}^{4} q_i \right) \prod_{i=1}^{4} \frac{d^3 \mathbf{q}_i}{(2\pi)^3 2E_i} . \quad \text{(E.2)}$$

Following refs. [253, 254], the phase space is expressed in terms of independent invariant masses (instead of using three-momenta and angles) as

$$d\Phi(p_P; q_{p_1}, q_{p_2}, q_{p_3}, q_{p_4}) = \frac{1}{8\pi^{10} M_P^2} \left(-B \right)^{-1/2} dM_{12}^2 dM_{34}^2 dM_{14}^2 dM_{124}^2 dM_{134}^2 , \quad \text{(E.3)}$$

where $M_{ij} = (q_i + q_j)^2$ and $M_{ijk} = (q_i + q_j + q_k)^2$. In the case that concerns us, B reads

$$B = m_\ell^8 + \left[M_{124}^2 M_{134}^2 - M_P^2 M_{14}^2 + M_{12}^2 \left(-M_{134}^2 + M_{14}^2 \right) \right]^2 + 2 \Bigg[\left(M_{12}^2 - M_{124}^2 \right) M_{124}^2 M_{134}^2 +$$

$$+ \left(M_{12}^2 M_{124}^2 + M_P^2 \left(-2M_{12}^2 + M_{124}^2 \right) + \left(M_{12}^2 + M_{124}^2 \right) M_{134}^2 \right) M_{14}^2 -$$

$$- \left(M_P^2 + M_{12}^2 \right) M_{14}^4 \Bigg] M_{34}^2 + \left(M_{124}^2 - M_{14}^2 \right)^2 M_{34}^4 m_\ell^4 \Bigg[M_{12}^4 + M_{124}^4 + 4M_{124}^2 M_{134}^2 + M_{134}^4 -$$

$$- 2M_P^2 \left(2 \left(M_{124}^2 + M_{134}^2 \right) + M_{14}^2 \right) + 2 \left(4M_{124}^2 + M_{134}^2 + M_{14}^2 \right) M_{34}^2 + M_{34}^4 +$$

$$+2M_{12}^2\left(M_{124}^2+4M_{134}^2+M_{14}^2+M_{34}^2\right)\Big] + m_\ell^6\Big[4M_P^2 - 2\left(3M_{12}^2+M_{124}^2+M_{134}^2+3M_{34}^2\right)\Big] -$$

$$-2m_\ell^2\Big[M_{12}^4\left(M_{134}^2+M_{14}^2\right) + \left(2M_P^2-M_{124}^2-M_{134}^2\right)\left(-M_{124}^2 M_{134}^2 + M_P^2 M_{14}^2\right) +$$

$$+\left(M_{124}^4 + \left(-3M_P^2+M_{124}^2+M_{134}^2\right)M_{14}^2\right)M_{134}^2 + \left(M_{124}^2+M_{14}^2\right)M_{34}^2 +$$

$$+M_{12}^2\left(M_{134}^2 - 3M_P^2 M_{14}^2 + M_{124}^2 M_{14}^2 + M_{134}^2 M_{14}^2 + \left(M_{124}^2+M_{134}^2-2M_{14}^2\right)M_{34}^2\right)\Big]\Bigg] \quad \text{(E.4)}$$

where m_ℓ is the lepton mass and the boundary of the physical allowed region is such that fulfils $B = 0$. ref. [253] points out that the choice of variables M_{12}^2, M_{34}^2, M_{14}^2, M_{124}^2, and M_{134}^2 is convenient because it facilitates the finding of the limits of integration of B since it only depends quadratically on each of the variables; other choices can lead to quartics.

E.2   Integration limits

In order to find the physical region of one variable, for instance M_{14}^2, one must solve $B = 0$ obtaining

$$M_{14}^{2\pm} = \frac{-b \pm 2\sqrt{G(M_{124}^2, M_{34}^2, M_{12}^2, m_\ell^2, M_P^2, m_\ell^2)G(M_{134}^2, M_{34}^2, M_{12}^2, m_\ell^2, M_P^2, m_\ell^2)}}{\lambda(M_{12}^2, M_{34}^2, M_P^2)} , \quad \text{(E.5)}$$

where $\lambda(a,b,c) = a^2 + b^2 + c^2 - 2ab - 2ac - 2bc$ is the basic two-particle kinematical function, the Kállen function, b is given by

$$
\begin{aligned}
b =\ & (M_{12}^2)^2(M_{134}^2 + m_\ell^2) + \\
& + (M_{34}^2 - M_2)[M_{34}^2(M_{124}^2 + m_\ell^2) + (M_{124}^2 - m_\ell^2)(-M_{134}^2 + m_\ell^2) - 2m_\ell^2 M_\ell^2] - \\
& - M_{12}^2[(M_{124}^2 - m_\ell^2)(M_{134}^2 - m_\ell^2) + \\
& + M_{34}^2(M_{124}^2 + M_{134}^2 + 2m_\ell^2 - 2M_P^2) + (M_{134}^2 + 3m_\ell^2)M_P^2] ,
\end{aligned}
\quad \text{(E.6)}
$$

and

$$
\begin{aligned}
G(x,y,z,u,v,w) =\ & u^2 z - uvw + uvx - uvz + uwy - uwz - uxy - uxz - uyz + \\
& + uz^2 + v^2 w + vw^2 - vwx - vwy - vwz - vxy + \\
& + vyz - wxy + wxz + x^2 y + xy^2 - xyz ,
\end{aligned}
\quad \text{(E.7)}
$$

is the basic four-particle kinematic function. As argued in ref. [253], the limits of integration of the remaining variables, M_{12}^2, M_{34}^2, M_{124}^2, and M_{134}^2 are obtained after

solving

$$G(M_{124}^2, M_{34}^2, M_{12}^2, m_\ell^2, M_P^2, m_\ell^2) = 0 \ , \quad G(M_{134}^2, M_{34}^2, M_{12}^2, m_\ell^2, M_P^2, m_\ell^2) = 0 \ , \quad \text{(E.8)}$$

while the dilepton invariant masses M_{12}^2 and M_{34}^2 range from threshold $4m_\ell^2$ to $(M_P - m_\ell)^2$ and $4m_\ell^2$ to $(M_P - M_{12})^2$, respectively.

E.3 Matrix element of the interference term

The last term in eq. (7.14) reads

$$
\begin{aligned}
\mathcal{A}_1 \mathcal{A}_2 &= \frac{e^8 |F(q^2, k^2)||F(q'^2, k'^2)|}{q^2 k^2 q'^2 k'^2} \times \\
&\times \varepsilon^{\mu\nu\alpha\beta} \varepsilon^{\mu'\nu'\alpha'\beta'} (q_1 + q_2)_\mu (q_3 + q_4)_\nu (q_1 + q_4)_{\mu'} (q_2 + q_3)_{\nu'} \times \\
&\times \mathrm{Tr}[(\not{q}_1 + m_\ell)\gamma_\alpha(\not{q}_2 - m_\ell)\gamma_{\beta'}(\not{q}_3 + m_\ell)\gamma_\beta(\not{q}_4 - m_\ell)\gamma_{\alpha'}] \ .
\end{aligned}
\quad \text{(E.9)}
$$

The trace and the corresponding contractions with both the product of Levi-Civita tensors and the different diphoton four momenta in eq. (E.9) have been computed with FormCalc. To give a result in the desired variables, some replacements in the former equation are mandatory. In this order are: i) $M_{23}^2 = 2(q_2 \cdot q_3 + 2m_\ell^2)$; ii) $q_i^2 = m_\ell^2$; iii) $q_2 \cdot q_3 = \frac{1}{2}(M^2 - 4m_\ell^2) - q_1 \cdot q_2 - q_1 \cdot q_3 - q_1 \cdot q_4 - q_2 \cdot q_4 - q_3 \cdot q_4$; iv) $q_2 \cdot q_4 = \frac{1}{2}(M_{124}^2 - 3m_\ell^2) - q_1 \cdot q_2 - q_1 \cdot q_4$; v) $q_1 \cdot q_3 = \frac{1}{2}(M_{134}^2 - 3m_\ell^2) - q_1 \cdot q_4 - q_3 \cdot q_4$; vi) $q_1 \cdot q_4 = \frac{1}{2}M_{14}^2 - m_\ell^2$, $q_1 \cdot q_2 = \frac{1}{2}M_{12}^2 - m_\ell^2$, $q_3 \cdot q_4 = \frac{1}{2}M_{34}^2 - m_\ell^2$. Finally, the desired expression for the interference term in eq. (E.9) reads

$$\frac{e^8 |F(M_{12}^2, M_{34}^2)||F(M_{14}^2, M_{23}^2)|}{M_{12}^2 M_{34}^2 M_{14}^2 (2m_\ell^2 + M_P^2 - M_{124}^2 - M_{134}^2 + M_{14}^2)^2} \times$$

$$\times \Bigg\{ -2m_\ell^8 + M_{12}^6 \left(M_{134}^2 - M_{14}^2\right) + 4m^6 \left(-M_{12}^2 + M_{124}^2 + M_{134}^2 - M_{34}^2\right) +$$

$$+ m^4 \Bigg[M_{12}^2 - 3\left(M_{124}^2 + M_{134}^2\right)^2 + 4M_P^2 M_{14}^2 + 2M_{12}^2 \left(M_{124}^2 + 5M_{134}^2 - 2M_{14}^2 - 5M_{34}^2\right) +$$

$$+ 2\left(5M_{124}^2 + M_{134}^2 - 2M_{14}^2\right) M_{34}^2 + M_{34}^4 \Bigg] -$$

$$- \Bigg[M_{124}^4 + M_{134}^4 - 2M_P^2 M_{14}^2 - 2M_{134}^2 M_{34}^2 + 2M_{14}^2 M_{34}^2 + M_{34}^4 \Bigg] \times$$

$$\times \Bigg[M_{124}^2 \left(M_{134}^2 - M_{134}^2\right) + M_{14}^2 \left(-M_P^2 + M_{34}^2\right) \Bigg] +$$

$$+ M_{12}^4 \Bigg[\left(M_P^2 + 2M_{134}^2 - 2M_{14}^2\right) M_{14}^2 + \left(-2M_{134}^2 + M_{14}^2\right) M_{34}^2 +$$

$$+ M_{124}^2 \left(-3M_{134}^2 + 2M_{14}^2 + M_{34}^2\right) \Bigg] + m^2 \Bigg[-M_{12}^6 + \left(M_{124}^2 + M_{134}^2\right)^3 -$$

$$
\begin{aligned}
& - \left(M_{124}^2 + M_{134}^2\right)\left(5M_{124}^2 + M_{134}^2 - 4M_{14}^2\right)M_{34}^2 + \left(M_{124}^2 + M_{134}^2 - 4M_{14}^2\right)M_{34}^4 - \\
& \qquad -M_{34}^6 + M_{12}^4\left(M_{124}^2 + M_{134}^2 - 4M_{14}^2 + M_{34}^2\right) + \\
& \qquad +M_{12}^2\Big(-\left(M_{124}^2 + M_{134}^2\right)\left(M_{124}^2 + 5M_{134}^2 - 4M_{14}^2\right) + \\
& +2M_P^2\left(M_{124}^2 - M_{134}^2 + 2M_{14}^2\right) + 2\Big(3\left(M_{124}^2 + M_{134}^2\right) + 4M_{14}^2\Big)M_{34}^2 + M_{34}^4\Big) - \\
& -2M_P^2\Big(M_{124}^4 + \left(M_{134}^2 + 2M_{14}^2\right)\left(M_{134}^2 - M_{34}^2\right) + M_{124}^2\left(-2M_{134}^2 + 2M_{14}^2 + M_{34}^2\right)\Big)\bigg] + \\
& \qquad + M_{12}^2\bigg[M_{134}^6 + M_{124}^4\left(3M_{134}^2 - M_{14}^2 - 2M_{34}^2\right) - M_{134}^2\left(M_{14}^2 + 2M_{34}^2\right) - \\
& \qquad -2M_{124}^2\left(M_P^2 M_{14}^2 + M_{134}^2 M_{14}^2 - M_{134}^2 M_{34}^2 + 2M_{14}^2 M_{34}^2 + M_{34}^4\right) + \\
& \qquad\qquad + M_{134}^2\Big(-2M_P^2 M_{14}^2 + M_{34}^2\left(-4M_{14}^2 + M_{34}^2\right)\Big) + \\
& \qquad\qquad + M_{14}^2\Big(M_{34}^2\left(4M_{14}^2 + M_{34}^2\right) + M_P^2\left(4M_{14}^2 + 6M_{34}^2\right)\Big)\bigg]\bigg]\bigg\}
\end{aligned}
\tag{E.10}
$$

Bibliography

[1] D. J. Gross and F. Wilczek, Phys. Rev. Lett. **30**, 1343 (1973).

[2] D. J. Gross and F. Wilczek, Phys. Rev. D **8**, 3633 (1973).

[3] H. D. Politzer, Phys. Rev. Lett. **30**, 1346 (1973).

[4] The Clay Mathematics Institute, http://www.claymath.org/millennium-problems

[5] S. Weinberg, Physica A **96**, 327 (1979).

[6] J. Gasser and H. Leutwyler, Annals Phys. **158**, 142 (1984).

[7] J. Gasser and H. Leutwyler, Nucl. Phys. B **250**, 465 (1985).

[8] R. Kaiser and H. Leutwyler, Eur. Phys. J. C **17**, 623 (2000), hep-ph/0007101.

[9] H. B. Li, J. Phys. G **36**, 085009 (2009) hep-ex/0902.3032.

[10] M. Unverzagt [Crystal Ball at MAMI Collaboration], Nucl. Phys. Proc. Suppl. **198**, 174 (2010) hep-ex/0910.1331; EPJ Web Conf. **72**, 00024 (2014).

[11] P. Moskal [KLOE-2 and WASA-at-COSY Collaborations], Fizika B **20**, 223 (2011) hep-ex/1102.5548.

[12] K. Inami *et al.* [Belle Collaboration], Phys. Lett. B **672**, 209 (2009) hep-ex/0811.0088.

[13] R. Escribano, S. Gonzàlez-Solís and P. Roig, JHEP **1310**, 039 (2013) hep-ph/1307.7908.

[14] D. R. Boito, R. Escribano and M. Jamin, Eur. Phys. J. C **59**, 821 (2009) hep-ph/0807.4883.

[15] D. R. Boito, R. Escribano and M. Jamin, JHEP **1009**, 031 (2010) hep-ph/1007.1858.

[16] R. Escribano, S. Gonzàlez-Solís, M. Jamin and P. Roig, JHEP **1409**, 042 (2014) hep-ph/1407.6590.

[17] B. Aubert *et al.* [BaBar Collaboration], Phys. Rev. D **76**, 051104 (2007) hep-ex/0707.2922.

[18] R. Escribano, S. Gonzàlez-Solís and P. Roig, hep-ph/1601.03989.

[19] M. Fujikawa *et al.* [Belle Collaboration], Phys. Rev. D **78**, 072006 (2008).

[20] P. Masjuan, S. Peris and J. J. Sanz-Cillero, Phys. Rev. D **78**, 074028 (2008) hep-ph/0807.4893.

[21] P. Masjuan, Phys. Rev. D **86**, 094021 (2012) hep-ph/1206.2549.

[22] R. Escribano, P. Masjuan and P. Sanchez-Puertas, Phys. Rev. D **89**, no. 3, 034014 (2014) hep-ph/1307.2061.

[23] R. Escribano, P. Masjuan and P. Sanchez-Puertas, Eur. Phys. J. C **75**, no. 9, 414 (2015) hep-ph/1504.07742.

[24] H. J. Behrend *et al.* [CELLO Collaboration], Z. Phys. C **49**, 401 (1991); J. Gronberg *et al.* [CLEO Collaboration], Phys. Rev. D **57**, 33 (1998) hep-ex/9707031; B. Aubert *et al.* [BaBar Collaboration], Phys. Rev. D **80**, 052002 (2009) hep-ex/0905.4778; P. del Amo Sanchez *et al.* [BaBar Collaboration], Phys. Rev. D **84**, 052001 (2011) 1101.1142; S. Uehara *et al.* [Belle Collaboration], Phys. Rev. D **86**, 092007 (2012) hep-ex/71205.3249; M. Acciarri *et al.* [L3 Collaboration], Phys. Lett. B **418**, 399 (1998).

[25] M. Ablikim *et al.* [BESIII Collaboration], Phys. Rev. D **92**, no. 1, 012001 (2015) hep-ex/1504.06016.

[26] A. Pich, Rept. Prog. Phys. **58**, 563 (1995) hep-ph/9502366.

[27] A. Pich, hep-ph/9806303.

[28] A. Pich, hep-ph/0001118.

[29] S. Scherer, Adv. Nucl. Phys. **27**, 277 (2003) hep-ph/0210398.

[30] M. Jamin, QCD and Renormalisation Group Methods, *Lecture presented at Herbstschule für Hochenergiephysik, Maria Laach (2006).*

[31] M. Gell-Mann, CTSL-20, TID-12608.

[32] S. Bethke, Eur. Phys. J. C **64**, 689 (2009) hep-ph/0908.1135.

[33] F. Englert and R. Brout, Phys. Rev. Lett. **13**, 321 (1964).

[34] P. W. Higgs, Phys. Lett. **12**, 132 (1964).

[35] P. W. Higgs, Phys. Rev. Lett. **13**, 508 (1964).

[36] G. S. Guralnik, C. R. Hagen and T. W. B. Kibble, Phys. Rev. Lett. **13**, 585 (1964).

[37] K.A. Olive et al. (Particle Data Group), Chin. Phys. C, 38, 090001 (2014).

[38] C. Vafa and E. Witten, Nucl. Phys. B **234**, 173 (1984).

[39] Y. Nambu, Phys. Rev. Lett. **4**, 380 (1960); Phys. Rev. **117**, 648 (1960).

[40] Y. Nambu and G. Jona-Lasinio. Phys. Rev. **122**, 345 (1961); Phys. Rev. **124**, 246 (1961).

[41] J. Goldstone, Nuovo Cim. **19**, 154 (1961).

[42] J. Goldstone, A. Salam and S. Weinberg, Phys. Rev. **127**, 965 (1962).

[43] S. R. Coleman, J. Wess and B. Zumino, Phys. Rev. **177**, 2239 (1969).

[44] C. G. Callan, Jr., S. R. Coleman, J. Wess and B. Zumino, Phys. Rev. **177**, 2247 (1969). doi:10.1103/PhysRev.177.2247

[45] A. V. Manohar, Lect. Notes Phys. **479**, 311 (1997) hep-ph/9606222.

[46] M. Gell-Mann, R. J. Oakes and B. Renner, Phys. Rev. **175**, 2195 (1968).

[47] S. Okubo, Prog. Theor. Phys. **27**, 949 (1962).

[48] G. Ecker, J. Gasser, A. Pich and E. de Rafael, Nucl. Phys. B **321**, 311 (1989).

[49] G. 't Hooft, Nucl. Phys. B **72** (1974) 461.

[50] S. R. Coleman and E. Witten, Phys. Rev. Lett. **45**, 100 (1980).

[51] A. Pich, Published in 'Tempe 2002, Phenomenology of large N_C QCD' 239-258.

[52] F. Guerrero and A. Pich, Phys. Lett. B **412**, 382 (1997) hep-ph/9707347;

[53] G. Ecker, J. Gasser, H. Leutwyler, A. Pich and E. de Rafael, Phys. Lett. B **223**, 425 (1989).

[54] V. Cirigliano, G. Ecker, M. Eidemuller, A. Pich and J. Portoles, Phys. Lett. B **596**, 96 (2004) hep-ph/0404004.

[55] S. Weinberg, Phys. Rev. Lett. **18**, 507 (1967).

[56] M. Jamin, J. A. Oller and A. Pich, Nucl. Phys. B **622**, 279 (2002), hep-ph/0110193.

[57] Z. H. Guo and J. A. Oller, Phys. Rev. D **84**, 034005 (2011) hep-ph/1104.2849.

[58] Z. H. Guo, J. A. Oller and J. Ruiz de Elvira, Phys. Rev. D **86**, 054006 (2012) hep-ph/1206.4163.

[59] T. Ledwig, J. Nieves, A. Pich, E. Ruiz Arriola and J. Ruiz de Elvira, Phys. Rev. D **90**, no. 11, 114020 (2014) 1407.3750.

[60] M. F. L. Golterman and S. Peris, Phys. Rev. D **61**, 034018 (2000) hep-ph/9908252.

[61] K. Fujikawa, Phys. Rev. Lett. **42**, 1195 (1979).

[62] G. t Hooft, Nucl. Phys. B 72 (1974) 461; 75 (1974) 461; E. Witten, Nucl. Phys. B 160 (1979) 57.

[63] P. Di Vecchia and G. Veneziano, Nucl. Phys. B 171 (1980) 253; C. Rosenzweig, J. Schechter and T. Trahem, Phys. Rev. D 21 (1980) 3388; E. Witten, Ann. Phys. 128 (1980) 363; K. Kawarabayashi and N. Ohta, Nucl. Phys. B 175, 477 (1980).

[64] P. Herrera-Siklody, J. I. Latorre, P. Pascual and J. Taron, Nucl. Phys. B **497**, 345 (1997) hep-ph/9610549.

[65] B. Moussallam, Phys. Rev. D **51**, 4939 (1995) hep-ph/9407402.

[66] X. K. Guo, Z. H. Guo, J. A. Oller and J. J. Sanz-Cillero, JHEP **1506**, 175 (2015) hep-ph/1503.02248.

[67] A. Gomez Nicola and J. R. Pelaez, Phys. Rev. D **65**, 054009 (2002) hep-ph/0109056.

[68] M. Jamin, J. A. Oller and A. Pich, Nucl. Phys. B **587**, 331 (2000) hep-ph/0006045.

[69] R. Escribano, P. Masjuan and J. J. Sanz-Cillero, JHEP **1105**, 094 (2011) hep-ph/1011.5884.

[70] J. Wess and B. Zumino, Phys. Lett. B **37**, 95 (1971).

[71] E. Witten, Nucl. Phys. B **223**, 422 (1983).

[72] J. F. Donoghue, E. Golowich and B. R. Holstein, Dynamics Of The Standard Model, Camb. Monogr. Part. Phys. Nucl. Phys. Cosmol. 2 (1992) 1.

[73] A. Dobado, A. Gomez-Nicola, A. L. Maroto and J. R. Pelaez, Effective lagrangians for the standard model, N.Y., Springer-Verlag, 1997. (Texts and Monographs in Physics).

[74] E. Pallante and A. Pich, Nucl. Phys. B **592**, 294 (2001) hep-ph/0007208.

[75] J. F. Donoghue, hep-ph/9506205.

[76] J. F. Donoghue, hep-ph/9607351.

[77] M. E. Peskin and D. V. Schroeder, An Introduction to quantum field theory (Perseus Books, 1995).

[78] K. M. Watson, Phys. Rev. **95** (1954) 228.

[79] R. Omnes, Nuovo Cim. **8**, 316 (1958).

[80] A. Pich, Prog. Part. Nucl. Phys. **75**, 41 (2014) hep-ph/1310.7922.

[81] M. Davier, S. Descotes-Genon, A. Hocker, B. Malaescu and Z. Zhang, Eur. Phys. J. C **56**, 305 (2008) hep-ph/0803.0979.

[82] M. Beneke and M. Jamin, JHEP **0809**, 044 (2008) hep-ph/0806.3156.

[83] A. Pich, hep-ph/1107.1123.

[84] D. Boito, M. Golterman, M. Jamin, A. Mahdavi, K. Maltman, J. Osborne and S. Peris, Phys. Rev. D **85**, 093015 (2012) hep-ph/1203.3146.

[85] K. Maltman, C. E. Wolfe, S. Banerjee, J. M. Roney and I. Nugent, Int. J. Mod. Phys. A **23**, 3191 (2008) hep-ph/0807.3195.

[86] M. Antonelli, V. Cirigliano, A. Lusiani and E. Passemar, JHEP **1310**, 070 (2013) hep-ph/1304.8134.

[87] K. G. Chetyrkin, J. H. Kuhn and A. A. Pivovarov, Nucl. Phys. B **533** (1998) 473

[88] A. Pich and J. Prades, JHEP **9910** (1999) 004.

[89] J. G. Korner, F. Krajewski and A. A. Pivovarov, Eur. Phys. J. C **20** (2001) 259.

[90] J. Kambor and K. Maltman, Phys. Rev. D **62** (2000) 093023.

[91] S. Chen, M. Davier, E. Gamiz, A. Hocker, A. Pich and J. Prades, Eur. Phys. J. C **22** (2001) 31.

[92] E. Gámiz, M. Jamin, A. Pich, J. Prades and F. Schwab, JHEP **0301** (2003) 060.

[93] E. Gámiz, M. Jamin, A. Pich, J. Prades and F. Schwab, Phys. Rev. Lett. **94** (2005) 011803.

[94] P. A. Baikov, K. G. Chetyrkin and J. H. Kuhn, Phys. Rev. Lett. **95** (2005) 012003.

[95] E. Gámiz, M. Jamin, A. Pich, J. Prades and F. Schwab, PoS KAON (2008) 008.

[96] A. Pich and J. Portoles, Phys. Rev. D **63**, 093005 (2001) hep-ph/0101194;

[97] D. Gomez Dumm and P. Roig, Eur. Phys. J. C **73**, no. 8, 2528 (2013) hep-ph/1301.6973.

[98] R. Barate *et al.* [ALEPH Collaboration], Eur. Phys. J. C **11**, 599 (1999) hep-ex/9903015.

[99] G. Abbiendi *et al.* [OPAL Collaboration], Eur. Phys. J. C **35**, 437 (2004) hep-ex/0406007.

[100] D. Epifanov *et al.* [Belle Collaboration], Phys. Lett. B **654**, 65 (2007) hep-ex/0706.2231.

[101] B. Aubert *et al.* [BaBar Collaboration], Nucl. Phys. Proc. Suppl. **189**, 193 (2009) hep-ex/0808.1121.

[102] S. Ryu *et al.* [Belle Collaboration], Phys. Rev. D **89**, no. 7, 072009 (2014) hep-ex/1402.5213.

[103] M. Jamin, A. Pich and J. Portoles, Phys. Lett. B **640**, 176 (2006) hep-ph/0605096.

[104] B. Moussallam, Eur. Phys. J. C **53**, 401 (2008) hep-ph/0710.0548.

[105] M. Jamin, A. Pich and J. Portoles, Phys. Lett. B **664**, 78 (2008) hep-ph/0803.1786.

[106] V. Bernard, JHEP **1406**, 082 (2014) hep-ph/1311.2569.

[107] P. del Amo Sanchez *et al.* [BaBar Collaboration], Phys. Rev. D **83**, 032002 (2011) hep-ex/1011.3917.

[108] J. E. Bartelt *et al.* [CLEO Collaboration], Phys. Rev. Lett. **76**, 4119 (1996).

[109] D. Buskulic *et al.* [ALEPH Collaboration], Z. Phys. C **74**, 263 (1997).

[110] J. P. Lees *et al.* [BaBar Collaboration], Phys. Rev. D **86**, 092010 (2012) hep-ex/1209.2734.

[111] A. Pich, Phys. Lett. B **196**, 561 (1987).

[112] E. Braaten, R. J. Oakes and S. M. Tse, Int. J. Mod. Phys. A **5**, 2737 (1990).

[113] B. A. Li, Phys. Rev. D **55**, 1436 (1997) hep-ph/9606402.

[114] G. J. Aubrecht, II, N. Chahrouri and K. Slanec, Phys. Rev. D **24**, 1318 (1981).

[115] S. Actis *et al.* [Working Group on Radiative Corrections and Monte Carlo Generators for Low Energies Collaboration], Eur. Phys. J. C **66**, 585 (2010) hep-ph/0912.0749.

[116] D. Kimura, K. Y. Lee and T. Morozumi, PTEP **2013**, 053B03 (2013) Erratum: [PTEP **2014**, no. 8, 089202 (2014)] hep-ph/1201.1794.

[117] S. Jadach, J. H. Kuhn and Z. Was, Comput. Phys. Commun. **64**, 275 (1990).

[118] S. Jadach, Z. Was, R. Decker and J. H. Kuhn, Comput. Phys. Commun. **76**, 361 (1993).

[119] O. Shekhovtsova, T. Przedzinski, P. Roig and Z. Was, Phys. Rev. D **86**, 113008 (2012) hep-ph/1203.3955.

[120] I. M. Nugent, T. Przedzinski, P. Roig, O. Shekhovtsova and Z. Was, Phys. Rev. D **88**, 093012 (2013) hep-ph/1310.1053.

[121] J. Gasser and H. Leutwyler, Nucl. Phys. B **250**, 517 (1985).

[122] J. Erler, Rev. Mex. Fis. **50**, 200 (2004) hep-ph/0211345.

[123] F. Ambrosino *et al.* [KLOE Collaboration], Phys. Lett. B **648**, 267 (2007) hep-ex/0612029.

[124] J. Beringer *et al.* [Particle Data Group Collaboration], Phys. Rev. D **86** (2012) 010001.

[125] M. Antonelli *et al.* [FlaviaNet Working Group on Kaon Decays Collaboration], Eur. Phys. J. C **69**, 399 (2010) hep-ph/1005.2323.

[126] J. Bijnens, G. Colangelo and G. Ecker, JHEP **9902** (1999) 020,

[127] J. Bijnens, G. Colangelo and G. Ecker, Annals Phys. **280** (2000) 100.

[128] J. Bijnens, L. Girlanda and P. Talavera, Eur. Phys. J. C **23** (2002) 539.

[129] A. V. Manohar, Published in 'Les Houches 1997, Probing the standard model of particle interactions, Pt. 2' 1091-1169.

[130] J. A. Oller, E. Oset and J. E. Palomar, Phys. Rev. D **63**, 114009 (2001) hep-ph/0011096.

[131] M. Jamin, J. A. Oller and A. Pich, Phys. Rev. D **74**, 074009 (2006) hep-ph/0605095.

[132] V. Bernard, N. Kaiser and U. G. Meissner, Nucl. Phys. B **357**, 129 (1991).

[133] P. Masjuan and S. Peris, JHEP **0705**, 040 (2007) hep-ph/0704.1247.

[134] J. J. Sanz-Cillero and A. Pich, Eur. Phys. J. C **27**, 587 (2003) hep-ph/0208199.

[135] V. Mateu and J. Portoles, Eur. Phys. J. C **52**, 325 (2007) hep-ph/0706.1039.

[136] D. Gomez Dumm, A. Pich and J. Portoles, Phys. Rev. D **69**, 073002 (2004) hep-ph/0312183.

[137] P. D. Ruiz-Femenía, A. Pich and J. Portolés, JHEP **0307** (2003) 003.

[138] V. Cirigliano, G. Ecker, M. Eidemüller, R. Kaiser, A. Pich and J. Portolés, JHEP **0504** (2005) 006.

[139] V. Cirigliano, G. Ecker, M. Eidemüller, R. Kaiser, A. Pich and J. Portolés, Nucl. Phys. B **753** (2006) 139.

[140] K. Kampf and J. Novotny, Phys. Rev. D **84** (2011) 014036.

[141] D. Gomez Dumm, A. Pich and J. Portoles, Phys. Rev. D **62**, 054014 (2000) hep-ph/0003320.

[142] F. Guerrero, Phys. Rev. D **57**, 4136 (1998) hep-ph/9801305.

[143] M. Jamin, J. A. Oller and A. Pich, Eur. Phys. J. C **24**, 237 (2002) hep-ph/0110194.

[144] Z. H. Guo, J. A. Oller and J. Ruiz de Elvira, Phys. Lett. B **712**, 407 (2012) hep-ph/1203.4381.

[145] R. Escribano, A. Gallegos, J. L. Lucio M, G. Moreno and J. Pestieau, Eur. Phys. J. C **28**, 107 (2003) hep-ph/0204338.

[146] Y. Amhis *et al.* [Heavy Flavor Averaging Group], *Averages of B-Hadron, C-Hadron, and tau-lepton properties as of early 2012*, hep-ex/1207.1158.

[147] S. Weinberg, Phys. Rev. **112**, 1375 (1958).

[148] C. Leroy and J. Pestieau, Phys. Lett. B **72** (1978) 398.

[149] K. Hayasaka [Belle Collaboration], PoS EPS **-HEP2009**, 374 (2009).

[150] K. Hayasaka's talk at 2nd Belle II Theory Interface Platform (B2TiP) Workshop (26-29 April, Krakow (Poland))

[151] B. Aubert *et al.* [BaBar Collaboration], Phys. Rev. D **77**, 112002 (2008) hep-ex/0803.0772.

[152] T. Bergfeld *et al.* [CLEO Collaboration], Phys. Rev. Lett. **79**, 2406 (1997) hep-ex/9706020.

[153] D. G. Dumm and P. Roig, Phys. Rev. D **86** (2012) 076009.

[154] T. Abe *et al.* [Belle-II Collaboration], physics.ins-det/1011.0352.

[155] R. Escribano, PoS Hadron **2013**, 206 (2013) hep-ph/1403.7453.

[156] S. Gonzàlez-Solís, AIP Conf. Proc. **1701** (2016) 050004 hep-ph/1501.07520.

[157] J. F. Donoghue, J. Gasser and H. Leutwyler, Nucl. Phys. B **343**, 341 (1990).

[158] B. Moussallam, Eur. Phys. J. C **14**, 111 (2000) hep-ph/9909292.

[159] A. Celis, V. Cirigliano and E. Passemar, Phys. Rev. D **89**, no. 1, 013008 (2014) hep-ph/1309.3564.

[160] Y. Iwamura, Prog. Theor. Phys. **56**, 1812 (1976).

[161] O. Babelon, J.-L. Basdevant, D. Caillerie and G. Mennessier, Nucl. Phys. B **113**, 445 (1976).

[162] Y. Iwamura, S. Kurihara and Y. Takahashi, Prog. Theor. Phys. **58**, 1669 (1977).

[163] A. N. Kamal, Can. J. Phys. **57**, 1815 (1979).

[164] A. N. Kamal and E. D. Cooper, Z. Phys. C **8**, 67 (1981).

[165] A. N. Kamal and R. Sinha, Phys. Rev. D **36**, 3510 (1987).

[166] A. N. Kamal, N. Sinha and R. Sinha, Z. Phys. C **41**, 207 (1988).

[167] M. Albaladejo and B. Moussallam, arXiv:1507.04526 [hep-ph].

[168] J. Portolés, AIP Conf. Proc. **1322** (2010) 178.

[169] J. Schechter, A. Subbaraman and H. Weigel, Phys. Rev. D **48** (1993) 339. T. Feldmann and P. Kroll, Eur. Phys. J. C **5** (1998) 327; Phys. Scripta T **99** (2002) 13. T. Feldmann, P. Kroll and B. Stech, Phys. Rev. D **58** (1998) 114006; Phys. Lett. B **449** (1999) 339. T. Feldmann, Int. J. Mod. Phys. A **15** (2000) 159. R. Escribano and J. M. Frère, Phys. Lett. B **459** (1999) 288; JHEP **0506** (2005) 029. R. Escribano, P. Masjuan and J. J. Sanz-Cillero, JHEP **1105**, 094 (2011) hep-ph/1011.5884.

[170] R. Kaiser and H. Leutwyler, In *Adelaide 1998, Nonperturbative methods in quantum field theory* 15-29 hep-ph/9806336.

[171] P. Kroll, Mod. Phys. Lett. A **20**, 2667 (2005) hep-ph/0509031.

[172] F. Ambrosino *et al.*, JHEP **0907**, 105 (2009) hep-ph/0906.3819.

[173] V. Cirigliano, G. Ecker and H. Neufeld, Phys. Lett. B **513** (2001) 361.

[174] P. Roig, arXiv:1307.8277 [hep-ph].

[175] R. F. Dashen, Phys. Rev. **183**, 1245 (1969).

[176] P. Langacker and H. Pagels, Phys. Rev. D **8**, 4620 (1973).

[177] T. Feldmann, P. Kroll and B. Stech, Phys. Lett. B **449** (1999) 339 hep-ph/9812269.

[178] J. R. Peláez, Phys. Rev. Lett. **92** (2004) 102001; Mod. Phys. Lett. A **19** (2004) 2879. V. Cirigliano, G. Ecker, H. Neufeld and A. Pich, JHEP **0306** (2003) 012. I. Caprini, G. Colangelo and H. Leutwyler, Phys. Rev. Lett. **96** (2006) 132001. S. Descotes-Genon and B. Moussallam, Eur. Phys. J. C **48** (2006) 553.

[179] P. Roig, arXiv:1401.5038 [hep-ph]. To be published by the Institute of Physics (IOP) in the Journal of Conference Series.

[180] V. Bernard, D. R. Boito and E. Passemar, Nucl. Phys. Proc. Suppl. **218**, 140 (2011).

[181] J. A. Oller and E. Oset, Phys. Rev. D **60**, 074023 (1999).

[182] J. A. Oller, E. Oset and A. Ramos, Prog. Part. Nucl. Phys. **45**, 157 (2000).

[183] A. D. Martin and T. D. Spearman, Elementary Particle Theory, North-Holland, Amsterdam, 1970.

[184] J. D. Bjorken, Phys. Rev. Lett. **4**, 473 (1960).

[185] P. S. Lee, G. L. Shaw and D. Silverman, Phys. Rev. D **10**, 2251 (1974).

[186] C. Sorensen, Phys. Rev. D **23**, 2618 (1981).

[187] J.-L. Basdevant and E. L. Berger, Phys. Rev. D **19**, 239 (1979).

[188] J.-L. Basdevant and E. L. Berger, Phys. Rev. Lett. **40**, 994 (1978).

[189] A. Astier, L. Montanet, M. Baubillier and J. Duboc, Phys. Lett. B **25**, 294 (1967).

[190] S. Descotes-Genon and B. Moussallam, Eur. Phys. J. C **74** (2014) 2946.

[191] S. Tisserant and T. N. Truong, Phys. Lett. B **115** (1982) 264.

[192] A. Bramon, S. Narison and A. Pich, Phys. Lett. B **196**, 543 (1987).

[193] H. Neufeld and H. Rupertsberger, Z. Phys. C **68** (1995) 91.

[194] S. Nussinov and A. Soffer, Phys. Rev. D **78**, 033006 (2008).

[195] N. Paver and Riazuddin, Phys. Rev. D **82**, 057301 (2010).

[196] M. K. Volkov and D. G. Kostunin, Phys. Rev. D **86**, 013005 (2012).

[197] S. Nussinov and A. Soffer, Phys. Rev. D **80**, 033010 (2009).

[198] N. Paver and Riazuddin, Phys. Rev. D **84**, 017302 (2011).

[199] M. Ablikim *et al.* [BESIII Collaboration], Phys. Rev. D **87**, 032006 (2013).

[200] G. A. Baker and P. Graves-Morris, *Encyclopedia of Mathematics and Its Applications*, Cambridge University Press, Cambridge U.K. (1996).

[201] C. Bender and S. Orszag. Advanced Mathematical Methods for Scientists and Engineers I: asymptotic methods and perturbation theory. Springer 1999, section 8.6.

[202] J. S. R. Chisholm, Mathematics of Computation, **27** (124), 1973; J. S. R. Chisholm and J. McEwan. Proc. R. Soc. Lond. A, **336** 421-452, 1974; D. Levin, J. Inst. Maths. Applics, **18** 1–8, 1976; R. Hughes Jones, Journal of approx. theory, **16** 201–233, 1976.

[203] P. Masjuan and P. Sanchez-Puertas, hep-ph/1504.07001.

[204] S. Gonzàlez-Solís, P. Masjuan and P. Sánchez-Puertas. Quadratic approximants (work in progress).

[205] A. Beddall and A. Beddall, Eur. Phys. J. C **54**, 365 (2008).

[206] H. Berghauser *et al.*, Phys. Lett. B **701** (2011) 562.

[207] P. Aguar-Bartolome *et al.* [A2 Collaboration], Phys. Rev. C **89**, no. 4, 044608 (2014) hep-ex/1309.5648.

[208] M. Berlowski *et al.* [CELSIUS/WASA Collaboration], Phys. Rev. D **77**, 032004 (2008) hep-ex/0711.3531.

[209] P. Adlarson *et al.*, nucl-ex/1509.06588.

[210] R. Arnaldi *et al.* [NA60 Collaboration], Phys. Lett. B **677**, 260 (2009) hep-ph70902.2547.

[211] R. I. Dzhelyadin *et al.*, Sov. J. Nucl. Phys. **32** (1980) 520 [Yad. Fiz. **32** (1980) 1005].

[212] E. Abouzaid *et al.* [KTeV Collaboration], Phys. Rev. Lett. **100**, 182001 (2008) hep-ex/0802.2064.

[213] F. Ambrosino *et al.* [KLOE and KLOE-2 Collaborations], Phys. Lett. B **702**, 324 (2011) hep-ex/1105.6067.

[214] G. P. Lepage and S. J. Brodsky, Phys. Lett. B **87**, 359 (1979); Phys. Rev. D **22**, 2157 (1980).

[215] A. V. Manohar, Phys. Lett. B **244** (1990) 101.

[216] J. M. Gerard and T. Lahna, Phys. Lett. B **356**, 381 (1995) hep-ph/9506255.

[217] Z. H. Guo and P. Roig, Phys. Rev. D **82**, 113016 (2010) hep-ph/1009.2542.

[218] P. Roig and J. J. Sanz-Cillero, Nucl. Part. Phys. Proc. **258-259**, 98 (2015) hep-ph/1407.3192.

[219] V. A. Novikov, M. A. Shifman, A. I. Vainshtein, M. B. Voloshin and V. I. Zakharov, Nucl. Phys. B **237** (1984) 525.

[220] L. G. Landsberg, Phys. Rept. **128** (1985) 301.

[221] H. Czyz, S. Ivashyn, A. Korchin and O. Shekhovtsova, Phys. Rev. D **85**, 094010 (2012) hep-ph/1202.1171.

[222] P. Roig, A. Guevara and G. Lpez Castro, Phys. Rev. D **89**, no. 7, 073016 (2014) hep-ph/1401.4099.

[223] C. Hanhart, A. Kupść, U.-G. Meißner,, F. Stollenwerk and A. Wirzba, Eur. Phys. J. C **73**, no. 12, 2668 (2013) Erratum: [Eur. Phys. J. C **75**, no. 6, 242 (2015)] hep-ph/1307.5654.

Bibliography

[224] M. Hoferichter, B. Kubis, S. Leupold, F. Niecknig and S. P. Schneider, Eur. Phys. J. C **74**, 3180 (2014) hep-ph/1410.4691.

[225] F. Perrsson, hep-ph/0106130.

[226] C. C. Lih, J. Phys. G **38** (2011) 065001 hep-ph/0912.2147.

[227] C. Q. Geng and C. C. Lih, Phys. Rev. C **86**, 038201 (2012) Erratum: [Phys. Rev. C **87**, no. 3, 039901 (2013)] hep-ph/1209.0174.

[228] I. Balakireva, W. Lucha and D. Melikhov, Phys. Rev. D **85**, 036006 (2012) hep-ph/1110.6904.

[229] Y. Klopot, A. Oganesian and O. Teryaev, Phys. Rev. D **87**, no. 3, 036013 (2013) Erratum: [Phys. Rev. D **88**, no. 5, 059902 (2013)] hep-ph/1211.0874.

[230] Y. Klopot, A. Oganesian and O. Teryaev, JETP Lett. **99**, 679 (2014) hep-ph/1312.1226.

[231] S. S. Agaev, V. M. Braun, N. Offen, F. A. Porkert and A. Schfer, Phys. Rev. D **90**, no. 7, 074019 (2014) hep-ph/1409.4311.

[232] S. S. Agaev, V. M. Braun, N. Offen and F. A. Porkert, Phys. Rev. D **83**, 054020 (2011) hep-ph/1012.4671.

[233] T. Petri, nucl-th/1010.2378.

[234] C. Terschlüsen, B. Strandberg, S. Leupold and F. Eichstädt, Eur. Phys. J. A **49**, 116 (2013) hep-ph/1305.1181.

[235] P. Masjuan Queralt, hep-ph/1005.5683.

[236] R. Escribano, S. Gonzalez-Solis, P. Masjuan and P. Sanchez-Puertas, hep-ph/1512.07520.

[237] P. Masjuan and J. J. Sanz-Cillero, Eur. Phys. J. C **73**, 2594 (2013) hep-ph/1306.6308.

[238] P. Masjuan, E. Ruiz Arriola and W. Broniowski, Phys. Rev. D **87**, no. 1, 014005 (2013) hep-ph/1210.0760.

[239] A. R. Barker, H. Huang, P. A. Toale and J. Engle, Phys. Rev. D **67**, 033008 (2003) hep-ph/0210174.

[240] M. Knecht and A. Nyffeler, Phys. Rev. D **65**, 073034 (2002) hep-ph/0111058.

[241] F. Jegerlehner and A. Nyffeler, Phys. Rept. **477**, 1 (2009) hep-ph/0902.3360.

[242] H. Suura, T. F. Walsh and B. L. Young, Lett. Nuovo Cim. **4S2** (1972) 505 [Lett. Nuovo Cim. **4** (1972) 505].

[243] G. Kopp, T. F. Walsh and P. M. Zerwas, Nucl. Phys. B **70** (1974) 461.

[244] K. S. Babu and E. Ma, Phys. Lett. B **119** (1982) 449.

[245] C. W. Xiao, T. Dato, C. Hanhart, B. Kubis, U.-G. Meiner and A. Wirzba, hep-ph/1509.02194.

[246] I. Larin *et al.* [PrimEx Collaboration], Phys. Rev. Lett. **106**, 162303 (2011) nucl-ex/1009.1681.

[247] R. H. Dalitz, Proc. Phys. Soc. A **64** (1951) 667.

[248] D. W. Joseph, Nuovo Cim. **16** (1960) 997.

[249] T. Husek, K. Kampf and J. Novotny, Phys. Rev. D **92**, no. 5, 054027 (2015) hep-ph/1504.06178.

[250] N. M. Kroll and W. Wada, Phys. Rev. **98** (1955) 1355.

[251] T. Miyazaki and E. Takasugi, Phys. Rev. D **8** (1973) 2051.

[252] E. Byckling and K. Kajantie, *Particle Kinematics*, Wiley (1973).

[253] P. Nyborg, H. S. Song, W. Kernan and R. H. Good, Phys. Rev. **140** (1965) B914.

[254] N. Byers and C. N. Yang, Rev. Mod. Phys. **36** (1964) 595.

[255] P. Sanchez-Puertas and P. Masjuan, EPJ Web Conf. **81** (2014) 05025 hep-ph/1410.4327.

[256] P. Masjuan and M. Vanderhaeghen, J. Phys. G **42** (2015) 12, 125004 hep-ph/1212.0357.

[257] P. Masjuan, Nucl. Part. Phys. Proc. **260** (2015) 111 hep-ph/1411.6397.

[258] R. Escribano and S. Gonzàlez-Solís, hep-ph/1511.04916.

[259] P. Masjuan, J. Ruiz de Elvira and J. J. Sanz-Cillero, Phys. Rev. D **90** (2014) 9, 097901 hep-ph/1410.2397.

[260] P. Masjuan, J. J. Sanz-Cillero and J. Virto, Phys. Lett. B **668** (2008) 14 hep-ph/0805.3291.

[261] P. Masjuan and S. Peris, Phys. Lett. B **686** (2010) 307 hep-ph/0903.0294.

[262] B. Ananthanarayan, G. Colangelo, J. Gasser and H. Leutwyler, Phys. Rept. **353**, 207 (2001) hep-ph/0005297.

[263] B. Kubis and J. Plenter, Eur. Phys. J. C **75** (2015) 6, 283 hep-ph/1504.02588.

[264] T. Feldmann and P. Kroll, Phys. Rev. D **58** (1998) 057501 hep-ph/9805294.

[265] L. Ametller, J. Bijnens, A. Bramon and F. Cornet, Phys. Rev. D **45**, 986 (1992).

[266] A. Bramon and E. Masso, Phys. Lett. B **104**, 311 (1981).

[267] S. J. Brodsky and G. P. Lepage, Phys. Rev. D **24**, 1808 (1981).

[268] B. Aubert *et al.* [BaBar Collaboration], Phys. Rev. D **74**, 012002 (2006) hep-ex/0605018.

[269] R. Escribano and J. M. Frere, JHEP **0506**, 029 (2005) hep-ph/0501072.

[270] T. Feldmann, P. Kroll and B. Stech, Phys. Rev. D **58**, 114006 (1998) hep-ph/9802409.

[271] H. Leutwyler, Nucl. Phys. Proc. Suppl. **64**, 223 (1998) hep-ph/9709408.

[272] M. Benayoun, L. DelBuono and H. B. O'Connell, Eur. Phys. J. C **17**, 593 (2000) hep-ph/9905350.

[273] R. Escribano and J. Nadal, JHEP **0705**, 006 (2007) hep-ph/0703187.

[274] J. M. Gerard and A. Martini, Phys. Lett. B **730** (2014) 264 hep-ph/1312.3081.

[275] C. Michael *et al.* [ETM Collaboration], Phys. Rev. Lett. **111**, no. 18, 181602 (2013) hep-lat/1310.1207.